

UC San Diego

UC San Diego Electronic Theses and Dissertations

Title

The Physical Conditions of Atomic Gas at High Redshift

Permalink

<https://escholarship.org/uc/item/39d8p5k2>

Author

Neeleman, Marcel

Publication Date

2015

Peer reviewed|Thesis/dissertation

UNIVERSITY OF CALIFORNIA, SAN DIEGO

The Physical Conditions of Atomic Gas at High Redshift

A dissertation submitted in partial satisfaction of the
requirements for the degree
Doctor of Philosophy

in

Physics

by

Marcel Neeleman

Committee in charge:

Professor Alison Coil, Chair
Professor J. Xavier Prochaska, Co-Chair
Professor Kim Griest
Professor Kevin Quest
Professor Barney Rickett

2015

Copyright
Marcel Neeleman, 2015
All rights reserved.

The dissertation of Marcel Neeleman is approved, and it is acceptable in quality and form for publication on microfilm and electronically:

Co-Chair

Chair

University of California, San Diego

2015

DEDICATION

To Art Wolfe

whose passion for science
was an inspiration to all who knew him

EPIGRAPH

*We find them smaller and fainter
in constantly increasing numbers,
and we know
that we are reaching into space,
farther and farther,
until,
with the faintest nebulae that can be detected
with the greatest telescopes,
we arrive at the frontier
of the known universe*

–Edwin Powell Hubble

TABLE OF CONTENTS

	Signature Page	iii
	Dedication	iv
	Epigraph	v
	Table of Contents	vi
	List of Figures	ix
	List of Tables	x
	Acknowledgements	xi
	Vita	xiii
	Abstract of the Dissertation	xiv
Chapter 1	Introduction	1
	1.1 The Interstellar Medium	2
	1.1.1 Theoretical Description of the ISM	3
	1.1.2 Cooling of the Atomic ISM: Fine-Structure Lines	4
	1.1.3 Observational Studies of the Atomic ISM	5
	1.2 Galaxy Evolution	6
	1.3 Observational Studies of High-z Atomic Gas	8
	1.3.1 Emission Studies at High Redshift	8
	1.3.2 Absorption Studies at High Redshift	9
	1.4 Distribution of Atomic Gas in the Universe	11
	1.5 Statistical Measurements of Atomic Gas	12
	1.5.1 Metallicity	13
	1.5.2 Kinematics	14
	1.5.3 Physical Parameters	15
	1.6 Overview of the Thesis	16
	1.7 References for Chapter 1	17
Chapter 2	The Fundamental Plane of Damped Ly- α Systems	22
	2.1 Abstract	22
	2.2 Introduction	23
	2.3 Sample Selection, Parameter Definition and Sample Biases	27
	2.3.1 Observations and Reduction	27
	2.3.2 Methodology	28

	2.3.3	Systematic Errors and Biases due to Sample Selection Criteria	32
	2.4	Distributions and Correlations	38
	2.4.1	Distributions	38
	2.4.2	Correlations and Dependencies	42
	2.5	The Fundamental Plane(s) of DLAs	51
	2.6	Discussion	56
	2.6.1	Implications of Two Parameter Dependencies	57
	2.6.2	Implications of the Fundamental Plane of DLAs	61
	2.6.3	Comparison with Models	63
	2.7	Summary	67
	2.8	Acknowledgements	69
	2.9	References for Chapter 2	69
Chapter 3		Probing the Physical Conditions of Atomic Gas at High Redshift	76
	3.1	Abstract	76
	3.2	Introduction	77
	3.3	Sample Selection	80
	3.4	Measurements	83
	3.4.1	HI Column Density Measurements	83
	3.4.2	Metallicity Measurements	83
	3.4.3	Column Density Measurements	84
	3.5	Method	85
	3.5.1	Si II* and C II* Technique	87
	3.5.2	Applying the Technique	90
	3.5.3	Electron Density Constraint	95
	3.6	Results	96
	3.6.1	Physical Parameters of DLAs	99
	3.6.2	Correlations with Global DLA Properties	102
	3.6.3	Component Analysis	104
	3.7	Discussion	107
	3.7.1	Discussion of the Empirical Results	107
	3.7.2	Comparison with Previous Observations	110
	3.7.3	Comparison with the Two-Phase Model	117
	3.7.4	Implications for High- z Galaxies	118
	3.8	Summary	123
	3.9	Acknowledgements	125
	3.10	References for Chapter 3	125
Chapter 4		The HI Content of the Universe over the Past 10 Gyrs	131
	4.1	Abstract	131
	4.2	Introduction	132
	4.3	Sample Selection	134

	4.3.1	Statistical Sample	135
4.4	Method		136
	4.4.1	Resolution Considerations	139
	4.4.2	S/N Considerations	140
4.5	Results		142
	4.5.1	Total sample of DLAs	144
	4.5.2	$f(N_{\text{HI}}, X)$	146
	4.5.3	$\ell_{\text{DLA}}(X)$	147
	4.5.4	ρ_{HI}	149
4.6	Summary and Discussion		152
4.7	Acknowledgements		154
4.8	References for Chapter 4		155
Chapter 5	Conclusions and Future Work		158
	5.1	References for Chapter 5	162
Appendix A	Full Tables		164
Appendix B	Figures		222

LIST OF FIGURES

Figure 2.1:	Optical depth Profile of the DLAs	33
Figure 2.2:	Distributions of metallicity, ℓ_c , W_{1526} , and Δv_{90}	40
Figure 2.3:	Metallicity versus HI column density	46
Figure 2.4:	Redshift, Δv_{90} , W_{1526} , and ℓ_c plotted against HI column density . .	48
Figure 2.5:	Redshift evolution of Δv_{90} and W_{1526}	50
Figure 2.6:	Fundamental Plane of DLAs	52
Figure 2.7:	Projection of two correlations of the Fundamental Plane	53
Figure 2.8:	Projection of two correlations of the W_{1526} Fundamental Plane . . .	56
Figure 2.9:	Comparison of the two kinematic properties, Δv_{90} and W_{1526} . . .	59
Figure 2.10:	Distribution of the kinematic parameter, Δv_{90}	66
Figure 3.1:	Si II*, C II* and Si II transition for DLAs with detected Si II*	86
Figure 3.2:	Si and C ratios for a range of different physical parameters	89
Figure 3.3:	Example of a Monte Carlo Markov Chain run for DLA J1313+1441	91
Figure 3.4:	The likelihood functions for the different possible Si and C ratios . .	93
Figure 3.5:	1- σ constraints on the neutral hydrogen density, electron density, temperature, and pressure for all of the DLAs in the sample	97
Figure 3.6:	Temperature and neutral hydrogen density for the complete sample . . .	101
Figure 3.7:	Possible correlations between internal and external parameters . . .	103
Figure 3.8:	Temperature and neutral hydrogen density for the individual com- ponents for those DLAs with detectable levels of Si II*	106
Figure 3.9:	Correlation between pressure and r_C	109
Figure 3.10:	Allowed temperature and neutral hydrogen density parameter space for DLAs	114
Figure 3.11:	r_C and r_{Si} ratio for the complete sample	122
Figure 4.1:	Search path for the complete sample of quasars	138
Figure 4.2:	Resolution and S/N effects on HI column density measurement . . .	141
Figure 4.3:	HI fit of the HST-DLA sample	145
Figure 4.4:	HI column density distribution function, $f(N_{HI}, X)$ at low redshift . . .	148
Figure 4.5:	$\ell_{DLA}(X)$ and n_{DLA} for DLAs	150
Figure 4.6:	Mass density of HI in DLAs, ρ_{HI}	151
Figure B.1:	Optical depth Profile of the DLAs	223
Figure B.2:	HI fits of the HST-DLA sample	230

LIST OF TABLES

Table 2.1:	Journal of Observations for HIRES DLA Sample	28
Table 2.2:	HIRES DLA sample	37
Table 2.3:	Fitting Functions to the Distributions	39
Table 2.4:	Table of Potential Correlations	43
Table 3.1:	Fine Structure DLA sample	82
Table 3.2:	Results of Si II* and C II* Technique	98
Table 3.3:	Comparison between Temperature Measurements	111
Table 4.1:	HST QSO sample	135
Table 4.2:	DLA sample	143
Table A.1:	Journal of Observations for HIRES DLA Sample	165
Table A.2:	HIRES DLA sample	170
Table A.3:	Fine Structure DLA sample	176
Table A.4:	Results of Si II* and C II* Technique	181
Table A.5:	HST QSO sample	186

ACKNOWLEDGEMENTS

First, let me start off by recognizing the important role my former advisor, the late Arthur Wolfe, had in every aspect of the creation of this thesis. The wonderful conversations we had in his office sparked the research for all three of the papers that form the heart of this thesis. His insight and passion for science have shaped this thesis and my research more than anything else. He will be sorely missed.

I next would like to thank Xavier Prochaska, for his willingness to take over the role as advisor, allowing me to finish the work I started under Art. His guidance allowed me to continue to grow as a scientist. I also thank Alison Coil, for stepping in on the ‘UCSD-side’ as chair of my committee. I feel fortunate that, in essence, I had three advisors during my graduate studies; a luxury I cherish.

I thank my committee members, Kim Griest, Barney Rickett, and Kevin Quest, for agreeing to be on the committee and their willingness to read this work. I would also like to thank the support of the CASS department over the years. In particular, I would like to thank Marc Rafelski for his willingness to answer any questions I might have had independent of how stupid they may have been.

Finally, I would like to thank my family. My parents for their support over the years, and allowing me to move to the United States to get my education. My sister for her support and quirkiness, reminding me that life is short, so you better live it the way you want. Lastly, I would like to thank my wife who has supported me during all my years as a student. She has been the most important person in my life, and without her I would be lost. I appreciate all she has done for me, and hope I can provide the support and love she has always given me.

OFFICIAL ACKNOWLEDGEMENTS

Chapter 2, in full (with minor exceptions to conform to this thesis), is a reprint of

material previously published as “The Fundamental Plane of Damped Ly α Systems”, by Marcel Neeleman, Arthur M. Wolfe, J. Xavier Prochaska, & Marc Rafelski, published in the The Astrophysical Journal, 2013, Vol. 769, p.54. I was the primary investigator and author of this paper.

Chapter 3, in full (with minor exceptions to conform to this thesis), is a reprint of material previously published as “Probing the Physical Conditions of Atomic Gas at High Redshift”, by Marcel Neeleman, J. Xavier Prochaska, & Arthur M. Wolfe, published in the The Astrophysical Journal, 2015, Vol. 800, p.7. I was the primary investigator and author of this paper.

Chapter 4 is a draft of material that will be submitted as “The HI Content of the Universe over the Past 10 Gyrs”, by Marcel Neeleman, J. Xavier Prochaska, Joseph Ribaud, Nicolas Lehner, J. Christopher Howk, Marc Rafelski, & Nissim Kanekar to the The Astrophysical Journal. I am the primary investigator and author of this paper.

VITA

- 2006 B. S. in Physics and Mathematics, University of California, Santa Barbara
- 2015 Ph. D. in Physics, University of California, San Diego

PUBLICATIONS

Neeleman, M., Prochaska, J.X., Ribaud, J., Lehner, N., Howk, J.C., Rafelski, M., Kanekar, N., “The HI Content of the Universe over the Past 10 Gyrs”, 2015 in prep

Neeleman, M., Prochaska, J.X., Wolfe, A.M., “Probing the Physical Conditions of Atomic Gas at High Redshift”, 2015, *Astrophysical Journal*, 800, 7

Bird, S., Haehnelt, M., **Neeleman, M.**, Genel, S., Vogelsberger, M., Hernquist, L., “Reproducing the Kinematics of Damped Lyman-alpha Systems”, 2015, *Monthly Notices of the Royal Astronomical Society*, 447, 1834

Berg, T.A.M., **Neeleman, M.**, Prochaska, J.X., Ellison, S.L., Wolfe, A.M., “The Most Metal-Rich Damped Lyman Alpha Systems at $z > 1.5$ I: The Data”, 2015, *Publications of the Astronomical Society of the Pacific*, 127, 167

Pei, L., et al. “Reverberation mapping of the Kepler Field AGN KA 1858+4850”, 2014, *Astrophysical Journal*, 795, 38

Rafelski, M., **Neeleman, M.**, Fumagalli, M., Wolfe, A.M., Prochaska, J.X., “The Rapid Decline in Metallicity of Damped Ly α Systems at $z \sim 5$ ”, 2014, *Astrophysical Journal Letters*, 782, 29

Neeleman, M., Wolfe, A.M., Prochaska, J.X., Rafelski, M., “The Fundamental Plane of Damped Ly- α Systems”, 2013, *Astrophysical Journal*, 769, 54

Rafelski, M., Wolfe, A.M., Prochaska, J.X., **Neeleman, M.**, Mendez, A.J., “The Metallicity Evolution of Damped Ly α Systems out to $z \sim 5$ ”, 2012, *Astrophysical Journal*, 755, 89

ABSTRACT OF THE DISSERTATION

The Physical Conditions of Atomic Gas at High Redshift

by

Marcel Neeleman

Doctor of Philosophy in Physics

University of California, San Diego, 2015

Professor Alison Coil, Chair
Professor J. Xavier Prochaska, Co-Chair

In this thesis we provide insight into the chemical composition, physical conditions and cosmic distribution of atomic gas at high redshift. We study this gas in absorption against bright background quasars in absorption systems known as Damped Ly α Systems (DLAs). These systems contain the bulk of the atomic gas at high redshift and are the likely progenitors of modern-day galaxies.

In Chapter 2, we find that the atomic gas in DLAs obeys a mass-metallicity relationship that is similar to the mass-metallicity relationship seen in star-forming galaxies. The evolution of this relationship is linear with redshift, allowing for a planar equation to

accurately describe this evolution, which provides a more stringent constraint on simulations modeling DLAs. Furthermore, the concomitant evolution of the mass-metallicity relationship of atomic gas and star-forming galaxies suggests an intimate link between the two.

We next use a novel way to measure the physical conditions of the gas by using fine-structure line ratios of singly ionized carbon and silicon. By measuring the density of the upper and lower level states, we are able to determine the temperature, hydrogen density and electron density of the gas. We find that the conditions present in this high redshift gas are consistent with the conditions we see in the local interstellar medium (ISM). A few absorbers have higher than expected pressure, which suggests that they probe the ISM of star-forming galaxies.

Finally in Chapter 4, we measure the cosmic neutral hydrogen density at redshifts below 1.6. Below this redshift, the Ly- α line of hydrogen is absorbed by the atmosphere, making detection difficult. Using the archive of the Hubble Space Telescope, we compile a comprehensive list of quasars for a search of DLAs at redshift below 1.6. We find that the incidence rate of DLAs and the cosmic neutral hydrogen density is smaller than previously measured, but consistent with the values both locally and at redshifts of about 2.

Altogether, these results improve our understanding of atomic gas at high redshift and help illuminate how this important component shapes the galaxies we see today.

Chapter 1

Introduction

Starting from its humble prehistoric beginnings, astronomy has interested the human mind for millennia. Although astronomy has undergone a vast transformation from a phenomenological description of the motion of the celestial objects to a science rooted deeply in physics, this interest has not wavered. We know now that our Sun is just a single star in a vast collection of stars which form our Galaxy, the Milky Way, which in turn is just a single galaxy of which countless more exist.

By using a large variety of telescopes, we are able to collect photons from almost the full range of the electromagnetic spectrum. These observations have allowed us a detailed look into the inner workings of the constituents that make up a galaxy. We broadly can divide these constituents into three categories: the stars, the dark matter and everything else that is remaining, which is termed the interstellar medium (ISM). In this thesis we will focus on the latter, although we will discuss the others as the interplay between the three constituents is critical in providing us with a complete view of how galaxies have formed and evolved into the structures we see today.

1.1 The Interstellar Medium

The interstellar medium (ISM) is broadly defined as everything in the galaxy between the stars (Draine, 2011). This includes gas, dust, photons, cosmic rays, and the interstellar magnetic field. Arguably the most important component of the ISM in the majority of galaxies is the interstellar gas. This gas can contain a significant fraction of the total baryonic mass of the galaxy, and it provides the fuel for stars to form. A detailed understanding of the chemical composition, physical characteristics and kinematic structure of interstellar gas is therefore critical in understanding star formation and the appearance of galaxies as a whole.

Interstellar gas is composed largely out of hydrogen and helium, the primary elements produced in big bang nucleosynthesis. However, the gas is enriched with heavy elements such as carbon and oxygen mainly by supernova explosions. Temperatures and densities vary strongly in the interstellar gas, creating a highly complex structure. However, we can broadly define five different ‘phases’, based on the density, temperature and ionization of the gas. It is critical to remember that these ‘phases’ are not clear distinct phases as each phase includes a wide range of allowed temperatures and densities.

The hottest phase is known as the hot ionized medium (HIM; $T > 10^{5.5}$ K) and is composed of hydrogen gas that is ionized by supernova shock heating (McKee & Ostriker, 1977). A somewhat cooler ($T \sim 10^4$ K) ionized gas is known as the warm ionized medium (WIM). This phase is the result of photoionization of the gas mainly by bright, young stars. The densest regions of the WIM, which are closest to the ionizing stars, are known as H II regions. The next two phases describe the neutral, atomic gas, where hydrogen has not been ionized. These two phases, known as the warm neutral medium (WNM) and the cold neutral medium (CNM) are the study of this thesis, and are described in detail below¹. Finally, the last phase is cold ($T < 50$ K) and dense

¹Although we refer to this phase as the neutral atomic phase, this only refers to the hydrogen, not the

enough for hydrogen to exist in its molecular form, known therefore as the molecular phase. When this phase becomes dense enough, the gas becomes self-gravitating. This results in dense molecular clouds.

1.1.1 Theoretical Description of the ISM

As the temperature decreases and density increases in the interstellar gas, there comes a point where most of the hydrogen ions and electrons recombine to form neutral hydrogen. Current models (Wolfire et al., 1995, 2003) suggests this occurs around a density of $n_{\text{H}} > 0.2 \text{ cm}^{-3}$ and $T < 7000 \text{ K}$. We will refer to this gas as atomic gas. The atomic gas phase of the ISM is of interest because there exists a close link with star formation. To be specific, as the surface density of gas increases, so does the star formation rate density (e.g. Kennicutt Jr, 1998; Bigiel et al., 2008). Such a link is expected as denser and colder conditions are needed for gas to condense and form stars.

The first theoretical description of the atomic gas phase was performed by Field et al. (1969). At the heart of their analysis are two assumptions: 1) The gas is in pressure equilibrium with its surroundings, and 2) the gas is in thermodynamic equilibrium, i.e. the heating of the gas is balanced by the cooling of the gas. Under these assumptions, Field et al. (1969) showed that for a range of pressures, a single pressure allows two stable phases to coexist under pressure equilibrium. One dense, cold phase (the CNM) with typical temperatures below 500 K and a warmer, less dense phase (the WNM) with typical temperatures around 6000 K.

Subsequent authors have improved upon this ‘two-phase’ model. In particular, McKee & Ostriker (1977) showed that the HIM must also be in pressure equilibrium with the atomic gas, otherwise the atomic gas would rapidly dissipate as it is swept up

other elements in the gas. For instance, neutral carbon has a ionization potential below 13.6 eV and is almost completely ionized in all but the densest regions.

by the shockwaves of supernova explosions. D’Hendecourt & Léger (1987) showed that the primary source of heating of this gas is not due to cosmic-ray heating as was assumed by Field et al. (1969), but instead is due to photoelectric heating. Photoelectric heating is the heating of the gas by electrons that are ejected from large molecules such as polyaromatic carbohydrates (PAH) and dust when ionized by ultraviolet starlight. Although these improvements have changed some of the specifics of the two phase model (see e.g. Wolfire et al., 1995, 2003), the model is still the accepted paradigm of the neutral atomic phase of the ISM.

1.1.2 Cooling of the Atomic ISM: Fine-Structure Lines

As was already appreciated by Bahcall & Wolf (1968), the most efficient way to cool atomic gas in the ISM is by way of fine-structure line cooling. Quantum mechanically, fine structure splitting of an energy level in an ion is due to spin-orbit coupling. This coupling causes the energy levels between two different quantum mechanical states with the same electron configuration, total orbital angular momentum (L) and total spin orbital angular momentum (S) to differ slightly.

The energy difference between the different fine-structure states is on the order of 0.01 eV for elements like singly ionized carbon (referred to in this thesis as either C^+ or $C\text{ II}$), neutral oxygen ($O\text{ I}$), and other common elements seen in the ISM. This means that under the conditions present in the atomic phase, upper level fine-structure states can easily be populated by collisional excitation. Because radiative de-excitation far exceeds collisional de-excitation in these conditions, the excited ion will radiate away a photon that escapes the gas taking away some energy from the gas, cooling it in the process.

Several species of ions are important coolants of the ISM, such as Si II and $O\text{ I}$, especially at higher temperatures. However, the dominant coolant for the CNM in the

Milky Way is the C II fine structure line transition (Wright et al., 1991; Malholtra et al., 2001). This transition has a rest wavelength of $157.7 \mu\text{m}$, and is therefore often referred to as the [C II] $158 \mu\text{m}$ line. This fine-structure line is proving to be a powerful tool to discover atomic gas phases in distant galaxies, because the line can be observed from Earth with the Atacama Large Millimeter/sub-millimeter Array (ALMA) (e.g. Ota et al., 2014; Capak et al., 2015), which is discussed further in Chapter 5.

1.1.3 Observational Studies of the Atomic ISM

Observational measurements of the atomic ISM have come historically from the detection of the 21 cm hyperfine-structure line emitted by neutral hydrogen. Several large scale surveys such as the Leiden-Argentine-Bonn (LAB) survey (Bajaja et al., 2005; Kalberla et al., 2005) have mapped this emission in great detail. In the Milky Way, most of the gas is constrained to a thin disk, which extends about three times as far as the stellar disk (Kalberla & Kerp, 2009).

By studying the 21 cm line in *absorption* towards background radio sources, Heiles & Troland (2003a) were able to measure the temperatures of the absorbing ISM atomic gas. Their results and others (Heiles & Troland, 2003b; Pineda et al., 2014) show that a significant fraction of the atomic gas ($\sim 40\%$) is in a cold phase with median temperature weighted by column density of 70 K. The remaining atomic gas occupies a range of temperatures from 500 K to about 10000 K, a result corroborated by more recent results (Roy et al., 2013a,b). It is interesting to note that the two phase model pioneered by Field et al. (1969) does not allow for gas temperatures in the range between 500 K and 5000 K as these temperatures will yield unstable thermodynamic solutions. However observations suggest that at least 30% of the atomic gas fall within this temperature range (Heiles & Troland, 2003b; Roy et al., 2013b). One possible solution for this discrepancy between the model and observations would be to introduce turbulence

to the two phase model, which in effect would break global pressure equilibrium, but maintain local pressure equilibrium (Gazol et al., 2005; Walch et al., 2011).

Finally, one can observe tracers of the atomic gas such as carbon. One such tracer that has been used to study the ISM is neutral carbon. Neutral carbon, however, traces more dense regions, where carbon is not singly ionized as it is in the atomic gas phase. Jenkins & Tripp (2001, 2011) show that C I traces components with very cold temperatures. The pressures they derive ($P/k_B \sim 3800 \text{ K cm}^{-3}$), however, are consistent with the pressures expected from the two-phase model, indicating that these cold components of the ISM are in pressure equilibrium with remaining gas. Recently, a more reliable tracer of the atomic ISM, the [C II] $158 \mu\text{m}$, was used to map atomic gas in our Milky Way (Pineda et al., 2014). Their results show that the CNM is mostly concentrated in the inner part, whereas the WNM is more abundant in the outer parts of our Galaxy.

1.2 Galaxy Evolution

Understanding what the role of the ISM is in the formation and evolution of galaxies is a major research area in astrophysics. A large variety of independent measurements suggest we inhabit a universe described well by a cosmological model known as Λ cold dark matter (ΛCDM). In this model, the Universe is composed mainly out of dark energy (the Λ), which is responsible for the accelerated expansion rate of the Universe. About one fourth of the energy budget of our Universe is dark matter; matter not in the form of baryons. It is generally believed that the dark matter is ‘cold’ meaning it moves slowly and does not undergo collisions or dissipate energy. Finally, only about one twentieth of our Universe is in the form of baryonic matter, i.e. the matter that makes up everything we can see.

Galaxies in this model form via hierarchical mergers, known as the hierarchical Λ CDM model. In this model, small seeds of dark matter overdensities in the early universe pull in matter via gravitational interactions. These protogalactic clumps collide with each other forming subsequently larger and larger galaxies. Numerical simulations based upon this model have shown great promise in reproducing both the large scale structure as well as reproducing the large variety of observed galaxies (e.g. Springel et al., 2005; Boylan-Kolchin et al., 2009; Kereš et al., 2012; Sijacki et al., 2012).

One of the key questions and challenges for these simulations is understanding how the gaseous component of galaxies, which accounts for the majority of the baryons, can be linked to the dark matter. Interstellar gas plays a pivotal role in shaping the observational characteristics of galaxies, from star formation in young star-forming galaxies to dust obscuration of metal-rich old galaxies. However, the exact physics of this gas is hard to implement as processes such as correct radiative transfer and realistic feedback by active galactic nuclei (AGN), supernova, and stars are computationally expensive and/or poorly understood/constrained.

Providing observational measurements of interstellar gas at *all* stages of the formation and evolution of galaxies allows an accurate picture of the role of this gas in galaxy formation and evolution, which in turn, provides stringent constraints on simulations modeling galaxies. This is the goal of this thesis, using observational measurements to provide insight into the physical characteristics of the neutral atomic phase over cosmic time, with as ultimate goal to provide a deeper understanding of how this gas affects the formation and evolution of galaxies.

1.3 Observational Studies of High- z Atomic Gas

Modern-day telescopes allow us to study galaxies to unprecedented distances. As light has a finite speed, the light emitted by distant galaxies will take a longer time to arrive to our telescopes. Indeed the furthest known galaxies have light travel times of greater than 13 billion years, allowing us a glimpse into the universe when it was less than a billion years old. By studying galaxies at varying distances we can therefore probe galaxies at varying stages in their evolution.

We measure distances to distant galaxies by their redshift. As light travel towards us, the expansion of the Universe causes the frequency of light to decrease. This shifts the light towards longer/redder wavelengths, which is known as redshift, z . The longer the light travel time, the larger the redshift of the light, i.e. $\lambda = \lambda_0 \cdot (1 + z)$.

Observationally the goal is therefore clear, to study the atomic gas over a large range of redshifts. This will allow us to provide a detailed picture of how atomic gas has evolved over cosmic time, and how it has shaped the galaxies we see today. Unfortunately, making the observations are not as easy as defining the goal. The next sections detail some efforts of measuring the atomic gas phase at high redshift.

1.3.1 Emission Studies at High Redshift

The most direct way of measuring atomic gas is by direct detection of the 21 cm line. This line has shown great promise in detecting many thousands of nearby galaxies (ALFALFA; Giovanelli et al., 2005). Unfortunately, the strength of this hyperfine line prevents observations at even moderate redshifts. Currently, the furthest observed 21 cm line has a redshift of $z \sim 0.25$ (Catinella et al., 2008). Therefore with current and even near-future telescopes (i.e. the square kilometer Array (SKA)), this line will not provide a feasible way to probe the atomic ISM at $z > 1$.

A second method of studying the atomic ISM is by using elements which trace the HI gas. In Section 1.1.2, we have seen that fine-structure line emission from elements like O I and C II are the primary coolants of the atomic ISM. For high redshift galaxies, these lines are shifted into the sub-mm regime of the electromagnetic spectrum, which can be observed with the Atacama Large Millimeter/sub-millimeter Array (ALMA). Recent observations have shown the feasibility of these observations out to redshifts as large as $z \sim 6$ (Carilli & Walter, 2013; Capak et al., 2015)

Detecting fine-structure emission lines therefore provides a way to pinpoint the position and characterize the properties of the neutral ISM where direct measurement of the atomic gas via 21 cm emission is not feasible. This interesting possibility is discussed further in Chapter 5. One caveat to using these tracers is that one has to be sure that it actually accurately traces the gas one wants to study. This currently is an active field of research (Carilli & Walter, 2013).

1.3.2 Absorption Studies at High Redshift

A second approach for studying atomic gas at high redshift is by looking at the gas in absorption. To accomplish this, we observe a very bright light source, typically quasars (QSOs), but other bright compact sources such as gamma-ray bursts (GRBs) have also been used. As the light from this bright source travels towards us, it encounters intervening gas along its path. This gas will absorb only some of the light as the atoms and molecules in the gas can only absorb discrete frequencies of light, leaving a spectroscopic absorption signature of the gas in the light of the bright source. We can analyze this signature using spectrographs, which decompose the light into its individual frequencies.

The most prominent line we observe in absorption is the Lyman- α (Ly- α) line. This line is due to the absorption of a photon by the ground state of neutral hydrogen to

its first excited state. The strength of the line is related to the number of neutral hydrogen atoms we encounter along the line of sight. This quantity is known as the column density of hydrogen, N_{HI} , and is measured in particles/cm². The line will saturate (i.e. no light is transmitted at line center of the frequency of the line) when the density of particles is large.

The shape of the absorption profile of the Ly- α line (and any other absorption profile) is the convolution of two separate components. At line center, the profile is dominated by the Doppler broadening component, due to the individual motions of the atoms. Further away from line center, the profile is dominated by the natural broadening component due to the Heisenberg uncertainty principle, which causes an uncertainty in the energy of the transition due to its finite lifetime in the excited state. The convolution of the two separate components is known as a Voigt profile.

For large column densities of neutral hydrogen, the Ly- α line is strongly saturated at line center. The Doppler component is therefore hidden in the saturated region and the natural broadening component dominates the shape of the profile. This results in a very distinct absorption profile known as damping wings. The largest column density systems have HI column densities exceeding $2 \times 10^{20} \text{ cm}^{-2}$ and show distinct damping wings. These systems are therefore known as Damped Ly- α Systems (DLAs; Wolfe et al., 2005). The column density threshold of $2 \times 10^{20} \text{ cm}^{-2}$ is chosen because for larger column densities systems the majority of the hydrogen is neutral, whereas for smaller column density systems a large fraction of the hydrogen is ionized.

The goal for this thesis is to understand the physical conditions of the atomic gas component of the ISM at high redshift. We therefore focus on DLAs for the following three reasons: 1) As was mentioned, the majority of the gas is neutral allowing for direct observations of the atomic gas phase without the need for ionization corrections. 2) DLAs dominate the neutral gas content of the Universe for at least the last 12 billion

years, and contain enough mass to account for about 50 % of the mass in the visible Universe (Wolfe et al., 1986; Prochaska et al., 2005; O’Meara et al., 2007; Noterdaeme et al., 2009). 3) They are the likely progenitors of modern-day galaxies (Wolfe et al., 1995, 2005), and therefore *directly* probe the ISM of galaxies at high redshift.

1.4 Distribution of Atomic Gas in the Universe

One of the first quantities measured for atomic gas at high redshift, is its spatial distribution as a function of cosmic time (e.g. Wolfe et al., 1986; Lanzetta et al., 1991). We know that as our Universe expanded, electrons and protons combined during the era of recombination. The first stars and galaxies, however, reionized the neutral gas in the Universe; a process largely completed by $z \sim 6$. After this point, neutral hydrogen gas could only exist in regions dense enough such that the gas shields itself from the ionizing radiation. Λ CDM models suggest that such dense regions occur at the center of dark matter halos, which have a well-defined spatial distribution in large-scale cosmological simulations. Therefore the distribution of atomic hydrogen provides a direct observational constraint to these simulations.

It is common to describe the distribution of atomic gas by a quantity known as the column density distribution function, $f(N_{\text{HI}}, X)$. Here $f(N_{\text{HI}}, X)$ is defined in such a way that $f(N_{\text{HI}}, X)dNdX$ is the number of absorbers with column density between N and $N+dN$ and within the absorption distance X and $X+dX$. The absorption distance², dX , is a measure of distance like redshift, except with the benefit that $f(N_{\text{HI}}, X)$ will be constant for a non-evolving population of absorbers, i.e. it removes any redshift dependence due to the expansion of the Universe.

Two more quantities of interest can be derived from $f(N_{\text{HI}}, X)$. The first is the

² $dX \equiv \frac{H_0}{H(z)}(1+z)^2 dz$, with $H(z) = H_0[(1+z)^2(1+z\Omega_m) - z(z+2)\Omega_\Lambda]^{-1/2}$, where H_0 , Ω_m and Ω_Λ are Hubble’s constant, the mass density and the dark energy density of the chosen cosmology.

line density of atomic gas, $\ell_{\text{DLA}}(X)$. This quantity is the zeroth moment of $f(N_{\text{HI}}, X)$: $\ell_{\text{DLA}}(X) = \int_{N_{\text{DLA}}}^{\infty} f(N_{\text{HI}}, X) dN$. We integrate the function from the column density threshold of DLAs, N_{DLA} , because DLAs are mainly neutral, yet contain the majority of neutral gas. They, therefore, provide a meaningful lower limit to the true neutral atomic gas line density. The second quantity of interest is the mass density of atomic hydrogen, ρ_{HI} . This quantity is the first moment of $f(N_{\text{HI}}, X)$, $\rho_{\text{HI}} = \frac{m_{\text{H}}H_0}{c} \int_{N_{\text{DLA}}}^{\infty} N_{\text{HI}} f(N_{\text{HI}}, X) dN$, and describes the cosmic mass density in neutral hydrogen of the Universe.

There have been many previous measurements of the quantities, $f(N_{\text{HI}}, X)$, $\ell_{\text{DLA}}(X)$, and ρ_{HI} at a range of redshifts (e.g. Lanzetta et al., 1991; Prochaska et al., 2005; Rao et al., 2006; O’Meara et al., 2007; Noterdaeme et al., 2009). These studies have shown that $f(N_{\text{HI}}, X)$ is remarkably constant between redshifts 2 through 4. Moreover, it is consistent with the value measured locally from 21 cm line observations (Zwaan et al., 2005; Braun, 2012). This is in contrast with $\ell_{\text{DLA}}(X)$ and ρ_{HI} , which show a steady decline over this redshift range. Unfortunately due to the atmospheric absorption of ultraviolet (UV) radiation, it is difficult to measure these quantities with ground based telescopes for redshifts below $z < 1.6$. This lack is addressed in Chapter 4.

1.5 Statistical Measurements of Atomic Gas

The largest challenge with quasar absorption line studies is the inherent lack of spatial information in the observational measurements. A single sightline only probes a tiny volume of the atomic gas in and around the galaxy. Furthermore, the spatial density of quasars is sparse enough that it rarely happens that one absorption system gets probed by multiple sightlines. Combining this with the fact that it is hard to observe the absorber’s

host galaxies because of the inherent faintness of these systems (Krogager et al., 2012; Fumagalli et al., 2015), these sightlines provide us with little information on the size and extent of the gas around a galaxy.

Fortunately, this challenge is also one of its greatest assets. Because these systems are not preselected based upon the properties of the galaxy (i.e. luminosity, color, etc.), the sample is also not biased towards these properties as emission selected samples inherently are. As a result, absorption systems probe the neutral ISM of a more representative sample of galaxies than emission selected samples. Even though single sightlines might probe unique conditions, large statistical samples provide a way to probe the typical conditions of the ISM around a ‘typical’ galaxy. In the next sections we will discuss three such statistics that have been studied: metallicity, kinematics and the physical conditions of the neutral atomic gas.

1.5.1 Metallicity

The metallicity of the gas is defined as the ratio of metals to hydrogen compared to the solar abundance ratio: $[M/H] = \log_{10}(N_M/N_H) - \log_{10}(N_M/N_H)_\odot$, where M is some metal³. We can calculate the column density of the metal lines by the depth of the absorption profile using the apparent optical depth method (AODM), which is described in detail in Savage & Sembach (1991).

We find that DLAs are metal-poor, with a median metallicity of about 1/30 solar (Rafelski et al., 2012). Furthermore, the metallicity decreases with increasing redshift (Prochaska et al., 2003a; Kulkarni et al., 2005; Rafelski et al., 2012). This suggests that the atomic ISM is being enriched as the galaxy ages. This is a reasonable assessment, because stars during their lifetime eject some of the metals they produce in the surrounding gas. One of the interesting features is that the rate of metallicity evolution is roughly

³A metal is defined here in the usual astrophysical sense, i.e. as any element heavier than helium.

constant with redshift over the redshift range between $z = 2$ and $z = 4$. However, the rate significantly increases above $z > 4.7$ suggesting that some other physical process enriches the ISM or that more gas is neutral due to lower UV radiation fields at these redshifts (Rafelski et al., 2014).

1.5.2 Kinematics

A second statistic that can be studied for absorbers is the kinematical structure of the atomic gas. To do this we take an unsaturated low-ionization metal line, such as Si II, and look at the velocity structure of the line. Several statistics to describe the kinematic structure of this line were defined by Prochaska & Wolfe (1997). One particular statistic of interest is the width of the velocity profile that contains 90 % of the total optical depth, (Δv_{90} ; defined further in §2.3). This statistic, known as the velocity width, is thought to correlate with the mass of the neutral gas in the absorber, as larger masses occur in larger potential wells, and therefore produce larger velocities (Prochaska & Wolfe, 1997; Prochaska et al., 2008; Møller et al., 2013).

The link between velocity width and the mass of absorbing galaxy is further strengthened by the fact that there exists a clear correlation between the velocity width and the metallicity (Wolfe & Prochaska, 1998; Ledoux et al., 2006; Prochaska et al., 2008). If we take velocity width as a proxy for mass, this suggests that there exists a correlation between mass and metallicity for absorbing galaxies. Such a relation is known to exist for emission galaxies (Tremonti et al., 2004; Savaglio et al., 2005; Erb et al., 2006; Maiolino et al., 2008). The fact that a similar relationship holds for the atomic gas of DLAs gives further credence that DLAs probe the ISM or the circumgalactic gas (CGM) of galaxies.

1.5.3 Physical Parameters

The final statistics we describe here are the physical properties of the gas, in particular the volume density of hydrogen, n_{H} , the volume density of electrons, n_{e} , and the temperature, T . There are several ways these quantities can be measured in atomic gas. The first method uses 21 cm absorption. Using a bright radio source as a background light source, one can look for 21 cm absorption in a similar manner as one would look for Ly- α absorption. Since the strength of the 21 cm absorption, the column density of hydrogen from Ly- α , and the spin temperature of the gas are related by: $N_{\text{HI}} = C \times T_{\text{s}} \times \int \tau_{21 \text{ cm}} dV$, this method gives a measurement of the temperature of the gas (see e.g. Kanekar et al., 2014). Kanekar et al. (2014) found that the resulting temperature measurements span the range of both the CNM and WNM.

A second method uses the fine-structure lines of neutral carbon, C I. This method relies on the fact that the lowest energy state is divided into three fine-structure states. The ratio of these three states with each other is dependent on the temperature and density of the gas. This result has been used by Jenkins & Tripp (2011) to study the temperature and density of the coldest components of the ISM in the Milky Way. At high redshift, a similar analysis was used to study the coldest gas in DLAs by Jorgenson et al. (2010). This line is only detected in a select few DLAs, and therefore probes only those few systems with a large fraction of very cold gas and/or very large metal column densities. Their results show that at least a fraction of DLAs contain very cold gas with conditions consistent with that of the CNM.

The third method assumes that the two-phase model of the neutral atomic gas holds for gas in DLAs. As discussed in §1.1.2, most of the cooling occurs via emission through the fine-structure line of carbon. Therefore, if we can measure this cooling rate, we can work backwards to measure the density and temperature of the gas. Fortunately, the cooling rate of [C II] 158 μm can be measured from the absorption profile, because

the quantum state responsible for the [C II] 158 μm line also causes an absorption feature at C II*1335.7 Å (Wolfe et al., 2003a,b). From this assumption Wolfe et al. (2003b) found that the majority of DLAs with detectable levels of C II*1335.7 Å must have some gas in the CNM along the line of sight.

The combined results from these studies indicate that a large variety of physical conditions exist in the atomic ISM at high redshift. This is not surprising as even in our own Galaxy, we find a wide range of conditions. What is more striking is that the conditions of this high redshift gas are similar to our own Galaxy.

1.6 Overview of the Thesis

The aim of this thesis is to increase our understanding of atomic gas at high redshift. We know that atomic gas is an important component in the formation and evolution of galaxies, but directly measuring this gas in emission at high redshift, at the peak of galaxy growth, is difficult. By studying atomic gas in absorption in DLAs, we are able to provide detailed observations of the evolution of the chemical composition, physical conditions, and spatial distribution of the atomic gas phase at high redshifts.

Chapter 2 focusses on the evolution of the chemical composition and kinematic parameters of DLAs. Using a sample of 100 DLAs with high resolution spectrography, we show for the first time that the known velocity width - metallicity relationship, likely due to an underlying mass-metallicity relationship, evolves with redshift. This evolution can be described using a planar equation, described in this chapter. We note that the evolution is similar to the evolution in the mass-metallicity relationship in galaxies, suggesting that the atomic gas is well-mixed. The results of this study have been recently used to provide meaningful constraints on cosmological simulations studying galaxy evolution (Barnes & Haehnelt, 2014; Bird et al., 2015).

In Chapter 3, we discuss a new method to measure the hydrogen density, electron density and temperature of atomic gas at high redshift, using the fine-structure line transitions of singly ionized carbon and silicon. Using a Monte Carlo Markov Chain (MCMC) method, we are able to determine the physical conditions of atomic gas in a selection of DLAs. These conditions are similar to the conditions we see in the ISM of the Milky Way. A select sample of DLAs have higher pressures than locally measured values possibly indicating that these DLAs trace a population of active star-forming galaxies. The material in this chapter provide a unique new method to study the physical conditions in the bulk of the atomic gas, thereby providing a glimpse into the true nature of atomic gas at high redshift.

Chapter 4 is devoted to understanding the distribution of atomic gas at redshifts below $z \sim 1.6$. Below this redshift, the Ly- α line is redshifted below the atmospheric cut-off and can therefore not be observed from the ground. Using the large archive of observations taken with the Hubble Space Telescope (HST), we are able to perform a search for DLAs in this crucial redshift range covering the last 10 billion years of our Universe. Our results show that the incidence rate of DLAs is lower than previously expected, yet consistent both with extrapolations of the results at high redshift and the results from local measurements. This study is the largest conventional DLA search at these redshifts, filling in an important gap in our understanding that has existed for almost 30 years.

Chapter 5 summarizes the results in this thesis and provides future directions for research.

1.7 References for Chapter 1

- Bahcall, J. N. & Wolf, R. A. 1968, *ApJ*, 152, 701
- Bajaja, E., Arnal, E., Larrarte, J., Morras, R., Pöppel, W., & Kalberla, P. 2005, *A&A*, 440, 767
- Barnes, L. A. & Haehnelt, M. G. 2014, *MNRAS*, 440, 2313
- Bigiel, F., Leroy, A., Walter, F., Brinks, E., De Blok, W., Madore, B., & Thornley, M. 2008, *AJ*, 136, 2846
- Bird, S., Haehnelt, M., Neeleman, M., Genel, S., Vogelsberger, M., & Hernquist, L. 2015, *MNRAS*, 447, 1834
- Boylan-Kolchin, M., Springel, V., White, S. D., Jenkins, A., & Lemson, G. 2009, *MNRAS*, 398, 1150
- Braun, R. 2012, *ApJ*, 749, 87
- Capak, P., Carilli, C., Jones, G., Casey, C., Riechers, D., Sheth, K., Carollo, C., Ilbert, O., Karim, A., LeFevre, O., Lilly, S., Scoville, N., Smolcic, V., & Yan, L. 2015, *arxiv:1503.07596*
- Carilli, C. & Walter, F. 2013, *ARA&A*, 51, 105
- Catinella, B., Haynes, M. P., Giovanelli, R., Gardner, J. P., & Connolly, A. J. 2008, *ApJ*, 685, L13
- D'Hendecourt, L. & Léger, A. 1987, *A&A*, 180, 9
- Draine, B. T. 2011, *Physics of the Interstellar and Intergalactic Medium* (Princeton: Princeton University Press)
- Erb, D. K., Shapley, A. E., Pettini, M., Steidel, Charles, C., Reddy, N. A., & Adelberger, K. L. 2006, *ApJ*, 644, 813
- Field, G., Goldsmith, D., & Habing, H. 1969, *ApJ*, 155, L149
- Fumagalli, M., O'Meara, J., Prochaska, J. X., Rafelski, M., & Kanekar, N. 2015, *MNRAS*, 446, 3178
- Gazol, A., Vázquez-Semadeni, E., & Kim, J. 2005, *ApJ*, 630, 911
- Giovanelli, R., Haynes, M. P., Kent, B., Perillat, P., Saintonge, A., Brosch, N., Catinella, B., Hoffman, G., Stierwalt, S., Spekkens, K., Lerner, M., Masters, K., Momjian, E., Rosenberg, J., Springob, C., Boselli, A., Charmandaris, V., Darling, J., Davies, J., Garcia, L., Gavazzi, G., Giovanardi, C., Hardy, E., Hunt, L.K. and Iovino, A., Karachentsev, I., Karachentseva, V., Koopmann, R., Marinoni, C., Minchin, R., Muller, E., Putman, M., Pantoja, C., Salzer, J., Scodreggio, M., Skillman, E., Solanes, J., Valotto, C., Van Driel, W., & Van Zee, L. 2005, *AJ*, 130, 28598

- Heiles, C. & Troland, T. 2003a, *ApJS*, 145, 329
- . 2003b, *ApJ*, 586, 1067
- Jenkins, E. & Tripp, T. M. 2001, *ApJS*, 137, 297
- . 2011, *ApJ*, 734, 33
- Jorgenson, R. A., Wolfe, A. M., & Prochaska, J. X. 2010, *ApJ*, 722, 460
- Kalberla, P., Burton, W., Hartmann, D., Arnal, E., Bajaja, E., Morras, R., & Pöppel, W. 2005, *A&A*, 440, 775
- Kalberla, P. & Kerp, J. 2009, *ARA&A*, 47, 27
- Kanekar, N., Prochaska, J. X., Smette, A., Ellison, S. L., Ryan-Weber, E., Momjian, E., Briggs, F., Lane, W., Chengalur, J., Delafosse, T., Grave, J., Jacobsen, D., & de Bruyn, A. 2014, *MNRAS*, 438, 2131
- Kennicutt Jr, R. C. 1998, *ApJ*, 498, 541
- Kereš, D., Vogelsberger, M., Sijacki, D., Springel, V., & Hernquist, L. 2012, *MNRAS*, 425, 2027
- Krogager, J.-K., Fynbo, J., Møller, P., Ledoux, C., Noterdaeme, P., Christensen, L., Milvang-Jensen, B., & Sparre, M. 2012, *MNRAS*, 424, 1
- Kulkarni, V. P., Fall, S. M., Lauroesch, J. T., York, D. G., Welty, D. E., Khare, P., & Truran, J. W. 2005, *ApJ*, 618, 68
- Lanzetta, K. M., Wolfe, A. M., Turnshek, D. A., Lu, L., McMahon, R. G., & Hazard, C. 1991, *ApJ*, 77, 1
- Ledoux, C., Petitjean, P., Fynbo, J., Møller, P., & Srianand, R. 2006, *A&A*, 457, 71
- Maiolino, R., Nagao, T., Grazian, A., Cocchia, F., Marconi, A., Mannucci, F., Cimatti, A., Pipino, A., & Banero, S. 2008, *A&A*, 488, 463
- Malholtra, S., Kaufman, M., Hollenbach, D., Helou, G., Rubin, R., Brauher, J., Dale, D., Lu, N., Lord, S., Stacey, G., Contursi, A., Hunter, D., & Dinerstein, H. 2001, *ApJ*, 561, 766
- McKee, C. & Ostriker, J. P. 1977, *ApJ*, 218, 148
- Møller, P., Fynbo, J., Ledoux, C., & Nilsson, K. 2013, *MNRAS*, In Press
- Noterdaeme, P., Petitjean, P., Ledoux, C., & Srianand, R. 2009, *A&A*, 505, 1087

- O'Meara, J., Prochaska, J. X., Burles, S., Prochter, G., Bernstein, R., & Burgess, K. 2007, *ApJ*, 656, 666
- Ota, K., Walter, F., Ohta, K., Hatsukade, B., Carilli, C., Da Cunha, E., González-López, J., Decarli, R., Hodge, J., Nagai, H., Egami, E., Jiang, L., Iye, M., Kahikawa, N., Riechers, D., Bertoldi, F., Cox, P., Neri, R., & Weiss, A. 2014, *ApJ*, 792, 34
- Pineda, J., Langer, W., & Goldsmith, P. 2014, *A&A*, 570, 121
- Prochaska, J. X., Chen, H.-W., Wolfe, A. M., Dessauges-Zavadsky, M., & Bloom, J. S. 2008, *ApJ*, 672, 59
- Prochaska, J. X., Gawiser, E., Wolfe, A. M., Castro, S., & Djorgovski, S. 2003a, *ApJ*, 595, L9
- Prochaska, J. X., Herbert-Fort, S., & Wolfe, A. M. 2005, *ApJ*, 635, 123
- Prochaska, J. X. & Wolfe, A. M. 1997, *ApJ*, 487, 73
- Rafelski, M., Neeleman, M., Fumagalli, M., Wolfe, A. M., & Prochaska, J. X. 2014, *ApJ*, 782, L29
- Rafelski, M., Wolfe, A. M., Prochaska, J. X., Neeleman, M., & Mendez, A. 2012, *ApJ*, 755, 89
- Rao, S. M., Turnshek, D. A., & Nestor, D. B. 2006, *ApJ*, 636, 610
- Roy, N., Kanekar, N., Braun, R., & Chengalur, J. 2013a, *MNRAS*, 436, 2352
- Roy, N., Kanekar, N., & Chengalur, J. 2013b, *MNRAS*, 436, 2366
- Savage, B. D. & Sembach, K. R. 1991, *ApJ*, 379, 245
- Savaglio, S., Glazebrook, D., Le Borgne, D., Juneau, S., Abraham, R., Chen, H.-W., Crampton, D., McCarthy, P., Carlberg, R., Marzke, R., Roth, K., Jørgensen, I., & Murowinski, R. 2005, *ApJ*, 635, 260
- Sijacki, D., Vogelsberger, M., Kereš, D., Springel, V., & Hernquist, L. 2012, *MNRAS*, 424, 2999
- Springel, V., White, S. D., Jenkins, A., Frenk, C., Yoshida, N., Gao, L., Navarro, J., Thacker, R., Croton, D., Helly, J., Peacock, J., Cole, S., Thomas, P., Couchman, H., Evrard, A., Colberg, J., & Pearce, F. 2005, *Nature*, 435, 629
- Tremonti, C. A., Heckman, T. M., Kaufmann, G., Brinchmann, J., Charlot, S., White, S. D., Seibert, M., Peng, E. W., Schlegel, D. J., Uomoto, A., Fukugita, M., & Brinkmann, J. 2004, *ApJ*, 613, 898
- Walch, S., Wunsch, R., Burkert, A., Glover, S., & Whitworth, A. 2011, *ApJ*, 733, 47

- Wolfe, A. M., Gawiser, E., & Prochaska, J. X. 2003b, *ApJ*, 593, 235
- . 2005, *ARA&A*, 43, 861
- Wolfe, A. M., Lanzetta, K. A., Foltz, C. B., & Chaffee, F. H. 1995, *ApJ*, 454, 698
- Wolfe, A. M. & Prochaska, J. X. 1998, *ApJ*, 494, L15
- Wolfe, A. M., Prochaska, J. X., & Gawiser, E. 2003a, *ApJ*, 593, 215
- Wolfe, A. M., Turnshek, D. A., Smith, H. E., & Cohen, R. D. 1986, *ApJS*, 61, 249
- Wolfire, M., Hollenbach, D., McKee, C., Tielens, A., & Bakes, E. 1995, *ApJ*, 443, 152
- Wolfire, M., McKee, C., Hollenbach, D., & Tielens, A. 2003, *ApJ*, 587, 278
- Wright, E., Mather, J., Bennett, C., Cheng, E., Shafer, R., Fixsen, D., Eplee, R., & Isaacman, R. 1991, *ApJ*, 381, 200
- Zwaan, M., Meyer, M., Staveley-Smith, L., & Webster, R. 2005, *MNRAS*, 359, L30

Chapter 2

The Fundamental Plane of Damped Ly- α Systems

2.1 Abstract

Using a sample of 100 HI - selected damped Ly- α (DLA) systems, observed with the High Resolution Echelle Spectrometer on the Keck I telescope, we present evidence that the scatter in the well-studied correlation between the redshift and metallicity of a DLA is largely due to the existence of a mass-metallicity relationship at each redshift. To describe the fundamental relations that exist between redshift, metallicity and mass, we use a fundamental plane description, which is described by the following equation: $[M/H] = (-1.9 \pm 0.5) + (0.74 \pm 0.21) \cdot \log \Delta v_{90} - (0.32 \pm 0.06) \cdot z$. Here, we assert that the velocity width, Δv_{90} , which is defined as the velocity interval containing 90% of the integrated optical depth, traces the mass of the underlying dark matter halo. This description provides two significant improvements over the individual descriptions of the mass-metallicity correlation and metallicity-redshift correlation. Firstly, the fundamental equation reduces the scatter around both relationships by about 20%, providing

a more stringent constraint on numerical simulations modeling DLAs. Secondly, it confirms that the dark matter halos that host DLAs satisfy a mass-metallicity relationship *at each redshift* between redshifts 2 through 5.

2.2 Introduction

The study of high-redshift quasars has resulted in the detection of over 6000 damped Lyman α absorption systems (DLAs), which are absorption systems with an HI column density greater than $2 \times 10^{20} \text{ cm}^{-2}$ (Prochaska et al., 2005; Prochaska & Wolfe, 2009; Noterdaeme et al., 2009, 2012). DLAs are thought to be the progenitors of modern day galaxies (Wolfe et al., 1995), and therefore provide an important observational constraint on the formation and evolution of galaxies seen today. Most DLAs are found using low resolution instruments such as the Sloan Digital Sky Survey (SDSS; Abazajian et al., 2009). Although these instruments allow for accurately determining the column density of the neutral hydrogen, follow-up measurements of DLAs using high resolution instruments are needed to accurately measure the resonance line transitions of metals that are present in the DLAs. These measurements yield the column densities of the DLA's gas-phase constituents (for a review see: Wolfe et al., 2005), and allow for the determination of the metallicity of the gas (e.g. Prochaska et al., 2003b), the cooling rate of the neutral gas due to [C II] $158 \mu\text{m}$ emission (ℓ_c ; Wolfe et al., 2003a), and the dust-to-gas ratio (Pettini et al., 1994). Besides these quantities, the velocity profiles of the metal lines also gives us an insight into the kinematics of the gas (e.g. Prochaska & Wolfe, 1997; Ledoux et al., 1998). Together with the redshift of the DLA, these parameters individually provide us insight into the composition and nature of DLAs through the distribution that each of these parameters assumes. In turn, these data offer insight

into the properties of gas-rich and presumably starforming galaxies at high redshift. Furthermore, we may obtain additional information by considering how these parameters correlate to each other.

There are two such correlations for DLAs that have been extensively examined. The first of these correlations is the evolution of metallicity with redshift; as redshift decreases, metallicity increases (Prochaska et al., 2003a; Kulkarni et al., 2005; Rafelski et al., 2012). The second is the correlation between the kinematics and the metallicity of the DLA (Wolfe & Prochaska, 1998; Ledoux et al., 2006; Prochaska et al., 2008). This second relationship is thought to be caused by the underlying mass-metallicity relationship seen in galaxies (Tremonti et al., 2004; Savaglio et al., 2005; Erb et al., 2006; Maiolino et al., 2008), where the kinematics of the DLA is assumed to be related to the virial speed, hence the mass of the dark matter halo that hosts the DLA. Fynbo et al. (2010, 2011) used this correlation to image DLAs in emission. By selecting higher metallicity systems, they improved their rate of detection, which they assert is due to the larger mass of the DLA.

One of the main features of both correlations is the large intrinsic scatter, which is significantly larger than the observational uncertainty in the measurements. One possible cause for the large intrinsic scatter around either correlation is that the two correlations are dependent on each other, since they both correlate metallicity to a second parameter. To quantify the potential dependency of the two correlations, we can see if a linear combination of the two correlations is able to reduce the intrinsic scatter. Such a linear combination is called a ‘fundamental’ plane, because it traces out a plane in the three dimensional parameter space it describes.

The occurrence of fundamental planes in astronomy is relatively common. Indeed, in recent years there have been several publications on the existence of fundamental planes in a variety of astronomical areas, from black hole activity (Merloni et al.,

2003), to that of radio magnetars (Rea et al., 2012). To illustrate the advantage of using fundamental planes, we will consider one of the first fundamental planes, the fundamental plane of elliptical galaxies. Elliptical galaxies show a great diversity in their properties such as surface brightness and velocity dispersion. However, most of these properties are correlated to the luminosity of the elliptical galaxy (Kormendy, 1982). Indeed, both velocity dispersion and surface brightness show a correlation with luminosity. However, the scatter around both correlations is larger than the observational uncertainty. In an effort to reduce this scatter, Djorgovski & Davis (1987) noticed that when the luminosity, velocity dispersion and surface brightness are plotted on a three-dimensional plot, the points line up on a plane with a scatter around the plane that is within the observational uncertainty. This planar description therefore showed that the majority of the scatter in either of the correlations was caused by the other correlation. As such, the plane description provides a more stringent constraint on theoretical models than each of the individual correlations. In addition, the coefficients that describe this plane provide us insight into the galaxy population as a whole; deviations from the expected values could indicate variations in the initial mass function, dark matter fraction and stellar population effects (see e.g. Graves & Faber, 2010).

In this chapter, we explore the possibility of combining the redshift-metallicity and mass-metallicity correlation into a ‘fundamental’ plane for DLAs. We find that indeed such a plane exists, and applying this plane decreases the intrinsic scatter seen in both correlations significantly. We discuss new insights provided by this fundamental plane and we explore the physical origin of such a plane.

We conclude the chapter by looking for the existence of this fundamental plane in current numerical simulations. Since most numerical simulations do not accurately trace all parameters involved; direct evidence of the fundamental plane is difficult to find. Instead we focus on projections of the fundamental plane; i.e. we primarily com-

pare two parameter correlations and distributions of a single parameter. One distribution in particular that we examine is the velocity width distribution. This distribution has two notable features, a very large median and a tail toward large velocity widths. Previous modeling showed that only two models were able to recreate these two features of the distribution. The first model posed that DLAs are *thick* rapidly rotating disks (Prochaska & Wolfe, 1997), whereas the second model posed that DLAs are disk progenitors in a standard cold dark matter cosmology (Haehnelt et al., 1998). The latter, however, erroneously excluded systems with low velocity widths (Prochaska & Wolfe, 2010). Moreover, later numerical simulations based on Λ CDM models that included a more realistic transport of ionizing radiation (Razoumov et al., 2006; Pontzen et al., 2008) were unable to recreate the distribution of observed velocity widths. This inability of simulations based on Λ CDM models to produce the observed velocity width distribution is attributed to their difficulty in producing enough DLAs that reside in dark matter halos with large masses (Pontzen et al., 2008). We explore this hypothesis with the current data set.

This chapter is organized as follows. In Section 2.3 we describe our observational strategy and the reduction process we used. We explain the method used to measure the parameters described for each DLA, consider any biases in the sample, and explore their effects on the distribution of the parameters. Since a fundamental plane is dependent on the correlations between the parameters involved, it is crucial to explore these correlations. This is done in Section 2.4. In Section 2.5 we introduce the fundamental plane. Finally, we will discuss these results and compare them to numerical models in Section 2.6. The sample discussed in this chapter is the largest sample of DLAs for which the metal lines have been observed with a single high resolution ($R > 40000$) instrument (Keck/HIRES; Vogt et al., 1994), and to our knowledge, this is the first time that multi-parameter correlations, such as fundamental planes, are consid-

ered for DLAs.

2.3 Sample Selection, Parameter Definition and Sample Biases

In this section we discuss the reduction process used for the sample. We explain our sample selection and any biases that could influence our results.

2.3.1 Observations and Reduction

All of the spectra in this sample were obtained with the High Resolution Echelle Spectrometer (HIRES: Vogt et al., 1994) on the Keck I 10m telescope over the course of almost two decades of observing. Table 2.1 shows a detailed journal of observations. All observations prior to 2004 were carried out with the Tektronix 2048x2048 CCD; the remaining observations were made with a 3-chip mosaic of MIT-LL 2048x4096 CCDs. The FWHM resolution of each object, Δv_{res} , varies depending on the specified slit size and the atmospheric conditions, but most of the data were taken with a $0.86''$ or $1.15''$ slit, which results in a maximum Δv_{res} corresponding to 6 km s^{-1} , and 8 km s^{-1} respectively. Wavelength coverage was dependent on the redshift of the DLA. Finally, we computed the average signal to noise ratio (S/N) per 1.4 km s^{-1} pixel for each observation, by taking the central 200\AA of each observation and finding the median S/N for this range. If the range included too many absorption features (e.g. atmospheric waterlines, etc.) we shifted the range by 200\AA and computed the median S/N for this range. The raw data were reduced using the HIRedux routine, then extracted, coadded and continuum fit with `x_continuum`. These routines are all part of the publicly available XIDL reduction package developed by J.X. Prochaska (Prochaska et al., 2003b). The reasons

Table 2.1: Journal of Observations for HIRES DLA Sample

QSO	RA (J2000.0)	DEC (J2000.0)	z_{em} ^a	Date Observed (UT)	Exposure Time (s)	Δv_{res} ^b (km s^{-1})	S/N ^c
Q2359–02	00 01 50.0	–01 59 40.3	2.800	1997 Sep 29	14400	8	17
				1997 Sep 30	10800	8	
				1997 Oct 01	12516	8	
Q0000–2619	00 03 22.9	–26 03 16.8	4.110	1994 Sep 30	10800	8	15
				1994 Oct 01	3600	8	
BR0019–15	00 22 08.0	–15 05 38.8	4.530	1996 Sep 20	13500	8	18
				1996 Sep 21	12600	8	
				1996 Sep 22	14400	8	
J0040–0915	00 40 54.7	–09 19 26.9	4.976	2011 Jan 16	7200	6	7
				2011 Jan 24	3600	6	

Note. — Units of right ascension are in hours, minutes, and seconds, and units of declination are in degrees, arcminutes, and arcseconds.

^aThe emission redshift of the quasar.

^b Δv_{res} is defined as the FWHM resolution of the spectrum.

^cThe average signal to noise (S/N) ratio per 1.4 km s^{-1} pixel.

Note. — This table is shown in its entirety in the Appendix. A portion is shown here for guidance regarding its form and content

for choosing a single high resolution (i.e. $R > 40000$) instrument are discussed in §2.3.3.

2.3.2 Methodology

After the reduction process, we searched the reduced spectra for metal lines at the redshift of the DLA obtained from the Lyman alpha line in lower resolution data. The redshift of the DLA was then adjusted to coincide with the peak absorption feature in the metal lines, since metal lines are much narrower than the large width of the damped profile of the $\text{Ly}\alpha$ line. This provides a more accurate measurement of the DLA redshift. We also calculated the column densities of metals using the apparent optical depth method (AODM; Savage & Sembach, 1991), which yields accurate column densities even if some of the lines are slightly saturated. From the column densities of the metal lines and the column density of hydrogen, we can calculate the metallicity ($[M/H]$)

of the DLA, which is defined by:

$$[M/H] = \log_{10}(N_M/N_H) - \log_{10}(N_M/N_H)_\odot \quad (2.1)$$

The wavelengths and oscillator strengths used in this chapter are from Morton (2003), whereas the solar abundances are from Asplund et al. (2009).

Besides the metallicity we can also determine the cooling rate of neutral gas from these column densities. Pottasch et al. (1979) showed that, ℓ_c , the cooling rate per H atom due to [C II] 158 μm emission, which is the dominant coolant in the neutral ISM (Wright et al., 1991), is given by:

$$\ell_c = \frac{N_{\text{C II}^*}}{N_{\text{H II}}} A_{ul} h\nu_{ul}, \quad (2.2)$$

where A_{ul} and $h\nu_{ul}$ are the Einstein coefficient and energy of the transition from the excited to the ground state of C^+ (see e.g. Wolfe et al., 2003a). We are able to measure the column density of C II^* , because the $\text{C II}^* \lambda 1335.7$ fine structure line arises from the same state as the [C II] 158 μm line, and falls within the spectral regime covered by optical telescopes for the redshifts examined in this chapter.

Note that an accurate HI column density, n_{H} , is required to obtain accurate measurements of both metallicity and ℓ_c . We are generally unable to obtain the HI column density from the HIRES spectra, because accurate measurement of this quantity requires the spectrum to be fluxed and HIRES spectra are difficult to flux (Suzuki et al., 2003). We therefore relied mainly on spectra obtained from the Sloan Digital Sky Survey (SDSS; Abazajian et al., 2009) to measure n_{H} . However, for those 41 DLAs that were observed with the Echelette and Imaging Spectrometer (ESI; Sheinis et al., 2002) on the Keck II 10m telescope, we used the ESI spectra, because the improved resolution provides more reliable and precise HI column densities. The column density of HI is

determined from these spectra by simultaneously fitting a Voigt profile to the absorption profile of the Ly α line of the DLA, and fitting the continuum of the fluxed spectrum of the background quasar (see e.g. Prochaska et al., 2003a; Rafelski et al., 2012).

The final two quantities discussed here are the two kinematic parameters, W_{1526} and Δv_{90} . The reason for using two different kinematic parameters is that they describe different kinematical properties of the DLA. The Δv_{90} parameter describes the velocity width of the main neutral absorption complex by specifically ignoring weak outlying velocity components. On the other hand, the W_{1526} parameter is dominated by these outliers, since this absorption line is saturated in most cases (Prochaska et al., 2008). Hence the W_{1526} parameter describes the kinematics of the halo gas and/or weak satellite components.

The rest equivalent width of the Si II $\lambda 1526$ line, W_{1526} , is defined as $W_{1526} = W_{obs}/(1 + z)$, where W_{obs} is the observed equivalent width of the Si II $\lambda 1526$ transition. We choose the Si II $\lambda 1526$ line because the line is measured in the majority of spectra and its high oscillator strength causes the line to be saturated in most systems. It is important to stress that the W_{1526} statistic is almost independent of the column density of Si⁺, N_{Si^+} , if the absorption line is saturated. Saturated lines are on the flat part of the curve of growth where the column density and equivalent width scale as, $W_{1526} \propto \sqrt{\ln N_{Si^+}}$; any reasonable change in N_{Si^+} would only marginally change W_{1526} . There is therefore no *a priori* strong correlation expected between the equivalent width and any parameter which is derived from the column density of any metal lines, such as metallicity, if the equivalent width is obtained from a saturated line. Consequently, we were mindful to only select those DLAs with saturated Si II $\lambda 1526$ transition lines for the comparison of the W_{1526} parameter with any other parameter. However, the unsaturated lines were included in the distribution for W_{1526} ; otherwise we would bias this distribution towards higher equivalent widths, since low equivalent width systems are more

likely to be unsaturated due to the mass-metallicity relationship.

The velocity width, Δv_{90} , of an absorption system is defined to be the width of the absorption profile in velocity space. To measure the velocity width of a DLA, we employ the same strategy as in Prochaska & Wolfe (1997), with a few exceptions. We first select an unsaturated low-ion transition line. We require the line to be unsaturated, because a saturated line could overestimate the size of the velocity interval by including weak outlying velocity features that contain little of the total neutral gas of the DLA. As such we require that the normalized flux, defined as $F_{\text{norm}} = I(v)/I_c$, where I_c is the continuum intensity incident on the gas and $I(v)$ the transmitted intensity, is greater than 0.1 over the entire absorption profile. A low-ion transition line is chosen because low-ions, such as Fe II λ 1608 and Si II λ 1808, are likely to trace the neutral gas, which creates the damped Lyman α profile (Wolfe et al., 1995; Prochaska & Wolfe, 1997). By contrast, higher ionization transition lines such as C IV λ 1548, 1550 and Si IV λ 1393, 1402 exhibit different velocity structures (Wolfe & Prochaska, 2000; Fox et al., 2007). In addition, we require that the line is unblended from any other absorption feature.

After selecting the absorption profiles, we obtain an apparent optical depth profile;

$$\tau(\nu) = \ln[F_{\text{norm}}^{-1}]. \quad (2.3)$$

The resultant profile is smoothed to 8 km s^{-1} , the largest Δv_{res} of our sample, to prevent differences in resolution from affecting the Δv_{90} values. After smoothing, we select only those profiles for which the peak optical depth is detected at the 12σ detection limit, so that components one-fourth this peak optical depth are detected with a 3σ detection limit. This is important because these components could contain a significant fraction of the neutral gas content. This criterion is less restrictive than the criterion used by Prochaska & Wolfe (1997), because we believe that a 3σ detection limit is enough to discern small absorption features, since in almost all cases we have stronger absorption

lines that clearly show the presence of these small absorption features above the 5σ detection limit, and we are only after the velocity width of the line and not any of the other parameters described in Prochaska & Wolfe (1997). Finally, we find the width of the profile by stepping inward from both sides of the profile pixel-by-pixel, until we reach 5 percent of the total integrated optical depth on each side. This width is the measured Δv_{90} value. This last step prevents weak outlying absorption features from skewing the Δv_{90} statistic. The complete set of smoothed optical depths as a function of relative velocity for all DLAs is shown in Figure 2.1. For display purposes, we shift the data such that the left edge of the profile lines up with 0 km s^{-1} . The smoothed $1-\sigma$ error array is shown as a (red) dashed dotted line. The separation between the (green) dashed lines marks the velocity width. We assume an error of 10 km s^{-1} on these measurements, similar to that used by Prochaska et al. (2008).

2.3.3 Systematic Errors and Biases due to Sample Selection Criteria

There are two main concerns in selecting an appropriate sample for exploring correlations: systematic errors and biases caused by sample selection criteria. One source of systematic error could be the use of two different resolution instruments, which would in particular affect the velocity width measurement since it is measured by moving in pixel-by-pixel in the spectra. Lower resolution spectra, like the spectra taken with ESI which has a resolution of 44 km s^{-1} , would overestimate the velocity width. This motivated Prochaska et al. (2008) to reduce their ESI Δv_{90} measurements by 20 km s^{-1} . To circumvent the systematic errors caused by multiple instruments, we decided to restrict ourselves to velocity width measurements and metal column densities obtained from HIRES alone.

The other main concern is the effect of sample selection biases on the data. To

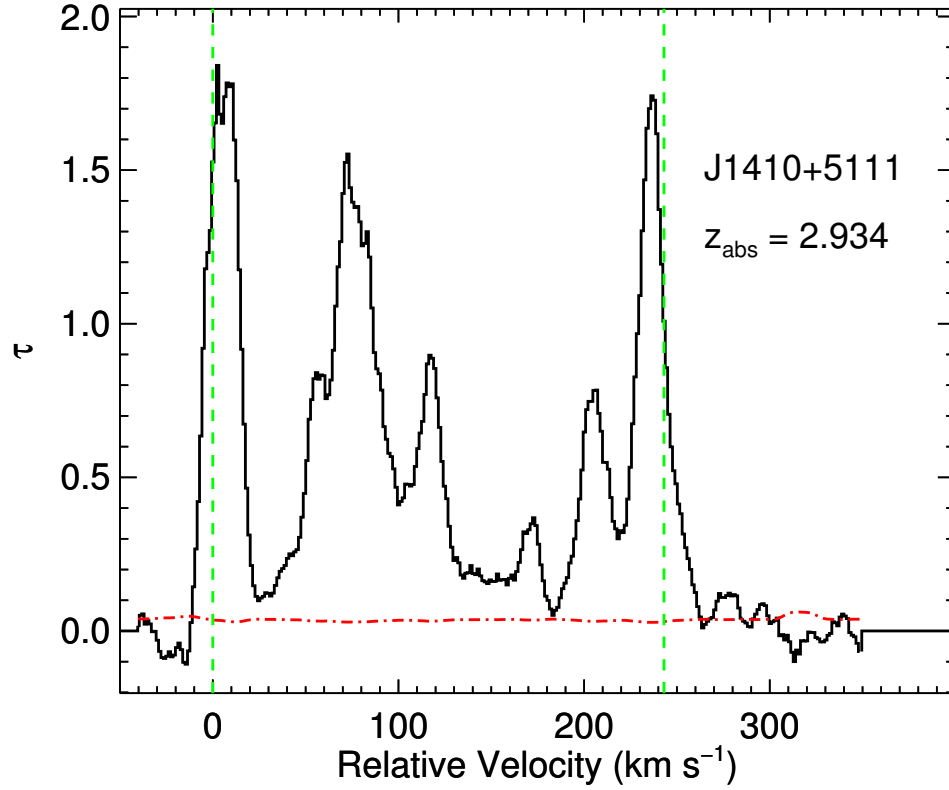


Figure 2.1: Optical depth profile as a function of relative velocity. The sample profile shown is of the DLA at redshift $z_{\text{abs}} = 2.9340$ towards QSO J1410+5111. The profile has been smoothed to 8 km s^{-1} , which is the largest Δv_{res} used in this sample. The dashed green lines mark the Δv_{90} interval, which is 243 km s^{-1} , and the dashed-dotted red line is the smoothed $1\text{-}\sigma$ uncertainty on the data. For the whole sample, the Δv_{90} values range between 17 km s^{-1} and 484 km s^{-1} . The full figure data set is shown in the appendix

assess this effect, we recorded the reason why each DLA was observed by our group with HIRES. The reason generally falls in one of the following four categories: (1) HI-selected, the DLA was selected based on just the column density of HI; (2) high redshift, the DLA was selected because of its high redshift; (3) metal content, the DLA exhibited very strong metal lines in its spectrum obtained from SDSS; and finally, (4) serendipitous, the DLA happened to fall in the same line-of-sight of the primary target. In addition, the majority of targets were observed because the flux of the background quasar exceeded a certain threshold; although the second and third reasons often drove our group to observe fainter targets. Each of these selection criteria needs to be examined for any bias that the corresponding subsample might contain. First, if the distance between the DLA and quasar is sufficient, then the DLA properties are unrelated to the properties of the background quasar. This indicates that selecting DLAs by the flux of the background quasar should not bias the DLA sample. Similarly for the serendipitous subsample, if the separation between the primary target and the serendipitous DLA is large enough, the serendipitous DLA should be unrelated to the primary target. We take a velocity separation of 3000 km s^{-1} to be sufficient for a DLA to be unaffected by another DLA or quasar (see e.g. Ellison et al., 2010), and we have made sure that no DLA in our sample violates this criterion. Secondly, the DLAs that were observed because of their metal column density (metal-strong DLAs, MSDLAs; Herbert-Fort et al., 2006) are not included in our sample. This subsample is biased in metallicity and W_{1526} , because metal-selected DLAs have on average higher metallicities and correspondingly higher W_{1526} values (Kaplan et al., 2010).

This leaves two sample selection criteria; the redshift and the HI column density of the DLA; both of these sample selection criteria cause a bias in the sample. The bias in the redshift is twofold. First, bright quasars are more abundant in the redshift range 2-3, and therefore any magnitude-limited selection of quasars will produce a majority of

DLAs within this range (Prochaska et al., 2005; Prochaska & Wolfe, 2009). Second, for a subset of the data we selected the quasars based on their high redshift, which biases that sample towards DLAs with high redshift. The HI column density selection criteria causes our sample to contain proportionally too few DLAs below a column density of $10^{20.5} \text{cm}^{-2}$ compared to the sample of DLAs from SDSS. Prochaska et al. (2007) ascribe this to our preference in selecting higher column density systems to ensure the absorber satisfies the DLA HI column density criterion.

To gauge the extent of the bias on the distribution of the remaining four parameters; we want to compare our biased sample to one that is ‘free’ of the bias caused by the redshift and HI column density selection criteria. To accomplish this, we randomly divide our sample of 100 DLAs in half. One half is left untouched, whereas we randomly pick 50 DLAs (with repeats) from the second half such that the redshift and HI column density of the second half reproduces the HI column density frequency distribution observed in DLAs, $(f(N_{\text{HI}}, X))$; Prochaska et al., 2005; Prochaska & Wolfe, 2009; Noterdaeme et al., 2009, 2012). This is indicative of a sample that is ‘free’ of biases in redshift and HI column density. To check for a bias in metallicity, $\Delta_{\text{V}90}$, W_{1526} , and ℓ_c of the untouched half, we look at the distribution that these parameters assume for both halves of the data set. We compare the distributions of each half, using a two-sided Kolmogorov-Smirnov test (KS) test and a Mann-Whitney U-test. The KS test provides a probability that both populations are drawn from the same parent population, whereas the U-test provides a probability that the two median values are significantly different. This procedure of randomly dividing the sample, reselecting one half of the sample and comparing the distribution is repeated 1000 times, to get a median value for the results of both tests.

The resultant median values of the KS test for all parameters are greater than 0.05 indicating that we cannot rule out the null hypothesis, which is that the two sub-

samples were drawn from the same parent population, at a 95 % confidence level (c.l.). Similarly, the U-test yields mean values greater than 0.05 for all parameters indicating that we also cannot reject this null hypothesis, which is that the medians of the two subsamples are the same. Hence, we see no evidence that the redshift and HI column density selection criteria have significantly affected the distribution of the remaining parameters. It is important to note that this does *not* mean that the redshift and HI column density show no correlation with the remaining parameters. It means that the effect of the two sample selection criteria does not significantly affect the distributions of the remaining four parameters. Together with the serendipitous sample, the HI-selected and redshift selected subsample comprises the complete sample used in this chapter. In total, it consists out of 100 DLAs for which we have accurate measurements of metallicity, redshift, HI column density, and Δv_{90} ; the full sample is shown in Table 2.2.

Table 2.2: HIRES DLA sample

QSO	z_{abs}	$\log N_{\text{HI}}$ (cm^{-2})	Metallicity	$\log \ell_c$ ($\text{ergs s}^{-1} \text{H}^{-1}$)	W_{1526} (\AA)	Δv_{90}^a (km s^{-1})	Transition ^b	Selection Criterion	References
Q1104-18	1.6613	20.80 ± 0.10	-0.99 ± 0.10	-26.87 ± 0.11	—	50	Si II λ 1808	H I - selected	6
Q1331+17	1.7763	21.14 ± 0.08	-1.34 ± 0.08	-26.60 ± 0.09	0.499 ± 0.001	72	Si II λ 1808	H I - selected	7, 13, 18, 24
Q0841+12	1.8640	21.00 ± 0.10	-1.46 ± 0.10	—	—	30	Si II λ 1808	Serendipitous	20
Q2230+02	1.8643	20.85 ± 0.08	-0.71 ± 0.09	—	1.500 ± 0.018	172	Si II λ 1808	H I - selected	7, 13
Q1210+17	1.8917	20.60 ± 0.10	-0.79 ± 0.10	—	0.419 ± 0.003	38	Si II λ 1808	H I - selected	13, 19

^aThe uncertainty on the Δv_{90} measurement is taken to be 10 km s^{-1} for each measurement.

^bTransition used to measure the Δv_{90} parameter.

References. — (1) Wolfe et al. (1994); (2) Lu et al. (1996); (3) Prochaska & Wolfe (1996); (4) Prochaska & Wolfe (1997); (5) Lu et al. (1998); (6) Lopez et al. (1999); (7) Prochaska & Wolfe (1999); (8) Molaro et al. (2000); (9) Petitjean et al. (2000); (10) Prochaska & Wolfe (2000); (11) Ellison et al. (2001a); (12) Molaro et al. (2001); (13) Prochaska et al. (2001a); (14) Ledoux et al. (2002); (15) Levshakov et al. (2002); (16) Prochaska & Wolfe (2002a); (17) Prochaska et al. (2003a); (18) Dessauges-Zavadsky et al. (2004); (19) Dessauges-Zavadsky et al. (2006); (20) Ledoux et al. (2006); (21) Dessauges-Zavadsky et al. (2007); (22) Prochaska et al. (2007); (23) Wolfe et al. (2008); (24) Jorgenson et al. (2010); (25) Vladilo et al. (2011); (26) Rafelski et al. (2012)

Note. — This table is shown in its entirety in the Appendix. A portion is shown here for guidance regarding its form and content

2.4 Distributions and Correlations

In this section, we compare the distribution of metallicity, ℓ_c , and W_{1526} parameters to previous studies specifically aimed at exploring these parameters, to show that our sample of 100 DLAs is a representative sample of each of the parameters. We explore our sample of 100 Δv_{90} measurements of DLAs, which to our knowledge is the most accurate distribution to date of this quantity. We also look at any potential correlations between the parameters, except for those that have been explored in detail before, such as the kinematics-metallicity correlation (Wolfe & Prochaska, 1998; Ledoux et al., 2006; Prochaska et al., 2008) and the metallicity-redshift correlation (Prochaska et al., 2003a; Kulkarni et al., 2005; Rafelski et al., 2012).

2.4.1 Distributions

The distributions of metallicity, ℓ_c , and W_{1526} of the sample are shown in Figure 2.2(a-c). These distributions have been discussed in detail in previous papers and here we give a short summary of the characteristics of each distribution. First, we scale each distribution such that its integrated area is normalized to unity. Consequently, we can interpret the y-axis of parameter, p , as the probability of finding a DLA within the parameter range $(p, p + dp)$. We then fit analytic functions to each of the distributions described above; these are shown as the solid (red) line in Figure 2.2. To prevent binning from affecting the fit, we do not fit the actual distributions, but instead fit the cumulative distribution function (shown as insets in Figure 2.2). The procedure used for the fitting process is as follows. We first use a chi-squared fitting technique to fit the cumulative distribution function of a single Gaussian distribution function to the cumulative distribution of the data; this fit is then compared using a one-sided KS-test. If the fit is unacceptable, we try for the fitting function a sum of two Gaussian distributions. The

Table 2.3: Fitting Functions to the Distributions

x	μ_1	σ_1^2	μ_2	σ_2^2	r
$\log \Delta v_{90}$	1.83	0.39	—	—	—
$\log W_{1526}$	-0.44	0.42	—	—	—
[M/H]	-1.46	0.55	—	—	—
$\log \ell_c$	-27.4	0.10	-26.7	0.28	0.55
Function Used					
(a)	$f(x; \mu_1, \sigma_1^2) = \frac{1}{\sqrt{2\pi\sigma_1^2}} e^{-\frac{(x-\mu_1)^2}{2\sigma_1^2}}$				
(b)	$f(x; \mu_i, \sigma_i^2) = \left(\frac{r}{1+r}\right)f(x; \mu_1, \sigma_1^2) + \left(\frac{1}{1+r}\right)f(x; \mu_2, \sigma_2^2)$				

Note. — (a) is a normalized Gaussian distribution function with mean, μ_1 and variance σ_1^2 . (b) is the sum of two Gaussian functions. The factors in front of the Gaussian terms are required such that the total integrated area under the function is equal to unity. The r-parameter is the ratio of the relative sizes of the two Gaussian distributions.

resultant equations to the fit are shown in Table 2.3. As expected, the ℓ_c statistic is best described by a bimodal fitting function (Wolfe et al., 2008), whereas the other parameters can be described by a single Gaussian distribution.

Figure 2.2a shows the metallicity distribution, which was recently published by Rafelski et al. (2012). They show that the distribution is reasonably well described by a Gaussian with a mean metallicity of -1.57 and a dispersion of 0.57. Our smaller data set with a mean metallicity of -1.46 and dispersion of 0.55 is consistent with their sample; a one-sided KS-test shows that the smaller second peak at -0.61 is not statistically significant. Secondly, the ℓ_c distribution, shown in Figure 2.2b, was first described by Wolfe et al. (2008); they found that their sample of 37 positive detections of ℓ_c showed a bimodal distribution. Our sample contains 32 positive detections, and shows a similar bimodality with peaks at $10^{-27.4}$ ergs s⁻¹ H⁻¹ and $10^{-26.7}$ ergs s⁻¹ H⁻¹ respectively. This allows the sample to be divided into two subsamples: a high-cool subsample, where $\ell_c > 10^{-27}$ ergs s⁻¹ H⁻¹, and a low-cool subsample for which $\ell_c < 10^{-27}$ ergs s⁻¹ H⁻¹. Finally, the W_{1526} distribution, discussed in Prochaska et al. (2008), is shown in Figure 2.2c. While most DLAs exhibit saturated Si II $\lambda 1526$ lines, this distribution in-

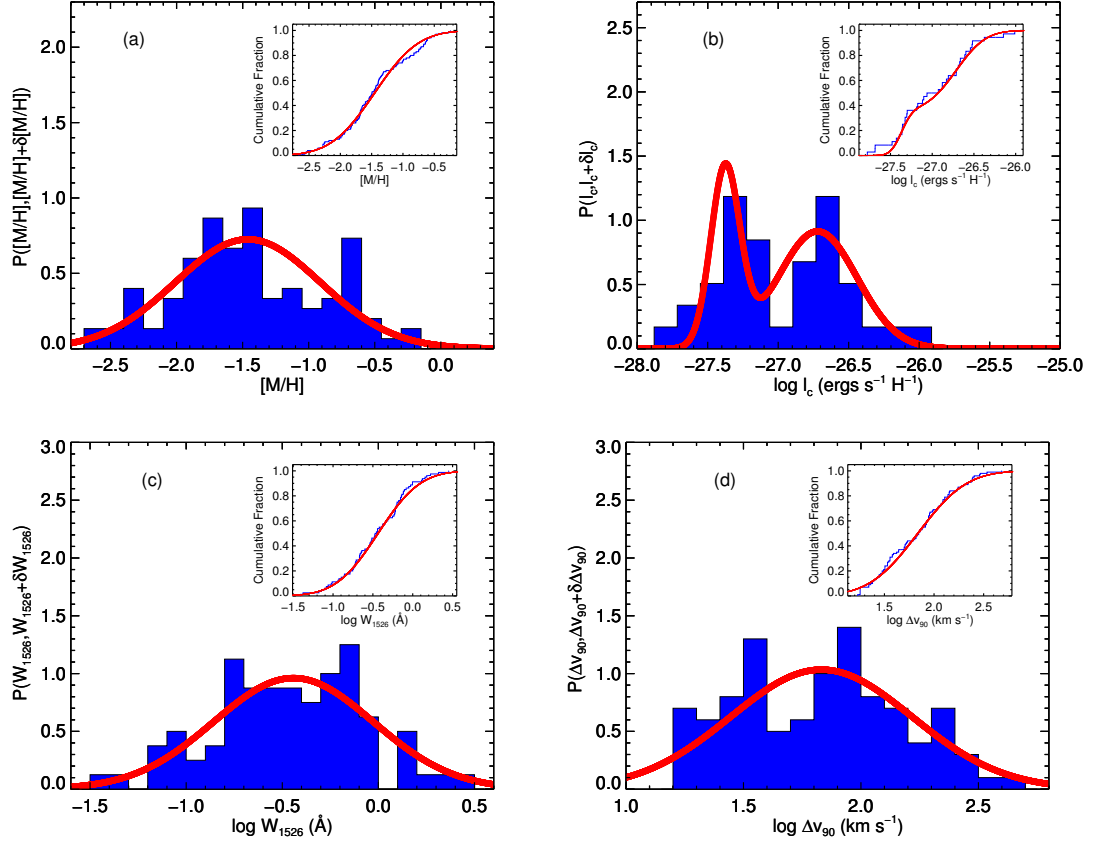


Figure 2.2: Distributions of metallicity, $158 \mu\text{m}$ cooling rate, equivalent width and velocity width of the sample of DLAs. The solid red line is a chi-squared best fit line to the cumulative distributions (shown as insets in the figure); the equations of these best fit parameters are given in Table 2.3. The distributions of metallicity, Δv_{90} and W_{1526} can all be described by a single Gaussian distribution. The ℓ_c parameter on the other hand, is clearly bimodal and is best described by a bimodal distribution. The distributions of metallicity, ℓ_c and W_{1526} are in good agreement with previous studies, indicating that the sample is a representative subsample of each of these parameters. The Δv_{90} distribution shows a large number of DLAs with $\Delta v_{90} > 100 \text{ km s}^{-1}$, which raises the median Δv_{90} value to $70^{+16}_{-13} \text{ km s}^{-1}$.

cludes DLAs with unsaturated Si II λ 1526 lines to prevent a bias against low equivalent widths (see Section 2.3.3). The distribution is fully consistent with the sample found in Prochaska et al. (2008). The fact that there exists good agreement between the sample considered in this chapter and the larger samples used to study these three parameters in detail, shows that the current sample is a representative sample of DLAs for each of these three parameters. This is crucial for a proper exploration of correlations between the parameters.

The last parameter we consider is the Δv_{90} statistic. The distribution is shown in Figure 2.2d. Unlike previous papers (Prochaska & Wolfe, 1997; Prochaska et al., 2008), we do not use linear bins, but divide the bins logarithmically. This choice was made because for the current sample size, the velocity width distribution is well-approximated by a log-normal distribution. The Δv_{90} distribution has two important characteristics. The first important characteristic of this distribution is the sharp decline with decreasing Δv_{90} of DLAs with Δv_{90} below 17 km s^{-1} ($\log \Delta v_{90} = 1.23$). This decline is not likely to be an observational limit, because even our lowest resolution data has a Δv_{res} of 8 km s^{-1} which corresponds to a Δv_{90} of 11 km s^{-1} for a single Gaussian component. Although some objects have been found with these small Δv_{90} values, they are extremely rare (Cooke et al., 2011; Pettini et al., 2008; Penprase et al., 2010). The rarity of these objects suggests that the majority of DLAs have at least one component with an internal velocity dispersion, σ , greater than 7 km s^{-1} or have multiple components which exhibit velocities of $\sim 10 \text{ km s}^{-1}$ relative to each other.

The second characteristic of the distribution of velocity widths is the large number of high Δv_{90} DLAs. When plotted in a linear histogram, these DLAs form a ‘tail’ in the distribution, as seen in Prochaska & Wolfe (1997); Prochaska et al. (2008). Most of these large Δv_{90} DLAs have Δv_{90} values below 200 km s^{-1} , but there are a few DLAs which show a velocity width significantly above this value (e.g. Petitjean et al., 2002).

These DLAs with very large velocity width are likely due to certain quasar sightlines encountering multiple galaxies or winds (Prochaska et al., 2008). As a result of the large number of high Δv_{90} DLAs, the resultant median Δv_{90} is significantly higher than expected from numerical simulations (Prochaska & Wolfe, 1997; Razoumov et al., 2006; Pontzen et al., 2008). The median value for our sample is 70^{+16}_{-13} km s⁻¹. The uncertainty on the median is the combined uncertainty of three different factors. First, due to the finite sampling of the Δv_{90} distribution, our sample of 100 DLAs might not evenly be divided by the true median of the sample. To estimate the uncertainty due to this factor, we note that this is a simple selection problem which can be described by the binomial distribution with $p = 0.5$. The binomial distribution has a $1-\sigma$ uncertainty of $1/2 \cdot \sqrt{n}$, where n is the number of data points. This means that for a sample of 100 DLAs, there is a probability of 0.68 that the true median of Δv_{90} is contained in the range between DLAs 45 and 55 when the DLAs are arranged in order of increasing Δv_{90} . To this uncertainty, we need to add in quadrature the uncertainty arising from the limited sampling of the data. This uncertainty we take to be the average spacing of the \sqrt{n} points centered around the median. Finally, we add in quadrature the mean observational uncertainty to get the uncertainty on the median.

2.4.2 Correlations and Dependencies

In this section we discuss some of the two-parameter correlations and dependencies that exist between the six parameters discussed in this chapter. Table 2.4 lists all 15 combinations of two parameters. For all 15 combinations of parameters, we are not only interested in any potential correlation, but we also want to know if the distribution of one parameter is dependent on the other. Therefore we apply a variety of different tests described below which test for both correlations and such dependencies.

To test for the existence of any potential correlation, we find a linear fit to the

Table 2.4: Table of Potential Correlations

Dependency		Linear regression line ^a		Kendall ^b	KS-test ^b	F-test ^b	U-test ^b	T-test ^b
(y)	(x)	(a)	(b)					
z	vs $\log n_{\text{H}}$	-0.24 ± 0.26	$8. \pm 5.$	0.211	0.403	0.677	0.160	0.392
$[M/H]$	vs $\log n_{\text{H}}$	0.04 ± 0.14	-2.3 ± 2.8	0.688	0.403	0.013	0.278	0.845
$\log \Delta v_{90}$	vs $\log n_{\text{H}}$	0.07 ± 0.10	0.4 ± 2.1	0.384	0.403	0.527	0.199	0.404
$\log W_{1526}$	vs $\log n_{\text{H}}$	0.21 ± 0.11	-4.8 ± 2.4	0.040	0.035	0.414	0.083	0.260
$\log \ell_c$	vs $\log n_{\text{H}}$	-0.58 ± 0.21	$-15. \pm 4.$	0.011	0.019	0.911	0.002	0.002
$[M/H]$	vs z	-0.30 ± 0.06	-0.53 ± 0.19	$1.22\text{E} - 5$	$1.65\text{E} - 4$	0.816	$3.06\text{E} - 5$	$1.84\text{E} - 5$
$\log \Delta v_{90}$	vs z	-0.00 ± 0.04	1.84 ± 0.13	0.862	0.811	0.487	0.232	0.648
$\log W_{1526}$	vs z	-0.10 ± 0.05	-0.08 ± 0.15	0.042	0.563	0.190	0.069	0.125
$\log \ell_c$	vs z	-0.05 ± 0.09	-26.83 ± 0.29	0.849	0.991	0.761	0.409	0.771
$\log \Delta v_{90}$	vs $[M/H]$	0.40 ± 0.04	2.40 ± 0.06	$< 1\text{E} - 6$	$< 1\text{E} - 6$	0.457	$< 1\text{E} - 6$	$< 1\text{E} - 6$
$\log W_{1526}$	vs $[M/H]$	0.58 ± 0.06	0.39 ± 0.08	$< 1\text{E} - 6$	$< 1\text{E} - 6$	0.464	$< 1\text{E} - 6$	$< 1\text{E} - 6$
$\log \ell_c$	vs $[M/H]$	0.26 ± 0.15	-26.63 ± 0.21	0.027	0.065	0.411	0.028	0.082
$\log W_{1526}$	vs $\log \Delta v_{90}$	0.83 ± 0.07	-1.91 ± 0.13	$< 1\text{E} - 6$	$< 1\text{E} - 6$	0.603	$< 1\text{E} - 6$	$< 1\text{E} - 6$
$\log \ell_c$	vs $\log \Delta v_{90}$	0.46 ± 0.25	-27.8 ± 0.5	0.006	0.019	0.182	0.007	0.026
$\log \ell_c$	vs $\log W_{1526}$	0.59 ± 0.29	-26.76 ± 0.11	0.011	0.009	0.157	— ^c	0.046

^aThese are the best fit parameters for the linear regression line of the form: $y = ax + b$

^bValues are probabilities that the null hypothesis of each test can be rejected

^cNot enough data points are available to get an accurate measurement

data using the MPFITEXY routine (Williams et al., 2010), which depends on the MPFIT package by Markwardt (2009). This routine takes into account the uncertainties in both parameters when calculating the slope and y-intercept of the best fit line. To calculate the uncertainty of the slope and y-intercept, we use a bootstrap method. The bootstrap method works by randomly selecting 100 DLAs from the original sample of 100 DLAs, but allowing for repeats. The resultant sample is then fitted using the same fitting routine as the original sample, and the slope and y-intercept are recorded. This sampling and fitting is repeated 1000 times, creating a distribution of slopes and y-intercepts. The $1-\sigma$ uncertainty on the slope and y-intercept is inferred from a Gaussian fit to these distributions. A second test for the existence of a correlation between the parameters is provided by the application of a Kendall Tau test. The resultant two-sided significance of its deviation from zero is shown in Table 2.4; here a small value indicates a probable correlation.

To test if the distribution of one parameter is dependent on a second, we appor-

tion our complete sample into three equally sized subsamples based on the value of the second parameter. We then compare the distribution of the first parameter for the subsamples with the smallest and largest values of the second parameter using four different tests. The first test we apply is a two-sided Kolmogorov-Smirnov (KS) test. This test will provide a probability that the two subsamples are drawn from the same parent population. A value smaller than 0.05 indicates that we can assume that the two populations were drawn from a different parent population at the 95 % confidence level (c.l.). To test if the variance of the two subsamples is significantly different, we use the F-statistic. Again a value of 0.05 or smaller indicates a significantly different variance in the two subsamples at the 95 % c.l. Finally, we used a Student's T-test and the Mann-Whitney U-test to compare the mean and median of the two subsamples, where again a smaller than 0.05 probability would indicate that the two subsamples have significantly different means or medians. The results of these tests for all 15 combinations are shown in Table 2.4.

In the next few subsections we will discuss some possible correlations that have not been discussed in previous papers; in particular the dependence of the HI column density to the other parameters. We also explore the possible correlation between redshift and kinematics, which is important for exploring the interplay between redshift, metallicity and mass of DLAs.

2.4.2.1 [M/H] vs n_{HI}

Figure 2.3 shows a plot of metallicity versus HI column density for the objects in our sample. The linear line was calculated using the method described in the previous section, and the shaded gray area marks the $1-\sigma$ uncertainty on this line. There are two features of this plot we would like to discuss. First, the sample shows a lack of high HI column density - high metallicity systems. Boissé et al. (1998) attributed this

lack to a dust bias; presumably these systems would have large enough dust fractions to block out all of the light from the QSO and therefore escape detection. This assertion has been questioned by many papers including Ellison et al. (2001b, 2005); Akerman et al. (2005); Jorgenson et al. (2006); Frank & Péroux (2010) who found that radio-selected DLAs do not differ significantly from those selected optically, and Kaplan et al. (2010) who detected certain metal-strong DLAs above the threshold found in Boissé et al. (1998). A second interpretation for this lack was put forth by Schaye (2001), which was further explored by Krumholz et al. (2009), who showed that the absence of high HI column density systems could be due to a transition from the atomic to molecular state of the atoms in the cold phase of a two-phase medium. However, both of these explanations only describe the lack of high column density - high metallicity systems, and are *unable to explain the second feature, which is the lack of high HI column density - low metallicity systems*. In fact, both features seem to be quite symmetric, in that the scatter plot exhibits a reflection symmetry about the line $[M/H] = -1.43$. To test if these features are statistically significant, we use the F-statistic. Table 2.4 shows that the F-statistic for the $[M/H]$ vs n_H correlation is 0.013. This indicates that the null hypothesis, which is that the smallest HI column density DLAs (i.e. DLAs with $n_H \leq 20.5$) and the largest HI column density DLAs (i.e. DLAs with $n_H \geq 20.85$) have the same variance, can be ruled out at a 95% confidence level. Hence, both features are not likely due to small number statistics; possible explanations for the existence of these two features and the symmetry between them are given in Section 2.6.1.

2.4.2.2 n_H Dependencies of the Remaining Parameters

Figure 2.4 shows the remaining four parameters plotted vs HI column density. Both redshift and Δv_{90} show no statistically significant correlation with n_H , and the distribution of these two parameters is also not dependent on n_H . For W_{1526} there is

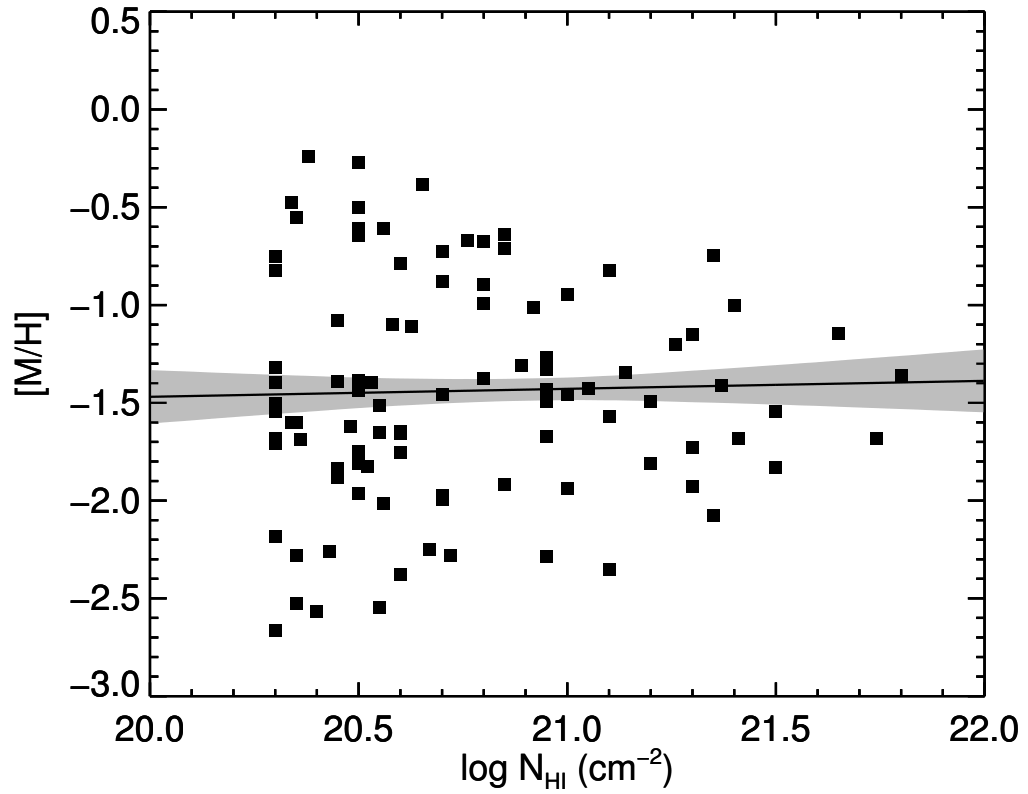


Figure 2.3: Metallicity versus HI column density. The square points mark our sample, and the solid line is a linear fit to the data, where the gray area marks the $1\text{-}\sigma$ error on this line. The sample shows a lack of high HI column density - high metallicity systems. The lack of these systems has been noted in previous papers such as Boissé et al. (1998). However, the sample also shows a lack of high HI column density - low metallicity systems. Using the F-statistic, we show that the lack of these systems is not likely (i.e. less than 5% probability) due to the small number of high HI column density systems.

a greater likelihood that we see evidence for an increase in equivalent width with HI column density as indicated by the Kendall tau parameter. However, this trend is not significant. This can be seen in the slope of the linear regression line which is consistent with no correlation at the $2\text{-}\sigma$ level. Finally, for the ℓ_c parameter, the high n_{H} subsample has a significantly smaller mean and median than the low n_{H} subsample. This is due to two effects. First, we can observe a similar trend as in the above case for metallicity that higher HI column density systems tend to have less variance compared to lower HI column density systems. Since the ℓ_c distribution is bimodal, the higher HI column density systems have values close to either of the two mean values, and therefore show a more distinct bimodality than the lower HI column density systems. Secondly, we are unable to measure low HI column density, low-cool systems, because we only use positive detections of the C II* $\lambda 1335.7$ line for calculating ℓ_c , and due to the limited signal to noise ratio of the spectra we are unable to positively detect the very low C II* column density systems. Both these effects contribute to the differing ℓ_c distribution for the low n_{H} and high n_{H} subsamples.

We would like to point out that this second effect also biases the relative sizes of the low-cool and high-cool subsamples. Wolfe et al. (2008) report relative sizes of the two subsamples to be 38 % for the low-cool subsample and 62 % for the high-cool sample using only positive detections. To gauge the extent of this bias, we estimate that for a spectrum with a signal to noise ratio of 30, the minimum value we can measure for the column density of C II* is approximately $10^{12.5} \text{ cm}^{-2}$. Using, equation 2.3 we can compute the corresponding ℓ_c value as a function of HI column density. This boundary, below which we cannot make any positive detections, is shown in Figure 2.4d by a dotted line. This shows that the result quoted in Wolfe et al. (2008) underestimates the number of DLAs in the low-cool sample. Comparing the number of DLAs in the two subsamples for DLAs with HI column density above $10^{20.7} \text{ cm}^{-2}$, for which this bias is

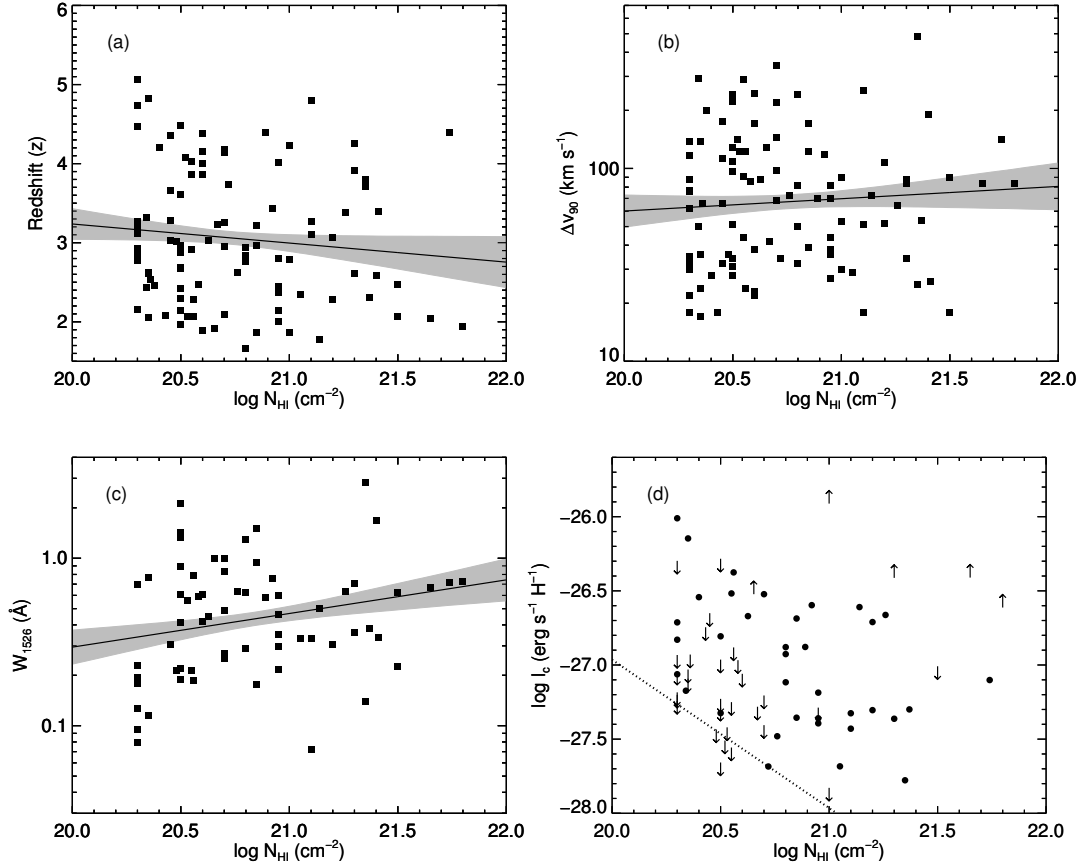


Figure 2.4: Remaining four parameters plotted against the HI column density. The figure markings are the same as Figure 2.3. Both redshift and Δv_{90} are consistent with no correlation, whereas W_{1526} shows a potential correlation with the HI column density, although this is not statistically significant for the sample size in this paper. The ℓ_c distribution tentatively shows that the bimodality is more evident at higher column densities. The dotted line indicates the line below which we cannot reasonably positively detect a cooling rate, because of the required S/N needed for a positive detection.

negligible, shows that there are in fact more DLAs in the low-cool subsample than the high-cool subsample. However, we caution that not enough data points are available to make a precise estimate of the sizes of the two subsamples.

2.4.2.3 Δv_{90} and W_{1526} vs Redshift

The last two possible correlations that we consider are the two kinematic properties, Δv_{90} and W_{1526} , as a function of redshift. The kinematical properties are believed to be strongly linked to the mass of the dark matter halo. This is a ubiquitous feature of almost all DLA models (e.g. Haehnelt et al., 1998; Prochaska & Wolfe, 1997). Since current Λ CDM models predict hierarchical galaxy formation, which in turn predict an increase in the mass of dark matter halos over time, we may expect to see a corresponding increase in the Δv_{90} and W_{1526} statistic of the DLAs as well. Again we use the tests described in Section 2.4.2 to see if there is any linear trend in the data, and/or if the distribution of Δv_{90} or W_{1526} is evolving with redshift.

Figure 2.5a shows Δv_{90} as a function of redshift. As in Figure 2.3, the solid black line indicates the best fit linear line to the data, and the gray area marks the $1-\sigma$ uncertainty on the parameters. The resultant best fit is: $\log_{10}(\Delta v_{90}) = (0.00 \pm 0.04) \cdot z + (1.84 \pm 0.13)$. This linear regression line is clearly consistent with no redshift evolution. Furthermore, all other tests show that the distribution of Δv_{90} is also consistent with no evolution.

This is in contrast with a previous result found by Ledoux et al. (2006), who found that the mean Δv_{90} decreased with increasing redshift when they apportioned their sample into two subsamples based on redshift. When we apportion our sample into two subsamples based on redshift, we find two main differences between their results and ours. First of all, our sample covers a larger redshift range; in particular our median values for each redshift subsample are 2.400 and 3.722 whereas their median redshifts

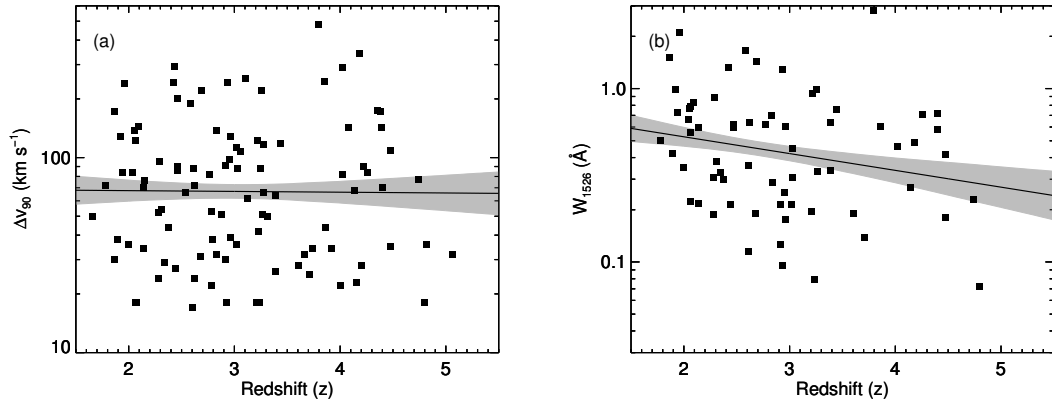


Figure 2.5: Redshift evolution of the two different kinematic parameters. The Δv_{90} statistic shows no evidence for any redshift evolution. The linear fit is clearly consistent with a flat line. The W_{1526} statistic shows potential evidence for redshift evolution as can be seen by the solid linear regression line. However, the sample size is too small to confirm this correlation.

are 2.087 and 2.796; any redshift evolution should therefore be more noticeable in our subsample. Second of all, their sample was smaller and no errors were reported in the median value of the velocity widths. Indeed, if we calculate the errors on the median for their two subsamples, we get a median of 69_{-13}^{+25} km s⁻¹ and 89_{-13}^{+20} km s⁻¹ for the high redshift and low redshift subsample respectively. This shows that the two medians are within 1- σ of each other, indicating that their sample is also consistent with no redshift evolution.

The second kinematic parameter we consider is W_{1526} , shown in Figure 2.5b. The data shows a lack of high-redshift large-equivalent width systems, and the Kendall Tau correlation test shows a small value of 0.042 indicating that a potential correlation could exist. However, a linear fit to the data gives $\log_{10}(W_{1526}) = (-0.10 \pm 0.05) \cdot z - (0.08 \pm 0.15)$, which indicates that the correlation is seen at only the 2- σ level. Moreover, when we compare the median and mean of the highest redshift DLAs with those of the lowest redshift DLAs, we do not see a significant difference in their value. Indeed the KS test shows a likelihood of 56 % that the two samples are drawn from the same parent

population. We therefore conclude that with the current sample size, the correlation between W_{1526} and redshift cannot be determined at $> 3\text{-}\sigma$ significance level.

2.5 The Fundamental Plane(s) of DLAs

As was discussed in the introduction, the aim of this chapter is to examine the interplay between multiple parameters of DLAs using the fundamental plane description. For this description to be useful, we need to have three parameters where two parameters are not strongly correlated, but each parameter shows a strong correlation to the third parameter. In Table 2.4 we list all of the correlations that exist between the six parameters discussed in this chapter. The only parameters that clearly satisfy this criterion are metallicity, redshift and Δv_{90} , and metallicity, redshift and W_{1526} . When we plot the first three parameters for each DLA on a three-dimensional scatter plot, we see that the points indeed fall close to a plane inside this space, although with scatter (Figure 2.6a). Figures 2.7a and 2.7b are two projections of this plane along the redshift and Δv_{90} axis respectively, where the third parameter is apportioned into two equally sized subgroups. Figure 2.7a is similar to Figure 2 of Ledoux et al. (2006) and Figure 2.7b is similar to Figure 11 of Rafelski et al. (2012). Figure 2.7a shows that the scatter in the Δv_{90} -metallicity correlation is in part due to redshift evolution of metallicity and similarly the scatter in the redshift-metallicity correlation is in part due to differences in the kinematics of the DLAs at each redshift.

To accurately describe the shape of the distribution in this three-dimensional space, we need to fit a plane equation to the scatter plot. To do this, we use the ‘direct fit’ least square fitting technique described in Bernardi et al. (2003), which fits a fundamental plane equation of the form $[M/H] = a \cdot \log \Delta v_{90} + b \cdot z + c$ to the data set. To account for measurement errors, we weigh each individual point by the inverse of the

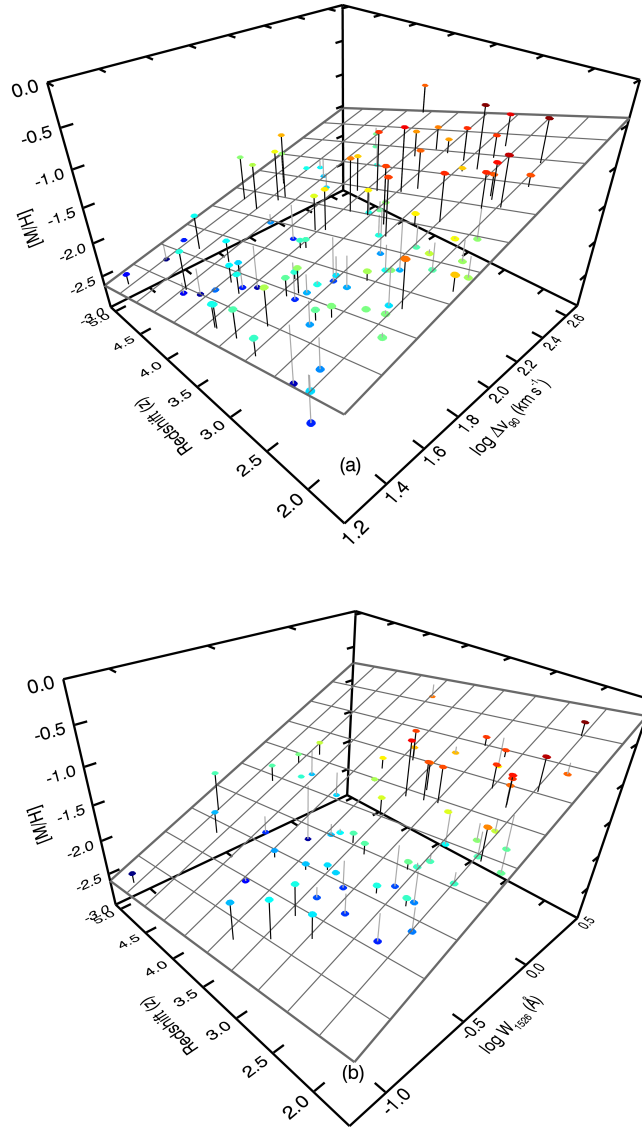


Figure 2.6: Panel (a) of this figure illustrates that when redshift, Δv_{90} and metallicity of a DLA are plotted on a three dimensional scatter plot, the points trace a plane in this parameter space, although with scatter. This plane is also seen when the Δv_{90} parameter is replaced by W_{1526} (panel (b)). The plane is marked by thick, dark gray lines. The data points are connected to this plane by solid black (gray) lines if they fall above (below) the plane. The color scale of the data points is correlated to the metallicity of the DLA.

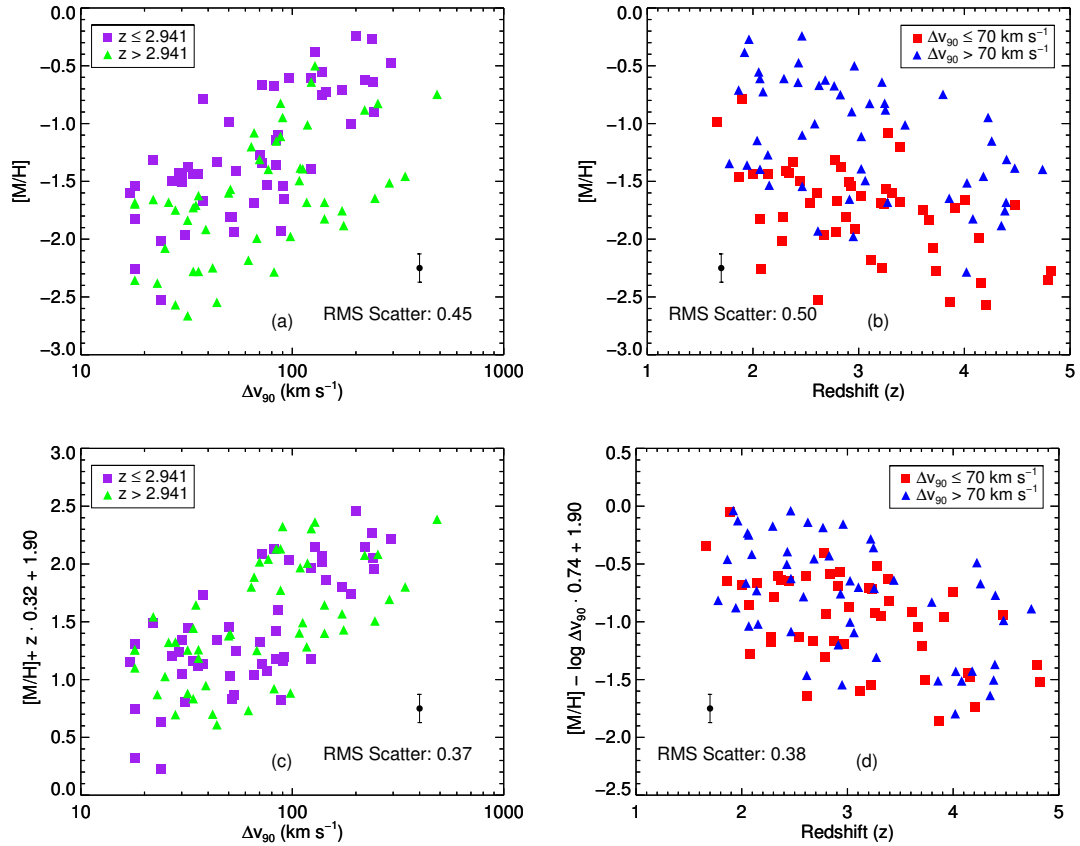


Figure 2.7: This figure illustrates the advantage of using the fundamental plane equation in describing the two correlations shown in the top two figures. Panel (a) shows the metallicity- Δv_{90} correlation where we have apportioned our sample into two equal subsamples based on redshift. The solid green triangles are the higher redshift DLAs, whereas the solid purple squares are lower redshift DLAs. This panel clearly shows that a large part of the scatter is due to the correlation between redshift and metallicity. Similarly, the scatter in the metallicity-redshift correlation (panel (b)) is due to the existence of a mass-metallicity correlation at each redshift. By applying the fundamental plane equation we can reduce this scatter as is shown in panels (c) and (d). The scatter is still bigger than the mean observational uncertainty, which is shown by the error bar.

estimated uncertainty using the methods described in Sheth & Bernardi (2012). This produces the following covariance matrix, R which is normalized by the RMS value of each quantity:

$$\begin{array}{c}
 \Delta v_{90} \quad z \quad [\text{M}/\text{H}] \\
 \Delta v_{90} \begin{pmatrix} 1.000 & 0.121 & 0.361 \\ 0.121 & 1.000 & -0.396 \\ 0.361 & -0.396 & 1.000 \end{pmatrix} \\
 z \\
 [\text{M}/\text{H}]
 \end{array}$$

From this matrix we can calculate the coefficients of the plane using the equations described in Bernardi et al. (2003). The resultant plane is described by the following equation:

$$[\text{M}/\text{H}] = (-1.9 \pm 0.5) + (0.74 \pm 0.21) \cdot \log \Delta v_{90} - (0.32 \pm 0.06) \cdot z \quad (2.4)$$

The uncertainty of the parameters are estimated using the bootstrap method discussed in Section 2.4.2. It is important to note that because Δv_{90} and redshift are not correlated (Figure 2.5a), the uncertainties in the coefficients of the fundamental plane are independent of each other. Figure 2.7c and 2.7d are plots in which we take into account the third parameter using the plane equation described above (i.e. this is like rotating the plane until it is edge-on). To quantify the reduction in scatter, we calculate the RMS scatter around a linear fit to the scatter plot before and after we apply the plane. The scatter in the correlations before we apply the plane equation is 0.45 dex (0.50 dex) for the metallicity- Δv_{90} (redshift-metallicity) relationship. After we apply the plane the scatter is reduced by approximately 20 % to 0.37 dex (0.38 dex) for each of the correlations. The reduction in scatter is clearly visible in Figures 2.7c and 2.7d. However, the scatter is still significantly bigger than the observational uncertainty on each measurement, which is on average 0.12 dex. We will comment more on the reduction in scatter

in Section 2.6.2.

The second fundamental plane of interest is similar to the first, except the Δv_{90} statistic is replaced by the other kinematic parameter, W_{1526} (Figure 2.6b). Prochaska et al. (2008) showed that the metallicity- W_{1526} correlation exhibits smaller scatter than the metallicity- Δv_{90} relationship, and a fundamental plane equation between metallicity, redshift and W_{1526} may reduce this scatter further. As in Sections 2.4.2 and 2.4.2, we are using just the subset of W_{1526} measurements with saturated W_{1526} values, although the inclusion of these systems does not significantly affect the shape or tilt of the fundamental plane. The equation of the fundamental plane between redshift, metallicity and W_{1526} is:

$$[M/H] = (-0.47 \pm 0.14) + (1.1 \pm 0.3) \cdot \log W_{1526} - (0.16 \pm 0.06) \cdot z \quad (2.5)$$

Figure 2.8a shows metallicity versus W_{1526} ; unlike Figure 2.7a where the Δv_{90} -metallicity trend moves downward with increasing redshift (i.e. at higher redshift, a given Δv_{90} corresponds to a lower metallicity), the W_{1526} -metallicity correlation does not evolve with redshift. The lower redshifts are higher on the correlation trend line because of the correlation between redshift and metallicity, but very little of the scatter is due to redshift, and therefore a fundamental plane description does not reduce the scatter significantly (Figure 2.8c) To be specific, the scatter is reduced by only 0.02 dex. Visually this means that we are already looking edge-on to the plane in Figure 2.8a. However, this second fundamental plane is able to reduce the scatter significantly (0.15 dex) in the redshift-metallicity relation (Figure 2.8d) as was the case with the previous fundamental plane. The measured scatter around the two correlations after applying this fundamental plane is 0.29 dex for the W_{1526} -metallicity correlation and 0.30 dex for the redshift-metallicity correlation. The scatter around this plane is significantly smaller

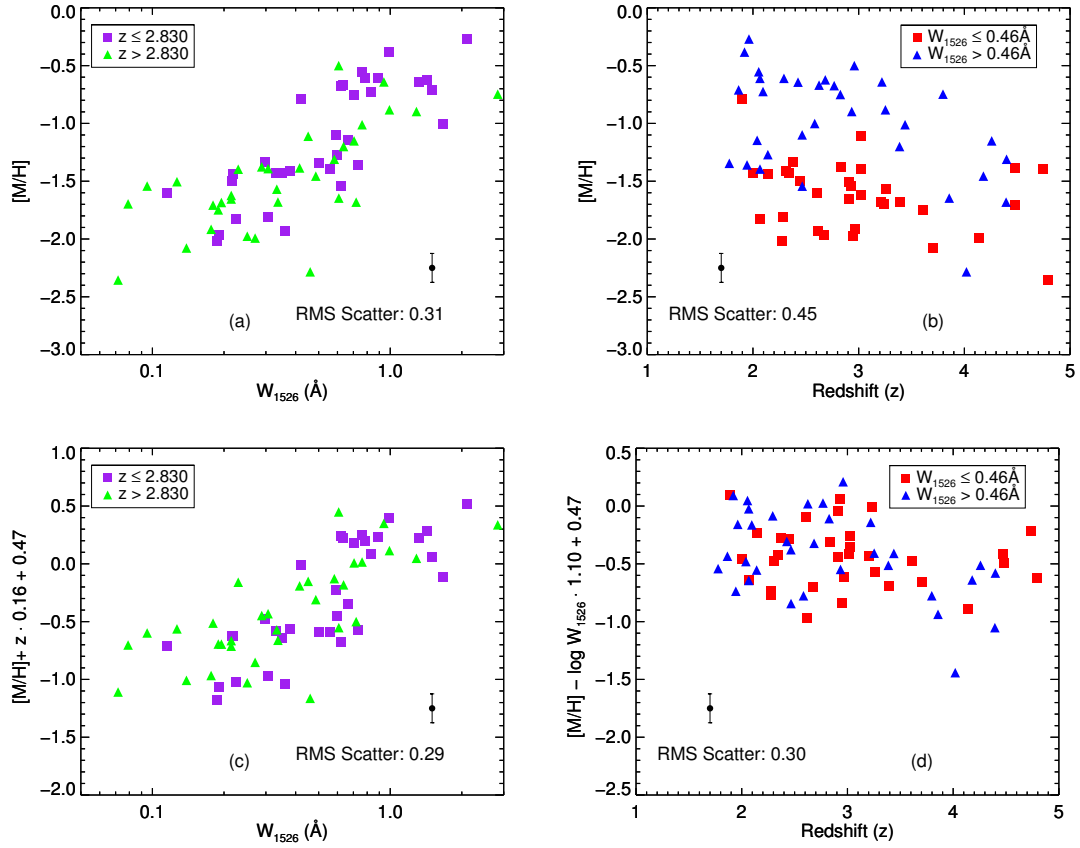


Figure 2.8: This figure illustrates the fundamental plane using the W_{1526} statistic instead of Δv_{90} . The panels are the same as Figure 2.7, except the kinematic parameter has been switched. Note that the scatter in the equivalent width-metallicity relationship is not significantly reduced by applying the fundamental plane equation. This is due to the fact that the plane is only slightly tilted in the redshift direction. This, in part, explains the observational result that the equivalent width-metallicity relationship exhibits the smallest scatter of any parameter with metallicity (Prochaska et al., 2008).

than the scatter around the fundamental plane found previously, which we discuss further in Section 2.6.2.

2.6 Discussion

The primary aim of this chapter has been to explore the fundamental relations that exist between the parameters that describe DLAs. In this section we discuss the

results of this study.

2.6.1 Implications of Two Parameter Dependencies

Table 2.4 lists all of the possible two parameter dependencies for DLAs that are explored in this chapter. The first notable dependency is that between the HI column density and the metallicity of the DLA (Section 2.4.2). Previous work (e.g. Boissé et al., 1998) observed a lack of high HI column density, high metallicity systems. Our sample, which was selected in a less biased way, shows that this lack of high HI column density, high metallicity systems is just half of the picture, and there is also a lack of high HI column density low metallicity systems. In Section 2.4.2 we have given two possible explanations for the lack of high HI column density, high metallicity systems, but we need an explanation for the lack of high HI column density, low metallicity systems.

One possibility is that this lower ‘envelope’ is not related to the upper ‘envelope’. The existence of just a lower envelope can be explained by the following two explanations: (1) higher HI column density DLAs are due to sightlines probing the inner part of galaxies, because of the metallicity gradients in DLAs (Chen et al., 2005), these sightlines should increase in metallicity. (2) Low metallicity DLAs are due to sightlines crossing cold flows, which because of their low density and high ionization level are unable to produce sightlines with a high HI column density. The latter is seen in simulations modeling cold flows by Fumagalli et al. (2011) who find that only at higher redshifts cold flows are able to host low HI column density, low metallicity DLAs.

The main problem with both these explanations is that they do not explain the striking symmetry that exists between the upper and lower envelope, and instead attribute the symmetry to coincidence. Two possible explanations that instead take the symmetry as a premise are (1) the fundamental plane equation is HI column density dependent. If indeed the tilt of the plane is slightly different for higher column density

systems (i.e. their metallicity does not evolve with redshift as much and/or their mass-metallicity correlation has a slightly different slope), then this could reduce the scatter in their metallicity. Our current data set is lacking enough high HI column density DLAs to confirm or refute this explanation. (2) Higher HI column density systems contain more absorption components than lower HI column density systems. The thought behind this is that each dark matter halo consists of components with varying metallicities. A low HI column density sightline through this halo will only sample a few components, and therefore can experience a wide range in metallicities. On the other hand, a high HI column density sightline will sample many components, and its metallicity will be the average metallicity of all these components. As a result the scatter in metallicities for these large HI column density systems is smaller than for the low HI column density systems. By varying the average metallicities of each dark matter halo depending on redshift and mass, we can still reproduce all other correlations with this explanation. Both explanations are therefore fully consistent with current observations.

Besides the dependency between metallicity and HI column density, the second set of notable dependencies discussed in this chapter are those between redshift and the kinematic parameters, Δv_{90} and W_{1526} . Both kinematic parameters are believed to trace the mass of the dark matter halo that hosts the DLA, although with significant scatter (e.g. Ledoux et al., 2006; Prochaska et al., 2008, see further Section 2.6.2). Therefore, these two parameters should show a strong correlation as is displayed in Figure 2.9. In this figure we have apportioned the sample into a low redshift and high redshift subsample. Interestingly, the high redshift sample has twice the RMS scatter compared to the low redshift subsample. Moreover, the scatter at high redshift only increases upward of the Δv_{90} - W_{1526} trendline at low redshift, suggesting that for a given W_{1526} value, the maximum available velocity width, $\Delta v_{90,\max}$, increases with increasing redshift. Since the scatter around the W_{1526} -metallicity correlation is smaller than the scatter around

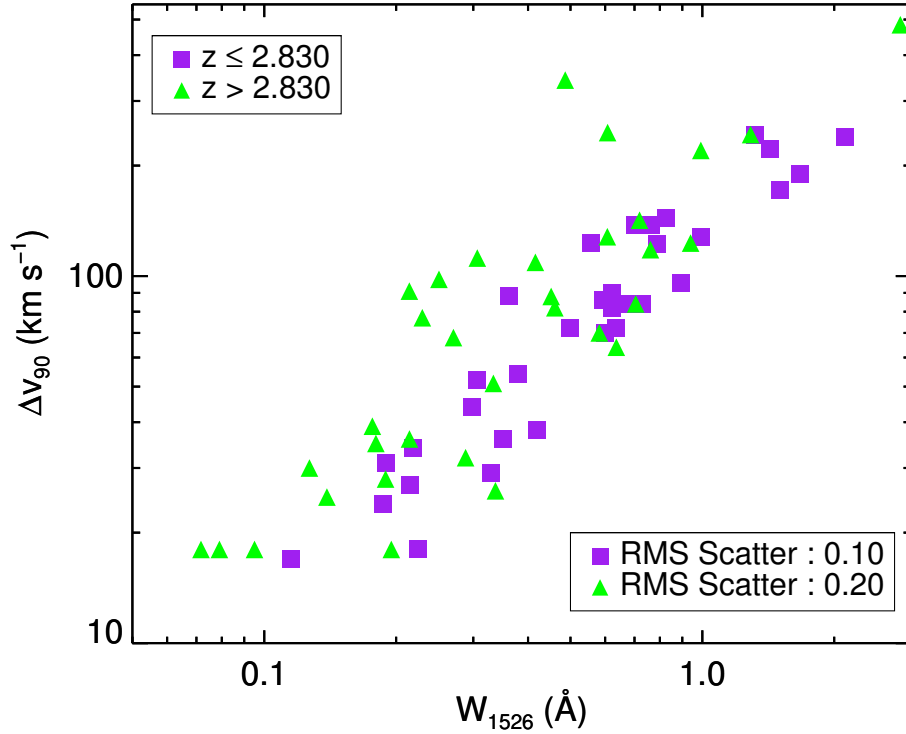


Figure 2.9: Plot of the two kinematic properties where the sample has been apporioned into two subgroups based on the redshift of the DLA. The low redshift subgroup, solid purple squares, shows a small scatter of 0.10 dex around a linear fit to the data, whereas the higher redshift sample, solid green triangles, shows a significantly larger scatter of 0.20 dex. This increase in scatter is only toward higher Δv_{90} values for a given W_{1526} value. In the text we provide two possible explanations for this observation.

the Δv_{90} -metallicity correlation, Prochaska et al. (2008) argues that W_{1526} is a better indicator of the dark matter halo mass than Δv_{90} . Under this assumption, the above result suggests that for a specific dark matter halo mass (i.e. a specific value of W_{1526}), $\Delta v_{90,\max}$ increases with redshift. This result, however, cannot be statistically confirmed with the current sample size.

Nevertheless, we provide here two potential explanations for the increase in scatter with increasing redshift around the Δv_{90} - W_{1526} correlation depending on which model is used to describe DLAs. If we assume that DLAs are large massive disks (e.g

Prochaska & Wolfe, 1997), then one way to interpret this result is that for a given dark matter halo mass, the rotational velocity structure of the neutral gas increases with increasing redshift, which will increase $\Delta v_{90, \text{max}}$. This is in agreement with the theoretical model of Mo et al. (1998), which predicts that for a given dark matter halo mass the rotational velocity of the galactic disk will increase with increasing redshift. If instead we assume that DLAs are a collection of low-mass protogalactic clumps (e.g Haehnelt et al., 1998), as in current Λ CDM models, we can interpret the result as a redistribution of the neutral gas content in dark matter halos with redshift. In this case, the $\Delta v_{90, \text{max}}$ for a specific dark matter halo mass at high redshift is larger, because some sightlines will probe satellite galaxies which move in the potential of the primary galaxy increasing the relative velocity of these objects. At low redshift, more satellite galaxies will have merged, decreasing the probability of these sightlines, and therefore decreasing $\Delta v_{90, \text{max}}$. Together with a decrease in galactic scale winds at low redshift, Cen (2012) has shown with numerical simulations that these two effects can decrease the $\Delta v_{90, \text{max}}$ with decreasing redshift.

Although we see tentative evidence for an evolution in the scatter around the correlation between Δv_{90} and W_{1526} with redshift, no correlation is found between redshift and Δv_{90} as shown in Figure 2.5a. Interestingly, this constancy in Δv_{90} with redshift is also seen in the numerical simulations by Cen (2012). Cen (2012) attributes this constancy to two countering processes: the growth of the dark matter halo mass with decreasing redshift, and the decrease in galactic scale winds due to reduced star formation at lower redshifts. Unlike Δv_{90} , W_{1526} shows a potential correlation with redshift. However, this correlation cannot be confirmed above the $3\text{-}\sigma$ level with the current sample size. Using a variety of different tests, we also looked at any potential evolution in the distributions of the kinematical parameters. Both distributions are consistent with no evolution. The lack of evolution of both the mean and distribution for both parameters is

significant for two reasons. First, the lack of evolution in the distribution of either kinematic parameter indicates that at each redshift, DLAs are embedded in a wide range of dark matter halo masses. Second, the weak correlation between redshift and kinematics allows us to combine two separate correlations, namely the redshift-metallicity correlation and the mass-metallicity correlation, into a single fundamental plane equation.

2.6.2 Implications of the Fundamental Plane of DLAs

The main result in this chapter is the existence of a fundamental plane for DLAs. In Section 2.5 we show that the redshift-metallicity and metallicity-velocity width correlations can be combined into a single planar equation (Equation 2.4). If instead we use the W_{1526} statistic, the equation becomes Equation 2.5. The underlying reason for the existence of both planes is thought to be similar. Since both kinematic parameters are tracers of mass, the fundamental plane simply combines the redshift-metallicity correlation and the mass-metallicity correlation, which are correlations known to exist for DLAs, into a single equation.

This equation provides a better description of the fundamental relation that exists between redshift, metallicity and kinematics than the two correlations for two reasons. First, it reduces the scatter around the correlations, and therefore provides a more stringent constraint for simulations modeling DLAs. The reduction in scatter is about 20 %, giving a reduced scatter of 0.37 dex and 0.38 dex around the correlations. This is still significantly larger than the observational uncertainty for each measurement, which is about 0.12 dex. However, we do not expect the scatter to reduce to the observational uncertainty because a single dark matter halo can produce a range in metallicities, velocity widths, and equivalent widths depending on where the quasar sightline intersects the dark matter halo. Hence, a certain amount of scatter is inherently part of the quasar absorption line experiment. To estimate the size of this scatter, we turn to numerical

simulations such as those presented by Pontzen et al. (2008). These simulations suggest a wide range of uncertainties depending on which model is used to describe DLAs, showing that a scatter of 0.38 dex can be reproduced from just intersecting dark matter halos at differing impact parameters. However, most models predict a scatter slightly smaller than this. The smaller scatter in the W_{1526} plane strengthens the idea that this parameter traces the kinematics of the halo gas (Prochaska et al., 2008), since the halo gas is assumed to be more spherically distributed than the neutral ISM, and therefore will be less affected by the impact parameter and inclination angle of the quasar sightline.

The second reason the fundamental plane description is a better description than the two individual correlations is that its existence confirms that the dark matter halos hosting DLAs satisfy a mass-metallicity correlation *at each redshift*. Ledoux et al. (2006) showed that this held true for their sample apportioned into a low redshift and high redshift subsample. Our result expands on their result and indicates that the mass-metallicity correlation holds over a larger redshift range. Moreover, we show that the zero point of the Δv_{90} -metallicity correlation is evolving with redshift. Figures 2.7a and 2.8a show that both subgroups of DLAs apportioned by redshift follow a similar mass-metallicity correlation. This can also be seen in Figures 2.7b and 2.8b where the more massive dark matter halos (i.e. larger Δv_{90} and larger W_{1526}) have at each redshift higher metallicities than the less massive dark matter halos. These two figures clearly show that at each redshift, the majority of the scatter in the metallicity-redshift correlation is caused by the existence of a mass-metallicity correlation. This result is consistent with the existence of mass-metallicity correlations found at both low and high redshift in star-forming galaxies (Tremonti et al., 2004; Savaglio et al., 2005; Erb et al., 2006; Maiolino et al., 2008). Although these studies used stellar mass and not total dynamical mass, there is a strong correlation expected between them (Brinchmann & Ellis, 2000).

We can use this dataset to explore the evolution of the mass-metallicity corre-

lation for DLAs over the redshift range $z = 2$ to $z = 5$. At redshifts below 0.75, the stellar mass-metallicity correlation evolves with redshift in a mass-independent way; the slope of the correlation stays the same, but the zero point of the correlation decreases with increasing redshift (Moustakas et al., 2011). Interestingly, this decrease in zero point and constancy of the slope is also seen in Figure 2.7a for the Δv_{90} -metallicity correlation. Moreover, the decrease in zero point for the our DLAs is about 0.3 dex per unit redshift, which is comparable to the decrease in the mass-metallicity relationship seen at redshifts below 0.75 (Moustakas et al., 2011) and between 0.7 and 3.5 (Maiolino et al., 2008) for mass-metallicity correlations determined from stellar masses. This suggests that DLAs are enriched in a similar manner as the star-forming galaxies used to determine the stellar mass-metallicity correlation. In a recent paper, Møller et al. (2013) conclude that the zero point of the mass-metallicity correlation might not evolve past a redshift of 2.6. This is in contrast to our result, which shows that the zero point is steadily evolving over the redshift range $z=2$ to $z=5$. Currently the sample of unbiased DLAs is too small to distinguish one scenario from the other. On the other hand, the zero point of the W_{1526} -metallicity correlation is not evolving with redshift. This suggests that the Δv_{90} parameter is a better indicator of the total stellar mass inside the dark matter halo compared to the W_{1526} parameter. This is not surprising since Δv_{90} describes the kinematics of the neutral gas, which should be more strongly correlated to the stellar mass than the mass of the dark matter halo.

2.6.3 Comparison with Models

We conclude this chapter by comparing the fundamental plane equation with numerical models which have specifically modeled DLAs. To date, DLA simulations have tried to reproduce some of the distributions of parameters such as metallicity and Δv_{90} (Pontzen et al., 2008; Tescari et al., 2009), and the observed two-parameter corre-

lations (Pontzen et al., 2008; Cen, 2012), but this chapter introduces a more restrictive criterion which should be satisfied, the fundamental plane of DLAs. A successful simulation should be able to populate the fundamental plane in a similar manner to what is observed. However, currently no simulation tracks these three parameters accurately. Instead we therefore consider only projections of the fundamental plane. In particular, the projection along the $\Delta_{v_{90}}$ axis gives the metallicity-redshift correlation; its agreement with models has been discussed in detail in Rafelski et al. (2012). The projection along the redshift axis leads to the metallicity- $\Delta_{v_{90}}$ correlation. This correlation has been compared to simulations in both Tescari et al. (2009) and Pontzen et al. (2008), where the latter finds a correlation equation of: $\log_{10}\Delta_{v_{90}} = 2.5 + 0.58 \cdot [M/H]$ at redshift 3. They compared this to the observational correlation equation of Ledoux et al. (2006) and noted the good agreement except for the significantly larger observational scatter. Comparing the model of Pontzen et al. (2008) to the new fundamental plane equation at redshift 3 (i.e. setting $z = 3$ in the fundamental plane equation) gives a similar agreement. The main improvement here, however, is in the scatter around this relationship. The scatter in previous observations was too large, because these observational analyses did not take into account the redshift evolution of metallicity. Using the fundamental plane reduces the scatter by about 20 %, and therefore the scatter in the Pontzen et al. (2008) simulation is in better agreement with the observational data than previously assumed.

Finally, we also compare the distributions of each of the parameters. Of these, the $\Delta_{v_{90}}$ distribution is the most interesting, because of the long standing inability of models in reproducing this distribution (Prochaska & Wolfe, 1997; Haehnelt et al., 1998; Razoumov et al., 2006; Pontzen et al., 2008). As was discussed in the introduction and shown in Section 2.4.1, this distribution has two characteristics that are difficult to reproduce by simulations based on Λ CDM models; namely the large median velocity, and

the high-velocity tail of the distribution. It is believed that the inability of reproducing these features of the Δv_{90} distribution is due to the inability of the numerical simulations to produce enough DLAs that reside in massive dark matter halos compared to less massive dark matter halos (Pontzen et al., 2008; Tescari et al., 2009). We test this hypothesis by comparing the numerical simulations to just those DLAs that are believed to reside in smaller dark matter halos.

To do this we select only the DLAs from our sample that have low cooling rates, ℓ_c . Wolfe et al. (2008) suggests that these DLAs reside in less massive dark matter halos compared to the high cooling rate DLAs. Figure 2.10a shows the Δv_{90} distribution of the complete sample (shaded red histogram); the gray solid histogram is the distribution obtained from the simulations by Pontzen et al. (2008). As can be seen from the inset and the KS test probability, there is a less than 1×10^{-6} probability the two distributions are drawn from the same parent population. On the other hand, Figure 2.10b shows that the DLAs with a low cooling rate (shaded green histogram) have a Δv_{90} distribution similar to that obtained from the numerical simulation. This result supports the hypothesis that the numerical simulations are capable of reproducing the Δv_{90} distribution of the DLAs in less massive dark matter halos, but have difficulty producing enough DLAs that reside in more massive dark matter halos. This conclusion was also recently drawn in Font-Ribera et al. (2012) using the cross-correlation between DLAs and the Lyman α forest.

One way numerical simulations try to mitigate the discrepancy in the observed and simulated velocity width distribution is by adding in galactic scale outflows (Tescari et al., 2009; Hong et al., 2010; Cen, 2012). These outflows are capable of decreasing the cross section of less massive dark matter halos, somewhat decoupling the Δv_{90} statistic from the mass, and increasing the cross section of the more massive dark matter halos. All of these effects increase the relative number of DLAs in more massive dark matter halos. With the addition of galactic scale outflows, these models have been relatively

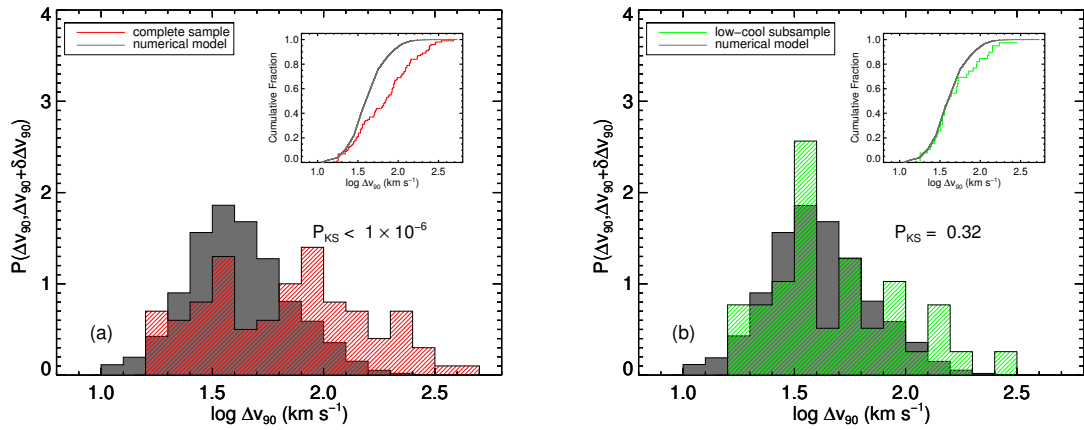


Figure 2.10: Distribution of the kinematic parameter Δv_{90} for both the observational data and the numerical model by Pontzen et al. (2008). The solid gray distribution is the distribution of the numerical model by Pontzen et al. (2008). The hashed red sample in panel (a) is the complete sample, whereas the hashed green sample in panel (b) is just the subset of DLAs that are part of the low-cool population of DLAs as defined in (Wolfe et al., 2008). The left panel shows that the complete sample is inconsistent with the numerical model, since a two-sided KS test gives a probability less than 1×10^{-6} that the two populations are drawn from the same parent distribution. On the other hand, the right panel shows that the low-cool subsample of DLAs is consistent with the velocity distribution found from the numerical model. Since low-cool DLAs are believed to arise from less massive dark matter halos, this result corroborates the hypothesis that numerical simulations are underproducing the occurrences of DLAs that reside in massive dark matter halos.

successful in reproducing the Δv_{90} distribution of DLAs (Tescari et al., 2009; Hong et al., 2010; Cen, 2012), which is supported by the sample in this chapter. However, Font-Ribera et al. (2012) suggest that this process still might not produce enough DLAs hosted within massive dark matter halos, indicating that there is still some discrepancy between the observations and the simulations.

2.7 Summary

We have studied the spectra of 100 DLAs taken with a single high resolution instrument, the High Resolution Echelle Spectrometer on the Keck telescope, to determine the fundamental relations that exist between the measured parameters (Table 2.4). We find the following new results.

1. The metallicity-H I dependency shown in Figure 2.3 shows a lack of high H I column density, low metallicity systems besides the known lack of high H I column density, high metallicity systems (Boissé et al., 1998). Possible explanations for the lack of high H I column density, low metallicity systems are that (1) low metallicity systems arise from cold flows which are not dense enough to form high H I column density systems (Fumagalli et al., 2011), or (2) that higher H I column density systems arise from sightlines probing the inner part of galaxies, which have higher metallicity because of an existing metallicity gradient (Chen et al., 2005). However, neither of these explanations can explain the reflection symmetry that exists about the line $[M/H] = -1.43$. One possible explanation that takes this reflection symmetry as a premise, is that higher H I column density systems probe a larger number of components. The larger number of components results in a smaller probability of encountering a sightline with a very low or very high metallicity. Hence, this will decrease the variance around the mean metallicity

value of -1.43 for higher column density systems.

2. The $\Delta_{v_{90}}$ parameter is not evolving between redshift 2 through 5 (Figure 2.5a). This indicates that at all redshifts, DLAs are hosted by a wide variety of dark matter halo masses, and it allows for a combined description of the $\Delta_{v_{90}}$ -metallicity and redshift-metallicity correlations.
3. The main result of the chapter is that we can describe the relations that exist between the redshift, metallicity and mass of a DLA by a single fundamental plane equation: $[M/H] = (-1.9 \pm 0.5) + (0.74 \pm 0.21) \cdot \log \Delta_{v_{90}} - (0.32 \pm 0.06) \cdot z$. This plane equation has as advantage that it reduces the scatter around either of the correlations; providing a more stringent constraint for numerical simulations. Secondly, it confirms the existence of a mass-metallicity relationship at each redshift between redshift 2 through 5, where the zero point evolves with redshift. This evolution in the zero point with redshift is consistent with the evolution of the zero point of the mass-metallicity relationship seen in star forming galaxies.
4. Finally, we compare the sample data to numerical models, and find that numerical models are unable to reproduce the $\Delta_{v_{90}}$ distribution of the complete sample (Figure 2.10a). However, these models are able to reproduce the $\Delta_{v_{90}}$ distribution of the low-cool subset of the sample (Figure 2.10b). These low-cool DLAs are believed to reside in smaller dark matter halos (Wolfe et al., 2008). This result therefore supports the hypothesis that numerical models fail to produce enough DLAs in massive dark matter halos (Pontzen et al., 2008; Tescari et al., 2009).

2.8 Acknowledgements

Support for this work was provided by NSF grant 11-09447. The data presented herein were obtained at the W.M. Keck Observatory, which is operated as a scientific partnership among the California Institute of Technology, the University of California and the National Aeronautics and Space Administration. The Observatory was made possible by the generous financial support of the W.M. Keck Foundation. The authors wish to recognize and acknowledge the very significant cultural role and reverence that the summit of Mauna Kea has always had within the indigenous Hawaiian community. We are fortunate to have the opportunity to conduct observations from this mountain.

This Chapter, in full (with minor exceptions to conform to this thesis), is a reprint of material previously published as “The Fundamental Plane of Damped Ly α Systems”, by Marcel Neeleman, Arthur M. Wolfe, J. Xavier Prochaska, & Marc Rafelski, published in the The Astrophysical Journal, 2013, Vol. 769, p.54. I was the primary investigator and author of this paper.

2.9 References for Chapter 2

Abazajian, K. N., Adelman-McCarthy, J. K., Agüeros, M. A., Allam, S. S., Allende Prieto, C., An, D., Anderson, K. S. J., Anderson, S. F., Annis, J., Bahcall, N. A., Bailer-Jones, C. A. L., Barentine, J. C., Bassett, B. A., Becker, A. C., Beers, T. C., Bell, E. F., Belokurov, V., Berlind, A. A., Berman, E. F., Bernardi, M., Bickerton, S. J., Bizyaev, D., Blakeslee, J. P., Blanton, M. R., Bochanski, J. J., Boroski, W. N., Brewington, H. J., Brinchmann, J., Brinkmann, J., Brunner, R. J., Budavári, T., Carey, L. N., Carliles, S., Carr, M. A., Castander, F. J., Cinabro, D., Connolly, A. J., Csabai, I., Cunha, C. E., Czarapata, P. C., Davenport, J. R. A., de Haas, E., Dilday, B., Doi, M., Eisenstein, D. J., Evans, M. L., Evans, N. W., Fan, X., Friedman, S. D., Frieman, J. A., Fukugita, M., Gänsicke, B. T., Gates, E., Gillespie, B., Gilmore, G., Gonzalez, B., Gonzalez, C. F., Grebel, E. K., Gunn, J. E., Györy, Z., Hall, P. B., Harding, P., Harris, F. H., Harvanek, M., Hawley, S. L., Hayes, J. J. E., Heckman, T. M., Hendry, J. S., Hennessy, G. S., Hindsley, R. B., Hoblitt, J., Hogan, C. J., Hogg, D. W., Holtzman, J. A., Hyde, J. B., Ichikawa, S.-i., Ichikawa, T., Im, M., Ivezić, Ž., Jester, S.,

- Jiang, L., Johnson, J. A., Jorgensen, A. M., Jurić, M., Kent, S. M., Kessler, R., Kleinman, S. J., Knapp, G. R., Konishi, K., Kron, R. G., Krzesinski, J., Kuropatkin, N., Lampeitl, H., Lebedeva, S., Lee, M. G., Lee, Y. S., French Leger, R., Lépine, S., Li, N., Lima, M., Lin, H., Long, D. C., Loomis, C. P., Loveday, J., Lupton, R. H., Magnier, E., Malanushenko, O., Malanushenko, V., Mandelbaum, R., Margon, B., Marriner, J. P., Martínez-Delgado, D., Matsubara, T., McGehee, P. M., McKay, T. A., Meiksin, A., Morrison, H. L., Mullally, F., Munn, J. A., Murphy, T., Nash, T., Nebot, A., Neilsen, Eric H., J., Newberg, H. J., Newman, P. R., Nichol, R. C., Nicinski, T., Nieto-Santisteban, M., Nitta, A., Okamura, S., Oravetz, D. J., Ostriker, J. P., Owen, R., Padmanabhan, N., Pan, K., Park, C., Pauls, G., Peoples, John, J., Percival, W. J., Pier, J. R., Pope, A. C., Pourbaix, D., Price, P. A., Purger, N., Quinn, T., Raddick, M. J., Re Fiorentin, P., Richards, G. T., Richmond, M. W., Riess, A. G., Rix, H.-W., Rockosi, C. M., Sako, M., Schlegel, D. J., Schneider, D. P., Scholz, R.-D., Schreiber, M. R., Schwope, A. D., Seljak, U., Sesar, B., Sheldon, E., Shimasaku, K., Sibley, V. C., Simmons, A. E., Sivarani, T., Allyn Smith, J., Smith, M. C., Smolčić, V., Snedden, S. A., Stebbins, A., Steinmetz, M., Stoughton, C., Strauss, M. A., SubbaRao, M., Suto, Y., Szalay, A. S., Szapudi, I., Szkody, P., Tanaka, M., Tegmark, M., Teodoro, L. F. A., Thakar, A. R., Tremonti, C. A., Tucker, D. L., Uomoto, A., Vanden Berk, D. E., Vandenberg, J., Vidrih, S., Vogeley, M. S., Voges, W., Vogt, N. P., Wadadekar, Y., Watters, S., Weinberg, D. H., West, A. A., White, S. D. M., Wilhite, B. C., Wonders, A. C., Yanny, B., Yocum, D. R., York, D. G., Zehavi, I., Zibetti, S., & Zucker, D. B. 2009, *ApJS*, 182, 534
- Akerman, C., Ellison, S. L., Pettini, M., & Steidel, C. C. 2005, *A&A*, 440, 499
- Asplund, M., Grevesse, N., Sauval, A. J., & Scott, P. 2009, *ARA&A*, 47, 481
- Bernardi, M., Sheth, R. K., Annis, J., Burles, S., Eisenstein, D. J., Finkbeiner, D. P., Hogg, D. W., & Lupton, R. H. 2003, *AJ*, 125, 1866
- Boissé, P., Le Brun, V., Bergeron, J., & Deharveng, J.-M. 1998, *A&A*, 333, 841
- Brinchmann, J. & Ellis, R. 2000, *ApJ*, 536, L77
- Cen, R. 2012, *ApJ*, 748, 121
- Chen, H.-W., Kennicutt Jr, R. C., & Rauch, M. 2005, *ApJ*, 620, 703
- Cooke, R., Pettini, M., Steidel, C. C., & Rudie, G. C. 2011, *MNRAS*, 417, 1534
- Dessauges-Zavadsky, M., Calura, F., Prochaska, J. X., D’Odorico, S., & Matteucci, F. 2004, *A&A*, 416, 79
- . 2006, *A&A*, 445, 93
- . 2007, *A&A*, 470, 431

- Djorgovski, S. & Davis, M. 1987, *ApJ*, 313, 59
- Ellison, S. L., Hall, P. B., & Lira, P. 2005, *AJ*, 130, 1345
- Ellison, S. L., Pettini, M., Steidel, C. C., & Shapley, A. E. 2001a, *ApJ*, 549, 770
- Ellison, S. L., Prochaska, J. X., Hennawi, J., Lopez, S., Usher, C., Wolfe, A. M., Russell, D. M., & Benn, C. R. 2010, *MNRAS*, 406, 1453
- Ellison, S. L., Yan, L., Hook, I., Pettini, M., Wall, J., & Shaver, P. 2001b, *A&A*, 379, 393
- Erb, D. K., Shapley, A. E., Pettini, M., Steidel, Charles, C., Reddy, N. A., & Adelberger, K. L. 2006, *ApJ*, 644, 813
- Font-Ribera, A., Miralda-Escudé, J., Arnau, E., Carithers, W., Lee, K.-G., Noterdaeme, P., Pâris, I., Petitjean, P., Rich, J., Rollinde, E., Ross, N., Schneider, D. P., White, M., & York, D. G. 2012, *JCAP*, 11, 59, arXiv:1209.4596v1
- Fox, A. J., Ledoux, C., Petitjean, P., & Srianand, R. 2007, *A&A*, 473, 791
- Frank, S. & Péroux, C. 2010, *MNRAS*, 406, 2235
- Fumagalli, M., Prochaska, J. X., Kasen, D., Dekel, A., Ceverino, D., & Primack, J. R. 2011, *MNRAS*, 418, 1796
- Fynbo, J., Laursen, P., Ledoux, C., Møller, P., Durgapal, A., Goldoni, P., & Gullberg, B. 2010, *MNRAS*, 408, 2128
- Fynbo, J., Ledoux, C., Noterdaeme, P., Christensen, L., Møller, P., Durgapal, A., Goldoni, P., & Kaper, L. 2011, *MNRAS*, 413, 2481
- Graves, G. J. & Faber, S. M. 2010, *ApJ*, 717, 803
- Haehnelt, M. G., Steinmetz, M., & Rauch, M. 1998, *ApJ*, 495, 647
- Herbert-Fort, S., Prochaska, J. X., Dessauges-Zavadsky, M., Ellison, S. L., Howk, J. C., Wolfe, A. M., & Prochter, G. E. 2006, *PASP*, 118, 1077
- Hong, S., Katz, N., Davé, R., Fardal, M., Dušan, K., & Oppenheimer, B. D. 2010, arXiv:1008.4242v2
- Jorgenson, R. A., Wolfe, A. M., & Prochaska, J. X. 2010, *ApJ*, 722, 460
- Jorgenson, R. A., Wolfe, A. M., Prochaska, J. X., Lu, L., Howk, J. C., Cooke, J., Gawiser, E., & Gelino, D. 2006, *ApJ*, 646, 730
- Kaplan, K. F., Prochaska, J. X., Herbert-Fort, S., Ellison, S. L., & Dessauges-Zavadsky, M. 2010, *MNRAS*, 409, 619

- Kormendy, J. 1982, in Proc. 12th Saas-Fe Advanced Course Morphology and Dynamics of Galaxies (Geneva Obs. Pub.), 113–288
- Krumholz, M. R., Ellison, S. L., Prochaska, J. X., & Tumlinson, J. 2009, *ApJ*, 701, L12
- Kulkarni, V. P., Fall, S. M., Lauroesch, J. T., York, D. G., Welty, D. E., Khare, P., & Truran, J. W. 2005, *ApJ*, 618, 68
- Ledoux, C., Petitjean, P., Bergeron, J., Wampler, E. J., & Srianand, R. 1998, *A&A*, 337, 51
- Ledoux, C., Petitjean, P., Fynbo, J., Møller, P., & Srianand, R. 2006, *A&A*, 457, 71
- Ledoux, C., Srianand, R., & Petitjean, P. 2002, *A&A*, 392, 781
- Levshakov, S. A., Dessauges-Zavadsky, M., D’Odorico, S., & Molaro, P. 2002, *ApJ*, 565, 696
- Lopez, S., Reimers, D., Rauch, M., Sargent, W. L., & Smette, A. 1999, *ApJ*, 513, 598
- Lu, L., Sargent, W. L., & Barlow, T. A. 1996, *ApJ Supp.*, 107, 475
- . 1998, *AJ*, 115, 55
- Maiolino, R., Nagao, T., Grazian, A., Cocchia, F., Marconi, A., Mannucci, F., Cimatti, A., Pipino, A., & Banero, S. 2008, *A&A*, 488, 463
- Markwardt, C. B. 2009, *ADASS*, 411, 251
- Merloni, A., Heinz, S., & Di Matteo, T. 2003, *MNRAS*, 345, 1057
- Mo, H. J., Mao, S., & White, S. D. 1998, *MNRAS*, 295, 319
- Molaro, P., Bonifacio, P., Centurión, M., D’Odorico, S., Vladilo, G., Santin, P., & Di Marcantonio, P. 2000, *ApJ*, 541, 54
- Molaro, P., Levshakov, S. A., D’Odorico, S., Bonifacio, P., & Centurión, M. 2001, *ApJ*, 549, 90
- Møller, P., Fynbo, J., Ledoux, C., & Nilsson, K. 2013, *MNRAS*, In Press
- Morton, D. C. 2003, *ApJS*, 149, 205
- Moustakas, J., Brown, M., Cool, R. J., Dey, A., Eisenstein, D. J., Gonzalez, A. H., Jannuzi, B., Jones, C., Kochanek, C. S., Murray, S. S., & Wild, V. 2011, arXiv:astro-ph/1112.3300
- Noterdaeme, P., Petitjean, P., Carithers, W., Pâris, I., Font-Ribera, A., Bailey, S., Auborg, E., Bizyaev, D., Ebelke, G., & Finley, H. 2012, *A&A*, 547, L1

- Noterdaeme, P., Petitjean, P., Ledoux, C., & Srianand, R. 2009, *A&A*, 505, 1087
- Penprase, B. E., Prochaska, J. X., Sargent, W. L., Toro-Martinez, I., & Beeler, D. J. 2010, *ApJ*, 721, 1
- Petitjean, P., Srianand, R., & Ledoux, C. 2000, *A&A*, 364, L26
- . 2002, *MNRAS*, 332, 383
- Pettini, M., Smith, L. J., Hunstead, R. W., & King, D. L. 1994, *ApJ*, 426, 79
- Pettini, M., Zych, B. J., Steidel, C. C., & Chaffee, F. H. 2008, *MNRAS*, 385, 2011
- Pontzen, A., Governato, F., Pettini, M., Booth, C., Stinson, G., Wadsley, J., Brooks, A., Quinn, T., & Haehnelt, M. 2008, *MNRAS*, 390, 1349
- Pottasch, S., Wesselius, P., & van Duinen, R. 1979, *A&A*, 74, L15
- Prochaska, J. X., Chen, H.-W., Wolfe, A. M., Dessauges-Zavadsky, M., & Bloom, J. S. 2008, *ApJ*, 672, 59
- Prochaska, J. X., Gawiser, E., Wolfe, A. M., Castro, S., & Djorgovski, S. 2003a, *ApJ*, 595, L9
- Prochaska, J. X., Gawiser, E., Wolfe, A. M., Cooke, J., & Gelino, D. 2003b, *ApJS*, 147, 227
- Prochaska, J. X., Herbert-Fort, S., & Wolfe, A. M. 2005, *ApJ*, 635, 123
- Prochaska, J. X. & Wolfe, A. M. 1996, *ApJ*, 470, 403
- . 1997, *ApJ*, 487, 73
- . 1999, *ApJ Supp.*, 121, 369
- . 2000, *ApJ*, 533, L5
- . 2002a, *ApJ*, 566, 68
- . 2009, *ApJ*, 696, 1543
- . 2010, *arXiv:astro-ph/1009.3960*
- Prochaska, J. X., Wolfe, A. M., Howk, J. C., Gawiser, E., Burles, S. M., & Cooke, J. 2007, *ApJS*, 171, 29
- Prochaska, J. X., Wolfe, A. M., Tytler, D., Burles, S., Cooke, J., Gawiser, E., Kirkman, D., O'Meara, J. M., & Storrie-Lombardi, L. 2001a, *ApJ Supp.*, 137, 21

- Rafelski, M., Wolfe, A. M., Prochaska, J. X., Neeleman, M., & Mendez, A. 2012, *ApJ*, 755, 89
- Razoumov, A. O., Norman, M. L., Prochaska, J. X., & Wolfe, A. M. 2006, *ApJ*, 645, 55
- Rea, N., Pons, J. A., Torres, D. F., & Turolla, R. 2012, *ApJ*, 748, L12
- Savage, B. D. & Sembach, K. R. 1991, *ApJ*, 379, 245
- Savaglio, S., Glazebrook, D., Le Borgne, D., Juneau, S., Abraham, R., Chen, H.-W., Crampton, D., McCarthy, P., Carlberg, R., Marzke, R., Roth, K., Jørgensen, I., & Murowinski, R. 2005, *ApJ*, 635, 260
- Schaye, J. 2001, *ApJ*, 559, L1
- Sheinis, A., Bolte, M., Epps, H., Kibrick, R., Miller, J., Radovan, M., Bigelow, B., & Sutin, B. 2002, *PASP*, 114, 851
- Sheth, R. K. & Bernardi, M. 2012, *MNRAS*, 422, 1825
- Suzuki, N., Tytler, D., Kirkman, D., O'Meara, J. M., & Lubin, D. 2003, *PASP*, 115, 1050
- Tescari, E., Viel, M., Tornatore, L., & Borgani, S. 2009, *MNRAS*, 397, 411
- Tremonti, C. A., Heckman, T. M., Kaufmann, G., Brinchmann, J., Charlot, S., White, S. D., Seibert, M., Peng, E. W., Schlegel, D. J., Uomoto, A., Fukugita, M., & Brinkmann, J. 2004, *ApJ*, 613, 898
- Vladilo, G., Abate, C., Yin, J., Cescutti, G., & Matteucci, F. 2011, *A&A*, 530, 33
- Vogt, S., Allen, S., Bigelow, B., Bresee, L., Brown, B., Cantrall, T., Conrad, A., Couture, M., Delaney, C., Epps, H., Hilyard, D., Hilyard, D., Horn, E., Jern, N., Kanto, D., Keave, M., Kibrick, R., Lewis, J., Osborne, J., Pardeilhan, G., Pfister, T., Ricketts, T., Robinson, L., Stover, R., Tucker, D., Ward, J., & Wei, M. 1994, *Proc. SPIE*, 2198, 362
- Williams, M. J., Bureau, M., & Cappellari, M. 2010, *MNRAS*, 409, 1330
- Wolfe, A. M., Fan, X.-M., Tytler, D., Vogt, S., Keane, M. J., & Lanzetta, K. A. 1994, *ApJ*, 435, L101
- Wolfe, A. M., Gawiser, E., & Prochaska, J. X. 2005, *ARA&A*, 43, 861
- Wolfe, A. M., Lanzetta, K. A., Foltz, C. B., & Chaffee, F. H. 1995, *ApJ*, 454, 698
- Wolfe, A. M. & Prochaska, J. X. 1998, *ApJ*, 494, L15
- . 2000, *ApJ*, 545, 591

Wolfe, A. M., Prochaska, J. X., & Gawiser, E. 2003a, ApJ, 593, 215

Wolfe, A. M., Prochaska, J. X., Jorgenson, R. A., & Rafelski, M. 2008, ApJ, 681, 881

Wright, E., Mather, J., Bennett, C., Cheng, E., Shafer, R., Fixsen, D., Eplee, R., & Isaacman, R. 1991, ApJ, 381, 200

Chapter 3

Probing the Physical Conditions of Atomic Gas at High Redshift

3.1 Abstract

A new method is used to measure the physical conditions of the gas in damped Lyman- α systems (DLAs). Using high resolution absorption spectra of a sample of 80 DLAs, we are able to measure the ratio of the upper and lower fine-structure levels of the ground state of C^+ and Si^+ . These ratios are determined solely by the physical conditions of the gas. We explore the allowed physical parameter space using a Monte Carlo Markov Chain method to constrain simultaneously the temperature, neutral hydrogen density, and electron density of each DLA. The results indicate that at least 5 % of all DLAs have the bulk of their gas in a dense, cold phase with typical densities of $\sim 100 \text{ cm}^{-3}$ and temperatures below 500 K. We further find that the typical pressure of DLAs in our sample is $\log(P/k_B) = 3.4 \text{ [K cm}^{-3}\text{]}$, which is comparable to the pressure of the local interstellar medium (ISM), and that the components containing the bulk of the neutral gas can be quite small with absorption sizes as small as a few parsec. We show

that the majority of the systems are consistent with having densities significantly higher than expected from a purely canonical WNM, indicating that significant quantities of dense gas (i.e. $n_{\text{H}} > 0.1 \text{ cm}^{-3}$) are required to match observations. Finally, we identify 8 systems with positive detections of Si II*. These systems have pressures (P/k_{B}) in excess of 20000 K cm^{-3} , which suggest that these systems tag a highly turbulent ISM in young, star-forming galaxies.

3.2 Introduction

Galaxy formation and evolution is fundamentally dependent on the gas that forms the galaxy. From its inception as a gravitational bound collection of gas to the formation of stars inside an evolved galaxy, the physical properties of the gas affect the outcome of such processes. It is therefore of paramount importance to understand the physical properties of the gas inside and around galaxies.

Already early on, Field et al. (1969) noted that when heating and cooling sources of a neutral gas are in thermal equilibrium, the gas naturally segregates into two distinct phases. A cold, dense phase known as the cold neutral medium (CNM), and a warmer, less dense phase, the warm neutral medium (WNM). This model was improved upon by McKee & Ostriker (1977) to include a third phase, namely the hot ionized medium due to ionizing shock fronts produced by supernova. On the basis of this model, Wolfire et al. (1995, 2003) calculated the equilibrium pressures and temperatures of the neutral gas under a variety of different galactic conditions. This theoretical model, in its general form, still holds as the paradigm for the physical conditions of neutral galactic gas.

Observationally, the validity of this model has been tested for gas in the local universe. The observational studies range over a large part of the electromagnetic

spectrum from X-ray (Snowden et al., 1997) to radio (Heiles & Troland, 2003a). The results suggest that indeed some of the gas has properties of both the CNM and WNM. However, a large fraction of the WNM is actually found to be in the temperature region between 500 K and 5000 K (Heiles & Troland, 2003b; Roy et al., 2013a,b). One possible explanation for the existence of this gas in what is known as the ‘forbidden region’ comes from numerical simulations, which show that turbulence could produce the observed gas characteristics while still locally satisfying thermodynamic equilibrium (Gazol et al., 2005; Walch et al., 2011).

To understand the evolution of galaxies, it would be ideal to measure the properties of the gas over a range of redshifts and physical conditions. This, however, is difficult to do because the methods used at low redshift are not feasible for distant galaxies. In particular, 21 cm line emission has only been detected in galaxies up to $z \sim 0.26$ (Catinella et al., 2008). To circumvent this problem, we can study the gas in absorption against background sources (e.g. quasars). The absorbers with the largest HI gas column densities are known as damped Lyman- α systems (DLAs; for a review see Wolfe et al., 2005). DLAs have neutral hydrogen column densities (N_{HI}) equal or greater than $2 \times 10^{20} \text{ cm}^{-2}$, and are likely associated with galaxies as is suggested by both observations (e.g Wolfe et al., 2005) and numerical simulations (e.g. Fumagalli et al., 2011; Cen, 2012; Bird et al., 2014).

Observational studies of DLAs have focussed mainly on line-of-sight column density measurements. Although such studies are able to measure quantities such as the metallicity (e.g. Rafelski et al., 2012) and the velocity structure of the absorber (e.g Neeleman et al., 2013), these studies are unable to provide detailed information on the physical conditions of this gas such as the temperature and neutral hydrogen density. Several innovative methods have been devised to measure exactly these parameters for high redshift absorbers. The first method is to measure 21 cm line absorption in DLAs in

front of radio-loud quasars. The integrated optical depth of the 21 cm absorption and the measured HI column density will yield the spin temperature of the associated gas (see Kanekar et al., 2014, for a detailed description of this method and results). A second method is to measure the fine structure lines of neutral carbon, whose ratio is dependent on the physical conditions of the gas (Srianand et al., 2005; Jorgenson et al., 2010).

On the theoretical side, Wolfe et al. (2003a) extended the work of Wolfire et al. (1995) to the physical conditions pertinent to DLAs. Under the same assumptions as before, the gas in DLAs forms a two phase-medium, albeit at somewhat different density and temperatures. Observational measurements of high redshift DLAs show that indeed some of the gas has properties similar to both the CNM (Howk et al., 2005; Srianand et al., 2005; Carswell et al., 2010; Jorgenson et al., 2010) and WNM (Lehner et al., 2008; Carswell et al., 2012; Kanekar et al., 2014; Cooke et al., 2014). However, disagreement lies with the percentage of DLAs that contain a significant fraction of CNM. Based on several observational results, Wolfe et al. (2003b, 2004) claim that the star formation rate per unit area is too large for current observational constraints if DLAs occur solely in a WNM (see also Fumagalli et al., 2015). On the other hand the 21 cm absorption studies suggest that at least 90 % of DLAs contain a large fraction of WNM (Kanekar & Chengalur, 2003; Kanekar et al., 2014).

To address this issue and shed additional light on the physical conditions of gas probed by DLAs, we apply in this chapter a third method. This method was first described by Howk et al. (2005) for DLAs. It relies on the fact that the ratios of the fine-structure levels of the ground states of C^+ and Si^+ are solely determined by the physical parameters of the DLA (see also Silva & Viegas, 2002). Therefore a measurement of these ratios allows for a determination of the physical parameters of the DLA. This method has several advantages. Unlike C I, both Si II and C II are the dominant ionization states of these elements, and therefore they very likely trace the bulk of the neutral gas.

Furthermore, unlike the 21 cm method, this method does not use a radio source, which could probe different gas, as the radio source need not be as compact as the ultraviolet or optical source (Wolfe et al., 2003b; Kanekar et al., 2014).

This chapter is organized as follows. In Section 3.3, the selection of the sample used in this chapter is explained. In Section 3.4 we describe the measurements from the observations and literature sample. Section 3.5 explains in detail the method used in this chapter to measure the physical parameters of the DLA. The results are tabulated and described in Section 3.6. Finally we discuss these results in Section 3.7 and summarize them in Section 3.8.

3.3 Sample Selection

To apply the method described in this chapter, we require accurate measurements of the column density of the two fine structure levels of the ground state of both C^+ and Si^+ . We will denote the upper level of the ground state by an asterisk (e.g. $Si\ II^*$), whereas the lower level will be represented by the standard notation (e.g. $Si\ II$). To limit saturation issues and to enable individual component analysis, we restrict ourselves to high resolution data. In particular, we limit ourselves to data from the high resolution spectrograph (HIRES; Vogt et al., 1994) on the Keck I telescope, which resulted in spectra with a typical resolution of $\sim 8\text{ km s}^{-1}$. We further require that at least one of the transitions of both levels of the C^+ and Si^+ are clear of any forest lines or interloping features. In practice this means selecting those spectra which have clear spectral regions around $C\ II^* \lambda 1335.7$, $Si\ II^* \lambda 1264.7$, and $Si\ II \lambda 1808.0$. In rare cases we use $Si\ II^* \lambda 1533.4$ and other $Si\ II$ lines to determine the column densities of the Si^+ fine structure lines. We do not directly measure the $C\ II$ lower state because the $C\ II \lambda 1334.5$ line is too saturated to get accurate column densities (see Section 3.4.3).

There are 79 spectra that satisfy the above requirements. These DLAs can in general be divided into two categories, those that were selected based on the strength of the metal lines in their Sloan Digital Sky Survey (SDSS; Abazajian et al., 2009) spectra (Herbert-Fort et al., 2006), and those selected purely by their HI column density. We assume, as in Neeleman et al. (2013), that the latter subset is a less biased sample and represents an accurate subsample of the general DLA population. The metal line selected sample, on the other hand, is likely biased towards higher metallicity systems and may trace the more massive host galaxy halos (Neeleman et al., 2013). In Table 3.1 we have marked the 48 DLA that are part of the ‘unbiased’ sample described in Neeleman et al. (2013).

Table 3.1: Fine Structure DLA sample

Index Number	QSO	z_{abs}	$\log N_{\text{HI}}$ (cm^{-2})	Metallicity [M/H]	M ^a	$\log N_{\text{CII}^*}$ (cm^{-2})	$\log N_{\text{SiII}^*}$ (cm^{-2})	$\log N_{\text{SiII}}$ (cm^{-2})	N13 ^b	References
1	Q1157+014	1.9437	21.70 ± 0.10	-1.23 ± 0.10	Si	$> 14.75^c$	12.37 ± 0.03	15.97 ± 0.01	Y	5, 18
2	Q1215+33	1.9991	20.95 ± 0.06	-1.43 ± 0.07	Si	< 13.18	< 12.56	15.02 ± 0.02	Y	4, 7
3	Q0458-02	2.0395	21.65 ± 0.09	-1.11 ± 0.09	Si	$> 14.88^c$	< 12.58	16.04 ± 0.02^c	Y	4, 7
4	J2340-0053	2.0545	20.35 ± 0.15	-0.55 ± 0.15	S	13.72 ± 0.01	< 11.31	15.23 ± 0.01	Y	12, 17, 19
5	Q2206-19	2.0762	20.43 ± 0.06	-2.25 ± 0.07	Si	< 13.20	< 11.83	13.68 ± 0.03	Y	2, 4, 7

^aIon used for metallicity determination

^bPart of the Neeleman et al. (2013) sample

^cVPFIT used to determine the column density

Note. — This table is shown in its entirety in the Appendix. A portion is shown here for guidance regarding its form and content

References. — (1) Lu et al. (1996);(2) Prochaska & Wolfe (1997);(3) Lu et al. (1998);(4) Prochaska & Wolfe (1999);(5) Petitjean et al. (2000);(6) Prochaska & Wolfe (2000);(7) Prochaska et al. (2001a);(8) Levshakov et al. (2002);(9) Prochaska & Wolfe (2002a);(10) Prochaska et al. (2003a);(11) Dessauges-Zavadsky et al. (2004);(12) Khare et al. (2004);(13) Ledoux et al. (2006);(14) O'Meara et al. (2006);(15) Herbert-Fort et al. (2006);(16) Dessauges-Zavadsky et al. (2007);(17) Prochaska et al. (2007);(18) Wolfe et al. (2008);(19) Jorgenson et al. (2010);(20) Kaplan et al. (2010);(21) Rafelski et al. (2012);(22) Kulkarni et al. (2012);(23) Berg et al. (2013);(24) This Work;(25) Berg et al. (2014)

3.4 Measurements

This section describes the measurements taken for each absorber. The measurements for all of the DLAs in the sample are tabulated in Table 3.1.

3.4.1 HI Column Density Measurements

The HI column density of the DLAs is measured by adopting the procedure outlined in Prochaska et al. (2003a). We determine the HI column density, N_{HI} , of an absorber in a quasar spectrum by simultaneously fitting the continuum of the background quasar and fitting a Voigt profile to the Ly- α line of the absorber. This method provides accurate column density measurements if the continuum can be accurately placed. The measurements and their uncertainties are displayed in Table 3.1.

3.4.2 Metallicity Measurements

For each of the DLAs found, we have measured the metallicity, defined by:

$$[\text{M}/\text{H}] = \log_{10}(N_{\text{M}}/N_{\text{H}}) - \log_{10}(N_{\text{M}}/N_{\text{H}})_{\odot} \quad (3.1)$$

The column density of the metals was found using the apparent optical depth method (AODM; Savage & Sembach, 1991), where we have used the wavelengths and oscillator strengths from Morton (2003) and the solar abundances from Asplund et al. (2009). We apply the same procedure as outlined in Rafelski et al. (2012), to determine which metal to use as a tracer of the metals in a DLA. In particular, we avoid using Fe as a metal tracer for the DLAs chosen by their metal lines, as Fe is more depleted at higher metallicity (Prochaska & Wolfe, 2002a; Ledoux et al., 2003; Vladilo, 2004; Rafelski et al., 2012). In Table 3.1 we list all of the metallicities of the DLAs and the line used

for the determination of the metallicity.

3.4.3 Column Density Measurements

For unsaturated lines and slightly saturated lines, the AODM provides an accurate way of determining the column density of the metals in an absorber. However, when a line is slightly blended or strongly saturated, the resultant limits for the column density found using the AODM are very conservative. Stronger constraints to the column density for such metal lines can be found by fitting the lines with χ^2 Voigt profile fitting routines such as VPFIT¹. Since in all cases Si II* is unsaturated; we only use VPFIT for our measurements of saturated C II* lines, and for Si II in 8 systems where all the available Si II lines could potentially be saturated.

To fit the saturated lines, we select an unsaturated low-ion line such as Si II or Zn II to determine the redshifts of the components of the low-ion lines. We then tie the Doppler parameters of the C II* and low-ion lines by assuming that they arise solely from thermal broadening. This assumption is unphysical as turbulent broadening is likely important for this gas. However, we are after a conservative lower limit to the column density *independent* of the physical model used. Since the low-ion used for selecting components is heavier than the fitted ion, a thermally linked gas will provide a conservative lower limit to the column density. We finally require that the relative number of components is equal across the species and allow only the total column density of the saturated line to change. The lower limits measured using this method are marked in Table 3.1.

The above methods are used to determine the column densities of Si II, Si II*, and C II*. However, we cannot directly measure the C II column density because in all cases the resonance lines of C II are too saturated. We instead use the column den-

¹<http://www.ast.cam.ac.uk/~rfc/vpfit.html>

sity of Si as a proxy for C. Here we assume that both Si and C are not depleted onto dust grains and that C likely traces Fe (Wolfe et al., 2003a). Under these assumptions, $[C/H]_{\text{gas}}=[Fe/H]_{\text{int}}=[Si/H]_{\text{gas}}+[Fe/Si]_{\text{int}}$, where we take $[Fe/Si]_{\text{int}}$, which is the intrinsic alpha enhancement of the DLA gas, to be -0.3 dex as measured by Rafelski et al. (2012). Since both Si II and C II are the dominant ionization state in the gas, $N(C)\approx N(C\text{ II})$ and $N(Si)\approx N(Si\text{ II})$. Hence the column density of C II is assumed to be: $\log N(C\text{ II})=\log N(Si\text{ II})+0.62$.

We have summarized all of these measurements in Table 3.1. We record a total of 7 detections of Si II* from a sample of 79 DLAs. None of these detections have been analyzed previously, although two of these detections have been mentioned in the literature (i.e. J1417+4132 (Berg et al., 2013), and Q1755+578 (Jorgenson et al., 2010)). The detection of 7 new Si II* measurements is noteworthy, because this state is only very rarely seen in DLAs along quasar sight lines (QSO-DLAs), yet is seen regularly in DLAs detected in gamma ray bursts (GRB-DLAs). Here the GRB is likely responsible for optically pumping the excited fine structure state (Prochaska et al., 2006). Together with the recent analysis of Si II* in QSO-DLA J1135–0010 by Kulkarni et al. (2012), this sample contains all of the known detections to date of Si II* in QSO-DLAs. For completeness, we have therefore included J1135–0010 in our sample. The 7 new Si II* measurements are shown in Figure 3.1. We have also plotted a representative low-ion line to show the similarity in velocity structure between the Si II* line and the low-ion lines, which is discussed further in Section 3.6.3.

3.5 Method

In this section we detail the method used in this chapter to determine the physical parameters of the gas using the Si II* and C II* fine-structure lines. We further describe

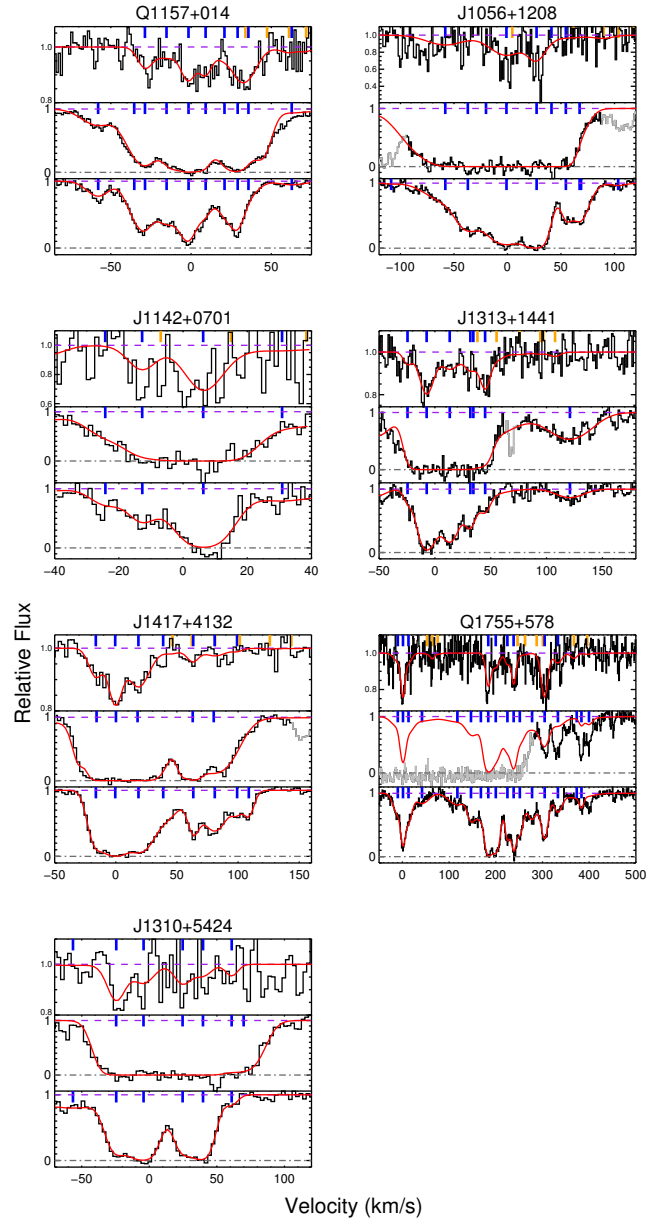


Figure 3.1: (top) Si II^* , (middle) C II^* and (bottom) Si II transitions for the 7 DLAs with detections of Si II^* in our sample. The blue vertical lines indicate the central position of the velocity components used for the line fit from VPFIT shown by the solid red line. In the top panel, the orange vertical lines indicate the position of the weaker Si II^* $\lambda 1265.0$ line. Note that in all 7 DLAs the C II^* transition is strongly saturated (or blended in the case of Q1755+578). We therefore take these fits as lower limits (see text). For the analysis discussed in this paper, we only consider the sum of the individual components, except for Section 3.6.3 in which we discuss the component-by-component analysis.

how this method is applied to all of the DLAs in our sample.

3.5.1 Si II* and C II* Technique

The technique of using Si II* and C II* to determine the gas temperature of DLAs was first used by Howk et al. (2005). Here we will describe the technique. The 2P fine-structure states of Si II and C II can be well approximated by a two-level atom for temperatures below 30,000 K as electrons are unable to excite the atom through collisions to higher energy levels (Silva & Viegas, 2002). As such we can write the steady state equation for both Si II and C II as:

$$\frac{n_2}{n_1} = \frac{B_{12}u_{\nu 12}(z) + \Gamma_{12} + \sum_k n_k \gamma_{12}^k}{A_{21} + B_{21} * u_{\text{CMB}}(z) + \Gamma_{21} + \sum_k n_k \gamma_{21}^k} \quad (3.2)$$

Here n_2 refers to the $^2P_{3/2}$ state of Si II and C II (i.e. $n(\text{Si II}^*)$ and $n(\text{C II}^*)$), and n_1 refers to the lower level $^2P_{1/2}$ state of these atoms (i.e. $n(\text{Si II})$ and $n(\text{C II})$). A_{12} , B_{12} and B_{21} are the Einstein coefficients for the given transitions, u_{CMB} is the energy density of the cosmic microwave background radiation field and Γ_{12} and Γ_{21} are the fluorescence rates. We assume the fluorescence rates are negligible because of the opacity of the ground-state transitions (see e.g. Sarazin et al., 1979; Wolfe et al., 2003b), and because of the lack of Fe^+ excited fine-structure lines in the DLAs (Prochaska et al., 2006).

Finally, the excitation and de-excitation terms due to collisions (i.e. the $n_k \gamma_{21}^k$ terms) are considered. These terms are proportional to the number density of the species and the collision rate with that species. In the case of DLAs, we consider collisions with electrons, protons, and atomic hydrogen. The fraction of molecular hydrogen is assumed to be small for DLAs (Jorgenson et al., 2010; Ledoux et al., 2003), such that we can ignore collisions with this species. All of the collision rates are taken from Silva & Viegas (2002), and references therein.

Considering all these processes, the ratios of the upper to lower fine-structure levels of the ground state of C^+ and Si^+ become a function of redshift (z), temperature (T), neutral hydrogen density (n_H), and electron density (n_e). Since the redshift of the DLA is well-determined from the metal lines; this leaves the three internal parameters that set the two ratios. Figure 3.2 shows the dependence of the carbon ratio ($r_C = \frac{n_{C\text{II}^*}}{n_{C\text{II}}}$) and silicon ratio ($r_{Si} = \frac{n_{Si\text{II}^*}}{n_{Si\text{II}}}$) on temperature for a variety of different hydrogen and electron densities. The ratios correlates strongly with temperature for temperatures below 500 K. Furthermore, at low hydrogen densities ($n_H \lesssim 10 \text{ cm}^{-3}$) collisions with electrons dominate. Hence the ratios show a strong correlation with electron density. On the other hand, at large hydrogen densities ($n_H \gtrsim 10 \text{ cm}^{-3}$) the collisions with neutral hydrogen dominate and the ratios show a strong correlation with the neutral hydrogen density.

Finally, we note that the observable that we measure is the ratio of the column densities, not the ratio of the actual densities. However, the two quantities are related by:

$$\frac{N_2}{N_1} \approx \frac{\int n_2 ds}{\int n_1 ds} = \frac{\int \frac{n_2}{n_1} n_1 ds}{\int n_1 ds} \quad (3.3)$$

The ratio of the two column densities is therefore simply the metal density weighted average of the density ratio over the path length. Since $dN_1 \approx n_1 ds$, the ratio of column densities is also approximately equal to the mean of the density ratio weighted by the metal column density of the individual components. Under the assumption that the amount of neutral gas in the individual components is correlated to the column density of the components (i.e. the metallicity of the individual components is similar), then the measured ratio of the column densities will be equal to the mean of the density ratio weighted by the amount of neutral gas in each component.

We assume for this chapter that the observed ratio of the column densities provides a good estimate of the density ratio for the bulk of the gas, as the column density ratio is weighted by the amount of neutral gas. One scenario where this assumption

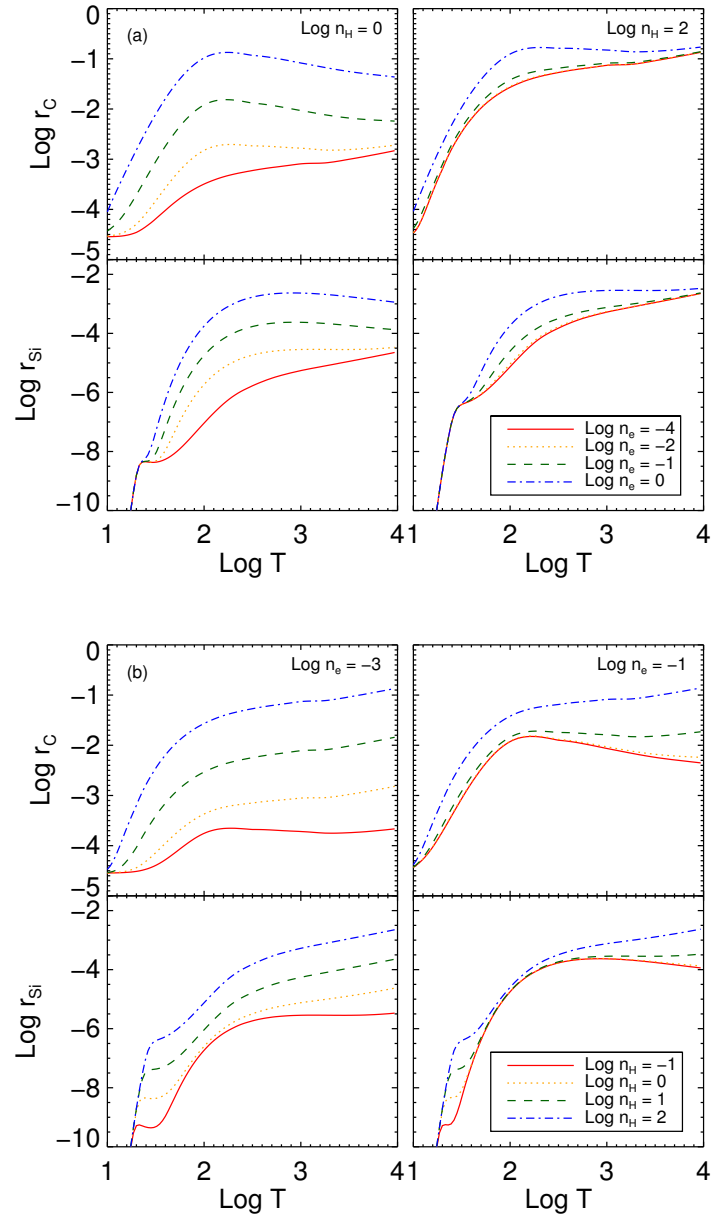


Figure 3.2: Si and C ratios for a range of different physical parameters. Panel (a) shows how both $r_C = \frac{n_{C\text{II}^*}}{n_{C\text{II}}}$ and $r_{Si} = \frac{n_{Si\text{II}^*}}{n_{Si\text{II}}}$ vary with temperatures under a variety of different electron densities as the neutral hydrogen density is held constant. In panel (b) the electron density is held constant while the neutral hydrogen density is varied. These plots show that at low neutral hydrogen density, the fine-structure level ratios of C^+ and Si^+ are strongly dependent on the electron density, whereas at higher neutral hydrogen densities the ratios only dependent on the neutral hydrogen density.

might lead to inaccurate predictions of the physical conditions of the gas is the case where the column density of the upper level arises from one phase whereas the bulk of the gas is in another phase. This is indeed expected to happen in the two-phase model where the CNM will produce the majority of C II^* , even though C II could come from either phase. However, requiring that the two phases are in pressure equilibrium implies the carbon density ratio, r_C , between the CNM and WNM differ at most by a factor of 25. Therefore even in a 60 % WNM and 40 % CNM mixture, the density obtained using this technique will overestimate the density for the bulk of the gas (i.e. the WNM component) by less than an order of magnitude. We explore this assumption further and compare the results from individual velocity components to each other and the system as a whole in Section 3.6.3.

3.5.2 Applying the Technique

To explore the parameter space of all possible electron densities, neutral hydrogen densities and temperature, we apply a Monte Carlo Markov Chain (MCMC) method using the Hastings-Metropolis algorithm. This allows us to sample the complete parameter space and find the probability distribution function (PDF) for each of the physical parameters. The likelihood function used in the algorithm is discussed in Section 2.4.2.1. At each step in the MCMC, this likelihood is then evaluated and multiplied by the priors. The Hastings-Metropolis algorithm is finally used to accept the step or discard it. To test for convergence, we run the MCMC five different times with varying starting points. We run the chains for 10^6 steps, and discard the first 30 % of the chain as our burn-in period. After the run, the PDF of each of the parameters is compared for the five different chains to check for convergence. Figure 3.3 shows an example of the results for one such run.

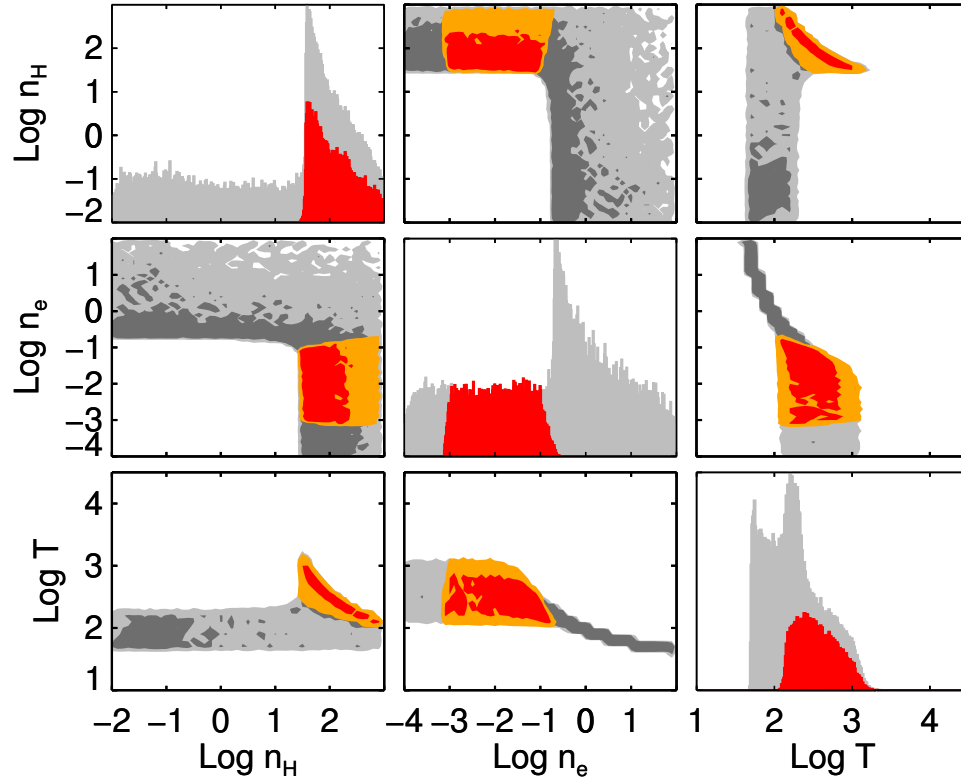


Figure 3.3: Example of a Monte Carlo Markov Chain run for DLA J1313+1441. The upper left panel, middle panel and bottom right panel display the PDF for the individual parameters. The other panels show the parameter space that is covered by the MCMC. The light gray (dark gray) shaded regions are the $3\text{-}\sigma$ ($1\text{-}\sigma$) boundaries for the complete chain. The orange and red regions are the $3\text{-}\sigma$ ($1\text{-}\sigma$) boundaries for just the solutions that satisfy the electron density constraint described in Section 3.5.3.

3.5.2.1 Likelihood Function and Priors of the MCMC

The likelihood function used in the MCMC method is the product of the likelihood functions of the two individual ratios:

$$\mathcal{L} = \prod_k^{Si,C} \mathcal{L}_k \quad (3.4)$$

Here \mathcal{L}_k can take on different forms depending on if the column densities measured in the ratios are detections, upper limits, lower limits or some combination of the two. In our sample we have 5 different cases which are schematically shown in Figure 3.4. Note that for all cases r_k are linear quantities, not logarithmic.

When both the numerator and denominator in the ratio are detections (Fig. 3.4a), we can approximate the PDFs of the individual measurements by Gaussians. The resultant PDF of the ratio will then also be approximately Gaussian, i.e.

$$\mathcal{L}_k = e^{-\chi_k^2/2}, \text{ where } \chi_k^2 = \left(\frac{\Gamma_{k,\text{obs}} - \Gamma_{k,\text{mod}}}{\sigma_{r_k}} \right)^2 \quad (3.5)$$

Here r_k are the quotient of the upper to lower level fine structure states of C^+ and Si^+ ; the subscripts refer to either the observed or measured values and those from the model. σ_{r_k} is the uncertainty on the observed ratios calculated by standard error propagation. The prior PDF in this case is uniform.

For upper limits on the column density measurement, we assume a Gaussian PDF centered around zero where the uncertainty is given by the 1- σ upper limit measurement. The likelihood of a ratio consisting of an upper limit and a detection (Fig. 3.4c) will then also be given by Equation 3.5. Of course negative ratios are unphysical, and therefore we assume a prior which is zero for ratios smaller than zero and uniform for ratios greater than zero.

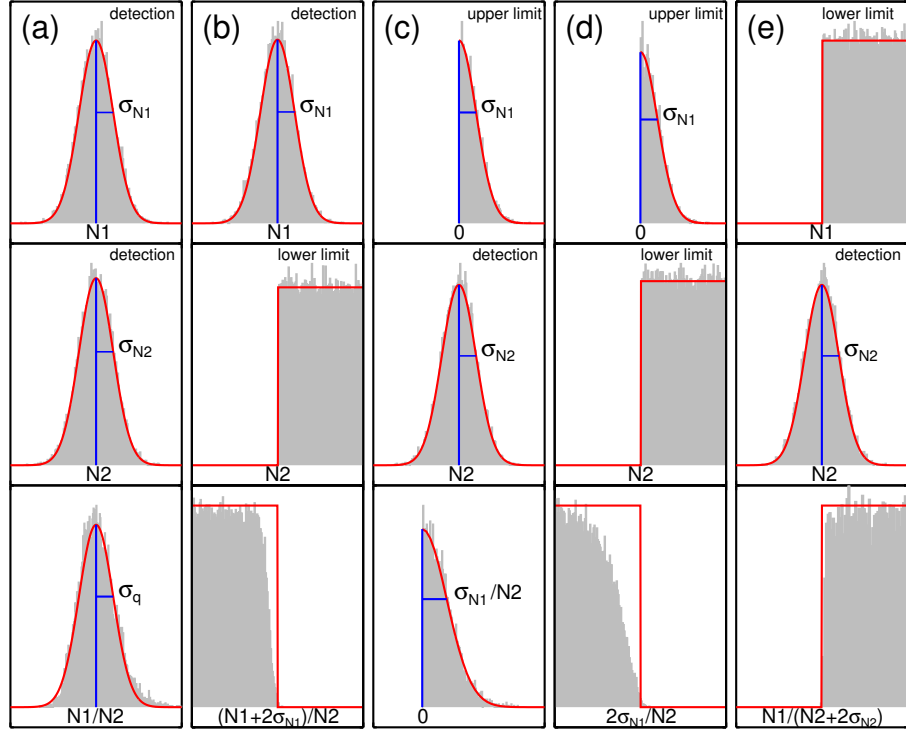


Figure 3.4: The likelihood functions for the different possible ratios. The solid red line is the likelihood function used to describe the ratio. In gray a sample PDF with the given parameters is shown, scaled to the likelihood function. The top panel in each of the subfigures depicts the numerator, the middle panel the denominator and the bottom panel the ratio of the two. In (a) the likelihood can be approximated by a Gaussian with mean $= \frac{N1}{N2}$ and $\sigma_q = \sqrt{\left(\frac{\sigma_{N1}}{N2}\right)^2 + \left(\frac{N1\sigma_{N2}}{N2^2}\right)^2}$. In (c) the likelihood function of the ratio is also Gaussian. For the remaining cases (b), (c), and (e) the likelihood functions are approximated by step functions. These step functions contain $> 99.9\%$ of the PDF. Here we have assumed a PDF for the lower limits that is flat in $\log(N)$.

Lower limit measurements of the column density are more difficult to deal with, as it is hard to estimate an appropriate uncertainty on the measurement, because the uncertainty is strongly dependent on the model used to fit the absorption line. If the lower limit measurement is in the denominator of the silicon or carbon ratio (Fig. 3.4b and d), the resultant measured ratio is an upper limit. In this case, ratios derived from the model should have a high likelihood when they are smaller than the measured ratio and small when they are bigger than the measured ratio. We therefore adopt the following conservative likelihood function:

$$\mathcal{L}_k = \begin{cases} 1 & r_{k,\text{mod}} \leq r_{k,\text{obs}} \\ 0 & r_{k,\text{mod}} > r_{k,\text{obs}} \end{cases} \quad (3.6)$$

This step function rules out models that produce ratios greater than $r_{k,\text{obs}}$, and will give equal likelihood for all ratios below $r_{k,\text{obs}}$. Here $r_{k,\text{obs}}$ is the $2\text{-}\sigma$ upper limit of the detection or upper limit divided by the lower limit. As Figure 3.4b and 3.4c show, this is a conservative approach, as $>99.9\%$ of a mock generated PDF falls below this limit. Again the prior is assumed to be uniform for ratios greater than zero, and zero for ratios smaller than zero.

Similarly, for the few cases where the lower limit is in the numerator (Fig. 3.4e) we use the following likelihood function:

$$\mathcal{L}_k = \begin{cases} 0 & r_{k,\text{mod}} < r_{k,\text{obs}} \\ 1 & r_{k,\text{mod}} \geq r_{k,\text{obs}} \end{cases} \quad (3.7)$$

This step function rules out all models that produce ratios smaller than $r_{k,\text{obs}}$. Here $r_{k,\text{obs}}$ is the lower limit divided by the $2\text{-}\sigma$ upper limit of the detection. Note that in these cases we assume a uniform prior.

3.5.3 Electron Density Constraint

When we apply the MCMC chain, we allow the temperature, hydrogen density and electron density to vary independently. This can clearly result in unphysical situations for DLAs where we expect the fractional ionization to be significantly smaller than 1. To apply this constraint, we assume that the fractional ionization of hydrogen, $x(\text{H}^+)$, satisfies the following steady state equation (Draine, 2011):

$$\begin{aligned} \zeta_{\text{CR+X}}(1 + \phi_s)[1 - x(\text{H}^+)] = \\ \alpha_{\text{rr}}(\text{H}^+)n_{\text{H}}^2[x(\text{H}^+) + x(\text{M}^+)]x(\text{H}^+) + \\ \alpha_{\text{gr}}(\text{H}^+)n_{\text{H}}^2x(\text{H}^+) \end{aligned} \quad (3.8)$$

Here, $\zeta_{\text{CR+X}}$ is the primary ionization rate of both cosmic rays and strong X-rays, ϕ_s are the secondary ionization rates, α_{rr} is the rate coefficient for radiative recombination of H^+ which is a function of temperature, and α_{gr} is the effective rate coefficient for grain-assisted recombination of H^+ , which is a function of temperature, electron density and the UV radiation field. The ionization of metals is assumed to be the same as it is for local ISM scaled to the metallicity of the DLA. Using the estimates for these parameters in Draine (2011); and references therein, we can make an estimate for the electron density as a function of the neutral hydrogen density, temperature, primary ionization rate and the UV radiation field.

This constraint is imposed upon the Monte Carlo Markov Chain after the run. All the values that do not satisfy the above equation are rejected. Since the value of $\zeta_{\text{CR+X}}$ at these redshifts is uncertain (see e.g. Dutta et al., 2014), and the UV radiation field can likely take on a wide range of values depending on the separation between the DLA and any potential star forming region, we allow for a wide range of acceptable values. Specifically, the UV radiation field may range between 0.1 and 100 G_0 (Habing's

constant; $G_0 = 1.6 \times 10^{-3} \text{ergs cm}^{-3} \text{s}^{-1}$) and $\zeta_{\text{CR+X}}$ between 10^{-17} and 10^{-15}s^{-1} .

As a result of this constraint, the electron densities never exceed densities of about 0.1cm^{-3} , because such electron densities would require the gas to be significantly ionized. Similarly, electron densities below $\sim 10^{-4} \text{cm}^{-3}$ are ruled out because of the intrinsic electron density due to the singly-ionized metals such as carbon. One example of the application of this constraint to the MCMC chain are shown by the orange and red contours in Figure 3.3.

3.6 Results

This section describes the results from the Si II* and C II* technique. The output of the technique is a PDF on each of the three physical parameters (e.g. n_{H} , n_{e} and T). We have plotted the $1-\sigma$ ranges for each of these parameters in Figure 3.5; we also have included the pressure constraints of these systems in this figure (see Section 3.6.1). The results are tabulated in Table 3.2. Not all DLAs have well-determined ranges on all internal parameters, either due to low S/N spectra or because the resultant ratios are not strongly correlated with a specific internal parameter (see Section 3.5.1). Those DLAs that have well-determined ranges in both neutral hydrogen density and temperature are plotted in blue in Figure 3.5 and are shown in the abbreviated version of Table 3.2.

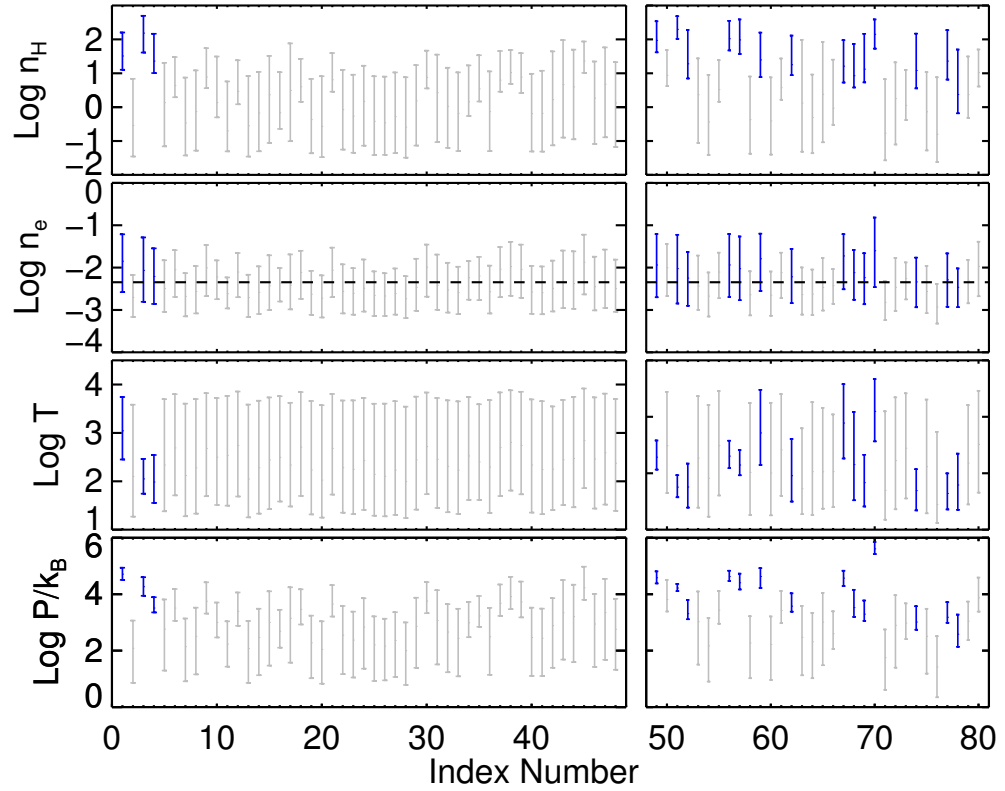


Figure 3.5: $1\text{-}\sigma$ constraints on the neutral hydrogen density, electron density, temperature, and pressure for all of the DLAs in the sample from the Si II^* and C II^* technique. The left panels are the results for the DLAs which are part of the unbiased sample of Neeleman et al. (2013), whereas the right panel shows the result for the metal selected sample. The index number for the DLAs are given in Tables 3.1 and 3.2. The DLAs marked in blue are those DLAs for which this method provides a well determined constraint on both n_{H} and T .

Table 3.2: Results of Si II* and C II* Technique

Index Number	QSO	z_{abs}	$\log n_{\text{H}}(2-\sigma)$ [cm^{-3}]	$\log n_{\text{e}}(2-\sigma)$ [cm^{-3}]	$\log T(2-\sigma)$ [K]	$\log Pk_{\text{B}}(2-\sigma)$ [K cm^{-3}]
1	Q1157+014	1.9437	1.1-2.2(0.9-2.8)	-2.6--1.2(-2.9--1.0)	2.5-3.7(2.2-4.1)	3.8-5.5(3.5-6.3)
3	Q0458-02	2.0395	1.6-2.7(1.3-2.9)	-2.8--1.3(-3.1--0.9)	1.7-2.5(1.5-3.2)	3.6-4.9(3.2-5.6)
4	J2340-0053	2.0545	1.0-2.2(0.8-2.8)	-2.9--1.5(-3.2--1.1)	1.6-2.5(1.4-3.2)	2.8-4.3(2.5-5.2)
49	J1056+1208	1.6093	1.6-2.5(1.5-2.9)	-2.7--1.2(-3.0--0.9)	2.2-2.8(2.1-3.2)	4.0-5.1(3.9-5.6)
51	J0927+1543	1.7311	2.0-2.7(1.8-2.9)	-2.8--1.2(-3.1--0.9)	1.7-2.1(1.6-2.3)	3.8-4.6(3.6-5.0)
52	J0008-0958	1.7675	0.8-2.3(0.6-2.8)	-2.9--1.6(-3.2--1.1)	1.5-2.4(1.3-2.9)	2.6-4.3(2.3-5.0)
56	J1313+1441	1.7947	1.7-2.5(1.6-2.9)	-2.7--1.2(-3.0--0.9)	2.3-2.8(2.2-3.1)	4.1-5.2(4.0-5.6)
57	J1310+5424	1.8005	1.6-2.6(1.4-2.9)	-2.8--1.3(-3.1--0.9)	2.1-2.6(2.0-3.0)	3.9-5.0(3.6-5.4)
59	J1142+0701	1.8407	0.9-2.2(0.6-2.8)	-2.6--1.2(-3.0--0.9)	2.3-3.9(2.0-4.4)	3.6-5.6(3.1-6.4)
62	J1024+0600	1.8950	0.9-2.1(0.7-2.8)	-2.8--1.6(-3.2--1.1)	1.6-2.9(1.4-3.8)	2.8-4.5(2.4-5.6)
67	Q1755+578	1.9692	0.7-2.0(0.5-2.7)	-2.5--1.2(-2.9--1.0)	2.5-4.0(2.2-4.4)	3.5-5.5(3.2-6.3)
68	J1305+0924	2.0184	0.6-1.9(0.3-2.8)	-2.8--1.6(-3.1--1.2)	1.6-3.4(1.4-4.2)	2.5-4.7(2.1-5.9)
69	J1509+1113	2.0283	0.7-2.2(0.4-2.8)	-2.9--1.7(-3.2--1.2)	1.5-2.5(1.3-3.3)	2.5-4.3(2.2-5.3)
70	J1135-0010	2.2068	1.7-2.6(1.5-2.9)	-2.5--0.8(-2.8--0.6)	2.8-4.1(2.6-4.4)	4.8-6.4(4.5-6.8)
74	J0812+3208	2.6263	0.6-2.2(0.2-2.8)	-2.9--1.8(-3.2--1.2)	1.4-2.3(1.3-2.7)	2.2-4.1(1.8-4.9)
77	J2100-0641	3.0924	0.8-2.3(0.5-2.8)	-2.9--1.7(-3.2--1.1)	1.4-2.2(1.3-2.5)	2.5-4.1(2.1-4.8)
78	J1155+0530	3.3260	-0.2-1.7(-0.7-2.7)	-2.9--2.0(-3.2--1.3)	1.4-2.6(1.2-3.8)	1.5-3.8(1.0-5.2)

Note. — (This table is available in its entirety at the end of this manuscript.)

3.6.1 Physical Parameters of DLAs

The top panel of Figure 3.5 shows the distribution of neutral hydrogen density in our sample. The range of allowed neutral hydrogen column densities varies significantly between DLAs. Several DLAs such as J0927+1543 are very dense, with $1-\sigma$ lower limits on the density of 100 cm^{-3} . These high values are driven by high r_C , and the non-detection of Si II*. On the other hand, several other DLAs have $1-\sigma$ upper limits of 10 cm^{-3} indicating that the gas in DLAs exhibits a wide range of neutral hydrogen density. It is important to note that the Si II* and C II* method cannot precisely measure neutral hydrogen densities below 1 cm^{-3} , because for these densities the interactions with neutral hydrogen becomes subdominant to collisions with electrons. As such, only DLAs with neutral hydrogen densities above this value have well-determined constraints on their neutral hydrogen density.

The second panel of Figure 3.5 shows the distribution of electron densities. One interesting feature of this distribution is that the variation in the range of electron densities is significantly less compared to the range of neutral hydrogen densities. This is a direct consequence of applying Equation 3.8, which makes the electron density only weakly dependent on the temperature and density of the gas. Specifically, Equation 3.8 gives an electron density of $n_e = 0.01 \text{ cm}^{-3}$ for both a canonical CNM ($n_H = 30 \text{ cm}^{-3}$ and $T = 50 \text{ K}$) and WNM ($n_H = 0.5 \text{ cm}^{-3}$ and $T = 5000 \text{ K}$) for local ISM conditions. Note that this is slightly higher than the median value of the complete DLA sample ($n_e = 0.0044 \pm 0.0028 \text{ cm}^{-3}$). The difference is likely due to the lower metallicity of the DLA sample and different UV radiation fields and ionization rates from cosmic rays and X-rays (Wolfire et al., 1995). As a result, we are unable to differentiate between the electron densities of DLAs, but a typical DLA will have an electron density of about $4 \times 10^{-3} \text{ cm}^{-3}$, which is consistent with the values found by Srianand et al. (2005).

The third panel of Figure 3.5 shows the temperature range for each of the DLAs

in our sample. Several DLAs have temperature ranges that are consistent with the temperatures expected from a CNM. To be specific, nine of the DLAs have $1-\sigma$ upper limits on the temperature of 500 K. On the other hand, there are several DLAs that have ranges that are at significantly higher temperature. We again would like to stress that the Si II* and C II* method is unable to measure the precise temperature above 500 K as r_C and r_{Si} become weak functions of temperature. Therefore only the coldest DLAs have well determined ranges on their temperature.

Finally, in the bottom panel of Figure 3.5 we have plotted the pressure range for each of the DLAs. The pressure was calculated from the MCMC chains by taking the product of the neutral hydrogen density and the temperature, since $P/k_B = n_H T$. As pressure shows the strongest correlation with r_{Si} and r_C , it is the best constrained parameter. The median pressure for the complete sample is $\log P/k_B = 3.0$ [K cm⁻³]. This is lower compared to the pressure of the ISM measured locally using the C I method (Jenkins & Tripp, 2011). We discuss this further in Section 3.7.2.

In Figure 3.6 we have plotted the temperature versus the density for the complete sample of DLAs. We have also indicated the typical ranges for a canonical CNM, WNM and the classically forbidden region defined by the two-phase model (see e.g. Heiles & Haverkorn, 2012). Nine DLAs with well-determined ranges on the temperature and neutral hydrogen density have physical conditions that are consistent with those expected from gas in a CNM. Two of these DLAs are from the 48 DLAs which are part of the unbiased sample of Neeleman et al. (2013). We therefore conclude that at least 5% of a random sample of DLAs contain significant fractions of CNM. This percentage is a lower limit because many DLAs with less well-determined ranges are consistent with gas in a CNM as is shown by the gray and dark gray contours.

The remaining DLAs are spread over a wide range of temperature and neutral hydrogen densities, all of them consistent with both canonical CNM and WNM con-

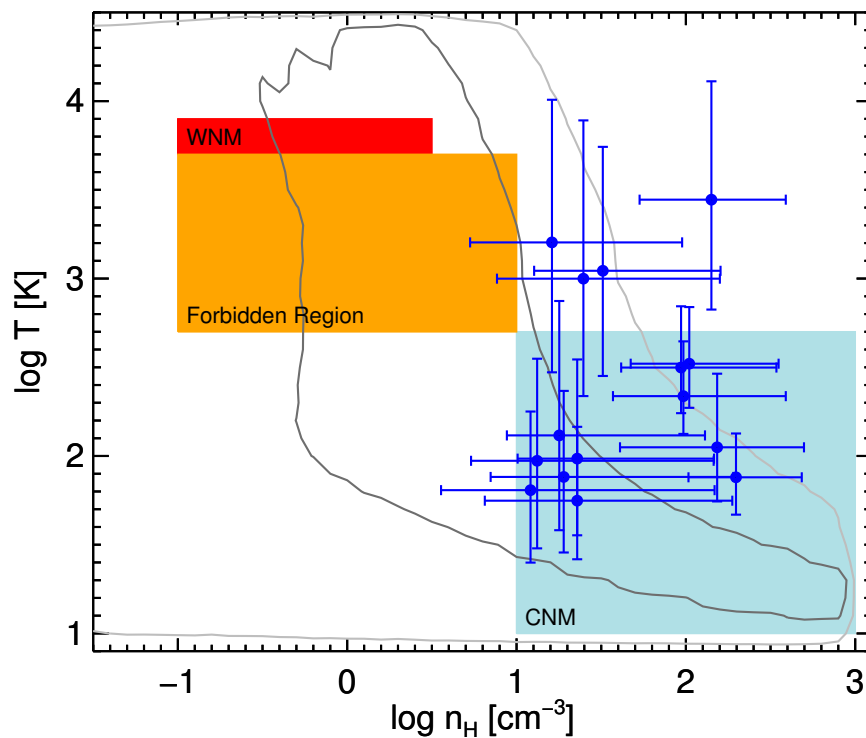


Figure 3.6: Temperature and neutral hydrogen density for the complete sample. The data points are those DLAs with well-defined ranges on n_{H} and T (see Figure 3.5). The dark gray (light gray) lines indicate the 68% (99%) confidence interval of the neutral hydrogen density and temperature for the remaining DLAs. We have also plotted the typical ranges for a canonical cold neutral medium, warm neutral medium, and the classically forbidden region.

ditions. In Figure 3.6 the 68 % and 99 % confidence contours for the temperature and neutral hydrogen density of the remaining DLAs are shown. These contours rule out the parameter space of high neutral hydrogen density and high temperature, as such physical conditions would produce too large r_{Si} and r_{C} (see Figure 3.2).

3.6.2 Correlations with Global DLA Properties

In this section we explore possible correlations between the physical parameters measured with the Si II* and C II* method and the global properties of the DLAs. We consider all of the global DLA parameters discussed in Neeleman et al. (2013). Figure 3.7 shows a selection of these correlations. As panel (a) of this figure shows, there is a clear correlation between the neutral hydrogen density and the 158 μm cooling rate of the DLAs (ℓ_{c} ; see e.g. Wolfe et al., 2003a). This result is due in part because the cooling rate is proportional to the C II* column density and larger C II* column densities result in larger r_{C} , which in turn yield higher neutral hydrogen column densities (see Figure 3.2). We consider this result evidence for the two-phase model described by Wolfe et al. (2003a), where higher star formation rates, and therefore higher cooling rates, result in higher stable equilibrium densities for hydrogen. Since ℓ_{c} is correlated to metallicity, redshift and the kinematical parameters (Wolfe et al., 2008; Neeleman et al., 2013), the neutral hydrogen density also shows a correlation (albeit weaker) with these parameters.

Panel (b) is a plot of neutral hydrogen density vs HI column density. The ratio of these components gives a crude estimate of the absorption length of the DLA. To be specific, the Si II* and C II* technique provides an estimate of the density of the bulk of the neutral gas (Section 3.5.1). Therefore the ratio of the neutral hydrogen density and HI column density will give an upper limit to the size of the component which contains the bulk of the neutral gas. The results show that for the majority of DLAs the absorption lengths for these components is less than 1 kpc. Indeed some absorption lengths are as

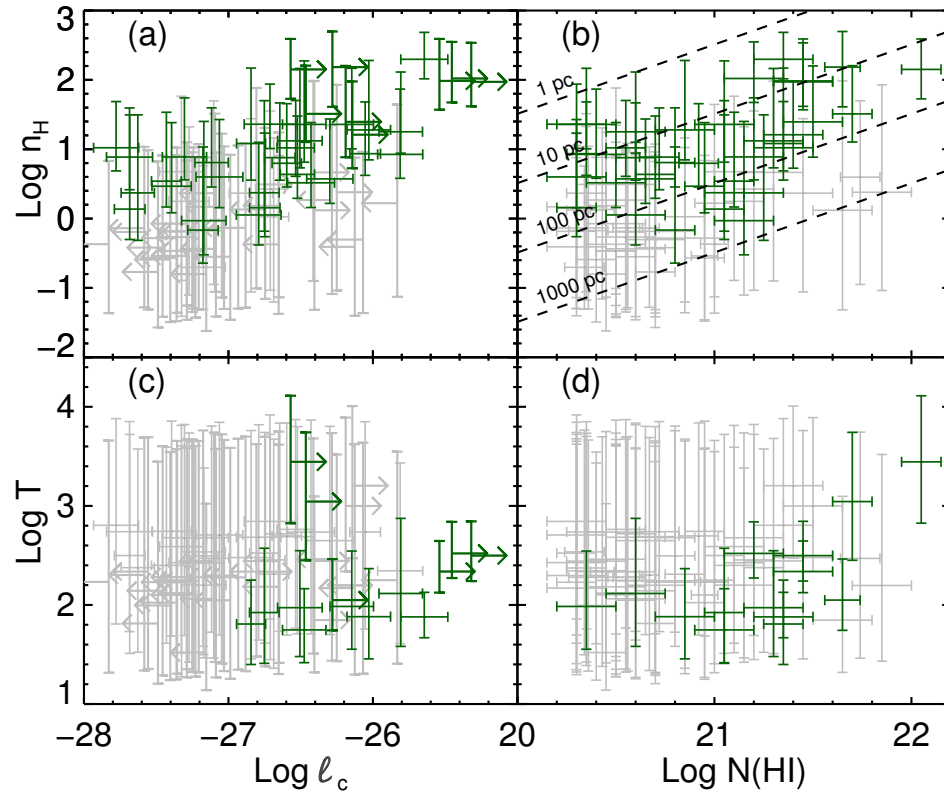


Figure 3.7: Selection of possible correlations seen in the data. The green data points are those points with strong constraints on their physical parameter from the MCMC analysis. Panel (a) shows the correlation between cooling rate and the hydrogen density. This correlation is expected as larger cooling rates indicate larger C II^* ratios which result in higher neutral hydrogen densities. Panel (b) plots hydrogen density vs neutral hydrogen column density. This plot indicates a maximum cloud size of DLAs of less than 1 kpc. The last two panels show that temperature is not strongly correlated with any of the external parameters.

small as a few tens of parsec. These very small absorption lengths correspond in general to those DLAs with well determined cold temperatures ($T \leq 500$ K). This suggests that for these DLAs the bulk of the gas is located in relatively small cold components.

Unlike the hydrogen density, the electron density shows no significant correlation with any of the global DLA parameters. Similarly, the temperature shows no significant correlation either. However, we would like to discuss two interesting features of the temperature measurements. The first feature is that the DLAs with the highest cooling rate have on average a lower temperature range (Figure 3.7c). This likely is related to the correlation between cooling rate and neutral hydrogen density, as higher neutral hydrogen densities likely correspond to colder environments (Figure 3.6). The second feature is that the two highest column density systems have the highest limits on the temperature (Figure 3.7d). A possible explanation for this result is that low temperature gas will form molecular gas, limiting the maximum allowed column density of neutral atomic hydrogen (Schaye, 2001). The molecular fraction is believed to be anti-correlated with temperature (Schaye, 2001; Richings et al., 2014b) and therefore larger atomic neutral hydrogen column densities are possible for higher temperature DLAs.

3.6.3 Component Analysis

In all of the analysis we have assumed that the ratio of column densities is approximately equal to the ratio of the densities of the bulk of the neutral gas. To explore this assumption, we have repeated the analysis on each of the individual velocity components of those DLAs with measurable Si II* (Figure 3.1). The results are displayed in Figure 3.8. As can be seen from the individual panels, the majority of the velocity components have physical parameters that are within $1-\sigma$ equal to the measurements from treating the system as a whole. This result is due to the similarity in the column density ratio between the upper and lower levels of the fine structure states of Si II. Note

that in Figure 3.1 the Si II* line traces the low-ion line quite well for the majority of DLAs. There are several exceptions such as the component at $+50 \text{ km s}^{-1}$ for DLA J1313+1441. This component has an r_{Si} five times greater than the mean value of the DLA, resulting in a temperature range inconsistent with that found for the total DLA. However, such components are uncommon; the mean deviation in r_{Si} and r_{C} from component to component is less than 50 % of the mean value, which results in similar ranges for the physical parameters.

The similarity between r_{Si} and r_{C} for the different velocity components strengthens the assumption to take the ratio of the total column densities to be equal to the ratio of the densities, since a per component analysis will produce similar results. One possible explanation for the similarity between the individual velocity components is that the distinct components are physically close to each other and experience similar exterior physical conditions, or a second explanation could be that external conditions are similar over a large portion of the absorbing galaxy.

There are three caveats to this results. The first caveat is that this result does not exclude the existence of *any* clumps of gas with strongly varying physical parameters along the quasar line of sight. It does, however, suggest that these clumps can only contribute a very small fraction of the total metal column density, and therefore are not likely to describe the bulk of the neutral gas. The second caveat is that the DLAs used in the individual component analysis all have measurable levels of Si II* and therefore might not be representative of the DLAs in general. We have tested this caveat by considering the ratio of C II* to Si II in a sample of DLAs for which both transitions are detected, and we find that this ratio is also not strongly varying between the individual components (see also Wolfe et al., 2003a,b). Therefore we believe that this is a general result holding for the majority of DLAs. Finally, the third caveat is that it could be that the individual velocity components are in actuality composed of a collection of smaller

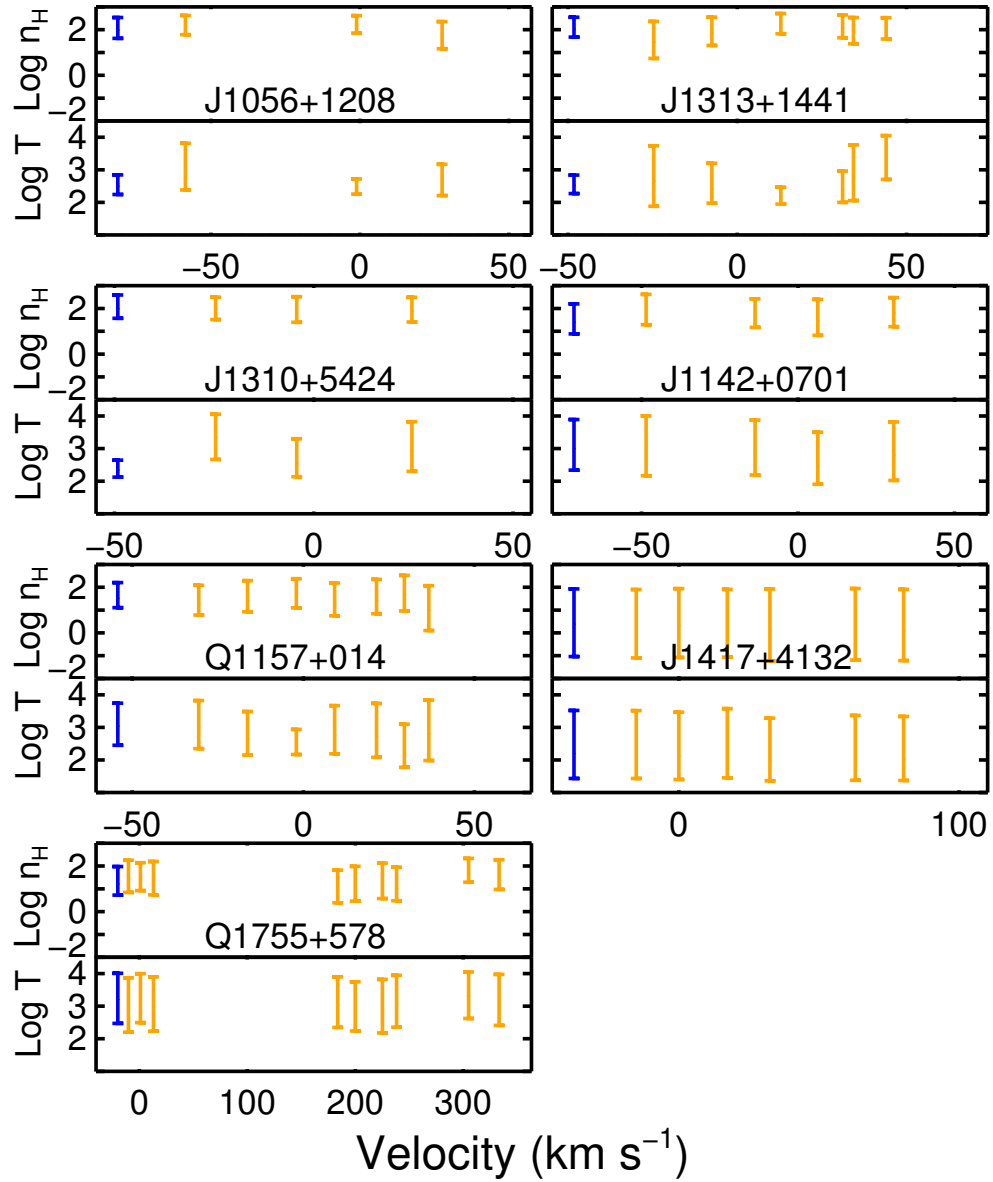


Figure 3.8: Temperature and neutral hydrogen density for the individual components for those DLAs with detectable levels of Si II*. The orange values are the measurements for the hydrogen density and temperature for the individual components, and are placed at the velocity center of the component. The blue data point is the result from the MCMC analysis by considering the system as a whole.

components. In this case, each individual component is averaged in a similar manner as the whole DLA, and therefore weighted most strongly by the component with the largest metal column density. As a result the Si II* and C II* technique will still recover the physical conditions of the bulk of the gas.

3.7 Discussion

The discussion section is organized as follows. In Section 3.7.1 we discuss the empirical results. We compare these results to previously measured data for both DLAs and the local ISM in Section 3.7.2. In Section 3.7.3 we discuss how the results of this chapter fit into models describing the ISM, in particular the two-phase model. Finally, in Section 3.7.4 we will comment on what these results suggest for the ISM of high redshift galaxies.

3.7.1 Discussion of the Empirical Results

We found in Section 3.6 that the temperature distribution of the full sample cannot precisely be determined because the Si⁺ and C⁺ ratios are insensitive to temperature changes when T exceeds 500 K. However, we can measure the minimum fraction of DLAs that have gas temperatures consistent with a CNM (i.e. $T < 500$ K). Using the ‘unbiased’ subsample of Neeleman et al. (2013), we find that at least 5 % of DLAs have the bulk of their neutral gas in cold, dense clouds with conditions similar to a CNM (Figure 3.6). We again note that this is a strict lower limit, as DLAs with less well-determined ranges on their physical parameters would increase this percentage.

As quasar lines of sight randomly probe the gas surrounding the DLA galaxy, we can convert this percentage to an approximate volume filling fraction of CNM in high redshift DLA galaxies. Depending on the exact geometry and distribution of the CNM,

the minimum volume filling fraction must be at least 1 %. This is very similar to the CNM filling fraction for the local ISM which is found to be approximately 1 % (Draine, 2011), and indicates that the volume filling fraction of CNM for high redshift galaxies is at least in rough agreement with the value measured for low redshift galaxies.

In Section 3.6.1, we showed that pressures vary significantly between DLAs and is correlated to r_C . This correlation is shown in Figure 3.9. The tracks are theoretical temperature paths for the indicated neutral hydrogen density assuming the measured median electron density of 0.0044 cm^{-3} . The black data points are detections or lower limits to r_C . This figure illustrates two things. Firstly, the majority of detections and lower limits in r_C cannot be produced in neutral gas with $n_H \lesssim 1 \text{ cm}^{-3}$, which means that a canonical WNM is rarely able to produce detectable levels of C II^* , and because r_C values can be measured in approximately 40 % of DLAs (see Neeleman et al., 2013) this indicates that these DLAs must contain some fraction of gas not in a canonical WNM. Secondly, the DLAs with the highest C^+ ratios have pressures and neutral hydrogen densities significantly higher than the median, and are in general those DLAs with well-defined limits on temperature and density.

Indeed, if we consider just the systems with well-defined ranges on temperature and density, we find that these systems show significantly higher velocity widths with a median velocity width of 131 km s^{-1} which is almost double the median value of a random DLA sample (Neeleman et al., 2013). They also show an increased metallicity and cooling rate, all suggesting that these systems are part of the most massive dark matter halos which give rise to DLAs (see further Section 3.7.4).

Finally a detailed look at the individual velocity components of DLAs shows that there exists little differences between the measured ratios between the individual velocity components. As was suggested in Section 3.6.3 this could be due to close proximity of the individual components. In particular, the observed $r_C = \text{C II}^*/\text{C II}$ is

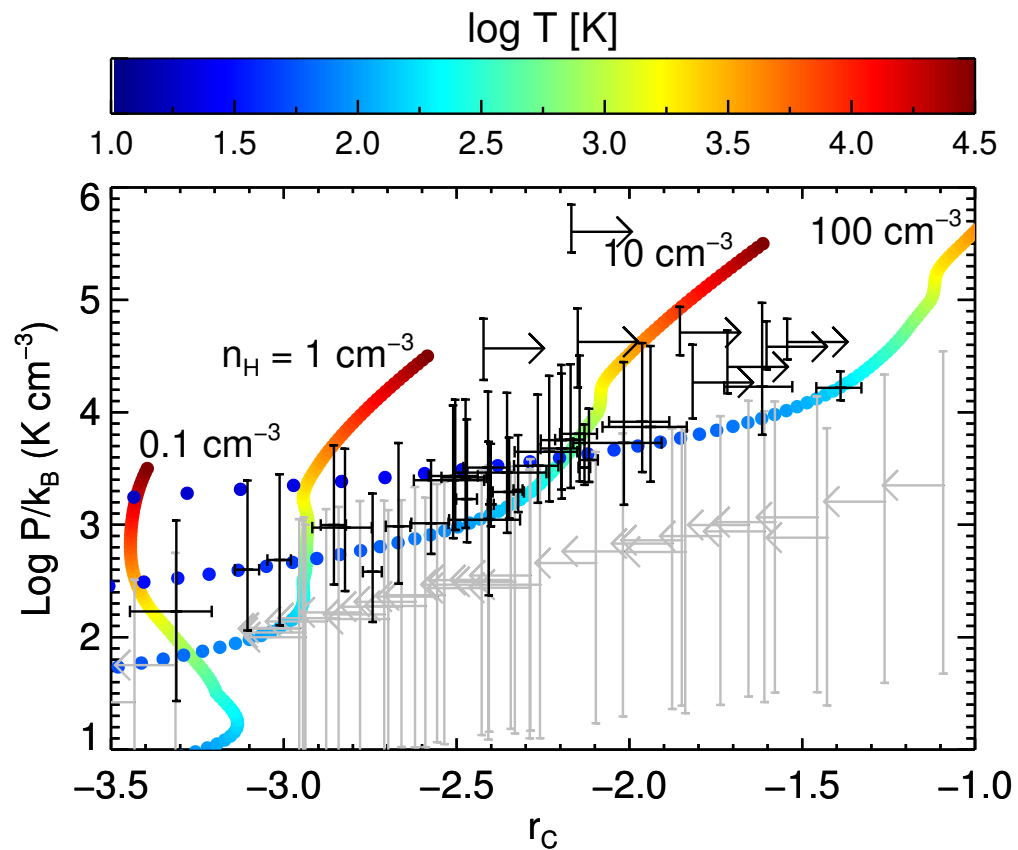


Figure 3.9: Correlation between pressure and r_C . The black data points are lower limits and measurements of r_C , whereas the gray data points are $2\text{-}\sigma$ lower limits. The colored tracks are the theoretical solutions to r_C and pressure for the given neutral hydrogen density and temperature assuming an electron density of $n_e = 0.0044 \text{ cm}^{-3}$. Most r_C detections, which account for about 40% of a random DLA sample, are inconsistent with the conditions found in a canonical WNM.

proportional to:

$$r_C \propto \frac{\ell_c}{[M/H]} \quad (3.9)$$

Hence, if we assume that the metallicity of the individual components does not vary significantly, then the constancy in r_C indicates that the cooling rates are the same across the individual components. This is indeed expected and assumed in the two phase model of Wolfe et al. (2003a), as they found that heating rate (and because of the assumed thermal equilibrium therefore also cooling rate) is a global property of the DLA and not a local property as it is in the local ISM. The constancy of r_C across the different components is therefore expected in the two-phase model, as it is a direct consequence of the global nature of the heating rate.

3.7.2 Comparison with Previous Observations

In Table 3.2 we have listed the results of our study on the neutral hydrogen density, electron density, temperature, and pressure of DLAs using the Si II* and C II* method. This is not the first study of these parameters as several other methods provide estimates. A comparison for those 7 DLAs which have measured temperatures from multiple methods is shown in Table 3.3. These DLAs suggest that there is a reasonable agreement between the physical parameters derived using the Si II* and C II* method and previous methods.

3.7.2.1 21 cm Absorption

As was discussed in the introduction, one method of measuring the spin temperature of DLAs is by measuring 21 cm absorption in DLAs located in front of radio-loud quasars. A comprehensive paper describing this method was recently published by Kanekar et al. (2014). They found that the median temperature of the gas inside DLAs

Table 3.3: Comparison between Temperature Measurements

QSO	T (K) ($1-\sigma$ constraint)		
	C II*/Si II*	Other	Method
Q0336–01	(28 - 5200)	> 8890	21 cm absorption
Q0458–02	(50 - 316)	(465 - 655)	21 cm absorption
Q1157+014	(260 - 5500)	(760 - 1270)	21 cm absorption
J0812+3208	(25 - 178)	(32 - 88)	C I
J2100–0641	(30 - 171)	(10 - 251)	C I
Q2206–19	> 25	(9200 - 15200)	line-fitting
J2340–0053	(36 - 375)	(55 - 200)	C I

responsible for 21 cm absorption in their sample was greater than 900 K. Furthermore, they found that only 2 out of the 23 DLAs above a redshift of 1.7 were consistent with having a significant fraction of CNM. We note that we found in our sample that this fraction must be at least 5 %. These results are consistent within the uncertainty of the measurements due to the small sample sizes of both methods. Because the former measurement is an upper limit and the latter a lower limit, the two methods suggest that roughly between 5 and 10 % of all DLAs have the bulk of their gas in a CNM phase.

This fraction is somewhat in conflict with the results from Wolfe et al. (2003b, 2004), who argued that the majority of all C II* detections in DLAs must come from gas in a CNM, and about 40 % of all DLAs have detectable levels of C II* (e.g. Neeleman et al., 2013). Kanekar et al. (2014) resolves this conflict by assuming that only a small fraction of the gas (10 - 20 %) in the DLAs with C II* detections is in actuality CNM, with the bulk of the gas in a WNM phase. There are two problems with this scenario. First, it is unclear why in this scenario, the C II*/Si II ratio would be relatively constant among the individual velocity components, as it is in observations. Secondly, using the technique described in this chapter, we can calculate the amount of C II needed in the CNM to produce the required amount of C II* observed. In the two cases mentioned in Kanekar et al. (2014) (i.e. DLAs Q1157+014 and Q0458–02), the resultant C II column

density needed in a canonical ($T = 100$ K) CNM to produce the observed $C\ II^*$ column density is larger than the observed *total* $C\ II$ column density. Hence, at least for these two DLAs, we can rule out a scenario where only 10 - 20 % of the gas is in a CNM.

A more plausible explanation for the conflicting results is that we cannot assume that a simple two-phase model consisting of a canonical CNM of $T = 100$ K and WNM of $T = 8000$ K is capable of reproducing the results for the large range of physical conditions applicable for all DLAs. Indeed considering the wide variety of ranges in metallicity, dust-to-gas ratios, and UV radiation fields, the results from both Wolfire et al. (1995) and Wolfe et al. (2003a) suggest that CNM temperatures can range from 10 K to 500 K, with higher temperatures more likely for lower metallicities, higher dust-to-gas ratios and higher UV radiation fields. From the $Si\ II^*$ and $C\ II^*$ technique we can conclude that DLA Q0458–02 likely contains the bulk of the gas at a temperature of ~ 300 K, still well within the range of a CNM phase as defined by Wolfe et al. (2003a), and fully consistent with the result found in Kanekar et al. (2014). DLA Q1157+014 is an exception as the results from this chapter suggest it has the bulk of its gas at a temperature of ~ 1000 K, which is inconsistent with a CNM or WNM, but again consistent with the temperature found in Kanekar et al. (2014). It is likely the case that Q1157+014 is not representative of the DLA population as a whole as it has measurable levels of $Si\ II^*$ (See Section 3.7.2.4). Furthermore, we would expect to find some DLAs with gas temperatures inconsistent with either the CNM or WNM as such gas is seen often in the local ISM (Roy et al., 2013b).

3.7.2.2 C I Fine-Structure Study

A second method used to measure the physical parameters of DLAs is by considering the fine structure lines of C I. This was done for several DLAs by Srianand et al. (2005) and Jorgenson et al. (2010). Jorgenson et al. (2010) found that the densities

and temperatures derived from this method could only result from very dense ($n_{\text{H}} \geq 30 \text{ cm}^{-3}$) and cold gas ($T \leq 150 \text{ K}$). They therefore surmise that C I traces very dense pockets of very cold gas at slightly higher pressures. This is indeed seen in Figure 3.10 where the results from Jorgenson et al. (2010) trace the coldest and densest measurements from our sample. Furthermore, the mean pressure from the Jorgenson et al. (2010) sample is higher than the median pressure for the complete sample in this chapter ($\log(P/k_{\text{B}}) = 3.0 [\text{K cm}^{-3}]$).

A comparison between the three DLAs that have been analyzed using both the C I and the C II* and Si II* analysis (Table 3.3) shows that both methods give remarkably similar temperatures and densities. This is somewhat at odds with the scenario put forth in Jorgenson et al. (2010). They suggest that C I traces small dense clumps of cold neutral gas in a larger less dense medium of cold gas. However, we find that for these three DLAs the C I method gives values in agreement with the measurements of the bulk of the gas from the Si II* and C II* technique, removing the need for this scenario in these DLAs.

One possible explanation for this result is that the C I analysis can only be performed when multiple C I fine-structure states can be measured. Such measurements are easiest for those DLAs with large column densities of the C I fine-structure states, which results in preferentially selecting DLAs which contain the bulk of their gas in a cold and dense phase. This assessment is corroborated by the fact that 5 out of the 9 DLAs with $1-\sigma$ temperature measurements below 500 K show C I absorption. For the unbiased DLA sample of Neeleman et al. (2013), the fraction of DLAs showing detectable levels of C I is more than 10 times smaller; only 4 out of the 80 DLAs show C I absorption. A positive detection of C I is therefore a strong indicator that the DLA contains a significant fraction of cold, dense gas.

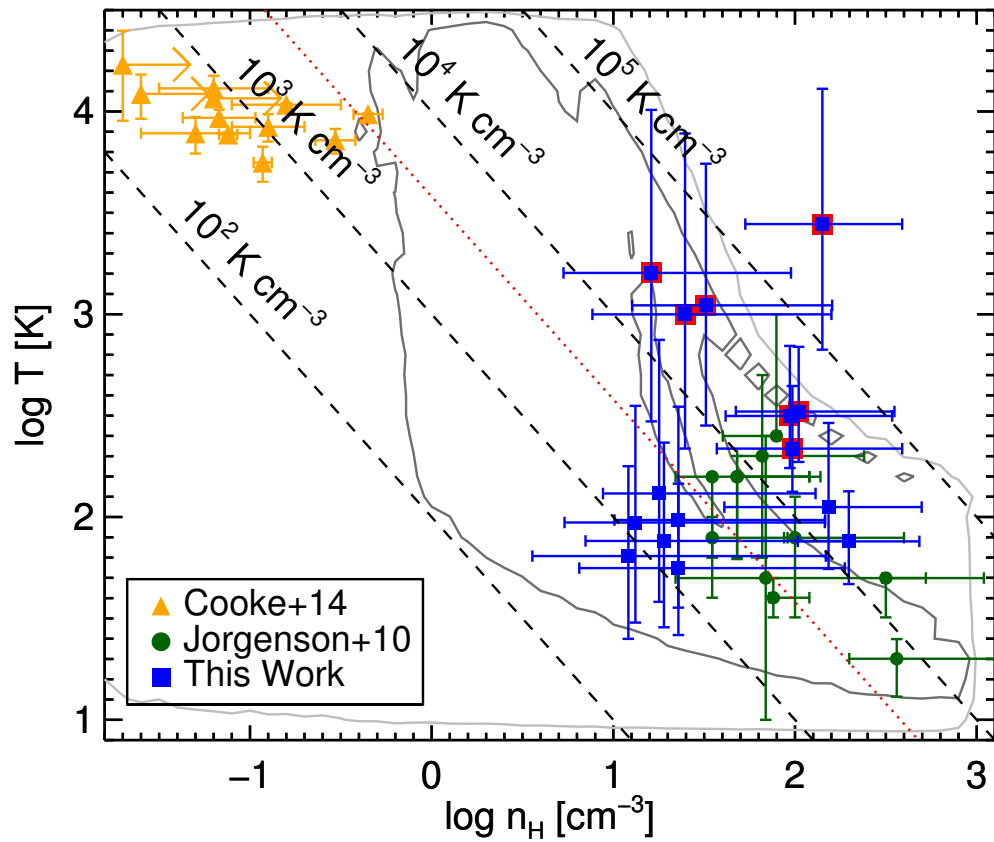


Figure 3.10: Allowed temperature and neutral hydrogen density parameter space for DLAs. The larger, outlined in red square data points are those with detectable levels of Si II^* . Overplotted on this figure are lines of constant pressure. The contours mark the 68 % (dark gray) and 99 % (light gray) confidence levels of the unbiased sample of Neeleman et al. (2013). The dotted red line is the pressure of the local ISM as measured by Jenkins & Tripp (2011).

3.7.2.3 Other Studies

The third and final method discussed here for measuring the temperature of DLAs is the use of fitting routines to measure the Doppler parameter of individual components. By measuring a wide range of ion species, one is able to untangle the thermal broadening of the Doppler parameter from the turbulent or bulk motion of the gas. The thermal broadening gives an estimate of the temperature of the gas. This method has been used to find the temperature of individual components in DLAs, resulting in detection of both cold and warm gas (Carswell et al., 2010, 2012). However, the multiple velocity components of a typical DLA, make this method daunting.

Recently this method has been used for a selection of very metal poor DLAs, which have simpler velocity structure (Cooke et al., 2014; Dutta et al., 2014). The result from these studies indicate that these DLAs have higher temperature and lower densities than the DLAs in our sample with conditions similar to those expected from a WNM. This suggests that the gas being traced by these very metal-poor DLAs is less likely to host star formation, which is corroborated by the lower metallicity of the gas.

Finally, we can compare our results to those found for the local ISM. Using C I, Jenkins & Tripp (2011) find that the CNM in the local ISM has an average pressure of $\log(P/k_B) = 3.58 \pm 0.18$ [K cm⁻³]. The median pressure for our sample is $\log(P/k_B) = 3.0$ [K cm⁻³]. However, if we include only those DLAs with well-determined ranges on their pressure, the median pressure becomes $\log(P/k_B) = 3.4$ [K cm⁻³]. We believe that this pressure is more representative of the complete DLA sample, as the large number of lower limits will artificially lower the median pressure. This pressure is very similar to the pressure found locally, although our sample has a larger range of allowed pressures. This extended range in pressures is easily explained by the fact that DLAs probe a variety of different galaxies, with a wider range of physical conditions compared to those seen in our own Galaxy.

3.7.2.4 Summary

Table 3.3 lists the results for the 7 DLAs which were previously examined using either 21 cm absorption, C I absorption or line profile fitting. These 7 DLAs show that for the limited sample of DLAs with temperature measurements from two different methods, the Si II* and C II* method measures temperatures that are in general agreement with the results from other techniques. Two discrepancies exist. The temperature measurement for Q0458–02 from the 21 cm absorption study is likely high because the optical and radio line of sight encounter different column densities of gas (see Kanekar et al., 2014). The only other measurement that is inconsistent within $1\text{-}\sigma$ is that of DLA Q0336–01; this discrepancy is also discussed in Kanekar et al. (2014). The remarkable agreement between the methods suggest that at least for the subset of DLAs with large fractions of cold gas, the Si II* and C II* method is able to accurately determine the temperature and density of the gas.

The results from this section are summarized in Figure (Figure 3.10). The gray contours are the 68 % and 99 % confidence intervals of the unbiased sample of Neeleman et al. (2013). The data points for our sample are those DLAs with well-defined ranges. Of these DLAs, the ones marked with larger squares (outlined in red) are those with measurable Si II*. The DLAs with detectable levels of Si II* fall outside the 68 % contour intervals, indicating that the conditions conducive to Si II* detections are not common in a random sample of DLAs. Indeed one DLA, J1135–0010, falls outside the 99 % contour; this DLA, however, is unique in several other ways (see Kulkarni et al., 2012; Noterdaeme et al., 2012) and therefore its physical conditions need not be similar to a typical DLA.

The measurements from the C I method by Jorgenson et al. (2010) are consistent with measurement for the coldest and densest DLAs in our sample. This is not unexpected as C I likely traces the coldest gas in DLAs. On the other hand the metal poor

sample of Cooke et al. (2014) have temperatures and densities consistent with a WNM. These DLAs fall outside the 68 % contour of the unbiased sample, suggesting that the low densities for this sample are not common in a typical DLA and could be due to the very low metallicity of these DLAs. Finally, the dotted line in Figure 3.10 is the average pressure of the local ISM (Jenkins & Tripp, 2011), which is consistent with the pressures found in DLAs.

3.7.3 Comparison with the Two-Phase Model

As discussed in the introduction, Wolfe et al. (2003a) adopted the two-phase medium model from Wolfire et al. (1995) to describe the physical conditions of the gas around DLA galaxies. The results from this chapter are able to test the validity of the two-phase model, since the Si II* and C II* method provides independent measurements of the temperature and density of the DLA gas.

The first such test is to check that the two-phase model is able to reproduce the range of allowed pressures. We find allowable pressures ranges of $\log(P/k_B)$ between 1 [K cm⁻³] and 6 [K cm⁻³]. This large range of pressures is allowed within the two-phase model (see Fig 5a and 5c of Wolfe et al., 2003a), since the lower metallicity of DLAs and varying star formation rate density can give rise to a large range of pressures that are able to maintain a stable two-phase structure.

A second test of the two-phase model is provided by comparing the star formation per unit area (Σ_{SFR}) predicted from the two-phase model with that measured from emission lines of the DLA galaxy. Detecting DLA galaxies in emission is rare (see e.g. Krogager et al., 2012); hence only 1 DLA (J1135–0010) in our sample has a published estimate for Σ_{SFR} from emission studies. We convert our pressure estimate and density measurement of this DLA into a star formation rate per unit area, in a similar way as was done in Figure 5 of Wolfe et al. (2003a). Using this method we find a star formation

rate of $0.3 M_{\odot} \text{ yr}^{-1} \text{ kpc}^{-2}$. This compares well with the observed rate predicted from emission lines, which is $\sim 1 M_{\odot} \text{ yr}^{-1} \text{ kpc}^{-2}$ (Noterdaeme et al., 2012).

Finally, we can compare the temperatures from the Si II* and C II* method, to see if we find any evidence for two distinct phases, which is a prediction of the two-phase model. As discussed in Section 3.7.2, we find that at least 5 % of DLAs have a significant fraction of cold gas, consistent with a canonical CNM (Figure 3.6). Unfortunately, we are not able to confirm the existence of gas in a WNM as our method provides weak constraints at high temperatures. However, from other studies such as Carswell et al. (2012) and Cooke et al. (2014), we know that such gas exists.

In conclusion, the results in this chapter are in general agreement with the two-phase model of Wolfe et al. (2003a,b). There are several DLAs, however, which have higher than predicted temperatures and densities; these DLAs are discussed further in Section 3.7.4.

3.7.4 Implications for High- z Galaxies

In this section we will speculate about the implications these results have on the physical conditions of DLA gas and the implication on the formation of high- z galaxies.

3.7.4.1 Implications for DLA Gas

In this chapter we have focussed on the physical conditions of the bulk of the neutral gas for a large sample of DLAs. This is unlike previous absorption studies using C I, which focus solely on the coldest and densest gas of DLAs as was noted by Jorgenson et al. (2010). The results from this chapter corroborates this assessment as the results from the C I analysis are consistent with the coldest and densest gas measurements from the Si II* and C II* method.

We find that the fraction of DLAs which have their bulk of gas in such a cold

and dense phase must be at least 5%. For the remaining DLAs the amount of gas in such a phase is unknown as the Si^+ and C^+ ratios do not provide stringent constraints on the temperature and density of the gas. Interestingly, we find that the upper levels of both the ground state of Si^+ and C^+ have the same velocity structure as the lower levels for the majority of DLAs, suggesting similar conditions for the majority of the velocity components in these DLAs.

The range of allowed temperatures and densities is summarized in Figure 3.10. The unbiased sample covers the parameter space between the metal-poor sample and the sample of C I detections. Several DLAs have temperature and density measurements which are inconsistent with the two-phase model of Wolfe et al. (2003a). The enhanced densities and temperatures in these DLAs increases r_{C} (see Figure 3.2), and therefore the observed cooling rate, ℓ_{c} . As a result, setting the observed cooling rate equal to the calculated cooling rate from a two-phase model will over predict the star formation rate for these DLAs.

This could partially provide the answer to the unsuccessful attempts of observing the DLAs in emission (Fumagalli et al., 2015). If a large fraction of DLAs have enhanced densities and temperatures compared to the two-phase model, the average star formation rate for DLAs will be systematically overestimated. One possible explanation for the enhanced temperatures and pressures could be turbulence. At least in numerical simulations turbulence is able to drive some of the gas into the classically forbidden region (Gazol et al., 2005). Such gas will have enhanced r_{C} ratios compared to those predicted from the two-phase model and therefore the two phase model will overestimate the star formation rate.

In conclusion, we suggest that the gas in DLAs follows in general the two-phase model of Wolfe et al. (2003a), as several studies have measured gas with properties very similar to both the WNM (Lehner et al., 2008; Carswell et al., 2012; Kanekar et al., 2014;

Cooke et al., 2014) and CNM (Howk et al., 2005; Srianand et al., 2005; Carswell et al., 2010; Jorgenson et al., 2010). However, the detection of Si II* in DLAs suggest that a fraction of DLAs have significantly higher densities and temperatures than expected from the two-phase model. For these systems the star formation rate obtained from the two-phase model is overestimated. Unfortunately, the exact fraction of these DLAs cannot be estimated from this study. However, in the local ISM this fraction is quite significant ($\sim 30\%$) (Roy et al., 2013b).

We would like to note that these higher temperatures are in agreement with the results from 21 cm absorption, thereby resolving two problems plaguing DLA studies at once; the lack of detections of DLAs in emission and the discrepancy between temperatures expected from the two-phase model and measurements from 21 cm studies. One possible adaptation to the two-phase model which could provide such a solution is to include turbulence, as numerical simulations show that turbulence could drive gas into the classically forbidden region.

3.7.4.2 Implications for High- z Galaxy Formation

By the nature of their selection, DLA sightlines represent a cross-section weighted sampling of high-surface density, neutral hydrogen gas at high- z . In aggregate, these systems also represent a major reservoir to fuel galaxy formation during the first few Gyr of the universe (Wolfe et al., 1995; Prochaska et al., 2005). Therefore, one generally associates this gas with the ISM of young galaxies. As such, the results presented here offer new insight into the nature of this ISM gas and its relationship to ongoing or future star-formation.

Restricting the discussion first to our random sample, we find that the incidence of very strong fine-structure absorption is rare: r_C exceeds 10^{-2} in only 4 out of the 46 DLAs from the random sample with measured r_C (see Figure 3.11). Such high r_C values

require gas densities $n_{\text{H}} \gtrsim 10 \text{ cm}^{-3}$ for the majority of neutral, atomic gas at high- z . In conjunction with the paucity of systems showing molecular gas and/or C I detection, which are both indicators of dense gas, these results suggest that a large fraction of DLA gas is uncondusive to star-formation. A result corroborated by the difficulty to directly measure the in-situ star-formation of a typical DLA (see e.g. Fumagalli et al., 2015). Indeed, this material may even form so-called ‘dark galaxies’ (Cantalupo et al., 2012).

A significant fraction of DLAs (9 out of 46) have measured r_{C} value in the range $10^{-2.5}$ to 10^{-2} . For the single-phase analysis performed in this manuscript, we derive $n_{\text{H}} \gtrsim 3 \text{ cm}^{-3}$ which exceeds the canonical value for the WNM. Together with the 18 DLAs which have upper limits to r_{C} that exceed $10^{-2.5}$, about half of all systems are consistent with moderate densities which exceed those expected in a canonical WNM. One might argue, however, that the systems with intermediate r_{C} values represent a mixture of dense and more diffuse gas with the dense gas contributing nearly all of the observed C II* absorption. Then, the bulk of the gas could (in principle) be very diffuse. However, as mentioned in Section 3.5.1, we disfavor extreme scenarios of this kind because the absorption profiles of C II* $\lambda 1335.7$ closely track the resonance lines, in velocity and optical depth. This shows that there are no substantial regions along the sightline of highly diffuse gas without corresponding dense gas. Furthermore, even if one adopts a two-phase medium in pressure equilibrium with the WNM dominating the column density, then the n_{H} value derived from a single-phase analysis only overestimates the mass-weighted value by a factor of a few.

Despite a large fraction of DLAs favoring modest densities, the majority of the DLAs have significant gas pressures ($P > 10^3 \text{ K cm}^{-3}$), which is a characteristic of an active ISM. Recent models of galaxy formation within hierarchical cosmology predict highly turbulent conditions driven by the accretion of cool gas and violent disk insta-

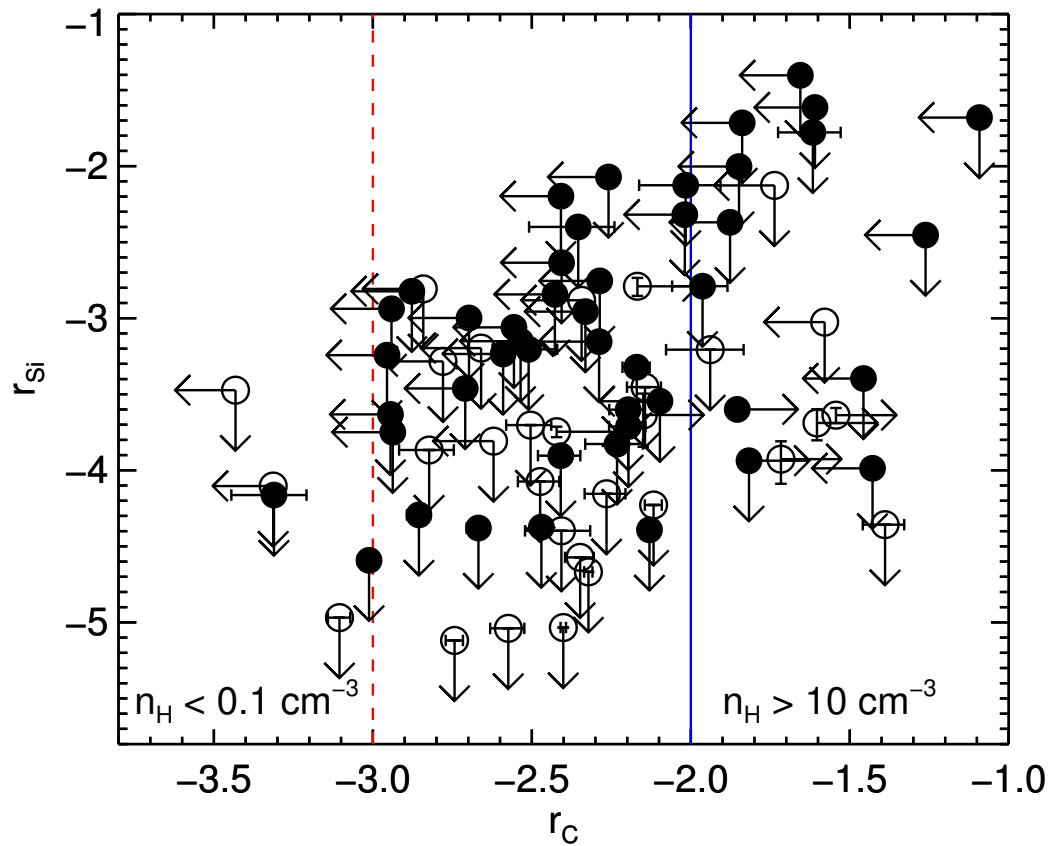


Figure 3.11: r_C and r_{Si} ratio for the complete sample. The filled circles are the 46 DLAs that are part of the unbiased sample of Neeleman et al. (2013) and have a well-defined r_C and r_{Si} . The region to the left of the dashed red line can only be occupied by DLAs with neutral hydrogen density less than 0.1 cm^{-3} , whereas the region to the right of the solid blue line can be occupied solely by DLAs with neutral hydrogen densities greater than 10 cm^{-3} .

bilities within the galaxies (e.g. Kereš et al., 2005; Dekel & Birnboim, 2006; Burkert et al., 2010; Fumagalli et al., 2011). Perhaps such processes explain the small, but non-negligible subset of DLA sightlines with $P > 10^4 \text{ K cm}^{-3}$. As noted in Section 3.7.1, these pressures are predominantly recorded in gas with high metallicity and large velocity widths.

3.8 Summary

In this chapter we have presented a new method of determining the physical conditions of gas in high redshift galaxies. Using the fine-structure lines of Si^+ and C^+ , we are able to provide constraints on the temperature and neutral hydrogen density of DLAs. We have applied this method to a sample of 80 DLAs, for which we are able to provide limits or detections of these fine-structure line transitions. This sample contains 5 new detections of the excited fine-structure line of Si^+ , which more than doubles the previously known detections. The results of this analysis are:

1. We find that 9 DLAs have temperatures consistent with gas in a cold neutral medium. The remaining DLAs provide less stringent constraints on their temperature for two reasons. Firstly, the ratios of fine-structure lines become insensitive to temperature changes above 500 K. Secondly, the low density of Si II^* and C II^* in these systems makes detection difficult; resulting in weak upper limits to the column density measurements of both fine-structure lines in these systems.
2. From the ‘unbiased’ subsample of DLAs part of the sample described in Neeleman et al. (2013), we find that at least 5 % of all DLAs have significant fractions of gas with properties similar to a canonical CNM along their line-of-sight. This result is consistent with the locally measured volume filling fraction of 0.01 for the CNM.

3. The results of the method show that the neutral hydrogen density of DLAs vary significantly from DLA to DLA. On the other hand the electron density varies little between DLAs with a median electron density of $0.0044 \pm 0.0028 \text{cm}^{-3}$. Furthermore, we can rule out the parameter space of high temperature and high neutral hydrogen density (see Figure 3.6) as such gas would produce upper to lower level fine-structure state ratios in excess of what we observe.
4. We find that there exist a correlation between the neutral hydrogen density and the cooling rate of the DLA. This is consistent with the predictions from the two phase model, where stronger star formation rates and therefore larger cooling rates result in higher stable neutral hydrogen equilibrium densities. Furthermore, the comparison between the neutral hydrogen density and the total H I column density gives a rough estimate of the total absorption length along the line-of-sight. These values range from about 1 kpc to only a few pc, suggesting that the bulk of the neutral gas at high redshift can be located in reasonably small dense components.
5. Finally, we find that the typical pressure of the DLAs in the sample is $\log(P/k_B) = 3.4 [\text{K cm}^{-3}]$, which is comparable to the pressure of the local ISM. However, the DLAs show a larger range in pressures, which can be easily explained by the fact that DLAs measure a range of different galaxies, with a wide range of different physical conditions.

We speculate that these results indicate that DLAs generally follow the two-phase model of Wolfe et al. (2003b). However, a fraction of DLAs have temperatures and densities inconsistent with this model. As a result, the two-phase model will over predict the star formation rate of these systems. By including a mechanism in the two-phase model which will increase the temperature and density of the gas for these DLAs, we can account for both the higher spin temperatures seen in 21 cm absorption (Kanekar

et al., 2014), and lower the star formation rates of DLAs as is suggested by recent observations (Fumagalli et al., 2015). One such mechanism is turbulence, which is able to drive gas into the unstable temperature regime (Gazol et al., 2005; Walch et al., 2011).

3.9 Acknowledgements

We wish to thank the referee for the helpful comments and N. Kanekar for reading a previous version of the manuscript. Support for this work was provided by NSF award AST-1109447. The data presented herein were obtained at the W.M. Keck Observatory, which is operated as a scientific partnership among the California Institute of Technology, the University of California and the National Aeronautics and Space Administration. The Observatory was made possible by the generous financial support of the W.M. Keck Foundation. The authors wish to recognize and acknowledge the very significant cultural role and reverence that the summit of Mauna Kea has always had within the indigenous Hawaiian community. We are most fortunate to have the opportunity to conduct observations from this mountain.

This chapter, in full (with minor exceptions to conform to this thesis), is a reprint of material previously published as “Probing the Physical Conditions of Atomic Gas at High Redshift”, by Marcel Neeleman, J. Xavier Prochaska, & Arthur M. Wolfe, published in the The Astrophysical Journal, 2015, Vol. 800, p.7. I was the primary investigator and author of this paper.

3.10 References for Chapter 3

Abazajian, K. N., Adelman-McCarthy, J. K., Agüeros, M. A., Allam, S. S., Allende Prieto, C., An, D., Anderson, K. S. J., Anderson, S. F., Annis, J., Bahcall, N. A., Bailer-Jones, C. A. L., Barentine, J. C., Bassett, B. A., Becker, A. C., Beers, T. C., Bell,

- E. F., Belokurov, V., Berlind, A. A., Berman, E. F., Bernardi, M., Bickerton, S. J., Bizyaev, D., Blakeslee, J. P., Blanton, M. R., Bochanski, J. J., Boroski, W. N., Brewington, H. J., Brinchmann, J., Brinkmann, J., Brunner, R. J., Budavári, T., Carey, L. N., Carliles, S., Carr, M. A., Castander, F. J., Cinabro, D., Connolly, A. J., Csabai, I., Cunha, C. E., Czarapata, P. C., Davenport, J. R. A., de Haas, E., Dilday, B., Doi, M., Eisenstein, D. J., Evans, M. L., Evans, N. W., Fan, X., Friedman, S. D., Frieman, J. A., Fukugita, M., Gänsicke, B. T., Gates, E., Gillespie, B., Gilmore, G., Gonzalez, B., Gonzalez, C. F., Grebel, E. K., Gunn, J. E., Györy, Z., Hall, P. B., Harding, P., Harris, F. H., Harvanek, M., Hawley, S. L., Hayes, J. J. E., Heckman, T. M., Hendry, J. S., Hennessy, G. S., Hindsley, R. B., Hoblitt, J., Hogan, C. J., Hogg, D. W., Holtzman, J. A., Hyde, J. B., Ichikawa, S.-i., Ichikawa, T., Im, M., Ivezić, Ž., Jester, S., Jiang, L., Johnson, J. A., Jorgensen, A. M., Jurić, M., Kent, S. M., Kessler, R., Kleinman, S. J., Knapp, G. R., Konishi, K., Kron, R. G., Krzesinski, J., Kuropatkin, N., Lampeitl, H., Lebedeva, S., Lee, M. G., Lee, Y. S., French Leger, R., Lépine, S., Li, N., Lima, M., Lin, H., Long, D. C., Loomis, C. P., Loveday, J., Lupton, R. H., Magnier, E., Malanushenko, O., Malanushenko, V., Mandelbaum, R., Margon, B., Marriner, J. P., Martínez-Delgado, D., Matsubara, T., McGehee, P. M., McKay, T. A., Meiksin, A., Morrison, H. L., Mullally, F., Munn, J. A., Murphy, T., Nash, T., Nebot, A., Neilsen, Eric H., J., Newberg, H. J., Newman, P. R., Nichol, R. C., Nicinski, T., Nieto-Santisteban, M., Nitta, A., Okamura, S., Oravetz, D. J., Ostriker, J. P., Owen, R., Padmanabhan, N., Pan, K., Park, C., Pauls, G., Peoples, John, J., Percival, W. J., Pier, J. R., Pope, A. C., Pourbaix, D., Price, P. A., Purger, N., Quinn, T., Raddick, M. J., Re Fiorentin, P., Richards, G. T., Richmond, M. W., Riess, A. G., Rix, H.-W., Rockosi, C. M., Sako, M., Schlegel, D. J., Schneider, D. P., Scholz, R.-D., Schreiber, M. R., Schwope, A. D., Seljak, U., Sesar, B., Sheldon, E., Shimasaku, K., Sibley, V. C., Simmons, A. E., Sivarani, T., Allyn Smith, J., Smith, M. C., Smolčić, V., Snedden, S. A., Stebbins, A., Steinmetz, M., Stoughton, C., Strauss, M. A., SubbaRao, M., Suto, Y., Szalay, A. S., Szapudi, I., Szkody, P., Tanaka, M., Tegmark, M., Teodoro, L. F. A., Thakar, A. R., Tremonti, C. A., Tucker, D. L., Uomoto, A., Vanden Berk, D. E., Vandenberg, J., Vidrih, S., Vogeley, M. S., Voges, W., Vogt, N. P., Wadadekar, Y., Watters, S., Weinberg, D. H., West, A. A., White, S. D. M., Wilhite, B. C., Wonders, A. C., Yanny, B., Yocum, D. R., York, D. G., Zehavi, I., Zibetti, S., & Zucker, D. B. 2009, *ApJS*, 182, 534
- Asplund, M., Grevesse, N., Sauval, A. J., & Scott, P. 2009, *ARA&A*, 47, 481
- Berg, T. A. M., Ellison, S. L., Venn, K. A., & Prochaska, J. X. 2013, *MNRAS*, 000, 00
- Berg, T. A. M., Neeleman, M., Ellison, S. L., & Prochaska, J. X. 2014, *PSAP*, submitted
- Bird, S., Vogelsberger, M., Haehnelt, M., Sijacki, D., Genel, S., Torrey, P., Springel, V., & Hernquist, L. 2014, *MNRAS*, 445, 2313
- Burkert, A., Genzel, R., Bouché, N., Cresci, G., Khochfar, S., & Sommer-Larsen, J. 2010, *ApJ*, 725, 2324

- Cantalupo, S., Lilly, S. J., & Haehnelt, M. G. 2012, MNRAS, 425, 1992
- Carswell, R., Becker, G., Jorgenson, R. A., Murphy, M., & Wolfe, A. M. 2012, MNRAS, 422, 1700
- Carswell, R., Jorgenson, R. A., Wolfe, A. M., & Murphy, M. 2010, MNRAS, 411, 2319
- Catinella, B., Haynes, M. P., Giovanelli, R., Gardner, J. P., & Connolly, A. J. 2008, ApJ, 685, L13
- Cen, R. 2012, ApJ, 748, 121
- Cooke, R., Pettini, M., & Jorgenson, R. A. 2014, AJ, In Prep
- Dekel, A. & Birnboim, Y. 2006, MNRAS, 368, 2
- Dessauges-Zavadsky, M., Calura, F., Prochaska, J. X., D'Odorico, S., & Matteucci, F. 2004, A&A, 416, 79
- . 2007, A&A, 470, 431
- Draine, B. T. 2011, *Physics of the Interstellar and Intergalactic Medium* (Princeton: Princeton University Press)
- Dutta, R., Srianand, R., Rahmani, H., Petitjean, P., Noterdaeme, P., & Ledoux, C. 2014, MNRAS, 440, 307
- Field, G., Goldsmith, D., & Habing, H. 1969, ApJ, 155, L149
- Fumagalli, M., O'Meara, J., Prochaska, J. X., Rafelski, M., & Kanekar, N. 2015, MNRAS, 446, 3178
- Fumagalli, M., Prochaska, J. X., Kasen, D., Dekel, A., Ceverino, D., & Primack, J. R. 2011, MNRAS, 418, 1796
- Gazol, A., Vázquez-Semadeni, E., & Kim, J. 2005, ApJ, 630, 911
- Heiles, C. & Haverkorn, M. 2012, Space Sci Rev, 166, 293
- Heiles, C. & Troland, T. 2003a, ApJS, 145, 329
- . 2003b, ApJ, 586, 1067
- Herbert-Fort, S., Prochaska, J. X., Dessauges-Zavadsky, M., Ellison, S. L., Howk, J. C., Wolfe, A. M., & Prochter, G. E. 2006, PASP, 118, 1077
- Howk, J. C., Wolfe, A. M., & Prochaska, J. X. 2005, ApJ, 622, L81
- Jenkins, E. & Tripp, T. M. 2011, ApJ, 734, 33

- Jorgenson, R. A., Wolfe, A. M., & Prochaska, J. X. 2010, *ApJ*, 722, 460
- Kanekar, N. & Chengalur, J. 2003, *A&A*, 399, 857
- Kanekar, N., Prochaska, J. X., Smette, A., Ellison, S. L., Ryan-Weber, E., Momjian, E., Briggs, F., Lane, W., Chengalur, J., Delafosse, T., Grave, J., Jacobsen, D., & de Bruyn, A. 2014, *MNRAS*, 438, 2131
- Kaplan, K. F., Prochaska, J. X., Herbert-Fort, S., Ellison, S. L., & Dessauges-Zavadsky, M. 2010, *MNRAS*, 122, 619
- Kereš, D., Katz, N., Weinberg, D. H., & Davé, R. 2005, *MNRAS*, 363, 2
- Khare, P., Kulkarni, V. P., Lauroesch, J. T., York, D. G., Crotts, A. P., & Nakamura, O. 2004, *ApJ*, 616, 86
- Krogager, J.-K., Fynbo, J., Møller, P., Ledoux, C., Noterdaeme, P., Christensen, L., Milvang-Jensen, B., & Sparre, M. 2012, *MNRAS*, 424, 1
- Kulkarni, V. P., Meiring, J., Som, D., Péroux, C., York, D. G., Khare, P., & Lauroesch, J. T. 2012, *ApJ*, 749, 176
- Ledoux, C., Petitjean, P., Fynbo, J., Møller, P., & Srianand, R. 2006, *A&A*, 457, 71
- Ledoux, C., Petitjean, P., & Srianand, R. 2003, *MNRAS*, 346, 209
- Lehner, N., Howk, J. C., Prochaska, J. X., & Wolfe, A. M. 2008, *MNRAS*, 390, 2
- Levshakov, S. A., Dessauges-Zavadsky, M., D’Odorico, S., & Molaro, P. 2002, *ApJ*, 565, 696
- Lu, L., Sargent, W. L., & Barlow, T. A. 1996, *ApJ Supp.*, 107, 475
- . 1998, *AJ*, 115, 55
- McKee, C. & Ostriker, J. P. 1977, *ApJ*, 218, 148
- Morton, D. C. 2003, *ApJS*, 149, 205
- Neeleman, M., Wolfe, A. M., Prochaska, J. X., & Rafelski, M. 2013, *ApJ*, 769, 54
- Noterdaeme, P., Laursen, P., Petitjean, P., Vergani, S., Maureira, M., Ledoux, C., Fynbo, J., Lopez, S., & Srianand, R. 2012, *A&A*, 540, 63
- O’Meara, J. M., Burles, S., Prochaska, J. X., Prochter, G. E., Bernstein, R. A., & Burgess, K. M. 2006, *ApJ*, 649, 61
- Petitjean, P., Srianand, R., & Ledoux, C. 2000, *A&A*, 364, L26

- Prochaska, J. X., Chen, H.-W., & Bloom, J. S. 2006, *ApJ*, 648, 95
- Prochaska, J. X., Gawiser, E., Wolfe, A. M., Castro, S., & Djorgovski, S. 2003a, *ApJ*, 595, L9
- Prochaska, J. X., Herbert-Fort, S., & Wolfe, A. M. 2005, *ApJ*, 635, 123
- Prochaska, J. X. & Wolfe, A. M. 1997, *ApJ*, 487, 73
- . 1999, *ApJ Supp.*, 121, 369
- . 2000, *ApJ*, 533, L5
- . 2002a, *ApJ*, 566, 68
- Prochaska, J. X., Wolfe, A. M., Howk, J. C., Gawiser, E., Burles, S. M., & Cooke, J. 2007, *ApJS*, 171, 29
- Prochaska, J. X., Wolfe, A. M., Tytler, D., Burles, S., Cooke, J., Gawiser, E., Kirkman, D., O'Meara, J. M., & Storrie-Lombardi, L. 2001a, *ApJ Supp.*, 137, 21
- Rafelski, M., Wolfe, A. M., Prochaska, J. X., Neeleman, M., & Mendez, A. 2012, *ApJ*, 755, 89
- Richings, A., Schaye, J., & Oppenheimer, B. D. 2014b, *MNRAS*, 442, 2780
- Roy, N., Kanekar, N., Braun, R., & Chengalur, J. 2013a, *MNRAS*, 436, 2352
- Roy, N., Kanekar, N., & Chengalur, J. 2013b, *MNRAS*, 436, 2366
- Sarazin, C., Rybicki, G., & Flannery, B. 1979, *ApJ*, 230, 456
- Savage, B. D. & Sembach, K. R. 1991, *ApJ*, 379, 245
- Schaye, J. 2001, *ApJ*, 559, L1
- Silva, A. & Viegas, S. 2002, *MNRAS*, 329, 135
- Snowden, S., Egger, R., Freyberg, M., McCammon, D., Plucinsky, P., Sanders, W., Schmitt, J., Trümper, J., & Voges, W. 1997, *ApJ*, 485, 125
- Srianand, R., Petitjean, P., Ledoux, C., Ferland, G., & Shaw, G. 2005, *MNRAS*, 362, 549
- Vladilo, G. 2004, *A&A*, 421, 479
- Vogt, S., Allen, S., Bigelow, B., Bresee, L., Brown, B., Cantrall, T., Conrad, A., Couture, M., Delaney, C., Epps, H., Hilyard, D., Hilyard, D., Horn, E., Jern, N., Kanto, D., Keave, M., Kibrick, R., Lewis, J., Osborne, J., Pardeilhan, G., Pfister, T., Ricketts, T., Robinson, L., Stover, R., Tucker, D., Ward, J., & Wei, M. 1994, *Proc. SPIE*, 2198, 362

- Walch, S., Wunsch, R., Burkert, A., Glover, S., & Whitworth, A. 2011, *ApJ*, 733, 47
- Wolfe, A. M., Gawiser, E., & Prochaska, J. X. 2003b, *ApJ*, 593, 235
- . 2005, *ARA&A*, 43, 861
- Wolfe, A. M., Howk, J. C., Gawiser, E., Prochaska, J. X., & Lopez, S. 2004, *ApJ*, 615, 625
- Wolfe, A. M., Lanzetta, K. A., Foltz, C. B., & Chaffee, F. H. 1995, *ApJ*, 454, 698
- Wolfe, A. M., Prochaska, J. X., & Gawiser, E. 2003a, *ApJ*, 593, 215
- Wolfe, A. M., Prochaska, J. X., Jorgenson, R. A., & Rafelski, M. 2008, *ApJ*, 681, 881
- Wolfire, M., Hollenbach, D., McKee, C., Tielens, A., & Bakes, E. 1995, *ApJ*, 443, 152
- Wolfire, M., McKee, C., Hollenbach, D., & Tielens, A. 2003, *ApJ*, 587, 278

Chapter 4

The HI Content of the Universe over the Past 10 Gyrs

4.1 Abstract

From the full Hubble Space Telescope (HST) archive of ultraviolet (UV) quasar spectroscopy, we construct and perform the first blind survey with HST for damped Ly α absorption (DLA) at low redshift. Our statistical sample includes data from 463 quasars with spectral coverage spanning a total redshift path $\Delta z = 123.3$ or an absorption path $\Delta X = 238.4$. Within this survey path, we identify 4 DLAs defined as absorbers with HI column density $n_{\text{H}} \geq 10^{20.3} \text{ cm}^{-2}$. This implies an incidence per absorption length $\ell_{\text{DLA}}(X) = 0.017_{-0.008}^{+0.013}$ at a median redshift $z = 0.623$; this is lower but consistent within the uncertainty with previous estimations at $z \approx 0$ from 21 cm emission. Our dataset is too small to properly sample the n_{H} frequency distribution function $f(N_{\text{HI}}, X)$, but we note that the observed distribution is consistent with previous estimations at $z > 2$. Adopting the high- z evaluation of $f(N_{\text{HI}}, X)$, we infer an HI mass density at $z \sim 0.5$ of $\rho_{\text{HI}} = 0.25_{-0.12}^{+0.19} \cdot 10^8 M_{\odot} \text{ Mpc}^{-3}$. This is significantly lower than

previous estimations from targeted DLA surveys with HST, and suggests that the neutral gas density of the universe has been slowly decreasing over the past 10 Gyrs.

4.2 Introduction

Galaxy formation and evolution are critically dependent on the gas within and surrounding a galaxy. As galaxies evolve, gas is accreted onto the galaxy and expelled through various processes such as AGN activity and stellar feedback. Providing observational constraints on this gas is therefore paramount in understanding these processes and galaxy formation in general. At low redshift, neutral gas has been studied in detail using the 21 cm line. Unfortunately such observations are limited with current facilities to low redshifts ($z \lesssim 0.25$) (Catinella et al., 2008).

To study how the mass and distribution of neutral gas has evolved over cosmic time, we need to measure the cosmic density of this gas over a large redshift range. Such a study can be done, by studying the gas in absorption through Ly- α absorption in quasar spectra (Wolfe et al., 1986). Previous studies have shown that the largest column density absorbers, the Damped Ly- α Systems (DLAs), which have neutral hydrogen column densities of $N_{\text{HI}} \geq 10^{20.3} \text{ cm}^{-2}$, contain the bulk of the neutral gas at high redshifts (Prochaska et al., 2005; Wolfe et al., 2005; O’Meara et al., 2007). Observations of DLAs therefore afford an excellent opportunity to constrain the neutral hydrogen content of our Universe over a large redshift range.

To quantify the overall HI content of our Universe, we use a single quantity known as the neutral hydrogen column density distribution function, $f(N_{\text{HI}}, X)$, (e.g. Lanzetta et al., 1991; Prochaska et al., 2005). $f(N_{\text{HI}}, X)$ is a quantitative description of the large scale neutral hydrogen distribution of our Universe. Moreover its zeroth and first moment yield the line density of DLAs, $\ell_{\text{DLA}}(X)$, and total hydrogen mass density

of our Universe, ρ_{HI} (see Section 4.5).

For redshifts above $z > 2$, $f(N_{\text{HI}}, X)$ for the highest column density systems has been measured by many authors (e.g. Prochaska & Wolfe, 2009; Noterdaeme et al., 2012), using large optical surveys such as the Sloan Digital Sky Survey (SDSS; Abazajian et al., 2009). These studies find that between $z \sim 2$ and $z \sim 3.5$, the shape of $f(N_{\text{HI}}, X)$ is invariant, however, a significant evolution is observed for its normalization factor, decreasing by a factor of 2 implying a concomitant decrease in $\ell_{\text{DLA}}(X)$ and ρ_{HI} . Such evolution may be explained by either gas conversion into stars over this redshift range or explosive feedback processes that expel the gas from the galaxy (e.g. Prochaska & Wolfe, 2009).

As remarkable, $f(N_{\text{HI}}, X)$ and its moments all appear to converge by $z \sim 2$ to the present-day measured values using 21 cm (Zwaan et al., 2005) studies, suggesting that over the last 10 billion years of galaxy evolution, these quantities have remained essentially unchanged. Unfortunately direct measurement of $f(N_{\text{HI}}, X)$ over this redshift range is difficult, because below a redshift of 2, the effectiveness of optical surveys plummets due to the atmospheric absorption of UV radiation (Lanzetta et al., 1995). To circumvent this problem, space-borne UV spectrographs such as the variety of spectrographs on the Hubble Space Telescope (HST) provide the answer. However, due to expense of these observations, large-scale blind surveys comparable to the SDSS have not been feasible within the limited allocations of single observing programs.

To increase the rate of detections of large column density absorbers along the line of sight for quasars, previous studies have used several types of preselection methods, with the most common approach using Mg II to preselect DLA candidates (Rao et al., 2006). For redshifts above $z \gtrsim 0.36$, the Mg II doublet is shifted within the optical regime. As the vast majority of DLAs show strong Mg II absorption (rest equivalent width, $W_0^{\lambda 2796} > 0.5 \text{ \AA}$), preselecting quasars with strong Mg II absorption will signif-

icantly increase the rate of DLAs in the sample. However, understanding the selection biases to get accurate measurements of $f(N_{\text{HI}}, X)$ for DLAs is difficult (see Rao et al., 2006).

Fortunately, 20 years of observations with a variety of UV-spectrographs have resulted in a large sample of observed quasars. As HST nears the end of its mission, the time has come to explore this large data set, and perform a study similar to those performed in the optical regime. In this chapter we provide a measurement of the distribution of neutral hydrogen between $z \sim 0.01$ and $z \sim 1.6$, covering the past 10 billion years of the Universe. The sample for this study is described in Section 4.3, and the method is described in Section 4.4. The results are presented in Section 4.5 and discussed in Section 4.6. Throughout this chapter we adopt an $(\Omega_{\text{M}}, \Omega_{\Lambda}, h) = (0.26, 0.74, 0.7)$ cosmology.

4.3 Sample Selection

To measure the amount of neutral hydrogen between $z \sim 0.01$ and $z \sim 1.6$, we have assembled a large sample of quasars observed with medium resolution spectrographs on the Hubble Space Telescope. Specifically, we performed an archival search for quasars observed with either the Space Telescope Imaging Spectrograph (STIS), the Faint Object Spectrograph (FOS) or the Cosmic Origins Spectrograph (COS). These instruments provide enough spectral resolution for a high fidelity search of strong absorption line systems (see Section 4.4.1). We did not include the Goddard High Resolution Spectrograph (GHRS) as its spectral coverage is too small to provide a meaningful search path. In total a sample of 878 quasars were found which were observed with at least one of these instruments.

Each of these observations were reduced according to the prescription described

Table 4.1: HST QSO sample

QSO	z_{em}^{a}	Instrument	Search Path			Statistical Path			Proposal ID
			$F_{\text{search}}^{\text{b}}$	Min z	Max z	$F_{\text{stat}}^{\text{c}}$	Min z	Max z	
J0000–1245	0.200	COS	1	0.010	0.299	1	0.010	0.188	12604
J0001+0709	3.234	STIS	1	—	—	0	—	—	8569
J0004–4157	2.760	FOS-H	1	1.501	1.695	0	—	—	6577
J0005+0524	1.900	FOS-H	1	0.829	1.695	1	0.829	1.695	4581,6705
J0005–5006	0.033	COS	1	0.010	0.133	1	0.010	0.022	12936

^aEmission redshift of quasar

^bSearch flag: (0) Low S/N or bad spectrum; (1) Included; (2) BAL quasar

^cStatistical flag: (0) Non-Statistical; (1) Statistical; (2) Galaxy Sample

Note. — This table is shown in its entirety in the Appendix. A portion is shown here for guidance regarding its form and content

in detail in Ribaldo et al. (2011) and Bechtold et al. (2002). For those quasars with multiple observations from different instruments, the observations were combined into a single spectrum. In cases with an overlap in spectral coverage, the higher resolution spectrum was chosen over the lower resolution spectrum. We then visually confirmed the emission redshift, and quality of the spectra for each of the quasars. Several quasars were not included either due to too low S/N or bad spectra ($n = 99$ quasars). We also excluded any quasars that exhibit strong broad absorption line (BAL) features ($n = 12$ quasars). A total of 767 quasars satisfy the above criteria and form the total sample in the remaining chapter. Table 4.1 lists the complete sample of quasars.

4.3.1 Statistical Sample

To provide an accurate measurement of the column density distribution function, it is critical to provide an unbiased sample, as the inclusion of quasar sightlines with known absorption systems would likely bias $f(N_{\text{HI}}, X)$ to higher values relative to the cosmic mean. Similarly the inclusion of quasar sightlines with a known absence of absorption systems would likely bias $f(N_{\text{HI}}, X)$ low. We have therefore carefully

considered the stated selection criteria for each of the observed quasars. In Table 4.1, we have included a flag that indicates if the observation of a quasar was observed for a biased reason with respect to strong N_{HI} absorption.

The statistical flag (f_{stat}) can take on three values. A flag of 0 indicates the observed quasar was known to contain either an absorber (known DLA or Mg II-system) or a lack of these systems along the line of sight. A flag of 1 indicates that the quasar was chosen independent of any known features along the line of sight. Finally a flag of 2 indicates that the quasar sightline crosses close to a previously recorded intervening galaxy. The true statistical sample defined in this chapter contains just the observations with a statistical flag equal to 1. This sample contains a total of 463 quasars. We also define an expanded sample in this chapter which contain both $f_{\text{stat}} = 1$ and $f_{\text{stat}} = 2$ quasars ($n = 677$ quasars).

4.4 Method

To search for absorption systems in the spectra observed with HST, we apply a method similar to that described in Prochaska et al. (2005) adapted slightly for lower redshifts. To be specific, we first define the search path for each quasar sightline. The lower limit of the search path is set by the signal-to-noise ratio (S/N) of the spectrum. We calculate the S/N for a wavelength by finding the median of a 20 pixel box around this wavelength. The lower limit to the search path is set to the wavelength for which this median S/N is greater than a minimum allowed S/N ratio, which we take to be 4, or the wavelength of Ly α at $z = 0$ ($\lambda_{\text{Ly}\alpha} = 1215.6701 \text{ \AA}$), whichever is greater. For an explanation of this minimum S/N value of 4 see Section 4.4.2. The upper limit to the search path is set to be either the end of the spectrum or the value: $(1 + z_{\text{em}} + \text{offset}) \cdot \lambda_{\text{Ly}\alpha}$, whichever is smaller. Here z_{em} is the redshift of the quasar and the offset is

added to allow for absorption systems to have slightly higher absorption redshift than the emission of the quasar. We take the offset to be 0.1 to encompass uncertainty in the reported emission redshifts. The total search path is shown in the left panel of Figure 4.1.

For those quasars that are part of the statistical or expanded sample, we also define a statistical search path, $g(z)$. The lower limit to the statistical path is set again by the wavelength where the median S/N exceeds the minimum S/N value of 4, or a wavelength of $(1 + \text{offset}) \cdot \lambda_{\text{Ly}\alpha}$ Å, whichever is greater. The offset here is chosen to be 0.01 which is $\sim 3000 \text{ km s}^{-1}$ from our Galaxy. This offset is introduced to prevent any biasing due to clustering in our own neighborhood. The upper limit is set to the end of the spectrum or the value $\sqrt{\frac{c-\Delta v}{c+\Delta v}}(1 + z_{\text{em}}) \cdot \lambda_{\text{Ly}\alpha}$ Å, whichever is greater. Here Δv is taken to be 3000 km s^{-1} which is to prevent any clustering around the quasar from affecting our measurements. The statistical search path for the statistical sample ($f_{\text{stat}} = 1$) is shown in the right panel of Figure 4.1.

After defining the search path, we run our search algorithm to find candidate absorption systems along the search path for each QSO. The algorithm searches regions of the spectrum that fall below a specified S/N cut, which happens in the absorption trough of strong absorbers. To be specific, the algorithm assigns to each pixel a DLA score, which is a measure of how many pixels in a 3 \AA window centered around this pixel fall below the assigned S/N cut per pixel. We take a 3 \AA window because this is the width of a $n_{\text{H}} = 10^{20.3} \text{ cm}^{-2}$ absorber at $z=0.01$, and the S/N cut is taken to be 2. The central pixels for which greater than 60 % of the surrounding pixels in the 3 \AA window fall below the S/N cut are flagged by the algorithm as candidate absorption systems. Altogether, we recorded 139 candidates from the complete sample.

The final step in the search for absorption systems is the visual follow-up of these candidate absorption systems. We fit individual absorption systems using a custom IDL Voigt fitting program for DLAs, `x.fitdla`, which is part of the publicly

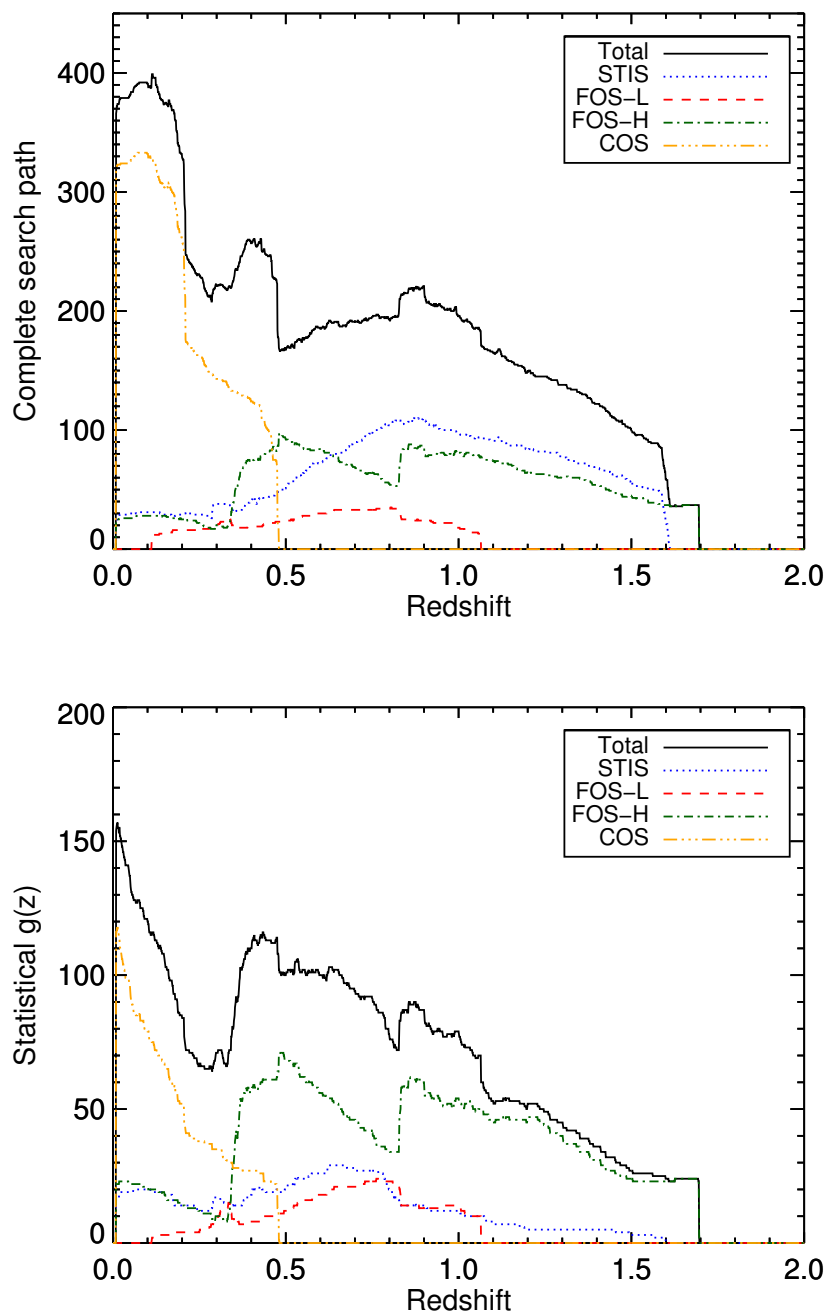


Figure 4.1: *left:* Complete search path for the sample ($n = 767$) of quasars. The search path of the individual spectrographs as well as the combined search path are plotted. *right:* Statistical search path $g(z)$ for the complete sample of quasars. The total number of quasars included in the statistical sample is 463.

available IDL library, XIDL¹. With this program we are able to simultaneously fit both the Voigt profile and the continuum of the quasar as described in detail in e.g. Prochaska et al. (2003a). The largest source of uncertainty stems from the continuum placement.

As this process has inherently a human aspect to it, two of the authors (i.e. MN and JXP) have both fitted the candidate systems individually. These fitting results from both authors were compared and for the large majority of systems ($> 90\%$) the measured HI column density from both authors fell within the estimated $1\text{-}\sigma$ uncertainty of the measurement. We therefore believe the column density measurements are robust.

4.4.1 Resolution Considerations

There are two ways that resolution of a spectrum can affect the results. First, they can affect the ability of the search algorithm to detect an absorption system. Secondly, the fitting of the DLA can be affected by either overestimating or underestimating the column density of the absorber. Both these effects on the results are explored in this section.

Low resolution spectra could result in an inaccurate column density measurements and/or non-detection of DLAs in the search algorithm. Our lowest resolution spectra are taken with the medium resolution gratings of the STIS G230L and FOS G160L, which have resolutions of approximately $R \sim 250$. For these resolutions, only about half of the resolution element falls within the DLA trough of low column density systems, and therefore small deviances could result in a non-detection of the DLA by the search algorithm.

To assess the impact of resolution on the recovery process, we created fake spectra with similar S/N and resolution to the observational data. We added in artificial DLAs to the spectra with a range of column densities. For this data, the algorithm was success-

¹<http://www.ucolick.org/~xavier/IDL/>

ful in recovering greater than 99 % of all of the absorbers with a column density above 10^{20} cm^{-2} . Therefore the resolution of the spectra is sufficient to accurately recover DLAs with this search algorithm.

Secondly, we randomly added DLAs to our lowest resolution spectra to test our ability to recover the column density measurement using the fitting procedure described in Section 4.4. In particular we added 50 DLAs with varying column densities to our lowest resolution spectra (i.e. both STIS and FOS-L) and measured the resulting column density from our fitting method. The results are shown in Figure 4.2. As can be seen from the fitting results, over the full range of fitted values, we are able to accurately recover the actual fitted column density. Furthermore, the lower resolution does not cause any systematical under or overestimation of the column density. The deviation from the actual value for this sample is 0.10 dex, which is comparable to the fitting errors assigned to the sample.

4.4.2 S/N Considerations

Similar to the resolution of a spectrum, its S/N affects both the search algorithm's efficacy and ability to accurately measure the column density of the absorption system during the fitting process. In case of the search algorithm, low S/N spectra will flag more false positives as more pixels will satisfy the S/N cut criteria defined in the search algorithm. To prevent high rates of false positive detections, we therefore set the minimum S/N ratio to be 4 over a 20 \AA window, which is $2\text{-}\sigma$ above the S/N cut of 2 per 3 \AA utilized in the search algorithm.

Secondly, we need to accurately determine the column density of the absorption systems with these S/N cuts. To test this, we insert artificial absorption systems in the real spectra and increase the noise level to the required S/N values. The fitting results are displayed in Figure 4.2. As this figure shows, we are able to accurately determine

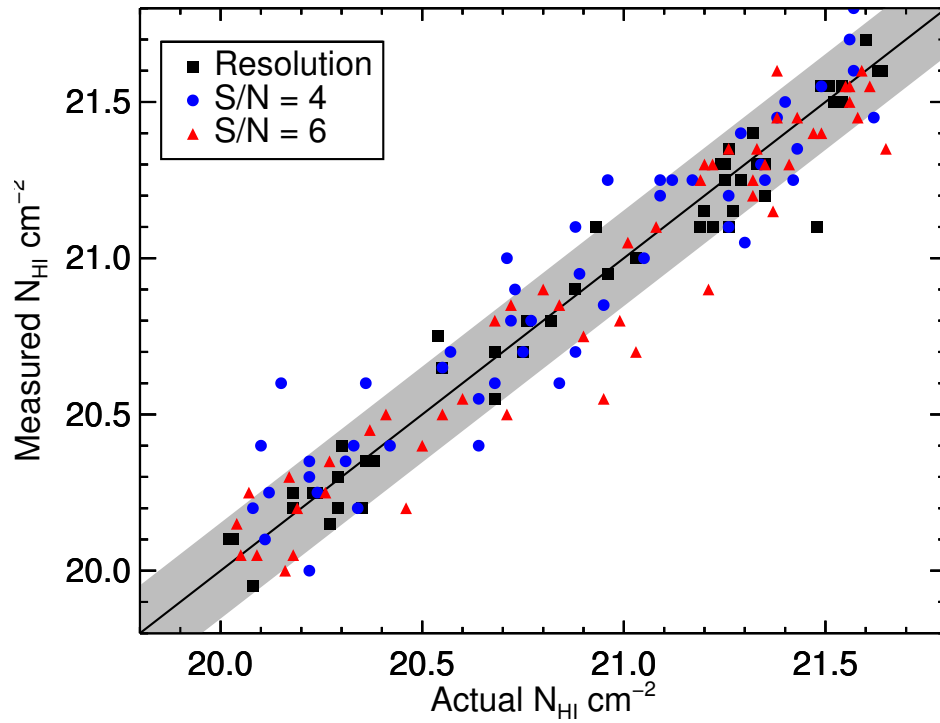


Figure 4.2: Results from various mock tests to quantify the effect of resolution and S/N on the ability to accurately determine the column density of absorbers. The gray area marks the 0.15 dex deviation value from the actual value and is the mean uncertainty on the measurements. The results shows that both low S/N data down to S/N of 4 and low resolution still allow for accurate determination of the column density of absorbers.

the column density of systems down to a S/N level of 4 for even the lowest resolution data in the sample. The deviation from the actual value for a spectrum with S/N value of 4 is 0.15 dex.

We therefore conclude that the S/N cut of 4 provides the ideal balance between maximizing the search path length and still provide the ability to reliably determine the column density systems of absorption systems.

4.5 Results

In this section we describe the results from the analysis. Table 4.2 lists all of the DLAs in the sample. From the statistical sample we provide estimates of $f(N_{\text{HI}}, X)$, $\log X$, and ρ_{HI} .

Table 4.2: DLA sample

QSO	z_{abs}	Statistical? ^a	$\log N_{\text{HI}}$ [cm^{-2}]	References
J0021-0128	1.2420	Y	20.55 ± 0.10	2
J0051+0041	0.7420	N	20.60 ± 0.10	3
J0102-0853	0.8945	N	20.45 ± 0.10	16
J0106+0105	1.3020	N	20.85 ± 0.20	1
J0122-2843	0.1856	Y	20.55 ± 0.10	4
J0126-0105	1.1930	N	20.65 ± 0.10	1
J0139-0023	0.6840	N	20.60 ± 0.15	1
J0153+0052	1.0610	N	20.35 ± 0.20	1
J0304-2212	1.0094	N	20.30 ± 0.10	5,6
J0452-1640	1.0090	N	21.00 ± 0.10	1
J0456+0400	0.8586	N	20.60 ± 0.10	7
J0741+3111	0.2220	N	20.60 ± 0.20	1
J0830+2410	0.5191	N	20.40 ± 0.20	1
J0930+2848	0.0227	N	20.75 ± 0.10	16
J0938+4128	1.3725	Y	20.45 ± 0.15	15
J0948+4323	1.2340	N	21.75 ± 0.15	16
J0953-0038	0.6390	N	20.30 ± 0.10	1
J0954+1743	0.2410	N	21.05 ± 0.20	1
J1001+5553	1.3913	N	20.30 ± 0.20	8
J1009+0713	0.1139	N	20.75 ± 0.10	9
J1009+0036	0.9730	N	20.30 ± 0.15	1
J1010+0003	1.2670	N	21.70 ± 0.10	1
J1017+5356	1.3070	N	20.70 ± 0.10	16
J1106-1821	1.6617	N	20.80 ± 0.10	10
J1107+0048	0.7410	N	21.00 ± 0.15	1
J1124-1705	0.6812	Y	20.35 ± 0.15	11
J1130-1449	0.3140	N	21.30 ± 0.15	1
J1224+0037	1.2350	N	20.75 ± 0.15	1
J1225+0035	0.7730	N	21.55 ± 0.10	1
J1232-0224	0.3950	N	20.85 ± 0.15	12

Table 4.2: — Continued

QSO	z_{abs}	Statistical? ^a	$\log N_{\text{H I}}$ [cm^{-2}]	References
J1251+4637	0.3965	N	20.60 ± 0.15	16
J1331+3030	0.6840	N	21.40 ± 0.15	13
J1420-0054	1.3470	N	20.85 ± 0.15	1
J1431+3952	0.6040	N	21.30 ± 0.15	16
J1501+0019	1.4840	N	20.90 ± 0.10	1
J1512+0128	0.0295	N	20.40 ± 0.10	16
J1527+2452	0.7345	N	20.40 ± 0.15	16
J1537+0021	1.1790	N	20.30 ± 0.10	1
J1616+4154	0.3210	N	20.65 ± 0.20	9
J1619+3342	0.0964	N	20.65 ± 0.10	9
J1624+2345	0.6556	N	20.30 ± 0.10	14
J1712+5559	1.2100	N	20.65 ± 0.15	1
J1727+5302	0.9480	N	21.25 ± 0.15	1
J1727+5302	1.0330	N	21.50 ± 0.15	1
J1733+5533	0.9990	N	20.80 ± 0.10	1
J2334+0052	0.4740	N	20.50 ± 0.15	1
J2339-0029	0.9680	N	20.60 ± 0.15	1
J2353-0028	0.6044	N	21.50 ± 0.10	1

^aDLA is part of the statistical sample

References. — (1) Rao et al. (2006); (2) Aracil et al. (2002); (3) Lacy et al. (2003); (4) Oliveira et al. (2014); (5) Lanzetta et al. (1995); (6) Pettini & Bowen (1997); (7) Steidel et al. (1995); (8) Zuo et al. (1997); (9) Meiring et al. (2011); (10) Lopez et al. (1999); (11) De la Varga et al. (2000); (12) Boissé et al. (1998); (13) Cohen et al. (1994); (14) Steidel et al. (1997); (15) Jannuzi et al. (1998); (16) This Work

4.5.1 Total sample of DLAs

In Figure 4.3 we have plotted all the absorbers with a measured column density greater than $10^{20.3} \text{ cm}^{-2}$. These absorbers are also listed in Table 4.2. Our sample contains a total of 46 DLAs with a mean redshift of $z = 0.796$. Of these 46 DLAs, 33 were selected based upon Mg II absorption, 6 were selected to cross near galaxies, 2 were 21 cm sources, and 2 were known DLAs. Only 4 were discovered ‘blindly’, and form the statistical sample of this chapter.

We can test our methodology by comparing our list of DLAs to those found in the Rao et al. (2006) publication, as the latter is a subset of this larger sample. We find that of the 37 DLAs in the Rao et al. (2006) sample covered by our spectra, our search algorithm recovered 28 of them, with a mean deviation in the column density

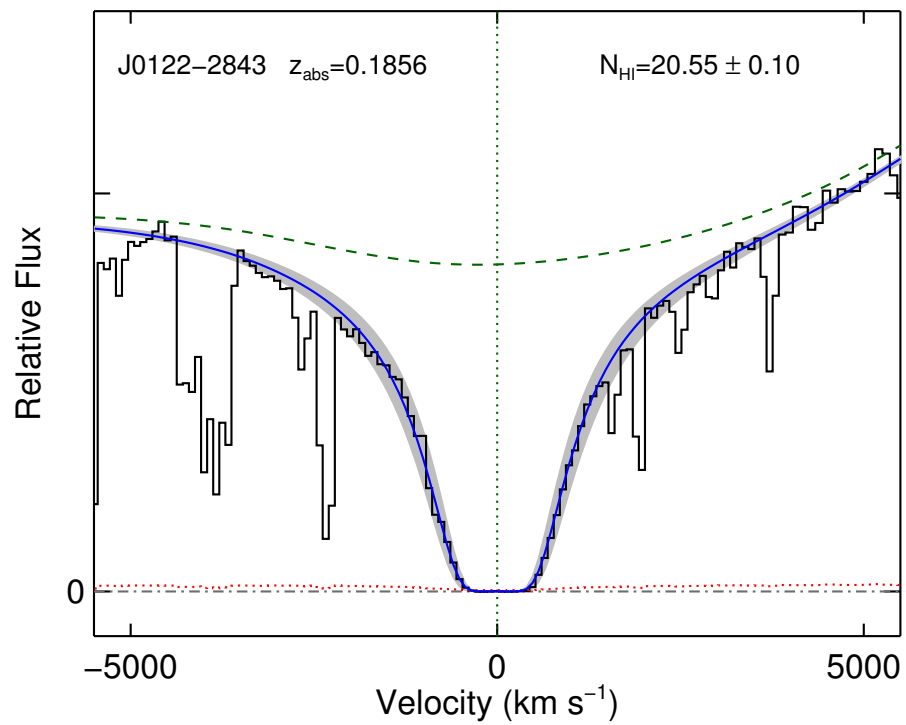


Figure 4.3: Example of the determination of the column density of the absorbers. We simultaneously fit the continuum (dashed green) and the Voigt profile of the absorber to determine the column density. The gray shaded regions mark the error on the fit (solid blue). The dotted red line marks the uncertainty of the data.

The complete set of all fits is shown in the appendix.

measurement between the data sets of 0.10 dex. Of the 9 DLAs not recovered by the search algorithm, 8 fell in a portion of the spectrum with S/N below our criterion (Section 4.4.2). The only DLA which did fall in the search algorithm's search path and was not detected, was not found because the trough of this potential DLA showed significant flux. This could be either due to Ly- α emission at the redshift of the DLA, or an issue with the zero point flux of the spectrum. We have visually checked all of the spectra and believe that this is a rare occurrence.

4.5.2 $f(N_{\text{HI}}, X)$

We can measure the column density distribution function according to the same method as described in e.g. Lanzetta et al. (1991). Here $f(N_{\text{HI}}, X) dN_{\text{HI}} dX$ is defined as the number of DLAs with column density between N_{HI} and $N_{\text{HI}} + dN$ within the absorption distance dX . Here dX is defined as:

$$dX \equiv \frac{H_0}{H(z)}(1+z)^2 dz, \quad (4.1)$$

where H_0 is Hubble's constant and $H(z)$ is the appropriate mathematical description of the chosen cosmology². The absorption distance is defined in this manner such that $f(N_{\text{HI}}, X)$ is constant for a non-evolving population of absorbers.

The statistical sample only contains 4 DLAs, and therefore we have poor constraints on the functional form of $f(N_{\text{HI}}, X)$. To increase the sample size, we include all sightlines selected to probe an intervening galaxy (i.e. those with a $f_{\text{stat}} = 2$ in Table 4.1). We note that the inclusion of these sight lines will likely bias the normalization of $f(N_{\text{HI}}, X)$ high. The resulting $f(N_{\text{HI}}, X)$ is shown in Figure 4.4a. Our results are consistent with the results from the local HI study from Zwaan et al. (2005) and those at

² $H(z) = H_0[(1+z)^2(1+z\Omega_m) - z(z+2)\Omega_\Lambda]^{-1/2}$.

higher redshift (e.g Prochaska & Wolfe, 2009; Noterdaeme et al., 2012). However, the sample size is too small to constrain $f(N_{\text{HI}}, X)$ at the highest column densities.

We have also plotted $f(N_{\text{HI}}, X)$ for the sample described in Rao et al. (2006). They note that their sample contains a large number of high column density systems, although they note this deviation is not statistically significant. We have broken up our sample into those DLAs that were found using the Mg II selection criteria defined in Rao et al. (2006) and the remaining DLAs. The cumulative distribution plotted in Figure 4.4b indeed shows that the Mg II-selected sample has a larger number high column density systems than the remaining DLAs, and the distribution from Noterdaeme et al. (2012). This corroborates the suggestion put forth by Prochaska & Wolfe (2009) that selecting sightlines by metal line absorption could bias the HI distribution toward high column density. This result is also seen in the recent work on metal-strong absorbers (Dessauges-Zavadsky et al., 2009; Kaplan et al., 2010; Berg et al., 2015).

4.5.3 $\ell_{\text{DLA}}(X)$

The line density of DLAs, $\ell_{\text{DLA}}(X)$, is defined as the zeroth moment of the neutral hydrogen column density distribution function, $f(N_{\text{HI}}, X)$:

$$\ell_{\text{DLA}}(X) = \int_{N_{\text{DLA}}}^{\infty} f(N_{\text{HI}}, X) dN, \quad (4.2)$$

where N_{DLA} is the threshold HI column density for DLAs. In practice $\ell_{\text{DLA}}(X)$ is estimated by measuring the number of DLAs in a given redshift bin and dividing by the total absorption path length in this redshift bin. A correlated quantity is the redshift number density, n_{DLA} , which divides the number of DLAs in a redshift bin by the redshift path length. Both of these quantities describe the incidence rate of DLAs along a line of sight.

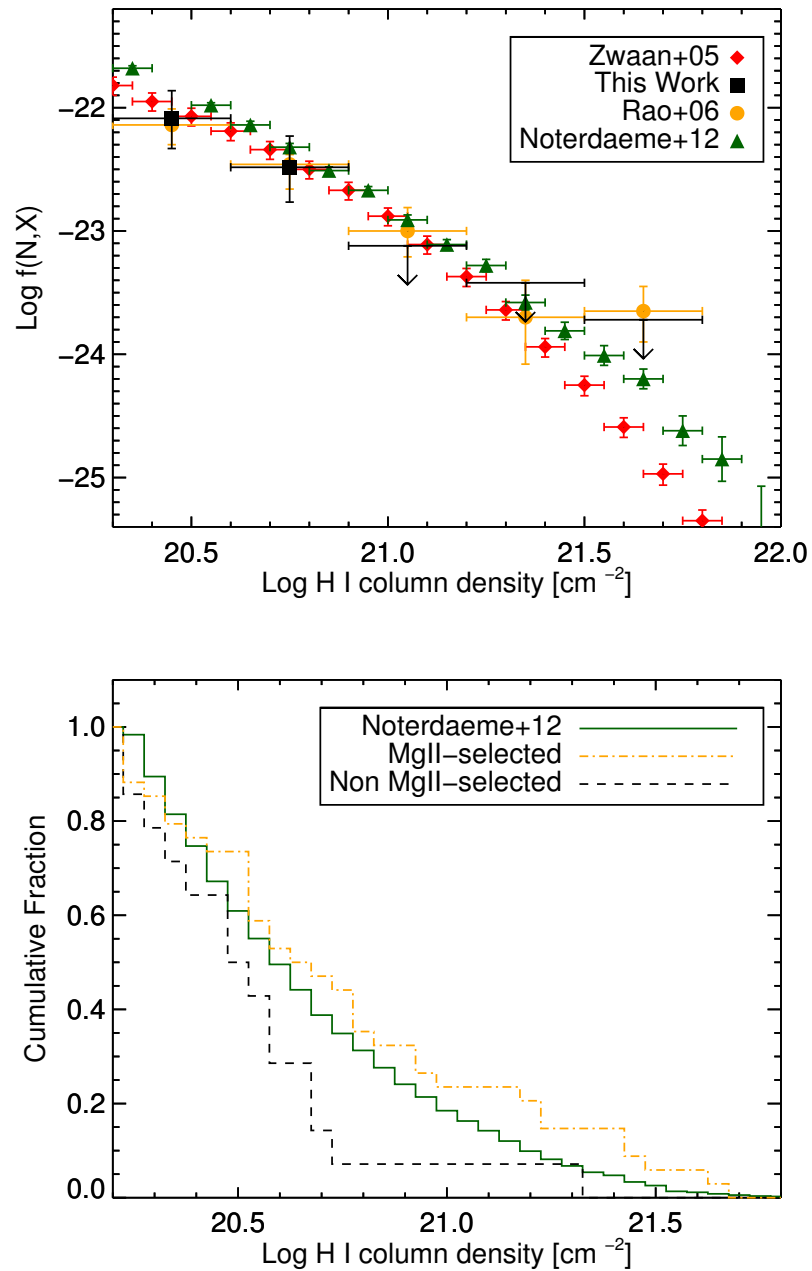


Figure 4.4: HI column density distribution function, $f(N_{\text{HI}}, X)$, at low redshift. The black data points are described in the text. The data points are consistent with both the distribution at low redshift as measured by Zwaan et al. (2005) and high redshift (Noterdaeme et al., 2012). The high value of $f(N_{\text{HI}}, X)$ found by Rao et al. (2006) at high column density could be due to a selection effect as is shown by the cumulative distribution on the right.

We have calculated $\ell_{\text{DLA}}(X)$ for the two redshift bins namely between redshifts $z = 0.01$ and $z = 0.9$ and $z = 0.9$ and $z = 1.6$. These bins were chosen to agree with the approximate bins of Rao et al. (2006). The resultant $\ell_{\text{DLA}}(X)$ for the bins was $0.014^{+0.018}_{-0.005}$ and $0.015^{+0.035}_{-0.013}$ respectively. These values and the values from other studies measuring these quantities are shown in Figure 4.5.

Figure 4.5 shows that the line density measured from this sample falls below the locally measured value from Zwaan et al. (2005) and Braun (2012), although the measurements are consistent with each other within $2\text{-}\sigma$. The resulting measurements are also lower than the measurements from Rao et al. (2006), although the systematical uncertainties for their measurements are difficult to quantify. We therefore believe that the line density of DLAs might be lower in this redshift range than previously measured. We discuss this result further in Section 4.6.

4.5.4 ρ_{HI}

The final quantity we consider is the first moment of $f(N_{\text{HI}}, X)$, which is the mass density of HI locked up in DLAs, ρ_{HI} . This quantity is defined by:

$$\rho_{\text{HI}} = \frac{m_{\text{H}}H_0}{c} \int_{N_{\text{min}}}^{N_{\text{max}}} N_{\text{HI}} f(N_{\text{HI}}, X) dN, \quad (4.3)$$

where m_{H} is the mass of the hydrogen atom. This quantity is related to the neutral gas mass density, Ω_{DLA} , by the conversion factor μ/ρ_c , where μ is the mean molecular mass of the gas and ρ_c is the critical density of the gas.

As with $f(N_{\text{HI}}, X)$, ρ_{HI} cannot be precisely determined because of the small sample size of the statistical sample. This small sample size underestimates the number of high column density ($\log N_{\text{HI}} > 21$) systems, because none are present in our survey. These systems likely contribute significantly to ρ_{HI} (Zwaan et al., 2005; O’Meara et al.,

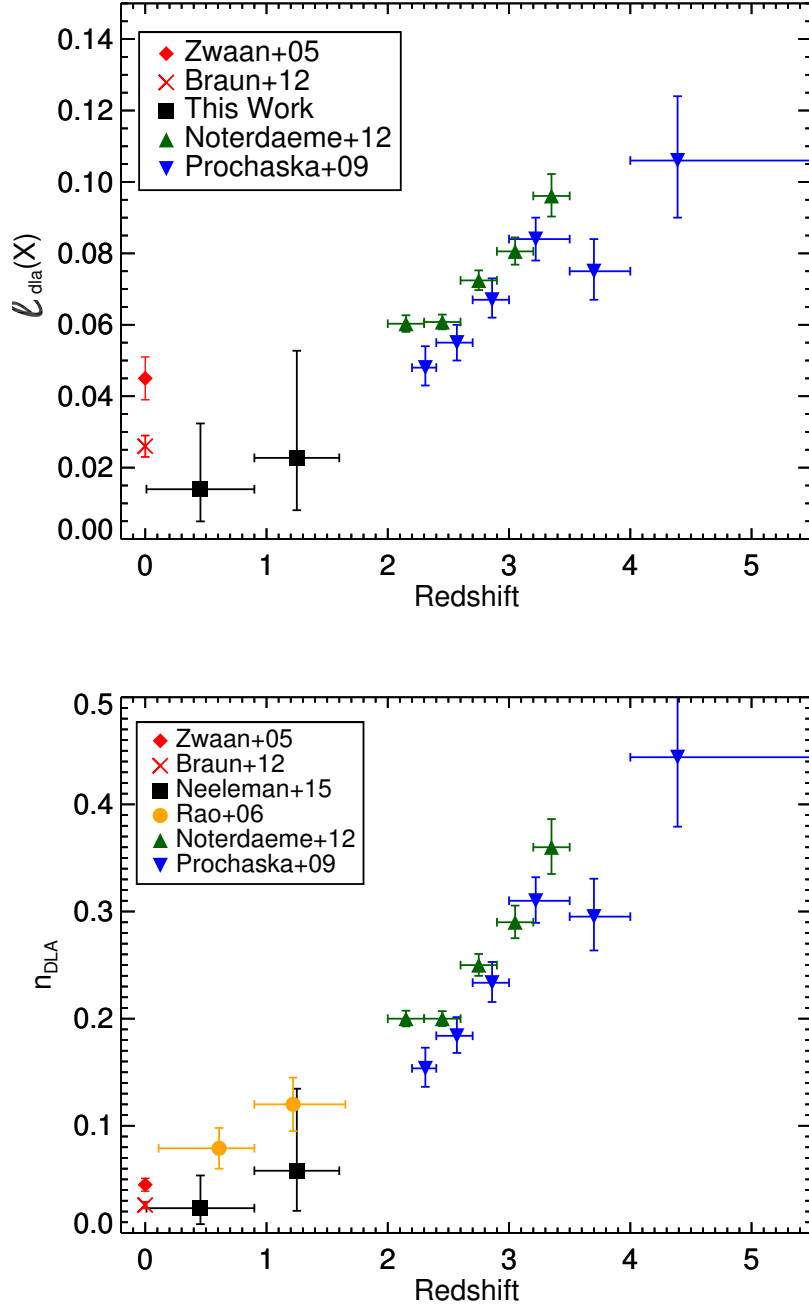


Figure 4.5: *left:* Line density of DLAs, $\ell_{\text{DLA}}(X)$ and *right:* redshift number density of DLAs, n_{DLA} . The line density of DLAs over the redshift interval $z \sim 0.01$ to $z \sim 1.6$ is likely lower than the measured line density at redshift $z \sim 2$. This lower line density is in agreement with the result from Braun (2012), suggesting a mild evolution in the line density over the past 10 Gyrs.

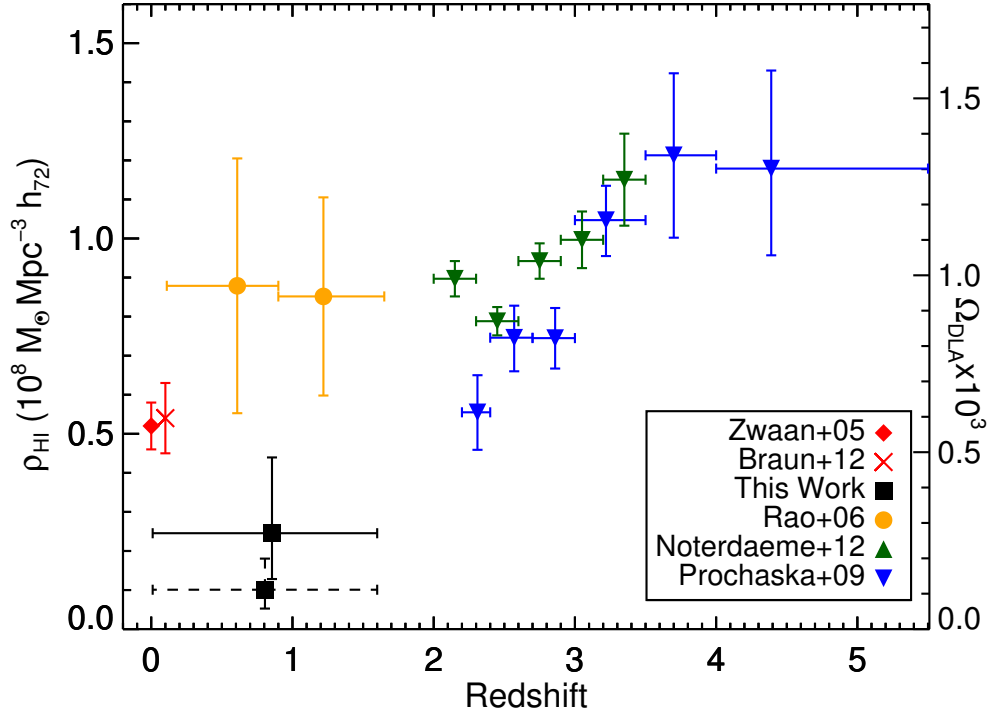


Figure 4.6: Mass density of HI in DLAs, ρ_{HI} . The dashed and adjusted solid point are explained in the text. The point suggest that ρ_{HI} slowly decreases over the past HI. One possible explanation for this is that the neutral hydrogen gets locked up in high column density components (Braun, 2012), which would explain the lower ρ_{HI} value for DLAs than from the HI emission studies at $z = 0$.

2007; Noterdaeme et al., 2012), therefore the given measurement is an underestimation of the underlying neutral gas density. To account for this, we assume that the mean column density of these low redshift systems is unchanged from the mean column density measurement at high redshift from Noterdaeme et al. (2012) (see Section 4.5.2).

This gives a value of $\rho_{\text{HI}} = 0.25^{+0.19}_{-0.12} \cdot 10^8 M_{\odot} \text{Mpc}^{-3}$ for the redshift range $z \sim 0.01$ to $z \sim 1.6$, which together with other measurements are plotted in Figure 4.6. The unadjusted value is also plotted in this figure, with dashed error bars.

4.6 Summary and Discussion

In this chapter we have used the large sample of quasars ($n = 767$) observed with the UV spectrographs on the Hubble Space Telescope to perform a search for low-redshift DLAs. Of the total 46 DLAs found in this study, only 4 are drawn from the statistical sample. The remainder were drawn from sightlines with foreknowledge of either an absorber or intervening galaxy along the line-of-sight.

This sample allows for a determination of the line density of DLAs, $\ell_{\text{DLA}}(X)$, over the redshift range between $z = 0.01$ and $z = 1.6$. We find that $\ell_{\text{DLA}}(X)$ is found to be $0.014_{-0.005}^{+0.018}$ in the redshift range $z = 0.01$ and $z = 0.9$ and $0.015_{-0.013}^{+0.035}$ in the redshift range $z = 0.9$ and $z = 1.6$. These values are smaller than previous measurements by (Rao et al., 2006), but have large uncertainties due to the small sample size.

Previous studies, e.g. Prochaska et al. (2005); Rao et al. (2006); Prochaska & Wolfe (2009); Noterdaeme et al. (2012), have claimed little evolution in the line density of DLAs in the past 10 Gyrs. However, these results together with the result from Braun (2012) indicate that the line density at low redshift might indeed be smaller than previously predicted, which would suggest a mild evolution in $\ell_{\text{DLA}}(X)$ from redshift 2 to redshift 0. This corroborates the assertion that the majority of galactic-scale dark matter halos are fully assembled by redshift 2, and that during the subsequent years HI slowly decreases due to a decrease of neutral hydrogen in these halos, either by star formation or feedback processes.

One caveat to this result are systematical errors which would bias the results low. Here we will discuss three of these biases. One potential bias to our sample is the exclusion of sightlines that were selected to be near galaxies. A random sample of quasars would contain some sightlines that pass-by intervening galaxies, by removing all these quasars from the sample, we could be biasing our result low. To estimate the

effect of this potential bias, we have included all sightlines that were specifically chosen to cross a near-by galaxy. The resultant $\ell_{\text{DLA}}(X)$ is 0.031 and 0.015 in the two redshift bins respectively. These values are well within the $1\text{-}\sigma$ statistical uncertainty of the measurement indicating that this bias is likely negligible.

A second bias could have been introduced by including sightlines above a redshift of $z \sim 0.3$. For these redshifts, metal lines (in particular Mg II) would fall within the optical part of the quasar spectrum. Selection criteria for the quasar may have included a lack of metal line systems in the optical part of the quasar spectrum. Similarly, by excluding all of the sightlines with known Mg II systems in it, we might be biasing ourselves against quasars with metal lines in it. To test our bias in our sample against Mg II systems, we have compared the line density of Mg II systems in our quasar sample with the line density in the sample of Seyffert et al. (2013). We find that the line density agrees very well, and we therefore do not believe this is biasing our result.

Finally, the third bias to consider is the selection bias against systems with large amount of dust. It has been shown extensively at high redshift that DLAs contain relatively little dust (e.g Ellison et al., 2001b; Akerman et al., 2005; Jorgenson et al., 2006), and a selection bias against dust for these studies has been refuted. However, at low redshift the bias might be amplified by the higher metallicity of these systems (Prochaska et al., 2003a; Rafelski et al., 2012, 2014). We believe dust is not a likely bias for two reasons. Firstly, the metallicity evolution of DLAs is small (~ 0.3 dex per unit redshift), therefore the results at high redshift are likely to hold at lower redshift as well. Secondly, the dust bias would bias against higher column density systems. However, high column density systems are well-represented in the sample of Rao et al. (2006).

We have also tried to estimate the HI column density distribution function, $f(N_{\text{HI}}, X)$, and the HI gas density, ρ_{HI} . However, due to the limited sample size these quantities are not well-defined. The results shows that the HI column density distribu-

tion function at low redshift is consistent with $f(N_{\text{HI}}, X)$ measured at high redshift. The potential increase in higher column density systems found by Rao et al. (2006) could be due to their selection process, but cannot be ruled out with the current dataset.

This study has compiled the largest sample of quasars observed in the UV with spectral resolution sufficient to search for low-redshift DLAs. Even with the total of 767 quasars, the sample of DLAs in these spectra is small as only 46 DLAs were found. This is in part due to the smaller than expected incidence rate of DLAs. A result that suggests that $\ell_{\text{DLA}}(X)$ might indeed be slowly decreasing over the past 10 Gyrs. This mild decrease in the line density of DLAs, could be due to consumption of neutral gas from star-formation or due to feedback processes in galaxies as they evolve over the past 10 Gyrs.

4.7 Acknowledgements

This research would not have been possible were it not for the guidance and insights of the late A.M. Wolfe during the initial phases of the project. He will be sorely missed. The work was based on observations made with the NASA/ESA Hubble Space Telescope, obtained from the data archive at the Space Telescope Science Institute. STScI is operated by the Association of Universities for Research in Astronomy, Inc. under NASA contract NAS 5-26555. Support for this work was provided by NASA through a grant from the Space Telescope Science Institute, which is operated by AURA, Inc., under NASA contract NAS 5-26555. MN and JXP further acknowledge support from NSF award AST-1109452

This is a draft of material that will be submitted as “The HI Content of the Universe over the Past 10 Gyrs”, by Marcel Neeleman, J. Xavier Prochaska, Joseph Ribaldo, Nicolas Lehner, J. Christopher Howk, Marc Rafelski, & Nissim Kanekar to

the The Astrophysical Journal. I am the primary investigator and author of this paper.

4.8 References for Chapter 4

Abazajian, K. N., Adelman-McCarthy, J. K., Agüeros, M. A., Allam, S. S., Allende Prieto, C., An, D., Anderson, K. S. J., Anderson, S. F., Annis, J., Bahcall, N. A., Bailer-Jones, C. A. L., Barentine, J. C., Bassett, B. A., Becker, A. C., Beers, T. C., Bell, E. F., Belokurov, V., Berlind, A. A., Berman, E. F., Bernardi, M., Bickerton, S. J., Bizyaev, D., Blakeslee, J. P., Blanton, M. R., Bochanski, J. J., Boroski, W. N., Brewington, H. J., Brinchmann, J., Brinkmann, J., Brunner, R. J., Budavári, T., Carey, L. N., Carliles, S., Carr, M. A., Castander, F. J., Cinabro, D., Connolly, A. J., Csabai, I., Cunha, C. E., Czarapata, P. C., Davenport, J. R. A., de Haas, E., Dilday, B., Doi, M., Eisenstein, D. J., Evans, M. L., Evans, N. W., Fan, X., Friedman, S. D., Frieman, J. A., Fukugita, M., Gänsicke, B. T., Gates, E., Gillespie, B., Gilmore, G., Gonzalez, B., Gonzalez, C. F., Grebel, E. K., Gunn, J. E., Györy, Z., Hall, P. B., Harding, P., Harris, F. H., Harvanek, M., Hawley, S. L., Hayes, J. J. E., Heckman, T. M., Hendry, J. S., Hennessy, G. S., Hindsley, R. B., Hoblitt, J., Hogan, C. J., Hogg, D. W., Holtzman, J. A., Hyde, J. B., Ichikawa, S.-i., Ichikawa, T., Im, M., Ivezić, Ž., Jester, S., Jiang, L., Johnson, J. A., Jorgensen, A. M., Jurić, M., Kent, S. M., Kessler, R., Kleinman, S. J., Knapp, G. R., Konishi, K., Kron, R. G., Krzesinski, J., Kuropatkin, N., Lampeitl, H., Lebedeva, S., Lee, M. G., Lee, Y. S., French Leger, R., Lépine, S., Li, N., Lima, M., Lin, H., Long, D. C., Loomis, C. P., Loveday, J., Lupton, R. H., Magnier, E., Malanushenko, O., Malanushenko, V., Mandelbaum, R., Margon, B., Marriner, J. P., Martínez-Delgado, D., Matsubara, T., McGehee, P. M., McKay, T. A., Meiksin, A., Morrison, H. L., Mullally, F., Munn, J. A., Murphy, T., Nash, T., Nebot, A., Neilsen, Eric H., J., Newberg, H. J., Newman, P. R., Nichol, R. C., Nicinski, T., Nieto-Santisteban, M., Nitta, A., Okamura, S., Oravetz, D. J., Ostriker, J. P., Owen, R., Padmanabhan, N., Pan, K., Park, C., Pauls, G., Peoples, John, J., Percival, W. J., Pier, J. R., Pope, A. C., Pourbaix, D., Price, P. A., Purger, N., Quinn, T., Raddick, M. J., Re Fiorentin, P., Richards, G. T., Richmond, M. W., Riess, A. G., Rix, H.-W., Rockosi, C. M., Sako, M., Schlegel, D. J., Schneider, D. P., Scholz, R.-D., Schreiber, M. R., Schwobe, A. D., Seljak, U., Sesar, B., Sheldon, E., Shimasaku, K., Sibley, V. C., Simmons, A. E., Sivarani, T., Allyn Smith, J., Smith, M. C., Smolčić, V., Snedden, S. A., Stebbins, A., Steinmetz, M., Stoughton, C., Strauss, M. A., SubbaRao, M., Suto, Y., Szalay, A. S., Szapudi, I., Szkody, P., Tanaka, M., Tegmark, M., Teodoro, L. F. A., Thakar, A. R., Tremonti, C. A., Tucker, D. L., Uomoto, A., Vanden Berk, D. E., Vandenberg, J., Vidrih, S., Vogeley, M. S., Voges, W., Vogt, N. P., Wadadekar, Y., Watters, S., Weinberg, D. H., West, A. A., White, S. D. M., Wilhite, B. C., Wonders, A. C., Yanny, B., Yocum, D. R., York, D. G., Zehavi, I., Zibetti, S., & Zucker, D. B. 2009, *ApJS*, 182, 534

- Akerman, C., Ellison, S. L., Pettini, M., & Steidel, C. C. 2005, *A&A*, 440, 499
- Aracil, B., Petitjean, P., Smette, A., Surdej, J., Mücket, J., & Cristiani, S. 2002, *A&A*, 391, 1
- Bechtold, J., Dobrzycki, A., Wilden, B., Morita, M., Scott, J., Dobrzycki, D., Tran, K.-V., & Aldcroft, T. L. 2002, *ApJS*, 140, 143
- Berg, T. A., Neeleman, M., Prochaska, J. X., Ellison, S. L., & Wolfe, A. M. 2015, *PSAP*, 127, 167
- Boissé, P., Le Brun, V., Bergeron, J., & Deharveng, J.-M. 1998, *A&A*, 333, 841
- Braun, R. 2012, *ApJ*, 749, 87
- Catinella, B., Haynes, M. P., Giovanelli, R., Gardner, J. P., & Connolly, A. J. 2008, *ApJ*, 685, L13
- Cohen, R. D., Barlow, T., Beaver, E., Junkkarinen, V. T., Lyons, R., & Smith, H. E. 1994, *ApJ*, 421, 453
- De la Varga, A., Reimers, D., Tytler, D., Barlow, T., & Burles, S. 2000, *A&A*, 363, 69
- Dessauges-Zavadsky, M., Ellison, S. L., & Murphy, M. 2009, *MNRAS*, 396, 61
- Ellison, S. L., Yan, L., Hook, I., Pettini, M., Wall, J., & Shaver, P. 2001b, *A&A*, 379, 393
- Jannuzi, B. T., Bahcall, J. N., Bergeron, J., Boksenberg, A., Hartig, G. F., Kirhakos, S., Sargent, W. L., Savage, B. D., Schneider, D. P., Turnshek, D. A., Weymann, R. J., & Wolfe, A. M. 1998, *ApJS*, 118, 1
- Jorgenson, R. A., Wolfe, A. M., Prochaska, J. X., Lu, L., Howk, J. C., Cooke, J., Gawiser, E., & Gelino, D. 2006, *ApJ*, 646, 730
- Kaplan, K. F., Prochaska, J. X., Herbert-Fort, S., Ellison, S. L., & Dessauges-Zavadsky, M. 2010, *MNRAS*, 122, 619
- Lacy, M., Becker, R., Storrie-Lombardi, L., Gregg, M., Urrutia, T., & White, R. 2003, *AJ*, 126, 2230
- Lanzetta, K. M., Wolfe, A. M., & Turnshek, D. A. 1995, *ApJ*, 440, 435
- Lanzetta, K. M., Wolfe, A. M., Turnshek, D. A., Lu, L., McMahon, R. G., & Hazard, C. 1991, *ApJ*, 77, 1
- Lopez, S., Reimers, D., Rauch, M., Sargent, W. L., & Smette, A. 1999, *ApJ*, 513, 598

- Meiring, J., Tripp, T., Prochaska, J. X., Tumlinson, J., Werk, J., Jenkins, E., Thom, C., O'Meara, J., & Sembach, K. 2011, *ApJ*, 732, 35
- Noterdaeme, P., Petitjean, P., Carithers, W., Pâris, I., Font-Ribera, A., Bailey, S., Auborg, E., Bizyaev, D., Ebelke, G., & Finley, H. 2012, *A&A*, 547, L1
- Oliveira, C., Sembach, K., Tumlinson, J., O'Meara, J., & Thom, C. 2014, *ApJ*, 783, 22
- O'Meara, J., Prochaska, J. X., Burles, S., Prochter, G., Bernstein, R., & Burgess, K. 2007, *ApJ*, 656, 666
- Pettini, M. & Bowen, D. V. 1997, *A&A*, 327, 22
- Prochaska, J. X., Gawiser, E., Wolfe, A. M., Castro, S., & Djorgovski, S. 2003a, *ApJ*, 595, L9
- Prochaska, J. X., Herbert-Fort, S., & Wolfe, A. M. 2005, *ApJ*, 635, 123
- Prochaska, J. X. & Wolfe, A. M. 2009, *ApJ*, 696, 1543
- Rafelski, M., Neeleman, M., Fumagalli, M., Wolfe, A. M., & Prochaska, J. X. 2014, *ApJ*, 782, L29
- Rafelski, M., Wolfe, A. M., Prochaska, J. X., Neeleman, M., & Mendez, A. 2012, *ApJ*, 755, 89
- Rao, S. M., Turnshek, D. A., & Nestor, D. B. 2006, *ApJ*, 636, 610
- Ribaudo, J., Lehner, N., & Howk, J. C. 2011, *ApJ*, 736, 42
- Seyffert, E. N., Cooksey, K. L., Simcoe, R. A., O'Meara, J., Kao, M. M., & Prochaska, J. X. 2013, *ApJ*, 779, 161
- Steidel, C. C., Bowen, D. V., Blades, J. C., & Dickinson, M. 1995, *ApJ*, 440, L45
- Steidel, C. C., Dickinson, M., Meyer, D. M., Adelberger, K. L., & Sembach, K. 1997, *ApJ*, 480, 568
- Wolfe, A. M., Gawiser, E., & Prochaska, J. X. 2005, *ARA&A*, 43, 861
- Wolfe, A. M., Turnshek, D. A., Smith, H. E., & Cohen, R. D. 1986, *ApJS*, 61, 249
- Zuo, L., Beaver, E., Burbidge, E., Cohen, R. D., Junkkarinen, V. T., & Lyons, R. 1997, *ApJ*, 477, 568
- Zwaan, M., Meyer, M., Staveley-Smith, L., & Webster, R. 2005, *MNRAS*, 359, L30

Chapter 5

Conclusions and Future Work

The work presented in this thesis increases our understanding of the critical role atomic gas plays during the formation and evolution of galaxies. By studying the gas in absorption, a wealth of information is obtained that allows for a detailed description of the gas kinematics, chemical composition and physical characteristics of the gas.

The work detailed in chapter two provides the first ever multi-parameter description of atomic gas in absorption. This planar equation, which links together redshift, metallicity, and velocity width, provides a more stringent constraint than two previously known correlations between the parameters. The existence of this planar equation indicates that the correlation between velocity width and metallicity, which is related to the mass-metallicity relationship in galaxies, is evolving with redshift. Remarkably, the mass-metallicity relation of emission-selected galaxies evolves concomitantly with the found relationship of atomic gas. This reaffirms the intimate link between the galaxies and their ISM. Moreover, it indicates that galaxies are efficient in enriching their ISM.

The third chapter describes a novel method in measuring the physical conditions of atomic gas. By measuring the fine-structure lines of Si^+ and C^+ in the absorption spectrum of high redshift atomic gas, we are able to determine the temperature, neutral

hydrogen density, and electron density of this gas. We use a Monte Carlo Markov Chain method to determine the posterior probability distribution function of each of the parameters. We find that the conditions in the majority of atomic gas is consistent with the theoretical models and observational measurements of our local ISM. The few systems with higher pressures could pinpoint galaxies with higher turbulence due to a higher star formation rates. This chapter describes a new working method to determine the physical properties of the bulk of the atomic gas at high redshift. This is in contrast with some other methods, such as the C I, which can only detect the coldest components.

Finally in the fourth chapter, we measure the distribution of neutral hydrogen in our Universe in the past 10 billion years. Using ground-based telescopes we are able to make accurate predictions of the neutral hydrogen content above a redshift of about 1.6, but our atmosphere prevents this measurement below this redshift. In this chapter, we use the complete archive of Hubble Space Telescope observations of quasars to determine the distribution of neutral hydrogen at $z < 1.6$. We find measurements of the incidence rate and cosmic hydrogen density that are lower than previous estimates at this redshift. The measurements are consistent, however, with the locally measured value using 21 cm emission, and the value at redshifts of about 2. The research in this chapter constitutes the largest conventional study of the atomic hydrogen density at redshifts below 1.6, filling a gap in our knowledge of this important quantity at these redshifts.

Study of atomic gas at high redshift does not stop here. There are many ways we can increase our knowledge of atomic gas at high redshift with current and near-future telescopes. In the next few paragraphs I will highlight a few interesting avenues of study that can be taken. These studies rely on the largest and most sophisticated telescopes that have been and will be built in the coming decades.

The first avenue open for research is to increase our understanding of the connec-

tion between absorption-selected galaxies and the galaxies we see in emission. Observational research, including the work done in this thesis, has strongly indicated that the atomic gas we see in absorption is intimately linked to the galaxies we see in emission. However, the most pressing question that has plagued the field of quasar absorption line study since its inception is understanding which galaxies are exactly linked to these absorbers. Is the gas we see in absorption linked primarily with small dwarf galaxies and protogalactic clumps, or are we seeing through the disks of large Milky Way-type galaxies?

To answer this question many have tried to image the galaxies using very deep imaging (Wolfe & Chen, 2006; Krogager et al., 2012; Rafelski et al., 2011; Fumagalli et al., 2015, e.g.). However, to date only a select sample of absorption-selected galaxies have been found. This at least qualitatively would indicate that these galaxies are small and therefore hard to detect, a result that is further corroborated by numerical models of Λ CDM models, which predict absorbers to be dominated by small protogalactic clumps (Haehnelt et al., 1998; Pontzen et al., 2008; Bird et al., 2014). However, these simulations have a hard time explaining the wide range of velocity widths of absorbers (see Chapter 2 of this thesis, and Bird et al. (2015)), and are at odds with clustering measurements (Font-Ribera et al., 2012), both suggesting more massive galaxies.

One way we can try to understand this problem is by imaging the galaxies in 21 cm. Current facilities, such as the Arecibo telescope, can probe only to redshifts of about 0.25. Previously, only a few absorbers were known at these redshifts due to the difficulty in observing at ultraviolet wavelengths, and in total just one absorber has detected 21 cm emission associated with the absorber (Bowen et al., 2001; Kanekar et al., 2001). The sample discussed in Chapter 4 provides a dramatic increase in possible sources for follow-up observation for 21 cm emission, which will allow for a more statistical description of the absorber-galaxy connection. Preliminary follow-up observations of this

sample has already tripled the sample of 21 cm emission detections from absorption-selected galaxies, providing a direct gauge of the ability to observe these absorbers at higher redshift with future facilities such as the Square Kilometer Array.

A second approach to increase our understanding of the connection between atomic gas and their associated galaxies comes from detecting the coolants of the atomic gas, i.e. the fine-structure lines. This method has been described in Chapter 1. Recent observations have shown the promise of increasing our knowledge of atomic gas at high redshift (Swinbank et al., 2012; Riechers et al., 2013). Using the Atacama Large Millimeter/submillimeter Array, these fine structure lines have been detected from galaxies as far away as redshift 6 (Capak et al., 2015) providing a way to probe a large range of redshifts with the same technique.

Currently, initial programs (ALMA Cycle 2) are on the way to observe these fine-structure lines for absorption-selected galaxies. Measurements of the strength of these lines will give estimates of the star formation rates of the galaxy (De Looze et al., 2011; Ota et al., 2014). By mapping the velocity structure of the fine-structure line, we will be able to determine the spatial extent of the ISM and determine the dynamic masses of the absorption-selected galaxy. This will finally determine if atomic gas seen in absorption is associated with small dwarf-like galaxies or more massive Milky Way-type galaxies.

The above research would be excellently complimented by the suite of near-infrared instruments that are expected to come online in the coming years, both in space (i.e. the James Webb Space Telescope) and on earth (through thirty meter class telescopes). Spectrographic observations in the near-infrared will allow for detection of higher ionization fine-structure lines from species such as O II and O III. These species occur mainly in ionized gas and provide us therefore with information on the extent and physical conditions of the ionized ISM. The combined picture of atomic and ionized gas

will provide a complete picture of the ISM at high redshift, allowing us to get one step closer in understanding the important role of the ISM in galaxy formation and evolution.

5.1 References for Chapter 5

- Bird, S., Haehnelt, M., Neeleman, M., Genel, S., Vogelsberger, M., & Hernquist, L. 2015, *MNRAS*, 447, 1834
- Bird, S., Vogelsberger, M., Haehnelt, M., Sijacki, D., Genel, S., Torrey, P., Springel, V., & Hernquist, L. 2014, *MNRAS*, 445, 2313
- Bowen, D. V., Huchmeier, W., Brinks, E., Tripp, T., & Jenkins, E. 2001, *A&A*, 372, 820
- Capak, P., Carilli, C., Jones, G., Casey, C., Riechers, D., Sheth, K., Carollo, C., Ilbert, O., Karim, A., LeFevre, O., Lilly, S., Scoville, N., Smolcic, V., & Yan, L. 2015, arxiv:1503.07596
- De Looze, I., Baes, M., Bendo, G., Cortese, L., & Fritz, J. 2011, *MNRAS*, 416, 2712
- Font-Ribera, A., Miralda-Escudé, J., Arnau, E., Carithers, W., Lee, K.-G., Noterdaeme, P., Pâris, I., Petitjean, P., Rich, J., Rollinde, E., Ross, N., Schneider, D. P., White, M., & York, D. G. 2012, *JCAP*, 11, 59, arXiv:1209.4596v1
- Fumagalli, M., O'Meara, J., Prochaska, J. X., Rafelski, M., & Kanekar, N. 2015, *MNRAS*, 446, 3178
- Haehnelt, M. G., Steinmetz, M., & Rauch, M. 1998, *ApJ*, 495, 647
- Kanekar, N., Chengalur, J., Subrahmanyam, R., & Petitjean, P. 2001, *A&A*, 367, 46
- Krogager, J.-K., Fynbo, J., Møller, P., Ledoux, C., Noterdaeme, P., Christensen, L., Milvang-Jensen, B., & Sparre, M. 2012, *MNRAS*, 424, 1
- Ota, K., Walter, F., Ohta, K., Hatsukade, B., Carilli, C., Da Cunha, E., González-López, J., Decarli, R., Hodge, J., Nagai, H., Egami, E., Jiang, L., Iye, M., Kahikawa, N., Riechers, D., Bertoldi, F., Cox, P., Neri, R., & Weiss, A. 2014, *ApJ*, 792, 34
- Pontzen, A., Governato, F., Pettini, M., Booth, C., Stinson, G., Wadsley, J., Brooks, A., Quinn, T., & Haehnelt, M. 2008, *MNRAS*, 390, 1349
- Rafelski, M., Wolfe, A. M., & Chen, H.-W. 2011, *ApJ*, 736, 48

- Riechers, D., Bradford, C., Clements, D., Dowell, C., Pérez-Fournon, I., Ivison, R., Bridge, C., Conley, A., Fu, H., Vieira, J., Wardlow, J., Calanog, J., Cooray, A., Hurley, O., Neri, R., Kamenetzky, J., Aguirre, J., Altieri, B., Arumugam, V., Benford, D., Béthermin, M., Bock, J., Burgarella, D., Cabrera-Lavers, A., Chapman, S., Cox, P., Dunlop, J., Earle, L., Farrah, D., Ferrero, P., Franceschini, A., Gavazzi, R., Glenn, J., Gonzalez-Solares, E., Gurwell, M., Halpern, M., Hatziminaoglou, E., Hyde, A., Ibar, E., Kovács, A., Krips, M., Lupu, R., Maloney, P., Martinez-Navajas, P., Matsuhara, H., Murphy, E., Naylor, B., Nguyen, H., Oliver, S., Omont, A., Page, M., Petitpas, G., Rangwala, N., Roseboom, I., Scott, D., Smith, A., Staguhn, J., Streblyanska, A., Thomson, A., Valchanov, I., Viero, M., Wang, L., Zemcov, M., & Zmuidzinas, J. 2013, *Nature*, 496, 329
- Swinbank, A., Karim, A., Smail, I., Hodge, J., Walter, F., Bertoldi, F., Biggs, F., De Breuck, C., Chapman, S., Coppin, K., Cox, P., Danielson, A., Dannerbauer, H., Ivison, R., Greve, T., Knudsen, K., Menten, K., Simpson, J., Schinnerer, E., Wardlow, J., Weiss, A., & Van der Werf, P. 2012, *MNRAS*, 427, 1066
- Wolfe, A. M. & Chen, H.-W. 2006, *ApJ*, 652, 981

Appendix A

Full Tables

Throughout the text, I included shorter versions of the tables. I include the full versions of the tables here in the appendix.

Table A.1: Journal of Observations for HIRES DLA Sample

QSO	RA (J2000.0)	DEC (J2000.0)	z_{em}^{a}	Date Observed (UT)	Exposure Time (s)	$\Delta v_{\text{res}}^{\text{b}}$ (km s^{-1})	S/N ^c
Q2359−02	00 01 50.0	−01 59 40.3	2.800	1997 Sep 29	14400	8	17
				1997 Sep 30	10800	8	
				1997 Oct 01	12516	8	
Q0000−2619	00 03 22.9	−26 03 16.8	4.110	1994 Sep 30	10800	8	15
				1994 Oct 01	3600	8	
BR0019−15	00 22 08.0	−15 05 38.8	4.530	1996 Sep 20	13500	8	18
				1996 Sep 21	12600	8	
				1996 Sep 22	14400	8	
J0040−0915	00 40 54.7	−09 19 26.9	4.976	2011 Jan 16	7200	6	7
				2011 Jan 24	3600	6	
PH957	01 03 11.4	+13 16 16.7	2.690	1994 Oct 01	11700	8	28
Q0149+33	01 52 34.5	+33 50 33.2	2.430	1997 Sep 29	8100	8	25
				1997 Sep 30	9500	8	
				1997 Oct 01	6300	8	
Q0201+11	02 03 46.5	+11 34 40.4	3.610	1997 Oct 29	22000	6	14
				1997 Oct 30	18500	6	
Q0201+36	02 04 55.6	+36 49 18.0	2.912	1994 Sep 30	11950	8	32
				1994 Oct 01	13030	8	
PSS0209+05	02 09 44.5	+05 17 17.3	4.170	2007 Sep 18	11100	6	27
Q0216+08	02 18 57.3	+08 17 27.8	2.992	1994 Oct 11	6000	6	16
				1994 Dec 27	6000	6	
J0255+00	02 55 18.6	+00 48 47.9	3.970	1999 Nov 08	9400	6	15
				2000 Nov 30	10800	6	
Q0336−01	03 39 00.9	−01 33 18.0	3.200	2003 Nov 01	10800	6	15
				2005 Oct 26	3600	8	
Q0347−38	03 49 43.5	−38 10 04.9	3.230	1996 Sep 20	4500	8	33
				1996 Sep 21	1900	8	
				1996 Sep 22	8100	8	
Q0450−13	04 53 13.8	−13 05 54.4	2.300	2004 Oct 03	4500	6	10
Q0458−02	05 01 12.8	−01 59 14.2	2.290	1995 Oct 31	16200	8	15
				1995 Nov 01	12600	8	

Table A.1: — Continued

QSO	RA (J2000.0)	DEC (J2000.0)	z_{em}^{a}	Date Observed (UT)	Exposure Time (s)	$\Delta v_{\text{res}}^{\text{b}}$ (km s ⁻¹)	S/N ^c
Q0528–2505	05 30 08.0	–25 03 29.9	2.779	1994 Dec 27	6000	6	18
				1995 Feb 23	6000	6	
Q0551–366	05 52 46.2	–36 37 28.5	2.318	1997 Jan 07	7200	8	10
HS0741+4741	07 45 21.8	+47 34 35.6	3.220	2000 Nov 30	5500	6	30
J0747+4434	07 47 49.7	+44 34 17.0	4.432	2011 Jan 16	3601	6	9
				2011 Jan 24	10800	6	
J0812+3208	08 12 40.7	+32 08 08.6	2.710	2002 Mar 03	10800	6	30
				2002 Nov 02	9900	6	
				2003 Mar 11	9900	6	
				2003 Mar 12	9900	6	
J0814+5029	08 14 35.2	+50 29 46.5	3.880	2008 Mar 25	10800	6	25
J0817+1351	08 17 40.5	+13 51 34.6	4.389	2011 Jan 16	7200	6	6
				2011 Jan 24	3600	6	
J0825+3544	08 25 40.1	+35 44 14.3	3.850	2008 Mar 25	10800	5	20
J0826+3148	08 26 19.7	+31 48 48.0	3.094	2006 Dec 26	7900	6	20
Q0836+11	08 39 33.0	+11 12 03.8	2.700	1998 Feb 26	10800	8	17
				2000 Mar 11	10100	8	
Q0841+12	08 44 24.3	+12 45 48.7	2.500	1997 Nov 02	7200	8	21
				1998 Feb 25	7200	8	
J0900+4215	09 00 33.5	+42 15 46.0	3.290	2005 Apr 14	4700	6	40
Q0913+072	09 16 14.0	+07 02 24.6	2.785	1999 Apr 15	3600	8	18
J0929+2825	09 29 14.5	+28 25 29.1	3.395	2007 Apr 27	3600	5	35
				2007 Apr 28	3600	5	
Q0930+28	09 33 37.8	+28 45 35.3	3.420	2001 Mar 01	7200	8	25
BR0951–04	09 53 55.7	–05 04 18.5	4.370	1997 Apr 05	14400	8	13
				1997 Apr 06	16200	8	
BRI0952–01	09 55 00.1	–01 30 06.9	4.430	1999 Mar 19	14400	8	15
				1999 Mar 20	14400	8	
PSS0957+33	09 57 44.5	+33 08 23.5	4.250	2000 Nov 30	7200	6	15
J1014+4300	10 14 47.1	+43 00 30.1	3.100	2005 Apr 13	5100	8	38
				2007 Apr 27	3600	5	

Table A.1: — Continued

QSO	RA (J2000.0)	DEC (J2000.0)	z_{em}^{a}	Date Observed (UT)	Exposure Time (s)	$\Delta v_{\text{res}}^{\text{b}}$ (km s ⁻¹)	S/N ^c
				2007 Apr 28	3600	5	
BR1013+0035	10 15 49.0	+00 20 20.0	4.405	2000 Mar 11	10800	8	12
				2002 Mar 02	5400	8	
Q1021+30	10 21 56.8	+30 01 31.3	3.120	2002 Mar 02	7200	6	15
J1035+5440	10 35 14.2	+54 40 40.1	2.990	2008 Mar 25	10800	6	18
J1051+3107	10 51 22.5	+31 07 49.3	4.253	2011 Jan 24	3600	6	15
				2011 Apr 23	5700	6	
J1051+3545	10 51 23.0	+35 45 34.2	4.900	2010 Apr 04	7800	6	12
Q1055+46	10 57 56.2	+45 55 44.3	4.130	1995 Apr 07	9600	6	20
				1996 May 05	5437	6	
J1100+1122	11 00 45.2	+11 22 39.1	4.707	2011 Jan 16	17400	6	8
Q1104-18	11 06 33.0	-18 21 09.8	2.310	1997 Feb 04	11500	6	40
BR11108-07	11 11 13.6	-08 04 02.5	3.920	1998 Feb 26	14400	8	20
				1999 Mar 19	7200	8	
				1999 Mar 20	5400	8	
J1131+6044	11 31 30.4	+60 44 20.7	2.921	2006 Dec 25	7200	6	17
HS1132+2243	11 35 08.0	+22 27 06.8	2.885	2006 Dec 25	6900	6	15
J1155+0530	11 55 38.6	+05 30 50.6	3.480	2005 Apr 14	7200	6	15
Q1157+014	11 59 44.8	+01 12 07.0	1.990	2002 Mar 02	10800	6	30
				2002 Mar 03	14200	6	
J1200+4618	12 00 36.7	+46 18 50.2	4.730	2011 Jan 24	7200	6	5
J1200+4015	12 00 39.8	+40 15 56.2	3.360	2008 Mar 25	10800	5	20
J1201+2117	12 01 10.3	+21 17 58.5	4.579	2011 Jan 24	5600	6	12
				2011 Jan 25	3300	6	
J1202+3235	12 02 07.7	+32 35 38.8	5.290	2010 Apr 04	14400	6	18
BR1202-07	12 05 23.7	-07 25 47.8	4.690	1995 Feb 23	18000	6	12
				1995 Apr 06	15000	6	
Q1209+0919	12 11 34.9	+09 02 22.8	3.297	2003 Mar 11	5400	6	15
				2003 Mar 12	5400	6	
Q1210+17	12 13 03.1	+17 14 23.0	2.540	2000 Mar 12	7200	8	20
Q1215+33	12 17 32.5	+33 05 38.4	2.610	1994 Apr 01	14040	8	20

Table A.1: — Continued

QSO	RA (J2000.0)	DEC (J2000.0)	z_{em}^{a}	Date Observed (UT)	Exposure Time (s)	$\Delta v_{\text{res}}^{\text{b}}$ (km s ⁻¹)	S/N ^c
Q1223+17	12 26 07.2	+17 36 49.0	2.920	1998 Feb 25	10100	8	30
				1998 Feb 26	9000	8	
J1240+1455	12 40 20.9	+14 55 35.6	3.085	2007 Apr 28	5473	6	7
J1304+1202	13 04 26.2	+12 02 45.5	2.977	2008 Mar 25	10800	5	18
Q1331+17	13 33 35.8	+16 49 04.0	2.080	1994 Apr 01	36000	6	80
Q1337+11	13 40 02.4	+11 06 29.6	2.917	2000 Mar 12	8100	8	12
BR11346-03	13 49 16.8	-03 37 15.1	3.990	1997 Apr 05	15900	8	29
				1997 Apr 06	14400	8	
J1353+5328	13 53 17.1	+53 28 25.4	2.920	2008 Mar 25	8400	6	15
PKS1354-17	13 57 05.9	-17 44 05.8	3.150	2007 Apr 28	3600	6	9
J1410+5111	14 10 30.6	+51 11 13.5	3.206	2007 Apr 27	3600	6	10
Q1425+6039	14 26 56.4	+60 25 42.7	3.170	1995 May 18	16800	6	80
				1995 May 19	20400	6	
J1435+5359	14 35 00.5	+53 59 53.7	2.640	2005 May 02	7200	6	25
J1438+4314	14 38 35.9	+43 14 59.2	4.610	2010 Apr 04	10800	6	33
PSS1443+27	14 43 31.2	+27 24 37.2	4.410	1999 Mar 19	10800	8	20
				1999 Mar 20	14400	8	
				2000 Mar 11	11000	8	
PSS1506+522	15 06 54.6	+52 20 04.8	4.180	2007 Apr 27	3600	6	14
				2007 Apr 28	3600	6	
J1541+3153	15 41 53.5	+31 53 29.4	2.550	2008 Mar 25	4800	5	20
J1607+1604	16 07 34.2	+16 04 17.4	4.798	2011 Apr 23	12600	6	10
J1654+2227	16 54 36.9	+22 27 33.7	4.678	2011 Apr 23	7300	6	9
Q1759+75	17 57 46.4	+75 39 16.0	3.050	1996 Sep 21	5044	6	33
				1996 Sep 22	5400	6	
J2036-0553	20 36 42.3	-05 53 00.2	2.580	2004 Oct 06	10800	6	15
Q2206-19	22 08 52.1	-19 43 57.6	2.560	1994 Sep 30	7200	8	40
				1994 Oct 01	7900	8	
Q2223+20	22 25 37.0	+20 40 17.8	3.561	1999 Sep 10	5400	8	8
Q2230+02	22 32 35.3	+02 47 55.1	2.150	1997 Sep 29	7200	8	26
				1997 Sep 30	10800	8	

Table A.1: — Continued

QSO	RA (J2000.0)	DEC (J2000.0)	z_{em}^{a}	Date Observed (UT)	Exposure Time (s)	$\Delta v_{\text{res}}^{\text{b}}$ (km s^{-1})	S/N ^c
Q2231–002	22 34 08.8	+00 00 02.0	3.018	1997 Oct 01	9600	8	30
				1995 Nov 01	9900	8	
				1997 Sep 30	10800	8	
BR2237–0607	22 39 53.4	–05 52 20.8	4.559	1994 Oct 10	12000	6	14
				1994 Oct 11	18000	6	
J2315+1456	23 15 43.6	+14 56 06.4	3.390	2006 Jun 04	4800	8	15
J2340–0053	23 40 23.7	–00 53 27.0	2.090	2003 Nov 01	3600	8	30
				2006 Aug 18	7200	6	
				2006 Aug 19	7800	6	
J2343+1410	23 43 52.6	+14 10 14.6	2.910	2006 Dec 25	7200	6	5
Q2343+125	23 46 28.2	+12 48 59.9	2.763	1995 Oct 18	9000	6	30
				1996 Nov 05	4889	6	
				1996 Nov 06	5500	6	
				1996 Dec 12	6000	6	
Q2344+12	23 46 45.8	+12 45 30.0	2.790	1996 Oct 17	12000	6	23
				1996 Oct 18	3000	6	
Q2348–01	23 50 57.8	–00 52 10.1	3.014	1999 Nov 08	10800	8	15
				2000 Nov 30	5400	8	
Q2348–14	23 51 29.9	–14 27 47.6	2.940	1996 Sep 20	4500	8	33
				1996 Sep 21	5400	8	
				1996 Sep 22	3600	8	

Note. — See notes from Table 2.1

Table A.2: HIRES DLA sample

QSO	z_{abs}	$\log N_{\text{HI}}$ (cm^{-2})	Metallicity	$\log \ell_c$ ($\text{ergs s}^{-1} \text{H}^{-1}$)	W_{1526} (\AA)	Δv_{90}^a (km s^{-1})	Transition ^b	Selection Criterion	References
Q1104-18	1.6613	20.80 ± 0.10	-0.99 ± 0.10	-26.87 ± 0.11	—	50	Si II λ 1808	H I - selected	6
Q1331+17	1.7763	21.14 ± 0.08	-1.34 ± 0.08	-26.60 ± 0.09	0.499 ± 0.001	72	Si II λ 1808	H I - selected	7, 13, 19, 28
Q0841+12	1.8640	21.00 ± 0.10	-1.46 ± 0.10	—	—	30	Si II λ 1808	Serendipitous	22
Q2230+02	1.8643	20.85 ± 0.08	-0.71 ± 0.09	—	1.500 ± 0.018	172	Si II λ 1808	H I - selected	7, 13
Q1210+17	1.8917	20.60 ± 0.10	-0.79 ± 0.10	—	0.419 ± 0.003	38	Si II λ 1808	H I - selected	13, 21
Q2206-19	1.9200	20.65 ± 0.07	-0.38 ± 0.07	> -26.52	0.992 ± 0.002	128	Si II λ 1808	H I - selected	4, 7, 13, 30
Q1157+014	1.9440	21.70 ± 0.10	-1.25 ± 0.10	> -26.51	0.729 ± 0.003	84	NI II λ 1741	H I - selected	9, 27
Q0551-366	1.9622	20.50 ± 0.08	-0.27 ± 0.14	—	2.111 ± 0.020	239	Si II λ 1808	H I - selected	15
Q1215+33	1.9991	20.95 ± 0.06	-1.43 ± 0.07	< -27.28	0.349 ± 0.004	36	Si II λ 1808	H I - selected	7, 13
Q0458-02	2.0395	21.65 ± 0.09	-1.11 ± 0.09	> -26.28	0.665 ± 0.008	84	Cr II λ 2056	H I - selected	7, 13
J2340-0053	2.0545	20.35 ± 0.15	-0.55 ± 0.15	-26.14 ± 0.15	0.762 ± 0.002	138	Si II λ 1808	H I - selected	20, 26, 28
Q2231-002	2.0661	20.56 ± 0.10	-0.61 ± 0.20	-26.37 ± 0.10	0.786 ± 0.004	122	Si II λ 1808	H I - selected	2, 7, 13, 19, 28
Q0450-13	2.0666	20.53 ± 0.08	-1.39 ± 0.08	< -27.42	0.556 ± 0.005	123	Fe II λ 2586	H I - selected	21
J0812+3208	2.0668	21.50 ± 0.20	-1.83 ± 0.20	—	0.224 ± 0.002	18	S II λ 1250	Serendipitous	18, 26, 25, 28
Q2206-19	2.0762	20.43 ± 0.06	-2.25 ± 0.07	< -26.74	—	18	Al II λ 1670	H I - selected	4, 7, 13
Q2359-02	2.0950	20.70 ± 0.10	-0.72 ± 0.10	-26.52 ± 0.11	0.828 ± 0.004	144	Si II λ 1808	H I - selected	7, 13
Q0149+33	2.1407	20.50 ± 0.10	-1.43 ± 0.11	< -27.22	0.218 ± 0.003	34	Fe II λ 1608	H I - selected	7, 13
Q0528-2505	2.1410	20.95 ± 0.05	-1.27 ± 0.06	—	0.599 ± 0.008	70	Si II λ 1808	H I - selected	2

Table A.2: — Continued

QSO	z_{abs}	$\log N_{\text{HI}}$ (cm^{-2})	Metallicity	$\log \ell_c$ ($\text{ergs s}^{-1} \text{H}^{-1}$)	W_{1526} (\AA)	Δv_{90}^a (km s^{-1})	Transition ^b	Selection Criterion	References
Q2359-02	2.1539	20.30 ± 0.10	-1.53 ± 0.10	< -25.34	0.278 ± 0.005	76	Si II λ 1526	H1 - selected	7, 13
Q2348-14	2.2794	20.56 ± 0.07	-2.01 ± 0.15	< -26.88	0.186 ± 0.002	24	Fe II λ 1608	H1 - selected	7, 13
J2036-0553	2.2805	21.20 ± 0.15	-1.81 ± 0.15	-27.30 ± 0.15	0.306 ± 0.003	56	S II λ 1259	H1 - selected	27
Q0216+08	2.2930	20.50 ± 0.10	-0.61 ± 0.10	—	0.891 ± 0.007	96	Si II λ 1808	H1 - selected	30, 2
PH957	2.3090	21.37 ± 0.08	-1.41 ± 0.08	-27.29 ± 0.09	0.380 ± 0.004	54	Ni II λ 1741	H1 - selected	1, 7, 13, 27
J1435+5359	2.3427	21.05 ± 0.10	-1.42 ± 0.10	-27.68 ± 0.10	0.330 ± 0.001	29	Si II λ 1808	H1 - selected	25
Q0841+12	2.3745	20.95 ± 0.08	-1.33 ± 0.09	—	0.298 ± 0.003	44	Si II λ 1808	H1 - selected	7, 13
Q2348-01	2.4263	20.50 ± 0.10	-0.64 ± 0.10	—	1.321 ± 0.007	242	Fe II λ 1608	H1 - selected	13
Q2343+125	2.4313	20.34 ± 0.10	-0.47 ± 0.10	-27.17 ± 0.15	1.028 ± 0.003	292	Si II λ 1808	H1 - selected	5, 19
J1541+3153	2.4435	20.95 ± 0.10	-1.49 ± 0.10	-27.39 ± 0.13	0.215 ± 0.003	35	Fe II λ 1608	H1 - selected	31
Q0201+36	2.4628	20.38 ± 0.04	-0.24 ± 0.04	—	—	200	Si II λ 1808	H1 - selected	3, 13
Q0836+11	2.4652	20.60 ± 0.10	-1.11 ± 0.11	< -26.98	0.593 ± 0.009	86	Fe II λ 1608	H1 - selected	13
Q1223+17	2.4660	21.50 ± 0.10	-1.54 ± 0.10	< -27.00	0.620 ± 0.003	90	Si II λ 1808	H1 - selected	10, 13
Q2344+12	2.5379	20.36 ± 0.10	-1.69 ± 0.10	< -27.03	—	66	Si II λ 1304	H1 - selected	2, 13
Q1209+0919	2.5841	21.40 ± 0.10	-1.00 ± 0.10	—	1.668 ± 0.009	190	Si II λ 1808	H1 - selected	26
J1155+0530	2.6077	20.35 ± 0.20	-1.60 ± 0.16	—	0.115 ± 0.002	17	Fe II λ 2374	Serendipitous	27
Q2348-01	2.6147	21.30 ± 0.10	-1.92 ± 0.12	—	0.361 ± 0.005	88	Al II λ 1670	H1 - selected	13
Q0913+072	2.6184	20.35 ± 0.10	-2.52 ± 0.10	< -27.09	—	24	Si II λ 1190	H1 - selected	22

Table A.2: — Continued

QSO	z_{abs}	$\log N_{\text{HI}}$ (cm^{-2})	Metallicity	$\log \ell_c$ ($\text{ergs s}^{-1} \text{H}^{-1}$)	W_{1526} (\AA)	Δv_{90}^a (km s^{-1})	Transition ^b	Selection Criterion	References
Q1759+75	2.6253	20.80 ± 0.10	-0.70 ± 0.10	-27.17 ± 0.10	0.634 ± 0.004	72	Si II λ 1808	H I - selected	7, 13
J2343+1410	2.6767	20.50 ± 0.15	-1.96 ± 0.22	< -26.96	0.189 ± 0.009	36	Fe II λ 1608	H I - selected	27
J1035+5440	2.6840	20.50 ± 0.20	-0.94 ± 0.20	> -26.80	1.424 ± 0.006	222	Fe II λ 1608	H I - selected	27
J0929+2825	2.7684	20.80 ± 0.10	-0.67 ± 0.10	—	0.621 ± 0.001	87	Si II λ 1808	Serendipitous	27
PKS1354-17	2.7800	20.30 ± 0.15	-1.31 ± 0.18	-27.06 ± 0.16	—	22	Fe II λ 1608	H I - selected	18, 27
HS1132+2243	2.7834	21.00 ± 0.07	-1.90 ± 0.07	< -27.82	0.272 ± 0.004	53	Fe II λ 1608	H I - selected	18
Q1337+11	2.7958	20.95 ± 0.10	-1.75 ± 0.10	< -27.35	—	38	S II λ 1259	H I - selected	18, 26
Q1425+6039	2.8268	20.30 ± 0.04	-0.75 ± 0.05	< -26.29	0.700 ± 0.010	138	Fe II λ 1608	H I - selected	2, 13, 26
J1353+5328	2.8349	20.80 ± 0.10	-1.37 ± 0.10	-27.11 ± 0.11	0.288 ± 0.003	36	S II λ 1253	H I - selected	31
J1131+6044	2.8757	20.50 ± 0.15	-1.80 ± 0.15	< -27.28	0.137 ± 0.004	53	Si II λ 1526	H I - selected	27
J0826+3148	2.9121	20.30 ± 0.15	-1.50 ± 0.15	< -27.20	0.126 ± 0.002	35	Fe II λ 1608	H I - selected	27
J1304+1202	2.9131	20.55 ± 0.15	-1.65 ± 0.15	< -27.25	0.215 ± 0.004	92	Fe II λ 1608	H I - selected	31
J1304+1202	2.9289	20.30 ± 0.15	-1.54 ± 0.15	< -27.04	0.094 ± 0.003	23	Fe II λ 1608	H I - selected	31
J1410+5111	2.9344	20.80 ± 0.15	-0.89 ± 0.15	-26.92 ± 0.15	1.288 ± 0.008	247	Fe II λ 1608	Serendipitous	27
Q1021+30	2.9489	20.70 ± 0.10	-1.97 ± 0.12	< -27.45	0.267 ± 0.008	98	Fe II λ 1608	H I - selected	13, 18
J1014+4300	2.9588	20.50 ± 0.10	-0.83 ± 0.10	-27.38 ± 0.11	0.611 ± 0.001	55	Si II λ 1808	Serendipitous	27
J1410+5111	2.9642	20.85 ± 0.20	-1.94 ± 0.15	< -27.35	0.176 ± 0.004	47	Fe II λ 1608	H I - selected	27
HS0741+4741	3.0174	20.40 ± 0.10	-1.54 ± 0.10	< -27.40	0.214 ± 0.001	36	S II λ 1259	H I - selected	13

Table A.2: — Continued

QSO	z_{abs}	$\log N_{\text{HI}}$ (cm^{-2})	Metallicity	$\log \ell_c$ ($\text{ergs s}^{-1} \text{H}^{-1}$)	$W_{1.526}$ (\AA)	Δv_{90}^a (km s^{-1})	Transition ^b	Selection Criterion	References
J1240+1455	3.0241	20.45 ± 0.10	-1.39 ± 0.13	< -26.65	0.306 ± 0.010	105	Si II $\lambda 1304$	Serendipitous	27
Q0347-38	3.0247	20.60 ± 0.10	-1.08 ± 0.10	-26.64 ± 0.10	0.451 ± 0.003	88	Fe II $\lambda 608$	H I - selected	7, 13, 16
Q0336-01	3.0620	21.20 ± 0.10	-1.49 ± 0.10	-26.71 ± 0.10	—	108	S II $\lambda 1250$	H I - selected	13
BR1013+0035	3.1040	21.10 ± 0.10	-0.82 ± 0.10	—	—	254	Si II $\lambda 1808$	High redshift	26
Q2223+20	3.1192	20.30 ± 0.10	-2.17 ± 0.10	—	0.097 ± 0.008	62	Si II $\lambda 1526$	H I - selected	18
J0825+3544	3.2073	20.30 ± 0.10	-1.68 ± 0.16	-26.01 ± 0.14	0.194 ± 0.007	26	Fe II $\lambda 608$	Serendipitous	31
J1200+4015	3.2200	20.85 ± 0.10	-0.64 ± 0.10	-26.68 ± 0.10	0.940 ± 0.004	127	Ni II $\lambda 1317$	H I - selected	31
PSS1506+522	3.2244	20.67 ± 0.07	-2.24 ± 0.17	< -27.28	0.039 ± 0.003	42	Al II $\lambda 1670$	H I - selected	18, 27
Q0930+28	3.2352	20.30 ± 0.10	-1.69 ± 0.11	< -27.24	0.079 ± 0.002	18	Fe II $\lambda 608$	H I - selected	17
J0900+4215	3.2458	20.30 ± 0.10	-0.82 ± 0.10	-26.74 ± 0.10	0.560 ± 0.001	88	Fe II $\lambda 608$	H I - selected	26, 25
J0255+00	3.2529	20.70 ± 0.10	-0.88 ± 0.10	—	0.992 ± 0.008	220	Fe II $\lambda 608$	High redshift	13
J0929+2825	3.2627	21.10 ± 0.10	-1.56 ± 0.10	-27.42 ± 0.10	0.333 ± 0.001	52	S II $\lambda 1259$	H I - selected	27
J2315+1456	3.2732	20.30 ± 0.15	-1.68 ± 0.16	< -26.93	—	122	Si II $\lambda 1304$	H I - selected	27
PSS0957+33	3.2795	20.45 ± 0.08	-1.08 ± 0.09	—	—	66	Fe II $\lambda 608$	High redshift	14, 13
Q1055+46	3.3172	20.34 ± 0.10	-1.60 ± 0.15	—	—	50	Fe II $\lambda 608$	H I - selected	5
Q0201+11	3.3868	21.26 ± 0.10	-1.20 ± 0.15	-26.66 ± 0.14	0.636 ± 0.031	64	Ni II $\lambda 1317$	High redshift	11
Q0000-2619	3.3901	21.41 ± 0.08	-1.68 ± 0.19	—	0.337 ± 0.003	26	Si II $\lambda 1808$	High redshift	2, 7, 8, 12
BR0019-15	3.4388	20.92 ± 0.10	-1.01 ± 0.11	-26.59 ± 0.10	0.761 ± 0.006	118	Fe II $\lambda 608$	High redshift	7, 13

Table A.2: — Continued

QSO	z_{abs}	$\log N_{\text{HI}}$ (cm^{-2})	Metallicity	$\log \ell_c$ ($\text{ergs s}^{-1} \text{H}^{-1}$)	$W_{\lambda 1526}$ (\AA)	Δv_{90}^a (km s^{-1})	Transition ^b	Selection Criterion	References
BR11108-07	3.6076	20.50 ± 0.10	-1.74 ± 0.10	< -27.65	0.189 ± 0.004	28	Fe II $\lambda 1608$	High redshift	10, 13
PSS0209+05	3.6662	20.45 ± 0.10	-1.83 ± 0.10	—	0.163 ± 0.001	32	Si II $\lambda 1526$	High redshift	18
J0814+5029	3.7075	21.35 ± 0.15	-2.07 ± 0.15	-27.77 ± 0.15	0.139 ± 0.002	30	Fe II $\lambda 608$	H I - selected	27
BR11346-03	3.7358	20.72 ± 0.10	-2.27 ± 0.10	-27.68 ± 0.15	0.118 ± 0.005	34	Si II $\lambda 1304$	High redshift	7, 13
J1201+2117	3.7975	21.35 ± 0.15	-0.74 ± 0.15	—	2.831 ± 0.010	485	Si II $\lambda 1808$	Serendipitous	31
BR0951-04	3.8566	20.60 ± 0.10	-1.64 ± 0.19	—	0.607 ± 0.008	246	Si II $\lambda 1526$	High redshift	7, 13
PSS0209+05	3.8635	20.55 ± 0.10	-2.54 ± 0.10	< -27.55	0.066 ± 0.001	44	Si II $\lambda 1526$	High redshift	18
J0255+00	3.9146	21.30 ± 0.05	-1.72 ± 0.05	-27.40 ± 0.06	—	34	S II $\lambda 1253$	High redshift	13
J1654+2227	4.0022	20.60 ± 0.15	-1.65 ± 0.16	—	—	29	Fe II $\lambda 608$	High redshift	31
J0747+4434	4.0196	20.95 ± 0.15	-2.28 ± 0.25	-27.18 ± 0.16	0.382 ± 0.015	83	Fe II $\lambda 608$	High redshift	31
BR10952-01	4.0244	20.55 ± 0.10	-1.51 ± 0.20	-26.51 ± 0.10	—	288	Fe II $\lambda 608$	High redshift	10, 13
BR2237-0607	4.0803	20.52 ± 0.11	-1.82 ± 0.11	< -27.50	0.290 ± 0.003	142	Al II $\lambda 1670$	High redshift	2
J1051+3107	4.1392	20.70 ± 0.20	-1.99 ± 0.21	< -27.20	0.270 ± 0.010	71	Si II $\lambda 1304$	High redshift	31
J1201+2117	4.1578	20.60 ± 0.15	-2.38 ± 0.15	—	0.086 ± 0.004	31	Si II $\lambda 1526$	High redshift	31
PSS0957+33	4.1798	20.70 ± 0.10	-1.45 ± 0.11	—	0.486 ± 0.012	342	Si II $\lambda 1526$	High redshift	14, 13
BR0951-04	4.2029	20.40 ± 0.10	-2.56 ± 0.10	< -26.56	0.041 ± 0.005	28	Si II $\lambda 190$	High redshift	7, 13
PSS1443+27	4.2241	21.00 ± 0.10	-0.94 ± 0.19	< -25.83	—	90	Ni II $\lambda 1370$	High redshift	10, 13
J0817+1351	4.2584	21.30 ± 0.15	-1.15 ± 0.15	> -26.41	0.704 ± 0.019	87	S II $\lambda 1253$	High redshift	31

Table A.2: — Continued

QSO	z_{abs}	$\log N_{\text{HI}}$ (cm^{-2})	Metallicity	$\log \ell_c$ ($\text{ergs s}^{-1} \text{H}^{-1}$)	W_{1526} (\AA)	Δv_{90}^a (km s^{-1})	Transition ^b	Selection Criterion	References
J1051+3545	4.3498	20.45 ± 0.10	-1.88 ± 0.10	—	0.192 ± 0.008	25	Si II λ 1808	High redshift	31
BR1202-07	4.3828	20.60 ± 0.14	-1.75 ± 0.14	< -27.05	0.361 ± 0.017	172	Si II λ 1304	High redshift	2
J1100+1122	4.3947	21.74 ± 0.10	-1.68 ± 0.21	-27.10 ± 0.10	0.718 ± 0.016	142	Ni II λ 1317	High redshift	31
J1438+4314	4.3990	20.89 ± 0.15	-1.31 ± 0.15	-26.87 ± 0.15	0.581 ± 0.011	75	Fe II λ 1608	High redshift	31
J1607+1604	4.4741	20.30 ± 0.15	-1.70 ± 0.15	-26.71 ± 0.17	0.179 ± 0.008	42	Si II λ 1304	High redshift	31
J1200+4618	4.4765	20.50 ± 0.15	-1.38 ± 0.22	< -26.28	0.415 ± 0.012	111	Si II λ 1304	High redshift	31
J0040-0915	4.7394	20.30 ± 0.15	-1.39 ± 0.17	—	0.229 ± 0.022	82	Si II λ 1304	High redshift	31
J1202+3235	4.7955	21.10 ± 0.15	-2.35 ± 0.22	-27.32 ± 0.15	0.071 ± 0.002	26	Si II λ 1526	High redshift	31
J1051+3545	4.8206	20.35 ± 0.10	-2.27 ± 0.10	< -27.03	0.082 ± 0.004	44	Si II λ 1526	High redshift	31
J1202+3235	5.0647	20.30 ± 0.15	-2.66 ± 0.15	< -27.18	0.163 ± 0.012	32	O I λ 1302	High redshift	31

Note. — See notes from Table 2.2

Table A.3: Fine Structure DLA sample

Index Number	QSO	z_{abs}	$\log N_{\text{HI}}$ (cm^{-2})	Metallicity [MH]	M^{a}	$\log N_{\text{CII}^*}$ (cm^{-2})	$\log N_{\text{SiII}^*}$ (cm^{-2})	$\log N_{\text{SiII}}$ (cm^{-2})	N13 ^b	References
1	Q1157+014	1.9437	21.70 ± 0.10	-1.23 ± 0.10	Si	$> 14.75^{\text{c}}$	12.37 ± 0.03	15.97 ± 0.01	Y	5, 18
2	Q1215+33	1.9991	20.95 ± 0.06	-1.43 ± 0.07	Si	< 13.18	< 12.56	15.02 ± 0.02	Y	4, 7
3	Q0458-02	2.0395	21.65 ± 0.09	-1.11 ± 0.09	Si	$> 14.88^{\text{c}}$	< 12.58	$16.04 \pm 0.02^{\text{c}}$	Y	4, 7
4	J2340-0053	2.0545	20.35 ± 0.15	-0.55 ± 0.15	S	13.72 ± 0.01	< 11.31	15.23 ± 0.01	Y	12, 17, 19
5	Q2206-19	2.0762	20.43 ± 0.06	-2.25 ± 0.07	Si	< 13.20	< 11.83	13.68 ± 0.03	Y	2, 4, 7
6	Q2359-02	2.0950	20.70 ± 0.10	-0.72 ± 0.10	Si	13.69 ± 0.06	< 12.05	15.48 ± 0.02	Y	4, 7
7	Q0149+33	2.1407	20.50 ± 0.10	-1.43 ± 0.11	Si	< 12.79	< 12.22	14.57 ± 0.04	Y	4, 7
8	Q2348-14	2.2794	20.56 ± 0.07	-2.01 ± 0.15	S	< 13.19	< 12.04	14.20 ± 0.02	Y	4, 7
9	J2036-0553	2.2805	21.20 ± 0.15	-1.81 ± 0.15	S	13.41 ± 0.03	< 11.86	14.99 ± 0.04	Y	18
10	J1435+5359	2.3427	21.05 ± 0.10	-1.42 ± 0.10	S	12.88 ± 0.03	< 11.30	15.12 ± 0.01	Y	16
11	Q2343+125	2.4313	20.34 ± 0.10	-0.47 ± 0.10	Si	12.68 ± 0.11	< 11.69	15.37 ± 0.01	Y	3, 11
12	J1541+3153	2.4435	20.95 ± 0.10	-1.49 ± 0.10	Si	13.07 ± 0.09	< 12.23	14.96 ± 0.03	Y	21
13	Q0836+11	2.4652	20.60 ± 0.10	-1.11 ± 0.11	Si	< 13.13	< 12.23	14.99 ± 0.04	Y	7
14	Q2344+12	2.5379	20.36 ± 0.10	-1.69 ± 0.10	Si	< 12.84	< 11.96	14.18 ± 0.01	Y	1, 7
15	Q0913+072	2.6184	20.35 ± 0.10	-2.52 ± 0.10	Si	< 12.77	< 12.41	13.33 ± 0.02	Y	13
16	Q1759+75	2.6253	20.80 ± 0.10	-0.70 ± 0.10	S	13.14 ± 0.03	< 11.60	15.53 ± 0.01	Y	4, 7
17	J1035+5440	2.6840	20.50 ± 0.20	-0.94 ± 0.20	Zn	> 13.21	< 11.69	> 15.10	Y	18
18	PKS1354-17	2.7800	20.30 ± 0.15	-1.31 ± 0.18	Si	12.75 ± 0.06	< 12.56	14.49 ± 0.11	Y	10, 18

Table A.3: — Continued

Index Number	QSO	z_{abs}	$\log N_{\text{HI}}$ (cm^{-2})	Metallicity [M/H]	M ^a	$\log N_{\text{CII}^*}$ (cm^{-2})	$\log N_{\text{SII}^*}$ (cm^{-2})	$\log N_{\text{SIII}}$ (cm^{-2})	N13 ^b	References
19	HS1132+2243	2.7834	21.00 ± 0.07	-1.90 ± 0.07	S	< 12.69	< 11.42	> 14.48	Y	10
20	Q1337+11	2.7958	20.95 ± 0.10	-1.75 ± 0.10	S	< 13.11	< 11.63	14.78 ± 0.06	Y	10, 17
21	J1353+5328	2.8349	20.80 ± 0.10	-1.37 ± 0.10	S	13.20 ± 0.05	< 11.46	14.81 ± 0.06	Y	21
22	J1131+6044	2.8757	20.50 ± 0.15	-1.80 ± 0.15	O	< 12.73	< 11.64	13.92 ± 0.01	Y	18
23	J1304+1202	2.9131	20.55 ± 0.15	-1.65 ± 0.15	S	< 12.81	< 11.58	14.25 ± 0.04	Y	21
24	J1304+1202	2.9289	20.30 ± 0.15	-1.54 ± 0.15	S	< 12.77	< 11.66	> 13.85	Y	21
25	Q1021+30	2.9489	20.70 ± 0.10	-1.97 ± 0.12	S	< 12.76	< 11.60	14.37 ± 0.08	Y	7, 10
26	J1014+4300	2.9588	20.50 ± 0.10	-0.83 ± 0.10	Si	12.63 ± 0.06	< 11.82	15.17 ± 0.01	Y	18
27	J1410+5111	2.9642	20.85 ± 0.20	-1.94 ± 0.15	Si	< 13.01	< 11.78	14.34 ± 0.02	Y	18
28	HS0741+4741	3.0174	20.40 ± 0.10	-1.54 ± 0.10	S	< 12.51	< 11.08	14.35 ± 0.01	Y	7
29	J1240+1455	3.0241	20.45 ± 0.10	-1.39 ± 0.13	S	< 13.31	< 12.54	> 14.37	Y	18
30	Q0347-38	3.0247	20.60 ± 0.10	-1.08 ± 0.10	Si	13.47 ± 0.03	< 12.17	15.02 ± 0.02	Y	4, 7, 8
31	Q0336-01	3.0620	21.20 ± 0.10	-1.49 ± 0.10	S	14.00 ± 0.01	< 11.65	> 14.87	Y	7
32	J1200+4015	3.2200	20.85 ± 0.10	-0.64 ± 0.10	S	13.68 ± 0.02	< 11.84	> 15.21	Y	21
33	Q0930+28	3.2352	20.30 ± 0.10	-1.69 ± 0.11	O	< 12.57	< 12.16	13.88 ± 0.02	Y	9
34	J0900+4215	3.2458	20.30 ± 0.10	-0.82 ± 0.10	S	13.07 ± 0.03	< 11.23	15.11 ± 0.01	Y	17, 16
35	J0929+2825	3.2627	21.10 ± 0.10	-1.56 ± 0.10	S	13.19 ± 0.02	< 11.26	15.04 ± 0.01	Y	18
36	J2315+1456	3.2732	20.30 ± 0.15	-1.68 ± 0.16	S	< 12.88	< 11.64	14.12 ± 0.01	Y	18

Table A.3: — Continued

Index Number	QSO	z_{abs}	$\log N_{\text{HI}}$ (cm^{-2})	Metallicity [M/H]	M ^a	$\log N_{\text{CII}^*}$ (cm^{-2})	$\log N_{\text{SiII}^*}$ (cm^{-2})	$\log N_{\text{SiII}}$ (cm^{-2})	N13 ^b	References
37	BR0019-15	3.4388	20.92 ± 0.10	-1.01 ± 0.11	Si	13.84 ± 0.01	< 12.41	15.41 ± 0.05	Y	4, 7
38	J0814+5029	3.7075	21.35 ± 0.15	-2.07 ± 0.15	S	13.09 ± 0.04	< 12.12	14.43 ± 0.07	Y	18
39	BR11346-03	3.7358	20.72 ± 0.10	-2.27 ± 0.10	Si	12.55 ± 0.12	< 12.30	13.95 ± 0.01	Y	4, 7
40	PSS0209+05	3.8635	20.55 ± 0.10	-2.54 ± 0.10	Si	< 12.51	< 11.91	13.51 ± 0.01	Y	10
41	J1051+3107	4.1392	20.70 ± 0.20	-1.99 ± 0.21	S	< 13.01	< 11.52	14.20 ± 0.01	Y	21
42	PSS1443+27	4.2241	21.00 ± 0.10	-0.94 ± 0.17	Fe	< 14.68	< 11.51	> 15.32	Y	6, 7
43	J0817+1351	4.2584	21.30 ± 0.15	-1.15 ± 0.15	S	> 14.40	< 11.83	> 14.93	Y	21
44	J1100+1122	4.3947	21.74 ± 0.10	-1.68 ± 0.21	Fe	14.15 ± 0.02	< 12.57	> 14.85	Y	21
45	J1607+1604	4.4741	20.30 ± 0.15	-1.70 ± 0.15	Si	13.10 ± 0.09	< 12.80	14.10 ± 0.01	Y	21
46	J1200+4618	4.4765	20.50 ± 0.15	-1.38 ± 0.22	Fe	< 13.73	< 13.11	> 14.55	Y	21
47	J1202+3235	4.7955	21.10 ± 0.15	-2.35 ± 0.22	Fe	13.29 ± 0.02	< 12.30	> 13.80	Y	21
48	J1051+3545	4.8206	20.35 ± 0.10	-2.27 ± 0.10	Si	< 12.83	< 12.34	13.58 ± 0.02	Y	21
49	J1056+1208	1.6093	21.45 ± 0.15	-0.47 ± 0.17	Si	$> 15.65^c$	12.79 ± 0.04	16.48 ± 0.08^c	N	20, 24, 25
50	J0044+0018	1.7250	20.35 ± 0.10	-0.23 ± 0.10	S	13.81 ± 0.03	< 12.36	15.34 ± 0.04	N	20, 25
51	J0927+1543	1.7311	21.35 ± 0.15	-0.86 ± 0.15	Si	$> 15.22^c$	< 12.11	15.99 ± 0.01	N	25
52	J0008-0958	1.7675	20.85 ± 0.15	-0.16 ± 0.15	S	14.34 ± 0.01	< 11.88	16.04 ± 0.01	N	15, 25
53	J1249-0233	1.7808	21.45 ± 0.15	-1.06 ± 0.15	S	14.12 ± 0.01	< 12.26	> 15.11	N	15, 25
54	J0233+0103	1.7850	20.60 ± 0.15	-1.34 ± 0.15	Si	< 13.03	< 12.44	14.77 ± 0.09	N	25

Table A.3: — Continued

Index Number	QSO	z_{abs}	Metallicity [M/H]	M^{a}	$\log N_{\text{CII}^*}$ (cm^{-2})	$\log N_{\text{SiII}^*}$ (cm^{-2})	$\log N_{\text{SiII}}$ (cm^{-2})	N13 ^b	References
55	J1454+0941	1.7884	-0.39 ± 0.16	S	13.59 ± 0.06	< 12.24	15.47 ± 0.03	N	25
56	J1313+1441	1.7947	-0.59 ± 0.15	Si	$> 15.26^{\text{c}}$	12.47 ± 0.02	$16.11 \pm 0.04^{\text{c}}$	N	24, 25
57	J1310+5424	1.8005	-0.51 ± 0.15	Si	$> 15.43^{\text{c}}$	12.51 ± 0.12	$16.44 \pm 0.04^{\text{c}}$	N	20, 24, 25
58	J1106+1044	1.8185	-0.32 ± 0.15	S	< 13.36	< 12.19	> 15.21	N	25
59	J1142+0701	1.8407	-0.85 ± 0.20	Si	$> 14.83^{\text{c}}$	12.51 ± 0.09	$16.15 \pm 0.13^{\text{c}}$	N	24, 25
60	J0815+1037	1.8462	-0.43 ± 0.47	Si	< 13.69	< 12.57	15.37 ± 0.44	N	25
61	J1335+0824	1.8560	-0.51 ± 0.15	S	13.87 ± 0.05	< 12.12	15.72 ± 0.03	N	25
62	J1024+0600	1.8950	-0.30 ± 0.15	S	14.31 ± 0.01	< 12.05	15.80 ± 0.02	N	25
63	J1524+1030	1.9409	-0.75 ± 0.15	Zn	$> 14.76^{\text{c}}$	< 11.55	$> 16.24^{\text{c}}$	N	24, 25
64	J1042+0628	1.9429	-0.77 ± 0.15	S	< 14.15	< 12.06	15.40 ± 0.07	N	25
65	J1417+4132	1.9508	-0.93 ± 0.15	Zn	$> 15.11^{\text{c}}$	12.43 ± 0.03	$> 16.41^{\text{c}}$	N	23, 24, 25
66	J1552+4910	1.9599	-0.96 ± 0.15	S	13.49 ± 0.03	< 11.49	15.98 ± 0.01	N	25
67	Q1755+578	1.9692	-0.18 ± 0.15	Zn	$> 14.77^{\text{c}}$	12.83 ± 0.03	$16.57 \pm 0.01^{\text{c}}$	N	24, 25
68	J1305+0924	2.0184	-0.15 ± 0.15	S	14.10 ± 0.04	< 12.07	15.75 ± 0.04	N	25
69	J1509+1113	2.0283	-0.76 ± 0.15	S	14.31 ± 0.03	< 11.94	16.04 ± 0.02	N	25
70	J1135-0010	2.2068	-1.07 ± 0.10	Si	$> 15.00^{\text{c}}$	13.70 ± 0.05	$16.49 \pm 0.03^{\text{c}}$	N	22, 24
71	J1211+0422	2.3765	-1.22 ± 0.10	S	< 12.73	< 11.90	14.94 ± 0.04	N	7, 16
72	J2241+1225	2.4179	-1.28 ± 0.20	Fe	13.39 ± 0.09	< 12.72	> 14.67	N	25

Table A.3: — Continued

Index Number	QSO	z_{abs}	$\log N_{\text{HI}}$ (cm^{-2})	Metallicity [M/H]	M ^a	$\log N_{\text{CII}^*}$ (cm^{-2})	$\log N_{\text{SiII}^*}$ (cm^{-2})	$\log N_{\text{SiIII}}$ (cm^{-2})	N13 ^b	References
73	J0211+1241	2.5951	20.60 ± 0.15	-0.57 ± 0.16	Si	13.32 ± 0.03	< 12.14	15.53 ± 0.07	N	25
74	J0812+3208	2.6263	21.35 ± 0.10	-0.55 ± 0.13	O	14.02 ± 0.01	< 11.78	15.98 ± 0.05	N	10, 17, 16, 19
75	J1558-0031	2.7026	20.67 ± 0.05	-1.74 ± 0.05	S	< 12.60	< 11.54	> 14.15	N	14
76	FJ2334-09	3.0569	20.45 ± 0.10	-0.99 ± 0.10	Si	< 12.81	< 11.97	14.96 ± 0.03	N	10
77	J2100-0641	3.0924	21.05 ± 0.15	-0.70 ± 0.15	S	14.09 ± 0.01	< 11.31	15.87 ± 0.01	N	15, 19, 20
78	J1155+0530	3.3260	21.05 ± 0.10	-0.79 ± 0.10	S	13.81 ± 0.02	< 11.29	15.94 ± 0.01	N	18
79	J0825+3544	3.6567	21.25 ± 0.10	-1.83 ± 0.13	Si	13.14 ± 0.05	< 11.00	14.92 ± 0.08	N	21
80	J0909+3303	3.6581	20.55 ± 0.10	-0.89 ± 0.10	S	13.53 ± 0.08	< 12.50	14.85 ± 0.08	N	21

Note. — See notes from Table 3.1

Table A.4: Results of Si II* and C II* Technique

Index Number	QSO	z_{abs}	$\log n_{\text{H}}(2-\sigma)$ [cm^{-3}]	$\log n_{\text{e}}(2-\sigma)$ [cm^{-3}]	$\log T(2-\sigma)$ [K]	$\log P/k_{\text{B}}(2-\sigma)$ [K cm^{-3}]
1	Q1157+014	1.9437	1.1-2.2(0.9-2.8)	-2.6--1.2(-2.9--1.0)	2.5-3.7(2.2-4.1)	3.8-5.5(3.5-6.3)
2	Q1215+33	1.9991	-1.5-0.8(-1.9-2.4)	-3.2--2.2(-3.6--1.6)	1.3-3.6(1.0-4.3)	0.3-3.6(-0.1-5.3)
3	Q0458-02	2.0395	1.6-2.7(1.3-2.9)	-2.8--1.3(-3.1--0.9)	1.7-2.5(1.5-3.2)	3.6-4.9(3.2-5.6)
4	J2340-0053	2.0545	1.0-2.2(0.8-2.8)	-2.9--1.5(-3.2--1.1)	1.6-2.5(1.4-3.2)	2.8-4.3(2.5-5.2)
5	Q2206-19	2.0762	-1.2-1.3(-1.8-2.6)	-3.0--1.8(-3.5--1.3)	1.4-3.7(1.1-4.3)	0.9-4.3(0.1-5.6)
6	Q2359-02	2.0950	0.3-1.5(0.0-2.7)	-2.7--1.6(-3.1--1.3)	1.7-3.8(1.3-4.3)	2.3-4.7(1.8-5.9)
7	Q0149+33	2.1407	-1.4-0.9(-1.9-2.4)	-3.2--2.1(-3.5--1.6)	1.3-3.6(1.1-4.3)	0.4-3.7(-0.1-5.3)
8	Q2348-14	2.2794	-1.3-1.1(-1.9-2.5)	-3.1--2.0(-3.5--1.4)	1.3-3.7(1.1-4.3)	0.7-4.0(0.0-5.5)
9	J2036-0553	2.2805	0.6-1.7(0.3-2.7)	-2.7--1.5(-3.1--1.1)	1.7-3.8(1.4-4.4)	2.5-5.0(2.1-6.0)
10	J1435+5359	2.3427	-0.3-1.5(-0.6-2.7)	-2.7--1.8(-3.1--1.3)	1.5-3.7(1.2-4.3)	1.6-4.5(1.2-5.8)
11	Q2343+125	2.4313	-1.3-0.8(-1.8-2.5)	-3.0--2.2(-3.3--1.6)	1.5-3.8(1.1-4.3)	0.6-3.7(0.1-5.5)
12	J1541+3153	2.4435	0.1-1.4(-0.3-2.6)	-2.7--1.7(-3.1--1.3)	1.7-3.9(1.3-4.4)	2.1-4.7(1.6-5.9)
13	Q0836+11	2.4652	-1.5-0.9(-1.9-2.4)	-3.2--2.2(-3.6--1.6)	1.3-3.6(1.0-4.3)	0.3-3.6(-0.2-5.2)
14	Q2344+12	2.5379	-1.3-1.0(-1.9-2.5)	-3.1--2.0(-3.5--1.4)	1.3-3.7(1.1-4.3)	0.6-3.9(0.0-5.5)
15	Q0913+072	2.6184	-1.1-1.5(-1.8-2.6)	-3.0--1.7(-3.4--1.1)	1.4-3.7(1.1-4.3)	1.1-4.5(0.2-5.7)
16	Q1759+75	2.6253	-0.6-1.0(-0.9-2.5)	-2.8--2.0(-3.1--1.5)	1.6-3.8(1.2-4.3)	1.3-4.1(0.8-5.6)
17	J1035+5440	2.6840	-1.0-1.9(-1.8-2.8)	-3.0--1.7(-3.4--1.1)	1.5-3.6(1.1-4.3)	1.1-4.7(0.2-5.8)
18	PKS1354-17	2.7800	0.2-1.4(-0.6-2.6)	-2.7--1.6(-3.1--1.3)	1.7-3.8(1.3-4.4)	2.2-4.7(1.5-5.9)

Table A.4: — Continued

Index Number	QSO	z_{abs}	$\log n_{\text{H}}(2-\sigma)$ [cm^{-3}]	$\log n_{\text{e}}(2-\sigma)$ [cm^{-3}]	$\log T(2-\sigma)$ [K]	$\log P/k_{\text{B}}(2-\sigma)$ [K cm^{-3}]
19	HS1132+2243	2.7834	-1.4-0.8(-1.9-2.4)	-3.1--2.1(-3.5--1.6)	1.3-3.7(1.1-4.3)	0.5-3.7(0.0-5.3)
20	Q1337+11	2.7958	-1.5-0.9(-1.9-2.4)	-3.2--2.2(-3.6--1.6)	1.2-3.6(1.0-4.3)	0.3-3.6(-0.2-5.2)
21	J1353+5328	2.8349	0.5-1.6(0.2-2.7)	-2.7--1.5(-3.1--1.2)	1.7-3.8(1.4-4.3)	2.5-4.9(2.0-6.0)
22	J1131+6044	2.8757	-1.3-1.1(-1.8-2.5)	-3.1--1.9(-3.5--1.4)	1.4-3.7(1.1-4.3)	0.7-4.0(0.1-5.5)
23	J1304+1202	2.9131	-1.3-1.0(-1.9-2.4)	-3.1--2.0(-3.5--1.5)	1.3-3.7(1.1-4.3)	0.6-3.9(0.0-5.4)
24	J1304+1202	2.9289	-1.1-1.2(-1.8-2.5)	-3.0--1.8(-3.5--1.3)	1.4-3.7(1.1-4.3)	0.9-4.3(0.2-5.6)
25	Q1021+30	2.9489	-1.4-0.9(-1.9-2.4)	-3.1--2.1(-3.5--1.5)	1.3-3.6(1.1-4.3)	0.4-3.7(-0.1-5.3)
26	J1014+4300	2.9588	-1.4-0.9(-1.9-2.4)	-3.1--2.1(-3.5--1.6)	1.3-3.6(1.1-4.3)	0.4-3.7(-0.1-5.3)
27	J1410+5111	2.9642	-1.4-1.0(-1.9-2.5)	-3.1--2.0(-3.5--1.5)	1.3-3.7(1.1-4.3)	0.5-3.9(0.0-5.4)
28	HS0741+4741	3.0174	-1.5-0.9(-1.9-2.4)	-3.2--2.2(-3.6--1.6)	1.2-3.5(1.0-4.3)	0.2-3.5(-0.2-5.2)
29	J1240+1455	3.0241	-1.1-1.2(-1.8-2.5)	-3.0--1.8(-3.5--1.3)	1.4-3.8(1.1-4.3)	1.0-4.3(0.2-5.6)
30	Q0347-38	3.0247	0.6-1.7(0.3-2.7)	-2.7--1.5(-3.1--1.2)	1.7-3.8(1.4-4.4)	2.6-5.0(2.2-6.0)
31	Q0336-01	3.0620	-1.0-1.6(-1.8-2.6)	-3.0--1.7(-3.4--1.1)	1.4-3.7(1.1-4.3)	1.1-4.6(0.3-5.8)
32	J1200+4015	3.2200	-1.2-1.2(-1.8-2.5)	-3.1--1.9(-3.5--1.4)	1.4-3.7(1.1-4.3)	0.8-4.1(0.1-5.5)
33	Q0930+28	3.2352	-1.3-1.0(-1.9-2.5)	-3.1--2.0(-3.5--1.4)	1.3-3.7(1.1-4.3)	0.6-3.9(0.0-5.5)
34	J0900+4215	3.2458	-0.3-1.2(-0.6-2.7)	-2.8--1.8(-3.1--1.4)	1.6-3.7(1.2-4.3)	1.7-4.3(1.2-5.8)
35	J0929+2825	3.2627	0.2-1.5(-0.1-2.7)	-2.8--1.7(-3.1--1.4)	1.6-3.6(1.3-4.3)	2.1-4.5(1.7-5.8)
36	J2315+1456	3.2732	-1.3-1.1(-1.9-2.5)	-3.1--2.0(-3.5--1.4)	1.3-3.7(1.1-4.3)	0.7-4.0(0.0-5.5)

Table A.4: — Continued

Index Number	QSO	z_{abs}	$\log n_{\text{H}}(2-\sigma)$ [cm^{-3}]	$\log n_{\text{e}}(2-\sigma)$ [cm^{-3}]	$\log T(2-\sigma)$ [K]	$\log P/k_{\text{B}}(2-\sigma)$ [K cm^{-3}]
37	BR0019-15	3.4388	0.5-1.7(0.2-2.7)	-2.7-1.5(-3.1-1.2)	1.7-3.8(1.4-4.4)	2.4-4.9(2.0-6.0)
38	J0814+5029	3.7075	0.7-1.7(0.4-2.7)	-2.7-1.4(-3.1-1.1)	1.8-3.9(1.4-4.4)	2.8-5.1(2.3-6.1)
39	BR11346-03	3.7358	0.4-1.6(-0.8-2.7)	-2.7-1.5(-3.1-1.1)	1.7-3.9(1.4-4.4)	2.5-4.9(1.4-6.0)
40	PSS0209+05	3.8635	-1.3-1.0(-1.9-2.5)	-3.1-2.0(-3.5-1.4)	1.4-3.7(1.1-4.3)	0.7-3.9(0.1-5.5)
41	J1051+3107	4.1392	-1.3-1.1(-1.9-2.5)	-3.1-2.0(-3.5-1.4)	1.3-3.7(1.1-4.3)	0.6-4.0(0.0-5.5)
42	PSS1443+27	4.2241	-1.1-1.6(-1.8-2.7)	-3.0-1.8(-3.5-1.3)	1.4-3.5(1.1-4.3)	0.9-4.4(0.1-5.7)
43	J0817+1351	4.2584	-0.9-2.0(-1.8-2.8)	-3.0-1.6(-3.4-1.0)	1.5-3.7(1.1-4.3)	1.3-4.9(0.3-5.9)
44	J1100+1122	4.3947	-1.0-1.7(-1.8-2.7)	-3.0-1.6(-3.4-1.0)	1.5-3.7(1.1-4.3)	1.2-4.8(0.3-5.9)
45	J1202+3235	4.4741	1.0-1.9(0.6-2.7)	-2.6-1.2(-3.1-0.9)	1.9-3.9(1.5-4.4)	3.2-5.4(2.7-6.3)
46	J1200+4618	4.4765	-1.1-1.3(-1.8-2.6)	-3.0-1.7(-3.4-1.2)	1.4-3.7(1.1-4.3)	1.0-4.4(0.2-5.7)
47	J1202+3235	4.7955	-0.9-1.8(-1.8-2.6)	-3.0-1.6(-3.4-1.0)	1.5-3.8(1.1-4.4)	1.4-4.9(0.4-5.9)
48	J1051+3545	4.8206	-1.2-1.3(-1.8-2.5)	-3.0-1.8(-3.5-1.2)	1.4-3.7(1.1-4.3)	0.9-4.3(0.2-5.6)
49	J1056+1208	1.6093	1.6-2.5(1.5-2.9)	-2.7-1.2(-3.0-0.9)	1.4-3.7(1.1-4.3)	4.0-5.1(3.9-5.6)
50	J0044+0018	1.7250	0.6-1.7(0.4-2.7)	-2.7-1.4(-3.1-1.1)	1.8-3.8(1.4-4.4)	2.6-5.0(2.2-6.1)
51	J0927+1543	1.7311	2.0-2.7(1.8-2.9)	-2.8-1.2(-3.1-0.9)	1.7-2.1(1.6-2.3)	3.8-4.6(3.6-5.0)
52	J0008-0958	1.7675	0.8-2.3(0.6-2.8)	-2.9-1.6(-3.2-1.1)	1.5-2.4(1.3-2.9)	2.6-4.3(2.3-5.0)
53	J1249-0233	1.7808	-1.1-1.4(-1.8-2.6)	-3.0-1.7(-3.4-1.2)	1.5-3.8(1.1-4.3)	1.1-4.5(0.3-5.7)
54	J0233+0103	1.7850	-1.4-1.0(-1.9-2.4)	-3.2-2.1(-3.6-1.5)	1.3-3.6(1.0-4.3)	0.4-3.7(-0.1-5.3)

Table A.4: — Continued

Index Number	QSO	z_{abs}	$\log n_{\text{H}}(2-\sigma)$ [cm^{-3}]	$\log n_{\text{e}}(2-\sigma)$ [cm^{-3}]	$\log T(2-\sigma)$ [K]	$\log Pk_{\text{B}}(2-\sigma)$ [K cm^{-3}]
55	J1454+0941	1.7884	0.2-1.4(-0.1-2.6)	-2.7-1.6(-3.1-1.3)	1.7-3.9(1.3-4.4)	2.2-4.7(1.7-5.9)
56	J1313+1441	1.7947	1.7-2.5(1.6-2.9)	-2.7-1.2(-3.0-0.9)	2.3-2.8(2.2-3.1)	4.1-5.2(4.0-5.6)
57	J1310+5424	1.8005	1.6-2.6(1.4-2.9)	-2.8-1.3(-3.1-0.9)	2.1-2.6(2.0-3.0)	3.9-5.0(3.6-5.4)
58	J1106+1044	1.8185	-1.4-0.9(-1.9-2.4)	-3.1-2.1(-3.5-1.6)	1.3-3.6(1.1-4.3)	0.5-3.7(-0.1-5.3)
59	J1142+0701	1.8407	0.9-2.2(0.6-2.8)	-2.6-1.2(-3.0-0.9)	2.3-3.9(2.0-4.4)	3.6-5.6(3.1-6.4)
60	J0815+1037	1.8462	-1.4-0.9(-1.9-2.4)	-3.1-2.1(-3.5-1.5)	1.3-3.6(1.1-4.3)	0.4-3.7(-0.1-5.3)
61	J1335+0824	1.8560	0.2-1.4(0.0-2.7)	-2.7-1.6(-3.1-1.3)	1.7-3.8(1.3-4.3)	2.2-4.7(1.8-5.9)
62	J1024+0600	1.8950	0.9-2.1(0.7-2.8)	-2.8-1.6(-3.2-1.1)	1.6-2.9(1.4-3.8)	2.8-4.5(2.4-5.6)
63	J1524+1030	1.9409	-1.3-2.0(-1.9-2.8)	-3.1-2.0(-3.5-1.2)	1.3-3.1(1.1-4.2)	0.4-4.2(-0.2-5.5)
64	J1042+0628	1.9429	-1.4-1.0(-1.9-2.5)	-3.1-2.0(-3.5-1.5)	1.3-3.6(1.1-4.3)	0.5-3.8(0.0-5.4)
65	J1417+4132	1.9508	-1.0-1.9(-1.8-2.8)	-3.0-1.8(-3.4-1.2)	1.4-3.5(1.1-4.3)	1.0-4.6(0.1-5.8)
66	J1552+4910	1.9599	-0.5-1.4(-0.9-2.7)	-2.9-2.0(-3.2-1.4)	1.5-3.4(1.2-4.2)	1.3-4.0(0.8-5.5)
67	Q1755+578	1.9692	0.7-2.0(0.5-2.7)	-2.5-1.2(-2.9-1.0)	2.5-4.0(2.2-4.4)	3.5-5.5(3.2-6.3)
68	J1305+0924	2.0184	0.6-1.9(0.3-2.8)	-2.8-1.6(-3.1-1.2)	1.6-3.4(1.4-4.2)	2.5-4.7(2.1-5.9)
69	J1509+1113	2.0283	0.7-2.2(0.4-2.8)	-2.9-1.7(-3.2-1.2)	1.5-2.5(1.3-3.3)	2.5-4.3(2.2-5.3)
70	J1135-0010	2.2068	1.7-2.6(1.5-2.9)	-2.5-0.8(-2.8-0.6)	2.8-4.1(2.6-4.4)	4.8-6.4(4.5-6.8)
71	J1211+0422	2.3765	-1.6-0.8(-1.9-2.3)	-3.2-2.3(-3.6-1.6)	1.2-3.4(1.0-4.3)	0.0-3.3(-0.3-5.0)
72	J2241+1225	2.4179	-1.1-1.3(-1.8-2.5)	-3.0-1.8(-3.5-1.2)	1.4-3.7(1.1-4.3)	1.0-4.4(0.2-5.7)

Table A.4: — Continued

Index Number	QSO	z_{abs}	$\log n_{\text{H}}(2-\sigma)$ [cm^{-3}]	$\log n_{\text{e}}(2-\sigma)$ [cm^{-3}]	$\log T(2-\sigma)$ [K]	$\log P/k_{\text{B}}(2-\sigma)$ [K cm^{-3}]
73	J0211+1241	2.5951	-0.4-1.1(-0.7-2.5)	-2.8--1.9(-3.1--1.5)	1.6-3.8(1.3-4.4)	1.6-4.3(1.1-5.7)
74	J0812+3208	2.6263	0.6-2.2(0.2-2.8)	-2.9--1.8(-3.2--1.2)	1.4-2.3(1.3-2.7)	2.2-4.1(1.8-4.9)
75	J1558-0031	2.7026	-1.3-1.0(-1.8-2.5)	-3.1--2.0(-3.5--1.4)	1.3-3.7(1.1-4.3)	0.7-4.0(0.1-5.5)
76	FJ2334-09	3.0569	-1.6-0.9(-1.9-2.4)	-3.3--2.4(-3.7--1.6)	1.1-3.0(1.0-4.2)	-0.2-3.0(-0.5-4.9)
77	J2100-0641	3.0924	0.8-2.3(0.5-2.8)	-2.9--1.7(-3.2--1.1)	1.4-2.2(1.3-2.5)	2.5-4.1(2.1-4.8)
78	J1155+0530	3.3260	-0.2-1.7(-0.7-2.7)	-2.9--2.0(-3.2--1.3)	1.4-2.6(1.2-3.8)	1.5-3.8(1.0-5.2)
79	J0825+3544	3.6567	-0.3-1.5(-1.4-2.6)	-2.8--1.8(-3.2--1.4)	1.5-3.6(1.2-4.3)	1.7-4.4(0.6-5.7)
80	J0909+3303	3.6581	0.6-1.7(-0.3-2.7)	-2.7--1.4(-3.1--1.1)	1.8-3.9(1.4-4.4)	2.7-5.1(1.9-6.1)

Table A.5: HST QSO sample

QSO	z_{em}^a	Instrument	Search Path			Statistical Path			Proposal ID
			F_{search}^b	Min z	Max z	F_{stat}^c	Min z	Max z	
J0000–1245	0.200	COS	1	0.010	0.299	1	0.010	0.188	12604
J0001+0709	3.234	STIS	1	—	—	0	—	—	8569
J0004–4157	2.760	FOS-H	1	1.501	1.695	0	—	—	6577
J0005+0524	1.900	FOS-H	1	0.829	1.695	1	0.829	1.695	4581,6705
J0005–5006	0.033	COS	1	0.010	0.133	1	0.010	0.022	12936
J0005+0202	0.234	FOS-H	1	—	—	1	—	—	5456
J0005+1609	0.450	COS	1	0.010	0.474	1	0.010	0.436	12038
		FOS-H	1	0.475	0.550	1	—	—	3791
J0006+2012	0.025	COS	1	0.010	0.124	1	0.010	0.014	11524
		FOS-H	1	—	—	1	—	—	5182
J0010+1058	0.090	COS	1	0.014	0.189	1	0.014	0.079	12569
		FOS-H	1	—	—	2	—	—	2717
J0012–0122	1.998	STIS	1	0.862	1.604	0	—	—	8569
J0012–1022	0.228	COS	1	0.010	0.328	2	0.010	0.215	12248
J0018+1629	0.553	FOS-H	1	0.378	0.652	2	0.378	0.537	6606
J0018–3529	3.190	STIS	0	—	—	1	—	—	8287
J0020+0226	0.401	FOS-H	1	0.369	0.500	1	0.369	0.387	5456
J0020+2842	0.509	FOS-H	1	—	—	2	—	—	6548
J0021+0104	1.829	STIS	1	0.288	1.589	0	—	—	9382
J0021+0043	1.243	STIS	1	0.505	1.343	0	—	—	9382
J0021–0128	1.588	STIS	1	0.816	1.607	1	0.816	1.562	8126
J0022–0128	1.040	STIS	1	0.410	1.139	1	0.410	1.019	8126
J0027+2242	1.108	FOS-H	1	0.366	1.207	1	0.366	1.087	2424,4117
		FOS-L	1	—	—	1	—	—	2424
J0028+4308	0.097	COS	0	—	—	2	—	—	12533
J0029+1316	0.142	COS	1	0.010	0.192	1	0.010	0.130	12569
		FOS-H	1	0.193	0.241	1	—	—	5451,5682
J0032–2144	0.806	STIS	1	0.533	0.905	1	0.533	0.788	8225
J0036+4316	0.120	COS	1	0.010	0.219	2	0.010	0.108	11632

Table A.5: — Continued

QSO	z_{em}^a	Instrument	Search Path			Statistical Path			Proposal ID
			F_{search}^b	Min z	Max z	F_{stat}^c	Min z	Max z	
J0036–3333	0.020	COS	0	—	—	2	—	—	13017
J0038–3501	1.199	STIS	1	0.404	1.298	1	0.404	1.177	8126
J0038–3504	1.519	STIS	1	0.576	1.610	1	0.576	1.493	8126
J0039–3529	1.095	STIS	1	0.396	1.194	1	0.396	1.074	8126
J0039–3528	0.836	STIS	1	0.424	0.935	1	0.424	0.817	8126
J0040–1109	0.027	COS	0	—	—	1	—	—	12557
J0042–1037	0.423	COS	1	0.010	0.476	2	0.010	0.409	11598
J0043–2622	3.053	STIS	1	1.204	1.608	0	—	—	8569
J0044+1026	0.583	FOS-H	1	0.563	0.682	1	0.563	0.567	5441
J0045+0410	0.384	FOS-H	1	0.369	0.483	1	0.369	0.370	2424
J0047+0319	0.624	COS	1	0.010	0.206	1	0.010	0.206	12275
		FOS-H	1	0.362	0.723	1	0.362	0.607	2424
		FOS-L	1	0.360	0.361	1	0.360	0.361	2424
J0048+3941	0.134	COS	1	0.010	0.233	2	0.010	0.122	11632
J0051+0041	1.188	STIS	1	0.516	1.287	0	—	—	9051
J0053+1241	0.060	COS	1	0.010	0.160	1	0.010	0.050	12569
		FOS-H	1	—	—	1	—	—	5057,5486
J0054+2525	0.155	FOS-H	1	—	—	1	—	—	4396
J0058–3606	0.162	COS	1	0.010	0.261	1	0.010	0.150	12604
J0100–5113	0.062	COS	1	0.010	0.161	1	0.010	0.051	12604
		STIS	1	—	—	2	—	—	9858
J0100+0211	1.954	FOS-H	1	0.526	0.901	0	—	—	6577
J0101+4229	0.190	COS	1	0.010	0.289	2	0.010	0.178	11632
J0102–0853	1.682	STIS	1	0.777	1.598	0	—	—	9051
J0102–2221	0.118	COS	1	0.010	0.179	2	0.010	0.106	12533
J0103+0220	0.394	FOS-H	1	0.362	0.493	1	0.362	0.380	4396,6612
J0103–3009	3.150	STIS	0	—	—	1	—	—	8287
J0104–2657	0.780	FOS-H	1	0.343	0.879	1	0.343	0.762	6007
J0105–2736	0.848	STIS	1	0.527	0.947	1	0.527	0.829	7359

Table A.5: — Continued

QSO	z_{em}^a	Instrument	Search Path			Statistical Path			Proposal ID
			F_{search}^b	Min z	Max z	F_{stat}^c	Min z	Max z	
J0106+0105	1.611	STIS	1	0.900	1.607	0	—	—	9382
J0107−0019	0.737	STIS	1	0.363	0.837	0	—	—	9382
J0109−2307	0.818	STIS	1	0.402	0.917	1	0.402	0.799	8225
J0109−2102	0.000	STIS	0	—	—	1	—	—	8287
J0109−1521	0.861	FOS-H	1	0.830	0.960	2	0.830	0.842	6548
J0110−0219	0.960	COS	1	0.010	0.480	1	0.010	0.480	11585
		FOS-H	1	0.481	0.901	1	0.481	0.901	5320,6100,6592
J0110−0216	0.728	COS	1	0.179	0.482	1	0.179	0.482	11585
J0110−0218	0.956	COS	1	0.010	0.480	1	0.010	0.480	11585
		FOS-H	1	0.481	0.901	1	0.481	0.901	5320,6100
J0110+0019	0.806	STIS	2	—	—	0	—	—	9382
J0111+1753	2.157	FOS-L	0	—	—	1	—	—	5095
J0115−0127	1.365	FOS-H	1	0.879	1.464	1	0.879	1.341	2578
J0116−0043	1.273	STIS	1	0.570	1.373	0	—	—	9382
J0118+0258	0.672	FOS-H	1	0.411	0.771	0	—	—	4260
J0120+2133	1.493	FOS-H	1	0.833	1.592	1	0.833	1.468	4396,5664,6109
		FOS-L	1	0.620	0.832	1	0.620	0.832	4396
J0121−2820	0.116	COS	1	0.010	0.215	1	0.010	0.104	12204
J0122−0421	1.925	FOS-H	1	0.833	1.695	0	—	—	6577,6589
J0122+1339	3.063	STIS	0	—	—	1	—	—	9067
J0122−2843	0.434	COS	1	0.010	0.479	1	0.010	0.419	12204
J0123−0058	1.549	STIS	1	0.867	1.590	0	—	—	9382
J0123−5848	0.047	COS	1	0.010	0.146	1	0.010	0.036	12604
		FOS-H	1	—	—	1	—	—	4045
J0125−0006	1.070	COS	1	0.158	0.477	2	0.158	0.477	13398
		FOS-H	1	0.478	1.169	1	0.478	1.049	2424
J0126−2222	0.717	STIS	1	0.375	0.816	1	0.375	0.699	8225
J0126−0105	1.609	STIS	1	0.677	1.597	0	—	—	9382
J0127−0619	0.005	FOS-H	1	—	—	1	—	—	5408

Table A.5: — Continued

QSO	z_{em}^a	Instrument	Search Path			Statistical Path			Proposal ID
			F_{search}^b	Min z	Max z	F_{stat}^c	Min z	Max z	
J0128–3029	0.475	STIS	1	0.010	0.411	1	0.010	0.411	9506
J0132+0116	1.786	STIS	0	—	—	0	—	—	9382
J0134+0051	1.522	STIS	1	0.855	1.597	0	—	—	9382
J0136+2057	0.425	FOS-H	1	0.380	0.524	1	0.380	0.410	3858
J0137–2430	0.831	STIS	1	0.350	0.930	1	0.350	0.812	8225
J0138–0005	1.340	STIS	1	0.701	1.439	0	—	—	9382
J0139–0023	1.384	STIS	1	0.608	1.483	0	—	—	9382
J0139+0619	0.396	STIS	1	0.010	0.495	1	0.010	0.382	9894
J0139+0131	0.260	FOS-H	1	0.010	0.359	1	0.010	0.247	5441
J0141–0024	2.611	STIS	1	1.447	1.598	0	—	—	9051
J0141+1340	0.045	COS	1	0.010	0.145	1	0.010	0.034	12275
J0144+3411	1.450	FOS-L	1	0.113	0.994	0	—	—	6577
J0145–0120	3.124	FOS-H	1	1.023	1.695	0	—	—	6577
J0145–3520	0.446	STIS	1	0.291	0.545	1	0.291	0.431	9507
J0148+3854	1.442	FOS-L	1	0.335	1.065	1	0.335	1.065	4396
J0152–2001	2.139	FOS-H	1	0.993	1.695	1	0.993	1.695	3199
		FOS-L	1	0.113	0.992	1	0.113	0.992	3051
J0152+0023	0.589	STIS	1	0.388	0.688	0	—	—	9382
J0153+0052	1.162	STIS	1	0.571	1.262	0	—	—	9382
J0153+0009	0.837	STIS	1	0.452	0.936	0	—	—	9382
J0154+0448	0.404	COS	1	0.010	0.211	0	—	—	12536
J0155–4506	0.451	COS	1	0.010	0.476	1	0.010	0.436	11541
J0155–0857	0.164	COS	1	0.010	0.264	2	0.010	0.153	12248
J0157–0048	1.545	STIS	1	0.843	1.604	0	—	—	9382
J0157–0106	3.562	STIS	0	—	—	1	—	—	9067
J0159+0023	0.163	COS	1	0.010	0.208	1	0.010	0.151	12569
J0159+1345	0.503	COS	1	0.010	0.208	2	0.010	0.208	12603
J0201–1132	0.669	COS	1	0.010	0.474	1	0.010	0.474	12038
		FOS-H	1	0.475	0.768	1	0.475	0.652	5664

Table A.5: — Continued

QSO	z_{em}^{a}	Instrument	Search Path			Statistical Path			Proposal ID
			$F_{\text{search}}^{\text{b}}$	Min z	Max z	$F_{\text{stat}}^{\text{c}}$	Min z	Max z	
J0202–7620	0.389	COS	1	0.010	0.457	1	0.010	0.375	12263
J0208–0503	1.850	STIS	1	0.752	1.601	0	—	—	9051
J0209–3939	2.813	FOS-H	1	1.627	1.695	1	1.627	1.695	6093
J0209–0438	1.130	COS	1	0.049	0.480	2	0.049	0.480	12264
J0210–0152	2.370	STIS	1	—	—	0	—	—	9051
J0212–0737	0.173	COS	1	0.010	0.273	2	0.010	0.162	12248
J0217+1104	0.408	FOS-H	1	0.370	0.507	1	0.370	0.393	5441
J0222+4221	1.181	COS	1	0.010	0.179	2	0.010	0.179	12904
J0222+4302a	0.340	COS	1	0.010	0.439	1	0.010	0.326	12863
J0222+4302b	0.444	FOS-H	1	0.010	0.543	0	—	—	4061
J0226+0015	0.615	COS	1	0.010	0.477	2	0.010	0.477	11598
J0228–4057	0.493	COS	1	0.010	0.476	1	0.010	0.476	11541
J0230–0859	0.016	COS	1	0.010	0.116	1	—	—	12212
J0231+1322	2.065	FOS-L	0	—	—	0	—	—	6577
J0232+3423	1.238	STIS	0	—	—	0	—	—	8569
J0234–0847	0.043	COS	1	0.010	0.142	1	0.010	0.032	12953
J0235–0401	1.450	FOS-H	1	0.829	1.549	1	0.829	1.425	4799,5664
J0235–0402	1.438	COS	1	0.010	0.480	1	0.010	0.480	11741
		FOS-L	1	0.516	1.065	1	0.516	1.065	4799
J0240–1851	0.631	COS	1	0.010	0.476	1	0.010	0.476	11541
		STIS	1	—	—	1	—	—	9506
J0241+0711	0.027	COS	1	0.010	0.127	1	0.010	0.017	12275
J0241–1514	2.786	STIS	1	—	—	0	—	—	8569
J0242–0759	0.375	COS	1	0.010	0.474	2	0.010	0.361	12248
J0243–7216	0.102	COS	1	0.010	0.201	1	0.010	0.091	12263
J0243–3030	0.670	COS	1	0.010	0.210	2	0.010	0.210	12988
J0244–2904	0.000	STIS	0	—	—	1	—	—	8287
J0245–3007	0.340	COS	1	0.010	0.210	2	0.010	0.210	12988
J0246–3007	0.522	COS	1	0.010	0.210	2	0.010	0.210	12988

Table A.5: — Continued

QSO	z_{em}^{a}	Instrument	Search Path			Statistical Path			Proposal ID
			$F_{\text{search}}^{\text{b}}$	Min z	Max z	$F_{\text{stat}}^{\text{c}}$	Min z	Max z	
J0248–3038	1.093	COS	1	0.010	0.210	2	0.010	0.210	12988
J0251+4315	1.310	FOS-L	1	0.113	0.994	0	—	—	6577
J0253+0107	1.035	STIS	1	0.722	1.135	0	—	—	9382
J0253–5441	0.537	STIS	1	0.294	0.636	1	0.294	0.521	9507
J0255–0818	0.625	COS	1	0.161	0.459	0	—	—	12593
J0256+0110	1.345	STIS	1	0.899	1.445	0	—	—	9382
J0256–0126	0.879	FOS-H	1	0.835	0.978	1	0.835	0.860	4396
		FOS-L	1	0.391	0.834	1	0.391	0.834	4396
J0256–3315a	1.915	FOS-H	1	1.064	1.695	1	1.064	1.695	5320,5631
J0256–3315b	1.863	STIS	1	0.012	0.411	0	—	—	8569
J0259+0037	0.533	COS	1	0.010	0.477	2	0.010	0.477	12248
J0304–0008	3.290	COS	1	0.067	0.200	0	—	—	12033
		STIS	1	0.060	1.607	1	0.060	1.607	7272,7575
J0304–2212	1.400	FOS-H	1	0.828	1.499	0	—	—	6224
J0307–7250	0.027	COS	1	0.010	0.127	1	0.010	0.017	12263
J0308–3250	0.247	STIS	1	0.020	0.346	1	0.020	0.234	9506
J0310–0049	0.080	COS	1	0.010	0.180	2	0.010	0.069	12248
J0311–6039	0.000	STIS	0	—	—	1	—	—	8287
J0318–2012	2.869	STIS	1	1.442	1.605	0	—	—	8569
J0319+4130	0.017	COS	1	—	—	1	—	—	12260
J0329–2357	0.895	STIS	1	0.871	0.994	1	0.871	0.876	8225
J0336–3607	1.093	FOS-H	1	1.027	1.192	1	1.027	1.072	4396
		FOS-L	1	0.730	1.026	1	0.730	1.026	4396
J0336+3218	1.258	FOS-H	1	1.130	1.357	1	1.130	1.235	5441
J0349–5344	0.130	STIS	1	0.010	0.229	2	0.010	0.118	9858
J0351–1429	0.614	COS	1	0.010	0.462	2	0.010	0.462	13398
		FOS-H	1	0.463	0.713	1	0.463	0.597	2424
J0352–0710	0.962	FOS-H	1	0.834	1.061	1	0.834	0.942	4396
J0354–2724	2.823	STIS	1	—	—	0	—	—	8569

Table A.5: — Continued

QSO	z_{em}^a	Instrument	Search Path			Statistical Path			Proposal ID
			F_{search}^b	Min z	Max z	F_{stat}^c	Min z	Max z	
J0355–5451	0.269	STIS	1	—	—	1	—	—	9507
J0357–4812	1.005	FOS-H	1	0.834	1.104	1	0.834	0.985	4396,6103
		FOS-L	1	0.720	0.833	1	0.720	0.833	4396,6103
J0401–0540	0.570	COS	1	0.010	0.476	2	0.010	0.476	11598
J0405–1308	0.571	FOS-H	1	0.434	0.670	1	0.434	0.555	2578
J0407–1211	0.574	COS	1	0.010	0.476	1	0.010	0.476	11541
		FOS-H	1	0.477	0.673	1	0.477	0.558	1025,3837
J0411–4956	0.817	STIS	1	0.289	0.916	1	0.289	0.798	9507
J0416–2056	0.807	STIS	1	0.383	0.907	1	0.383	0.789	8225
J0417–0554	0.781	FOS-H	1	0.346	0.880	1	0.346	0.763	3269,5664
J0423–0120	0.915	FOS-H	1	0.882	1.014	1	0.882	0.895	2424,4044,6799
		STIS	1	0.477	0.881	0	—	—	8569
J0424+0204	2.044	FOS-H	1	0.833	1.696	0	—	—	6577
J0426–5712	0.104	COS	1	0.010	0.203	2	0.010	0.093	11692
J0427–1303	2.159	FOS-H	1	1.299	1.696	0	—	—	6577
J0430–5336	0.039	COS	1	0.010	0.139	1	0.010	0.029	12275
J0436–5258	1.231	COS	1	0.010	0.476	1	0.010	0.476	11520
		STIS	1	—	—	1	—	—	9506
J0438–2608	0.690	STIS	2	—	—	1	—	—	9507
J0438–6147	0.069	COS	1	0.010	0.168	2	0.010	0.058	11692
J0439–2422	0.840	STIS	1	0.384	0.940	1	0.384	0.821	8225
J0439–5311	0.243	COS	1	0.010	0.342	1	0.010	0.230	11520
		STIS	1	—	—	1	—	—	9506
J0439–4540	0.224	STIS	1	0.010	0.323	1	0.010	0.211	9894
J0440–5248	1.053	COS	1	0.010	0.476	1	0.010	0.476	11520
		STIS	1	—	—	1	—	—	9506
J0441–4313	0.593	COS	1	0.010	0.179	0	—	—	12536
		FOS-H	1	0.343	0.692	1	0.343	0.577	4581
		STIS	1	0.180	0.342	0	—	—	9382

Table A.5: — Continued

QSO	z_{em}^a	Instrument	Search Path			Statistical Path			Proposal ID
			F_{search}^b	Min z	Max z	F_{stat}^c	Min z	Max z	
J0443–2820	0.155	STIS	1	—	—	1	—	—	9507
J0448+0950	2.110	STIS	0	—	—	0	—	—	8569
J0448–2044	1.896	FOS-L	0	—	—	1	—	—	4396
J0449–3911	1.288	FOS-L	1	0.292	1.065	1	0.292	1.065	4396
J0452–1640	2.600	STIS	1	0.583	1.606	0	—	—	8569
J0452–2953	0.286	FOS-H	1	—	—	1	—	—	6799
J0452–2201	0.898	STIS	1	0.626	0.998	1	0.626	0.879	8225
J0453–1305	2.300	STIS	1	1.319	1.605	0	—	—	8569
J0455–4216	2.660	FOS-H	1	1.489	1.695	0	—	—	6577
J0456–2159	0.533	COS	1	0.139	0.446	2	0.139	0.446	12252
		FOS-H	1	0.069	0.633	0	—	—	1026
J0456+0400	1.345	FOS-H	1	0.428	1.444	0	—	—	5351,5451
J0503–6633	0.064	COS	1	0.010	0.163	2	0.010	0.053	11692
J0504–2944	0.552	STIS	1	0.010	0.651	1	0.010	0.536	9506,9507
J0506–6109	1.093	FOS-H	1	0.988	1.192	1	0.988	1.072	4396
J0509–3232	1.567	STIS	0	—	—	1	—	—	9506
J0514–3326	1.569	STIS	1	0.615	1.611	0	—	—	9165
J0538–4405	0.894	FOS-H	1	0.878	0.993	1	—	—	4396
J0552–6402	0.680	COS	1	0.010	0.438	2	0.010	0.438	11692
J0559–5026	0.137	COS	1	0.010	0.236	2	0.010	0.125	11692
J0612–1415	0.035	COS	0	—	—	1	—	—	12275
J0623–6436	0.129	COS	1	0.010	0.228	2	0.010	0.117	11692
J0630+6904	0.374	FOS-H	1	0.010	0.473	1	0.010	0.360	3791,4112,4818,5664
J0635–7516	0.656	COS	1	0.010	0.438	2	0.010	0.438	11692
		FOS-H	1	0.439	0.755	1	0.439	0.639	4044
J0713+1146	0.768	FOS-H	1	0.426	0.867	1	0.426	0.750	2578
J0714+7408	0.371	COS	1	0.010	0.206	1	0.010	0.206	12275
J0719+7427	0.475	COS	1	0.010	0.206	1	0.010	0.206	12275
J0721+7120	0.300	COS	1	0.010	0.399	1	0.010	0.287	12025

Table A.5: — Continued

QSO	z_{em}^a	Instrument	Search Path			Statistical Path			Proposal ID
			F_{search}^b	Min z	Max z	F_{stat}^c	Min z	Max z	
J0732+6159	0.325	STIS	1	0.010	0.411	1	0.010	0.311	9506
J0739+8146	1.024	STIS	1	0.571	1.123	0	—	—	8569
J0741+3111	0.630	FOS-L	1	0.115	0.729	0	—	—	6577
J0743-6726	1.511	FOS-H	1	0.829	1.610	1	0.829	1.485	5225,6109
J0744+3753	1.063	FOS-H	1	0.942	1.162	1	0.942	1.042	2578
J0744+3208	1.051	STIS	0	—	—	0	—	—	9051
J0745+3143	0.462	FOS-H	1	0.387	0.561	1	0.387	0.447	3791
J0749+4152	3.105	STIS	0	—	—	1	—	—	9067
J0751+2919	0.914	COS	1	0.010	0.480	1	0.010	0.480	11741
J0753+4231	3.590	STIS	0	—	—	1	—	—	9067
J0800+4435	2.505	STIS	0	—	—	1	—	—	9067
J0800+3051	4.666	STIS	0	—	—	0	—	—	9759
J0801+5210	3.234	STIS	0	—	—	1	—	—	9506
J0803+4332	0.448	COS	1	0.010	0.476	2	0.010	0.434	11598
J0804+6459	0.148	STIS	2	—	—	1	—	—	7617
J0806+5041	2.432	STIS	1	0.784	1.599	0	—	—	9051
J0808+0514	0.360	COS	1	0.010	0.206	2	0.010	0.206	12603
J0809+4619	0.657	COS	1	0.010	0.477	2	0.010	0.477	12248
J0810+7602	0.100	COS	1	0.010	0.199	1	0.010	0.089	11686
J0813+4813	3.163	FOS-L	1	—	—	0	—	—	5351,3939,1193
J0814+5029	3.883	STIS	0	—	—	1	—	—	9067
J0820+2334	0.470	COS	1	0.010	0.476	2	0.010	0.455	11598
J0825+5127	3.511	STIS	0	—	—	1	—	—	9067
J0826-2230	0.910	FOS-H	1	0.828	1.009	0	—	—	6577
J0826+0742	0.310	COS	1	0.010	0.410	2	0.010	0.297	12248
J0827+1052	2.295	STIS	1	—	—	0	—	—	8569
J0830+2410	0.939	FOS-H	1	0.856	1.038	1	0.856	0.919	5441
		FOS-L	1	0.113	0.855	0	—	—	6577
J0835+2459	0.331	COS	1	0.010	0.430	1	0.010	0.317	12025

Table A.5: — Continued

QSO	z_{em}^a	Instrument	Search Path			Statistical Path			Proposal ID
			F_{search}^b	Min z	Max z	F_{stat}^c	Min z	Max z	
J0838+5406	0.029	COS	1	—	—	1	—	—	12557
J0839+5256	1.545	STIS	1	—	—	1	—	—	9067
J0840+1312	0.684	FOS-H	1	0.421	0.783	1	0.421	0.667	2578
J0843+4117	0.990	COS	1	0.010	0.476	2	0.010	0.476	12248
J0844+7653	0.131	COS	1	0.010	0.231	1	0.010	0.120	11520
J0845+1328	1.877	FOS-L	1	0.113	0.994	0	—	—	6577
J0847+3445	0.064	COS	1	0.010	0.163	1	0.010	0.053	12569
		FOS-H	1	—	—	2	—	—	2717
J0851+1612	1.936	FOS-H	1	1.200	1.697	1	1.200	1.697	6589
J0852+0313	0.297	COS	1	0.010	0.210	2	0.010	0.210	12603
J0853+4349	0.513	COS	1	0.010	0.124	2	0.010	0.124	13398
		FOS-H	1	0.366	0.612	1	0.366	0.497	2424
		FOS-L	1	0.279	0.365	1	0.279	0.365	2424
J0854+2006	0.306	FOS-H	1	—	—	1	—	—	3201,4817,5664
J0857+1855	1.892	STIS	0	—	—	0	—	—	8569
J0859+4637	0.923	FOS-L	1	0.496	1.022	1	0.496	0.903	4952
J0902−1415	1.327	FOS-H	1	0.889	1.426	1	0.889	1.303	3858
J0904+1309	0.000	STIS	0	—	—	1	—	—	8287
J0906+1646	0.411	FOS-H	1	0.376	0.510	1	0.376	0.396	2578
J0909+3236	0.808	COS	1	0.010	0.210	2	0.010	0.210	12603
J0909−0932	0.625	FOS-H	1	—	—	2	—	—	6548
J0909+4254	0.670	FOS-H	1	0.655	0.769	1	—	—	3858
J0910+1014	0.463	COS	1	0.010	0.477	2	0.010	0.448	11598
J0912+2450	0.654	STIS	1	0.011	0.410	1	0.011	0.410	9506
J0912+2957	0.305	COS	1	0.010	0.405	2	0.010	0.292	12248
J0914+0837	0.648	COS	1	0.010	0.210	2	0.010	0.210	12603
J0914+2823	0.735	COS	1	0.010	0.476	2	0.010	0.476	11598
J0915+4756	3.336	COS	1	0.010	0.124	0	—	—	12816
J0915+4426	3.944	STIS	0	—	—	0	—	—	9759

Table A.5: — Continued

QSO	z_{em}^a	Instrument	Search Path			Statistical Path			Proposal ID
			F_{search}^b	Min z	Max z	F_{stat}^c	Min z	Max z	
J0919+5521	0.122	COS	1	0.010	0.222	1	0.010	0.111	12029
J0919+5105	0.553	FOS-H	1	0.345	0.652	1	0.345	0.537	2424
		FOS-L	1	0.299	0.344	1	0.299	0.344	2424
J0925+4535	0.329	COS	1	0.010	0.429	2	0.010	0.316	12248
J0925+4004	0.470	COS	1	0.010	0.476	2	0.010	0.456	11598
J0925+1954	0.192	COS	1	0.010	0.193	1	0.010	0.180	12569
J0926+3055	4.190	STIS	0	—	—	1	—	—	8582
J0927+3902	0.699	FOS-H	1	0.355	0.798	1	0.355	0.682	2578,4052
J0928+6025	0.295	COS	1	0.010	0.395	2	0.010	0.282	11598
J0929+4644	0.240	COS	1	0.010	0.340	2	0.010	0.227	12248
J0930+2848	0.486	COS	1	0.010	0.210	2	0.010	0.210	12603
J0931+2628	0.778	COS	1	0.010	0.210	2	0.010	0.210	12603
J0935+0204	0.659	COS	1	0.010	0.476	2	0.010	0.476	11598
J0936+3207	1.149	COS	1	0.010	0.206	2	0.010	0.206	12603
J0937+1700	0.506	COS	1	0.010	0.207	2	0.010	0.207	12603
J0937+7301	2.528	FOS-H	1	1.516	1.695	0	—	—	6577
J0938+4128	1.937	FOS-H	1	0.856	1.696	1	0.856	1.696	5664,6237
J0943+0531	0.564	COS	1	0.010	0.476	2	0.010	0.476	11598
J0944+2554	2.910	STIS	1	1.472	1.592	0	—	—	8569
J0946+4711	0.230	COS	1	0.010	0.330	2	0.010	0.218	12248
J0947+1005	0.138	COS	1	0.010	0.238	2	0.010	0.127	12248
J0948+4323	1.892	STIS	1	0.804	1.598	0	—	—	9051
J0948+4039	1.252	FOS-H	1	0.901	1.351	1	0.901	1.229	5441
J0949+5445	1.376	COS	1	0.142	0.440	0	—	—	12593
J0949-0514	1.098	COS	1	0.167	0.460	0	—	—	12593
J0949+2955	1.221	STIS	2	—	—	0	—	—	8284,3200
J0949+3902	0.360	COS	1	0.010	0.459	2	0.010	0.346	12248
J0950+4831	0.588	COS	1	0.010	0.429	2	0.010	0.429	11598
J0950+5846	0.151	STIS	0	—	—	1	—	—	9067

Table A.5: — Continued

QSO	z_{em}^a	Instrument	Search Path			Statistical Path			Proposal ID
			F_{search}^b	Min z	Max z	F_{stat}^c	Min z	Max z	
J0950+5801	3.970	STIS	0	—	—	1	—	—	8582
J0951+3307	0.644	COS	1	0.012	0.210	2	0.012	0.210	12486
J0951+3542	0.400	COS	1	0.010	0.210	2	0.010	0.210	12603
J0953-0038	1.382	STIS	1	0.550	1.481	0	—	—	9382
J0954+1743	1.478	FOS-L	1	0.114	1.063	0	—	—	6577
J0955+5940	4.340	STIS	0	—	—	1	—	—	9067
J0956-0453	0.150	COS	1	0.010	0.206	1	0.010	0.138	12275
J0956+4115	0.234	COS	1	0.010	0.334	1	0.010	0.221	12038
		FOS-H	1	—	—	1	—	—	1018,3220
J0957+5440	2.584	FOS-H	1	1.649	1.695	0	—	—	6577
J0957+5522	0.909	FOS-H	1	0.437	1.008	1	0.437	0.889	4052
J0958+3224	0.530	FOS-H	1	0.143	0.630	1	0.143	0.514	3566,4952,5451
		STIS	1	0.010	0.142	1	0.010	0.142	9506
J0958+5550	1.021	COS	0	—	—	0	—	—	12593
J0959+3203	0.563	COS	1	0.010	0.205	2	0.010	0.205	12603
J0959+0503	0.161	COS	1	0.010	0.261	2	0.010	0.150	12248
J1000+0005	0.905	STIS	1	0.291	1.005	0	—	—	8569
J1001+5944	0.746	COS	1	0.010	0.476	2	0.010	0.476	12248
J1001+5553	1.415	FOS-H	1	0.830	1.514	1	0.830	1.390	5683,5781
		FOS-H	1	—	—	1	—	—	5683,5781
		STIS	1	0.808	0.829	0	—	—	8336,5683
		FOS-L	1	0.113	0.807	0	—	—	8336,5683
J1001+5454	1.750	FOS-H	1	1.058	1.697	1	1.058	1.697	5664
		FOS-L	1	0.993	1.057	0	—	—	6577
J1001+5610	3.216	STIS	0	—	—	1	—	—	8582
J1001+2847	0.185	FOS-H	1	—	—	1	—	—	6616
J1002+3240	0.828	COS	1	0.010	0.210	2	0.010	0.210	12603
J1003+6813	0.773	FOS-H	1	0.367	0.872	1	0.367	0.755	3791
		FOS-L	1	—	—	1	—	—	3791

Table A.5: — Continued

QSO	z_{em}^a	Instrument	Search Path			Statistical Path			Proposal ID
			F_{search}^b	Min z	Max z	F_{stat}^c	Min z	Max z	
J1004+2855	0.329	COS	1	0.010	0.428	1	0.010	0.315	12038
		FOS-H	1	—	—	1	—	—	3418,4044
J1004+0513	0.161	FOS-H	1	0.010	0.260	1	0.010	0.149	6247,6781
J1004+2225	0.974	FOS-H	1	0.929	1.073	1	0.929	0.954	5441
J1005+0134	1.077	COS	1	0.010	0.480	2	0.010	0.480	12264
J1007+0042	1.681	STIS	0	—	—	0	—	—	9382
J1007+1248	0.240	COS	1	0.010	0.193	1	0.010	0.193	12569
		STIS	1	—	—	1	—	—	9432
J1007+3638	1.034	COS	1	0.162	0.459	0	—	—	12593
J1008-0223	0.000	STIS	0	—	—	1	—	—	9067
J1008-0018	1.350	STIS	1	0.497	1.449	0	—	—	9382
J1009+0713	0.455	COS	1	0.023	0.476	2	0.023	0.441	11598
J1009-1226	0.693	STIS	1	0.289	0.792	1	0.289	0.676	9507
J1009-0026	1.244	STIS	1	0.532	1.343	0	—	—	9382
J1009+0036	1.702	STIS	1	0.686	1.590	0	—	—	9382
J1010+3003	0.255	COS	1	0.010	0.355	1	0.010	0.243	12025
J1010+0003	1.399	STIS	1	0.732	1.498	0	—	—	9382
J1010+4132	0.611	FOS-H	1	0.340	0.710	1	0.340	0.594	3791
		FOS-L	1	0.305	0.339	1	0.305	0.339	3791
J1010-0047	1.671	STIS	1	0.770	1.594	0	—	—	9382
J1011+1304	1.287	FOS-H	1	0.830	1.386	1	0.830	1.264	4581,4952
		FOS-L	1	0.437	0.829	1	0.437	0.829	4952
J1013+3551	0.070	COS	1	0.010	0.169	1	0.010	0.059	12275
		FOS-H	1	—	—	1	—	—	3065
J1013+0500	0.265	COS	1	0.010	0.210	2	0.010	0.210	12603
J1013+5615	3.613	STIS	0	—	—	1	—	—	8582
J1014-0418	0.058	COS	1	0.010	0.157	1	0.010	0.047	11524
J1014+4300	3.125	STIS	0	—	—	1	—	—	8287
J1016+4706	0.821	COS	1	0.010	0.430	2	0.010	0.430	11598

Table A.5: — Continued

QSO	z_{em}^{a}	Instrument	Search Path			Statistical Path			Proposal ID
			$F_{\text{search}}^{\text{b}}$	Min z	Max z	$F_{\text{stat}}^{\text{c}}$	Min z	Max z	
J1017+5924	0.850	COS	1	0.162	0.459	0	—	—	12593
J1017+5356	1.400	STIS	1	0.757	1.499	0	—	—	9051
J1019+2743	1.928	FOS-H	1	0.968	1.695	1	0.968	1.695	5664
J1021+3437	1.405	COS	1	0.231	0.460	0	—	—	12593
J1022+0132	0.789	COS	1	0.010	0.476	2	0.010	0.476	11598
J1022+3041	1.317	STIS	1	0.014	0.411	0	—	—	8569
J1022+3931	0.603	COS	1	0.162	0.460	0	—	—	12593
J1022+0101	1.563	STIS	1	0.929	1.593	0	—	—	9382
J1024+1912	0.828	FOS-L	1	0.312	0.927	1	0.312	0.809	2424
J1026+6136	3.848	STIS	0	—	—	1	—	—	9067
J1026+6746	1.181	STIS	0	—	—	1	—	—	9506
J1027+1834	2.840	COS	1	0.010	0.124	0	—	—	12816
J1028–0100a	1.437	FOS-H	1	0.830	1.536	1	0.830	1.412	6819
J1028–0100b	1.530	FOS-H	1	0.834	1.629	1	0.834	1.504	6819
		STIS	1	0.397	0.833	0	—	—	9382
J1031+3102	0.178	FOS-H	1	—	—	2	—	—	5934
J1031+5053	0.361	COS	1	0.010	0.460	1	0.010	0.347	12025
		STIS	1	—	—	1	—	—	9506
J1031–0036	1.258	STIS	0	—	—	0	—	—	9382
J1032+5051	0.173	COS	1	0.010	0.273	1	0.010	0.161	12025
		STIS	1	—	—	1	—	—	9506
J1032+6502	0.005	COS	1	—	—	1	—	—	12557
J1032+0003	1.190	STIS	1	0.652	1.289	0	—	—	9382
J1033+2112	0.315	COS	1	0.010	0.210	2	0.010	0.210	12603
J1037+0028	1.733	STIS	1	0.871	1.594	0	—	—	9382
J1038–2752	2.168	FOS-L	0	—	—	0	—	—	6577
J1040+1053	0.136	COS	0	—	—	2	—	—	12533
J1040+5145	4.045	STIS	0	—	—	0	—	—	9759
J1041+0610	1.270	COS	1	0.149	0.452	2	0.149	0.452	12252

Table A.5: — Continued

QSO	z_{em}^a	Instrument	Search Path			Statistical Path			Proposal ID
			F_{search}^b	Min z	Max z	F_{stat}^c	Min z	Max z	
		FOS-H	1	0.829	1.369	1	0.829	1.247	2424,5664
		FOS-L	1	0.453	0.828	1	0.453	0.828	2424
J1042+1203	1.028	FOS-L	1	0.433	1.065	1	0.433	1.007	2424
J1047+1304	0.399	COS	1	0.010	0.187	1	0.010	0.187	12198
J1047-0047	0.740	STIS	1	0.418	0.839	0	—	—	9382
J1048+1207	0.291	COS	1	0.010	0.187	1	0.010	0.187	12198
J1048+1306	0.218	COS	1	0.010	0.318	1	0.010	0.206	12198
J1048+0032	1.649	STIS	1	0.690	1.591	0	—	—	9382
J1050+5447	2.165	FOS-H	1	0.990	1.696	0	—	—	5948
J1051+1247	1.281	COS	0	—	—	2	—	—	12603
J1051+3359	0.167	COS	1	0.010	0.267	2	0.010	0.155	12024
J1051-0051	0.357	COS	1	0.010	0.456	2	0.010	0.343	12248
		FOS-H	1	—	—	1	—	—	2424
		STIS	1	—	—	2	—	—	7295
J1052+6125	0.421	FOS-L	1	0.114	0.520	0	—	—	6577
J1054-0020	1.021	STIS	1	0.290	1.120	0	—	—	9382
J1057-0139	0.000	STIS	0	—	—	1	—	—	9067
J1058+1951	1.110	FOS-H	1	1.019	1.209	1	1.019	1.088	2424,5441
		FOS-L	1	0.535	1.018	1	0.535	1.018	2424
J1059+0519	0.754	COS	1	0.010	0.210	2	0.010	0.210	12603
J1059+1441	0.630	COS	1	0.010	0.476	2	0.010	0.476	12248
J1059+1211	0.992	COS	1	0.010	0.207	2	0.010	0.207	12603
J1059+2517	0.662	COS	1	0.010	0.477	2	0.010	0.477	12248
J1100+1046	0.421	COS	1	0.010	0.205	2	0.010	0.205	12603
J1103+4141	0.401	COS	1	0.010	0.476	2	0.010	0.387	12248
J1103-2645	2.145	FOS-H	1	1.138	1.695	1	1.138	1.695	5664
J1103-3251	0.354	COS	1	0.010	0.206	1	0.010	0.206	12275
J1103-2329	0.186	COS	1	0.010	0.285	1	0.010	0.174	12025
J1103+3715	1.294	STIS	1	0.933	1.394	0	—	—	9051

Table A.5: — Continued

QSO	z_{em}^a	Instrument	Search Path			Statistical Path			Proposal ID
			F_{search}^b	Min z	Max z	F_{stat}^c	Min z	Max z	
J1104+3141	0.434	COS	1	0.010	0.457	2	0.010	0.420	12248
J1104+7658	0.311	FOS-H	1	0.010	0.410	1	0.010	0.297	2424,4939
J1104-1016	0.186	STIS	1	—	—	1	—	—	9507
J1104+3812	0.030	COS	1	0.010	0.130	1	0.010	0.020	11520
J1105+3425	0.509	COS	1	0.010	0.476	1	0.010	0.476	11541
J1106+6400	2.190	FOS-H	1	0.347	1.696	1	0.347	1.696	5950
J1106-0052	0.425	FOS-H	1	0.402	0.524	1	0.402	0.410	3858
		STIS	1	0.077	0.401	2	0.077	0.401	7295
J1106-1821	2.303	FOS-H	1	1.006	1.695	0	—	—	5951
		FOS-H	1	1.002	1.005	0	—	—	5951
J1106+7234	0.008	COS	1	0.010	0.108	1	—	—	12212
J1107+1628	0.634	FOS-H	1	0.342	0.733	1	0.342	0.617	3791
		FOS-L	1	—	—	1	—	—	3791
J1107+0048	1.390	STIS	1	0.502	1.490	0	—	—	9382
J1107+0003	1.726	STIS	1	0.788	1.590	0	—	—	9382
J1108+3133	2.243	STIS	1	0.884	1.599	0	—	—	9051
J1108-0802	0.340	STIS	1	—	—	1	—	—	9507
J1109+0051	0.957	STIS	1	0.423	1.056	0	—	—	9382
J1110+4831	2.960	STIS	0	—	—	1	—	—	9506
J1110+3019	1.521	STIS	1	0.795	1.593	0	—	—	9051
J1110+0048	0.761	STIS	0	—	—	0	—	—	9382
J1111+5547	0.765	COS	1	0.010	0.480	1	0.010	0.480	12025
J1112+3539	0.635	COS	1	0.010	0.476	2	0.010	0.476	11598
J1112+0013	1.433	STIS	1	0.290	1.532	0	—	—	9382
J1114+4037	0.734	FOS-H	1	0.406	0.833	1	0.406	0.716	2578
J1115+4249	0.300	COS	1	0.010	0.207	1	0.010	0.207	12275
J1115+0237	0.566	COS	1	0.010	0.210	2	0.010	0.210	12603
J1117+4413	0.144	FOS-H	1	0.010	0.243	1	0.010	0.132	6484,6781
J1117+2634	0.422	COS	1	0.010	0.457	2	0.010	0.407	12248

Table A.5: — Continued

QSO	z_{em}^a	Instrument	Search Path			Statistical Path			Proposal ID
			F_{search}^b	Min z	Max z	F_{stat}^c	Min z	Max z	
J1118+0746	1.722	FOS-H	1	0.830	1.696	1	0.830	1.694	5681,6222
		FOS-H	1	1.697	1.697	1	—	—	5681,6222
J1118+0745	1.735	COS	1	0.010	0.210	2	0.010	0.210	12603
J1118+4025	0.154	COS	1	0.010	0.254	2	0.010	0.143	11519
		FOS-H	1	—	—	1	—	—	6781
J1119+2119	0.176	COS	1	0.010	0.276	1	0.010	0.164	12038
		FOS-H	1	—	—	1	—	—	4115,6781
J1119+6004	2.638	STIS	0	—	—	1	—	—	9506
J1120+0413	0.545	COS	1	0.010	0.210	2	0.010	0.210	12603
J1120-4315	0.056	COS	1	0.010	0.156	1	0.010	0.046	12275
J1121+0325	0.152	COS	1	0.010	0.252	2	0.010	0.140	12248
J1121+1236	0.685	FOS-H	1	0.428	0.784	1	0.428	0.668	5441
J1122+0318	0.474	COS	1	0.010	0.210	2	0.010	0.210	12603
J1122+5755	0.900	COS	1	0.010	0.476	2	0.010	0.476	12248
J1124+4201	0.234	COS	1	0.010	0.333	2	0.010	0.221	12024
		FOS-H	1	—	—	1	—	—	5456
J1124-1705	2.400	FOS-H	1	0.347	1.696	1	0.347	1.696	5950
J1125+5910	0.852	COS	1	0.010	0.476	1	0.010	0.476	11520
		STIS	1	—	—	1	—	—	4952,9874
		FOS-L	1	0.548	0.952	1	0.548	0.833	4952,9874
J1126+0034	1.783	STIS	1	1.111	1.593	0	—	—	9382
J1126+3918	1.470	FOS-L	0	—	—	1	—	—	4952
J1126+5134	0.026	COS	0	—	—	1	—	—	12557
J1126-0141	0.046	COS	1	0.012	0.146	1	0.012	0.036	12275
J1127+2654	0.378	COS	1	0.010	0.205	2	0.010	0.205	12603
		FOS-H	1	—	—	2	—	—	6548
J1129-0424	0.060	COS	1	0.010	0.159	1	0.010	0.049	12569
J1129-1941	0.918	STIS	0	—	—	1	—	—	9506
J1130-1449	1.187	FOS-H	1	0.836	1.286	0	—	—	3483,3858,6577

Table A.5: — Continued

QSO	z_{em}^a	Instrument	Search Path			Statistical Path			Proposal ID
			F_{search}^b	Min z	Max z	F_{stat}^c	Min z	Max z	
		FOS-L	1	0.165	0.835	0	—	—	6577
J1131+3114	0.290	COS	1	0.010	0.390	2	0.010	0.277	11519
J1131+1556	0.182	COS	1	0.010	0.206	2	0.010	0.171	12603
J1132+1335	0.200	COS	1	0.010	0.210	2	0.010	0.188	12603
J1133+0327	0.525	COS	1	0.010	0.430	2	0.010	0.430	13033
J1133+1052	0.510	FOS-H	1	0.365	0.609	1	0.365	0.494	2424
J1134+2555	0.709	COS	1	0.010	0.447	2	0.010	0.447	12248
J1135-0318	0.237	FOS-H	1	—	—	1	—	—	5456
J1137+3907	1.026	STIS	2	—	—	0	—	—	9051
J1139-3744	0.009	COS	1	0.010	0.109	1	—	—	12212
J1139-1351	0.557	COS	1	0.010	0.206	1	0.010	0.206	12275
		FOS-H	1	0.352	0.656	1	0.352	0.541	2424
		FOS-L	1	0.334	0.351	1	0.334	0.351	2424
J1139+6547	0.652	COS	1	0.010	0.476	1	0.010	0.476	11541
		FOS-H	1	0.477	0.751	1	0.477	0.635	2424,2578,4044
J1141+0147	0.383	FOS-H	1	0.357	0.482	1	0.357	0.369	5456
J1142+3016	0.481	COS	1	0.010	0.207	2	0.010	0.207	12603
J1143+3452	3.130	STIS	0	—	—	1	—	—	8287
J1147-0132	0.382	FOS-H	1	0.377	0.481	1	—	—	5852
J1148+1050	1.010	FOS-H	1	0.387	0.901	1	0.387	0.901	5852
J1148+1048	1.010	FOS-H	1	0.427	0.902	1	0.427	0.902	5852
J1148+1047	1.100	FOS-H	1	0.365	0.902	1	0.365	0.902	5852
J1150-0023	1.980	FOS-L	1	0.135	1.065	1	0.135	1.065	5095
J1151+5437	0.975	COS	1	0.010	0.480	1	0.010	0.480	11741
		FOS-H	1	0.481	1.075	1	0.481	0.955	4952,6220
J1151+3825	1.304	FOS-L	1	0.174	1.063	0	—	—	6577
J1153+4931	0.334	FOS-H	1	0.298	0.433	1	0.298	0.320	5441
J1155+2922	0.520	COS	1	0.010	0.210	2	0.010	0.210	12603
J1157-0022	0.260	COS	1	0.010	0.360	2	0.010	0.247	11598

Table A.5: — Continued

QSO	z_{em}^a	Instrument	Search Path			Statistical Path			Proposal ID
			F_{search}^b	Min z	Max z	F_{stat}^c	Min z	Max z	
J1158+6254	0.594	FOS-H	1	—	—	1	—	—	4952
J1159+2107	0.349	FOS-H	1	0.298	0.448	1	0.298	0.335	5441
J1159+2915	0.729	FOS-H	1	0.354	0.828	1	0.354	0.711	3791,5441
J1200+3126	2.970	STIS	0	—	—	1	—	—	8287
J1201+0111	0.000	STIS	0	—	—	2	—	—	9874
J1201−1354	0.506	COS	1	0.010	0.206	1	0.010	0.206	12275
J1203+4431	0.002	COS	1	0.010	0.102	1	—	—	11834
J1203+1522	2.970	STIS	0	—	—	1	—	—	8287
J1204+2754	0.164	COS	1	0.010	0.264	2	0.010	0.152	12248
		FOS-H	0	—	—	1	—	—	4115
J1204−4343	0.014	COS	1	0.010	0.114	1	—	—	12275
J1205−2634	0.786	STIS	1	0.502	0.885	1	0.502	0.768	8225
J1205+1042	1.088	COS	1	0.010	0.187	2	0.010	0.187	11698
J1207+2624	0.323	COS	1	0.010	0.423	2	0.010	0.310	12248
J1208+4540	1.158	COS	1	0.010	0.480	1	0.010	0.480	11741
		FOS-H	1	0.481	1.257	1	0.481	1.136	2424
		FOS-L	1	—	—	1	—	—	2424
J1209+1036	0.394	COS	1	0.050	0.187	2	0.050	0.187	11698
J1209+0232	0.238	STIS	1	0.012	0.338	2	0.012	0.225	9874
J1209−0501	0.128	COS	0	—	—	2	—	—	12533
J1210+3157	0.388	COS	1	0.010	0.476	2	0.010	0.375	12248
J1210−2758	0.828	STIS	0	—	—	1	—	—	8225
J1211+3657	0.170	COS	1	0.010	0.270	2	0.010	0.159	12248
J1211+1030	2.193	FOS-L	0	—	—	0	—	—	5351
J1214+1403	0.085	FOS-H	1	0.010	0.184	0	—	—	1026
J1214+0825	0.585	COS	1	0.010	0.186	2	0.010	0.186	11698
J1214+1429	1.626	STIS	0	—	—	1	—	—	7359
J1216+0712	0.586	COS	1	0.010	0.183	2	0.010	0.183	11698
J1216+1747	0.375	FOS-H	1	0.356	0.474	1	0.356	0.361	5456

Table A.5: — Continued

QSO	z_{em}^a	Instrument	Search Path			Statistical Path			Proposal ID
			F_{search}^b	Min z	Max z	F_{stat}^c	Min z	Max z	
J1217+0809	0.342	COS	1	0.010	0.183	2	0.010	0.183	11698
J1217+6407	1.288	FOS-H	1	0.914	1.387	1	0.914	1.265	5441
J1218+1105	1.403	FOS-L	1	0.625	1.065	1	0.625	1.065	2424
J1218+5015	1.450	FOS-H	1	0.829	1.549	1	0.829	1.425	6432
J1218+1015	0.542	COS	1	0.010	0.187	2	0.010	0.187	11698
J1219+0638	0.331	COS	1	0.010	0.431	1	0.010	0.318	12025
		FOS-H	1	—	—	1	—	—	3791,4112
J1220+0641	0.286	COS	1	0.010	0.183	2	0.010	0.183	11698
J1220−2113	0.800	STIS	1	0.526	0.899	1	0.526	0.782	8225
J1220+3343	1.532	STIS	1	0.288	1.589	0	—	—	8569
J1220+3853	0.375	COS	1	0.010	0.475	2	0.010	0.361	11598
J1220−0040	1.411	STIS	1	0.556	1.510	0	—	—	9382
J1221+1554	0.229	COS	1	0.010	0.183	2	0.010	0.183	11698
J1221+4548	0.525	COS	1	0.106	0.210	2	0.106	0.210	12486
J1221+0430	0.094	FOS-H	1	0.010	0.193	2	0.010	0.083	5451
J1221+7518	0.070	FOS-H	1	0.010	0.169	1	0.010	0.059	1022,4952
J1223+0950	0.277	COS	1	0.010	0.183	2	0.010	0.183	11698
J1223+0923	0.681	COS	1	0.010	0.187	2	0.010	0.187	11698
J1223+1545	0.081	FOS-H	1	—	—	1	—	—	4952,5451
J1224+0037	1.482	STIS	1	0.742	1.581	0	—	—	9382
J1225−2938	0.816	STIS	1	0.412	0.915	1	0.412	0.797	8225
J1225+1218	0.411	COS	1	0.010	0.183	2	0.010	0.183	11698
J1225+0844	0.535	COS	1	0.010	0.183	2	0.010	0.183	11698
J1225+2235	2.046	FOS-H	1	0.679	0.901	1	0.679	0.901	2524,6577
J1225+3332	0.001	COS	1	0.010	0.101	1	—	—	12212
J1225+0035	1.226	STIS	1	0.637	1.325	0	—	—	9382
J1225−0052	0.964	STIS	2	—	—	0	—	—	9382
J1226−0006	1.118	STIS	1	0.709	1.217	0	—	—	9382
J1226−2630	0.768	STIS	1	0.753	0.867	1	—	—	8225

Table A.5: — Continued

QSO	z_{em}^{a}	Instrument	Search Path			Statistical Path			Proposal ID
			$F_{\text{search}}^{\text{b}}$	Min z	Max z	$F_{\text{stat}}^{\text{c}}$	Min z	Max z	
J1228+3128	2.219	FOS-H	1	1.107	1.696	1	1.107	1.696	5095
J1228+1018	2.304	STIS	1	1.050	1.597	0	—	—	8569
J1229+0203	0.173	COS	1	0.010	0.209	1	0.010	0.161	12038
J1230+0115	0.117	COS	1	0.010	0.216	1	0.010	0.105	11686
J1232−0224	1.045	COS	1	0.159	0.462	0	—	—	12593
		FOS-H	1	0.463	1.144	0	—	—	1193,3939,5351
		FOS-L	1	—	—	0	—	—	1193,3939
J1232+2009	0.063	COS	1	0.010	0.163	1	0.010	0.052	12569
J1232+5252	4.294	STIS	0	—	—	0	—	—	9759
J1233−0031	0.471	COS	1	0.010	0.476	2	0.010	0.456	12486
J1233+0931	0.420	FOS-H	1	0.362	0.519	1	0.362	0.405	4952
J1233+4758	0.381	COS	1	0.010	0.430	2	0.010	0.368	13033
J1234+0724	0.843	COS	1	0.010	0.183	2	0.010	0.183	11698
J1235+4736	4.447	STIS	0	—	—	1	—	—	8582
J1236+2641	0.209	COS	1	0.010	0.308	2	0.010	0.196	12248
J1236+0600	1.279	COS	1	0.061	0.186	2	0.061	0.186	11698
J1238+1750	0.449	STIS	2	—	—	1	—	—	7359
J1240+0949	1.045	COS	1	0.062	0.187	2	0.062	0.187	11698
J1241+2852	0.590	COS	1	0.010	0.207	2	0.010	0.207	12603
J1241+5721	0.583	COS	1	0.010	0.430	2	0.010	0.430	11598
J1242+0012	1.213	STIS	1	0.507	1.313	1	0.507	1.191	7359
J1244+1721a	1.283	FOS-H	1	0.829	1.382	1	0.829	1.260	4112
J1244+1721b	1.283	COS	1	0.169	0.462	0	—	—	12466
J1245+3356	0.717	COS	1	0.010	0.476	2	0.010	0.476	11598
J1246−0730	1.286	STIS	1	0.918	1.385	0	—	—	9076
J1247+3126	2.960	STIS	0	—	—	1	—	—	8287
J1249−0559	2.226	STIS	0	—	—	1	—	—	7295,4081
J1250+2631	2.043	FOS-H	1	0.829	1.695	1	0.829	1.695	5095,6705
J1250−2333	0.048	COS	1	0.010	0.147	2	0.010	0.037	13027

Table A.5: — Continued

QSO	z_{em}^a	Instrument	Search Path			Statistical Path			Proposal ID
			F_{search}^b	Min z	Max z	F_{stat}^c	Min z	Max z	
J1250+3016	1.061	FOS-H	1	0.990	1.160	1	0.990	1.040	5441
J1250+3951	1.030	FOS-H	1	0.351	1.129	1	0.351	1.009	5664
J1251+0554	1.377	COS	1	0.010	0.210	2	0.010	0.210	12603
J1251+4637	1.460	COS	1	0.158	0.462	0	—	—	12593
J1252+2913	0.820	FOS-H	1	0.337	0.901	1	0.337	0.801	6007
J1252+5634	0.321	FOS-H	1	—	—	1	—	—	2578
J1253+3106	0.780	FOS-H	1	0.332	0.879	1	0.332	0.762	6007
J1254+1141	0.870	FOS-H	1	0.363	0.969	1	0.363	0.851	2424
		FOS-L	1	—	—	1	—	—	2424
J1256−0547	0.538	FOS-H	1	0.060	0.637	1	0.060	0.522	2578,5936
J1256+5652	0.041	COS	1	0.010	0.141	1	0.010	0.031	12569
J1259+3423	1.375	FOS-H	1	0.835	1.474	1	0.835	1.351	5225
J1301+2819	1.355	FOS-H	1	0.830	1.454	2	0.830	1.331	5501
J1301+5902	0.472	COS	1	0.010	0.476	1	0.010	0.457	11541
		FOS-H	1	0.477	0.571	1	—	—	2424,3418
		STIS	1	—	—	2	—	—	7295
J1304−0037	3.035	STIS	0	—	—	1	—	—	9067
J1305+0357	0.545	COS	1	0.010	0.210	2	0.010	0.210	12603
J1305−1033	0.278	COS	1	0.010	0.378	1	0.010	0.265	12038
		FOS-H	1	—	—	1	—	—	3222,3791,5664
J1307+0641	0.602	FOS-H	1	0.366	0.701	1	0.366	0.586	5441
J1308+3005	0.806	FOS-H	1	—	—	1	—	—	4952
		FOS-L	1	0.173	0.905	1	0.173	0.788	4952
J1309+0819	0.154	COS	1	0.010	0.208	1	0.010	0.142	12569
		FOS-H	1	—	—	1	—	—	4953
J1310+4601	2.129	FOS-H	1	0.335	1.697	1	0.335	1.697	5950
J1312+3515	0.184	COS	1	0.010	0.194	1	0.010	0.172	12569
		FOS-H	1	0.195	0.283	1	—	—	6781
J1313−2716	2.186	STIS	1	1.024	1.591	0	—	—	8569

Table A.5: — Continued

QSO	z_{em}^{a}	Instrument	Search Path			Statistical Path			Proposal ID
			$F_{\text{search}}^{\text{b}}$	Min z	Max z	$F_{\text{stat}}^{\text{c}}$	Min z	Max z	
J1314+0201	0.306	FOS-H	1	—	—	1	—	—	5456
J1314–3105	0.000	STIS	0	—	—	1	—	—	8287
J1315+1525	0.449	COS	1	0.010	0.207	2	0.010	0.207	12603
J1317+3531	4.360	STIS	0	—	—	1	—	—	8582
J1318+2628	1.234	COS	1	0.010	0.210	2	0.010	0.210	12603
J1319+5147	1.055	FOS-H	1	0.834	1.154	1	0.834	1.034	4953
		FOS-L	1	0.471	0.833	1	0.471	0.833	4953
J1319–0158	0.225	FOS-H	1	—	—	1	—	—	5456
J1319+2728	1.022	COS	1	0.253	0.461	2	0.253	0.461	11667
		FOS-H	1	0.462	1.121	1	0.462	1.001	2424
		FOS-L	1	0.252	0.252	1	0.252	0.252	2424
J1321+2847a	1.703	FOS-H	1	0.611	0.901	1	0.611	0.901	1144,6007
		FOS-L	1	0.902	1.065	1	0.902	1.065	1144
J1321+2847b	0.549	FOS-H	1	0.352	0.648	1	0.352	0.533	1144,6007
J1321+1106	2.181	STIS	1	—	—	0	—	—	8569
J1322+4645	0.375	COS	1	0.010	0.430	2	0.010	0.361	13033
J1322+4739	1.101	STIS	1	0.474	1.201	1	0.474	1.080	8126
J1323+2910	0.966	FOS-H	1	0.411	1.065	1	0.411	0.946	4953,6007
		FOS-L	1	—	—	1	—	—	4953
J1323–0021	1.388	STIS	1	0.840	1.487	0	—	—	9382
J1323+3430	0.444	COS	1	0.152	0.450	0	—	—	12593
J1323+6541	0.168	FOS-H	1	0.010	0.267	1	0.010	0.156	6781
J1324+0537	0.205	FOS-H	1	—	—	1	—	—	6799
J1324+0446	0.021	COS	0	—	—	1	—	—	12557
J1325+2717	0.522	COS	1	0.010	0.210	2	0.010	0.210	12603
J1325+6515	1.618	FOS-H	1	0.975	1.697	0	—	—	6577
J1327+4435	0.330	COS	1	0.010	0.430	2	0.010	0.317	12248
J1328+5244	1.341	COS	1	0.162	0.459	0	—	—	12593
J1330–2056	1.169	FOS-H	1	0.830	1.268	1	0.830	1.147	5654

Table A.5: — Continued

QSO	z_{em}^a	Instrument	Search Path			Statistical Path			Proposal ID
			F_{search}^b	Min z	Max z	F_{stat}^c	Min z	Max z	
		STIS	1	—	—	0	—	—	9382
J1330+2813	0.416	COS	1	0.010	0.476	2	0.010	0.402	11598
J1330+3119	0.242	COS	1	0.010	0.342	2	0.010	0.229	12248
J1331+3030	0.849	FOS-H	1	0.343	0.948	0	—	—	1193,5351
		FOS-L	1	0.113	0.342	0	—	—	1193
J1331+4101	1.930	FOS-H	1	0.739	1.696	0	—	—	5948,6577
J1333+2539	3.030	STIS	0	—	—	1	—	—	8287
J1336+1725	0.554	FOS-H	1	0.353	0.653	1	0.353	0.538	2424
		FOS-L	1	—	—	1	—	—	2424
J1336-0048	2.801	FOS-L	1	0.763	1.065	1	0.763	1.065	3268
J1336-0049	2.783	FOS-H	1	0.353	1.696	1	0.353	1.696	5492
J1337+2422	0.108	FOS-H	1	—	—	1	—	—	5928
J1341+4123	1.219	COS	1	0.010	0.480	1	0.010	0.480	11741
		FOS-H	1	0.481	1.318	1	0.481	1.196	2424,3837,6612
		FOS-L	1	—	—	1	—	—	2424
J1341+0059	1.714	STIS	1	0.288	1.589	0	—	—	9382
J1342+0505	0.266	COS	1	0.010	0.366	2	0.010	0.253	12248
J1342+6021	0.960	FOS-H	1	0.834	1.060	1	0.834	0.941	3858
		STIS	1	0.010	0.833	1	0.010	0.833	7356
J1342+3829	0.171	COS	1	0.010	0.271	2	0.010	0.160	12248
J1342-0035	0.786	STIS	1	0.288	0.886	0	—	—	9382
J1342+1844	0.382	COS	1	0.010	0.476	2	0.010	0.368	12248
J1342-0054	0.326	FOS-H	1	0.348	0.425	1	—	—	5456
J1342-0053	0.325	COS	1	0.010	0.425	2	0.010	0.312	11598
J1343+2844	0.905	FOS-L	1	0.578	1.004	1	0.578	0.886	2424
J1345-0023	1.094	STIS	1	0.559	1.194	0	—	—	9382
J1348+2818	2.941	STIS	0	—	—	1	—	—	8287
J1348+2456	0.293	COS	1	0.010	0.206	2	0.010	0.206	12603
J1348+2622	0.598	FOS-H	1	—	—	2	—	—	6548

Table A.5: — Continued

QSO	z_{em}^a	Instrument	Search Path			Statistical Path			Proposal ID
			F_{search}^b	Min z	Max z	F_{stat}^c	Min z	Max z	
J1351–0007	1.444	FOS-L	1	0.641	1.065	1	0.641	1.065	4953
J1352–2649	0.934	STIS	1	0.896	1.033	1	0.896	0.914	8225
J1353+6918	0.030	COS	1	0.010	0.130	1	0.010	0.020	12212
J1353+6345	0.088	COS	1	0.010	0.187	1	0.010	0.077	12569
		FOS-H	1	—	—	2	—	—	2717
J1354+3138	1.326	FOS-H	1	0.856	1.425	1	0.856	1.302	5441
J1354+2430	1.878	COS	1	0.010	0.207	2	0.010	0.207	12603
J1354+1805	0.152	FOS-H	1	0.019	0.251	1	0.019	0.140	6781
J1354+0052	1.117	FOS-H	1	0.342	1.216	1	0.342	1.095	2424,6612
		FOS-L	1	0.114	0.341	1	0.114	0.341	2424
J1356+2515	0.164	COS	1	0.010	0.264	2	0.010	0.152	12248
J1357+1919	0.719	COS	1	0.139	0.442	2	0.139	0.442	13398
		FOS-H	1	0.443	0.819	1	0.443	0.702	2424,3858
		FOS-L	1	—	—	1	—	—	2424
J1357+1704	0.150	COS	1	0.010	0.250	2	0.010	0.139	12248
J1357+0435	1.231	COS	1	0.010	0.480	2	0.010	0.480	12264
J1358+5752	1.375	FOS-H	1	0.844	1.474	1	0.844	1.351	4504
J1358–2352	0.831	STIS	1	0.498	0.931	1	0.498	0.813	8225
J1359–4152	0.313	FOS-H	1	—	—	1	—	—	4953
J1359+5726	0.033	COS	1	0.010	0.133	2	0.010	0.023	12583
J1400+5535	0.840	COS	1	0.162	0.459	0	—	—	12593
J1402–2822	0.802	STIS	1	0.528	0.902	1	0.528	0.784	8225
J1404+0937	0.441	FOS-H	1	0.407	0.540	1	0.407	0.426	4953
J1404+3353	0.549	COS	1	0.010	0.207	2	0.010	0.207	12603
J1404–0130	2.522	STIS	1	1.059	1.612	0	—	—	8569
J1405+2555	0.164	FOS-H	1	0.010	0.263	1	0.010	0.152	4953,5456,6781
J1406+2223	0.098	FOS-H	1	0.010	0.197	1	0.010	0.087	6247
J1406+0157	0.426	COS	1	0.010	0.210	2	0.010	0.210	12603
J1407+5507	1.027	COS	1	0.010	0.210	2	0.010	0.210	12486

Table A.5: — Continued

QSO	z_{em}^a	Instrument	Search Path			Statistical Path			Proposal ID
			F_{search}^b	Min z	Max z	F_{stat}^c	Min z	Max z	
J1409+2618	0.945	COS	1	0.010	0.480	1	0.010	0.480	11741
		FOS-H	1	0.481	1.044	1	0.481	0.925	2424
		FOS-L	1	—	—	1	—	—	2424
J1410+2955	0.570	COS	0	—	—	0	—	—	12593
J1410+2304	0.795	COS	1	0.010	0.472	2	0.010	0.472	12958
J1413+4400	0.090	COS	1	0.010	0.189	1	0.010	0.079	12569
J1415+1634	0.743	COS	1	0.010	0.193	2	0.010	0.193	12486
J1417+4456	0.114	FOS-H	1	0.010	0.213	1	0.010	0.102	3566,6781
J1417+4330	0.002	COS	1	0.010	0.102	1	—	—	11579
		FOS-H	1	—	—	1	—	—	5408
J1417+2508	0.016	COS	1	0.010	0.116	1	—	—	12212
J1418+1703	0.821	FOS-L	1	0.524	0.920	1	0.524	0.802	2424
J1419-1310	0.129	FOS-H	1	—	—	1	—	—	6528
J1419+0628	1.436	FOS-H	1	0.830	1.535	1	0.830	1.411	6589
J1419+4207	0.873	COS	1	0.010	0.476	2	0.010	0.476	11598
J1419-0036	0.969	STIS	1	0.469	1.068	0	—	—	9382
J1420-0054	1.458	STIS	1	0.781	1.557	0	—	—	9382
J1421+2538	1.050	COS	1	0.142	0.440	0	—	—	12593
J1423+3252	1.904	STIS	1	0.872	1.612	0	—	—	8569
J1426+0051	1.333	STIS	1	0.485	1.432	0	—	—	9382
J1427+2348	0.160	COS	1	0.010	0.259	1	0.010	0.148	12612
J1427+1949	0.111	FOS-H	1	—	—	1	—	—	4953
J1427+2632	0.366	COS	1	0.010	0.205	2	0.010	0.205	12603
		FOS-H	1	0.297	0.465	1	0.297	0.352	6781
J1427-1203	0.805	FOS-H	1	0.381	0.904	1	0.381	0.787	2424
		FOS-L	1	—	—	1	—	—	2424
J1429+0321	0.253	COS	1	0.010	0.207	2	0.010	0.207	12603
J1429+4747	0.221	FOS-H	1	0.010	0.320	1	0.010	0.208	6781
J1430+0222	0.353	COS	1	0.053	0.179	2	0.053	0.179	12539

Table A.5: — Continued

QSO	z_{em}^a	Instrument	Search Path			Statistical Path			Proposal ID
			F_{search}^b	Min z	Max z	F_{stat}^c	Min z	Max z	
J1431+3952	1.215	STIS	1	0.383	1.315	0	—	—	9051
J1431+2442	0.406	COS	1	0.010	0.210	2	0.010	0.210	12603
J1431−0050	1.188	STIS	1	0.618	1.288	0	—	—	9382
J1435+3604	0.428	COS	1	0.010	0.476	2	0.010	0.414	11598
J1436+5847	0.031	COS	1	0.010	0.130	1	0.010	0.020	11505
J1436−0051	1.273	STIS	1	0.681	1.372	0	—	—	9382
J1436+6336	2.068	FOS-H	1	1.201	1.695	1	1.201	1.695	3221
J1436+4952	1.550	STIS	2	—	—	1	—	—	7359
J1437+5045	0.783	COS	1	0.010	0.476	2	0.010	0.476	11598
J1437−0147	1.310	COS	1	0.010	0.480	1	0.010	0.480	11741
		FOS-H	1	0.832	1.409	1	0.832	1.286	4953,6103
		FOS-L	1	0.803	0.831	1	0.803	0.831	6103,4953
J1438−0658	0.129	COS	1	0.010	0.192	1	0.010	0.117	12569
		STIS	1	—	—	1	—	—	9507
J1438+6211	1.090	STIS	1	0.291	1.189	0	—	—	8569
J1439+2954	2.990	STIS	0	—	—	1	—	—	8287
J1442+3526	0.077	COS	1	0.010	0.176	1	0.010	0.066	12569
		FOS-H	1	—	—	1	—	—	4953,6781
J1445+3428	0.697	COS	1	0.010	0.476	2	0.010	0.476	11598
J1446+4035	0.267	FOS-H	1	0.010	0.366	1	0.010	0.254	3566,6781
J1451+2709	0.064	COS	1	0.010	0.164	2	0.010	0.053	12248
J1454+3046	0.465	COS	1	0.010	0.210	2	0.010	0.210	12603
J1454−3747	0.314	FOS-H	1	0.297	0.413	0	—	—	4342,5948
J1455−0045	1.374	STIS	1	0.604	1.474	0	—	—	9382
J1459+7140	0.904	COS	1	0.010	0.210	2	0.010	0.210	12486
J1459+5319	0.338	COS	1	0.010	0.206	2	0.010	0.206	12276
J1500+5517	0.404	COS	1	0.010	0.206	2	0.010	0.206	12276
J1501+0019	1.930	STIS	1	0.288	1.589	0	—	—	9382
J1502+0645	0.287	COS	1	0.010	0.210	2	0.010	0.210	12603

Table A.5: — Continued

QSO	z_{em}^{a}	Instrument	Search Path			Statistical Path			Proposal ID
			$F_{\text{search}}^{\text{b}}$	Min z	Max z	$F_{\text{stat}}^{\text{c}}$	Min z	Max z	
J1502–4154	1.026	COS	1	0.072	0.210	1	0.072	0.210	11659
		STIS	1	0.620	1.125	1	0.620	1.005	8244
J1503+6105	3.682	STIS	0	—	—	0	—	—	9759
J1503+6810	0.114	COS	1	0.010	0.206	2	0.010	0.102	12276
J1503–4152	0.335	COS	1	0.010	0.211	1	0.010	0.211	11659
		STIS	1	0.212	0.434	1	0.212	0.321	8244
J1504+6856	0.318	FOS-H	1	—	—	2	—	—	6719
J1504+0122	0.967	STIS	1	0.020	0.412	2	0.020	0.412	9874
J1504+5649	0.358	COS	1	0.010	0.206	2	0.010	0.206	12276
J1505+0342	0.036	STIS	1	0.010	0.136	2	0.010	0.025	9874
J1508+6717	0.716	STIS	1	—	—	2	—	—	7762
J1508+6814	0.058	COS	1	0.010	0.158	2	0.010	0.047	12276
J1509+0702	0.417	COS	1	0.010	0.210	2	0.010	0.210	12603
J1509+1110	0.285	COS	1	0.010	0.179	0	—	—	12614
J1510+0058	0.070	STIS	1	0.010	0.169	2	0.010	0.059	9874
J1512+0128	0.265	COS	1	0.010	0.210	2	0.010	0.210	12603
J1513+1011	1.546	FOS-L	1	0.113	0.994	0	—	—	6577
J1514+3619	0.695	COS	1	0.065	0.477	2	0.065	0.477	11598
J1514+3650	0.371	FOS-H	1	0.334	0.470	1	0.334	0.357	2424,3538
J1515+0657	0.267	COS	1	0.010	0.207	2	0.010	0.207	12603
J1516+1900	0.190	STIS	1	0.010	0.289	1	0.010	0.178	9161
J1519+2346a	1.834	FOS-H	1	0.370	1.696	1	0.370	1.696	5320,5631
J1519+2346b	1.903	FOS-H	1	0.490	1.695	1	0.490	1.695	5320
J1519+5908	0.078	COS	1	0.010	0.178	2	0.010	0.067	12276
J1521–0009	1.318	STIS	1	0.676	1.417	0	—	—	9382
J1521+0337	0.126	COS	1	0.010	0.226	2	0.010	0.115	12248
J1521+5940	0.286	COS	1	0.010	0.206	2	0.010	0.206	12276
J1523+6339	0.204	COS	1	0.010	0.207	2	0.010	0.192	12276
J1524+0958	1.324	COS	1	0.010	0.480	1	0.010	0.480	11741

Table A.5: — Continued

QSO	z_{em}^a	Instrument	Search Path			Statistical Path			Proposal ID
			F_{search}^b	Min z	Max z	F_{stat}^c	Min z	Max z	
		FOS-H	1	0.481	1.423	0	—	—	3200,6705
		FOS-L	1	—	—	0	—	—	3200
J1525+0026	0.801	STIS	1	0.422	0.900	0	—	—	9382
J1527+2452	0.993	STIS	1	0.576	1.092	0	—	—	9051
J1527+6548	0.345	COS	1	0.010	0.206	2	0.010	0.206	12276
J1528+2825	0.450	COS	1	0.010	0.476	1	0.010	0.435	12038
J1529+5616	0.099	COS	1	0.010	0.199	2	0.010	0.088	12276
J1535+5754	0.030	COS	1	0.010	0.130	1	0.010	0.019	11524
J1536+5433	0.039	COS	1	0.010	0.138	2	0.010	0.028	12276
J1537+0021	1.754	STIS	1	1.018	1.589	0	—	—	9382
J1537+3358	1.025	STIS	1	0.463	1.124	0	—	—	9051
J1538+5736	0.073	COS	1	0.010	0.173	2	0.010	0.062	12276
J1539+4735	0.770	FOS-H	1	0.341	0.869	1	0.341	0.752	3791,4118
		FOS-L	1	0.331	0.340	1	0.331	0.340	3791
J1541+2817	0.375	COS	1	0.010	0.206	2	0.010	0.206	12603
J1544+5358	2.371	FOS-H	1	0.527	1.696	1	0.527	1.696	6293
J1544+5912	0.807	STIS	1	0.010	0.906	2	0.010	0.789	8485
J1544+2743	0.163	COS	1	0.010	0.206	2	0.010	0.151	12603
J1545+4846	0.400	FOS-H	1	0.010	0.499	1	0.010	0.386	4953,5451
J1545+0936	0.664	COS	1	0.111	0.457	2	0.111	0.457	12248
J1547+2052	0.264	COS	1	0.010	0.363	2	0.010	0.251	13398
		FOS-H	1	—	—	1	—	—	2578
J1550+4001	0.496	COS	1	0.010	0.476	2	0.010	0.476	11598
J1552+5705	0.366	COS	1	0.010	0.206	2	0.010	0.206	12276
J1553+3548	0.722	COS	1	0.010	0.476	2	0.010	0.476	11598
J1554+0822	0.119	STIS	1	—	—	1	—	—	9507
J1555+3628	0.713	COS	1	0.010	0.476	2	0.010	0.476	11598
J1555+1111	0.360	COS	1	0.010	0.459	1	0.010	0.346	12025
J1557–2029	1.947	STIS	1	1.211	1.609	0	—	—	8569

Table A.5: — Continued

QSO	z_{em}^a	Instrument	Search Path			Statistical Path			Proposal ID
			F_{search}^b	Min z	Max z	F_{stat}^c	Min z	Max z	
J1557+3304	0.942	FOS-H	1	0.902	1.041	1	0.902	0.922	3858
J1559-2442	2.818	STIS	0	—	—	0	—	—	8569
J1601+1714	1.952	FOS-L	1	0.944	1.065	1	0.944	1.065	5095
J1603+5730	2.850	COS	1	0.010	0.124	0	—	—	12816
J1605+1448	0.371	COS	1	0.010	0.179	0	—	—	12614
J1608+6018	0.178	COS	1	0.010	0.207	2	0.010	0.166	12276
J1613+3412	1.401	FOS-H	1	0.857	1.500	1	0.857	1.377	2578
J1613+6543	0.138	COS	1	0.010	0.238	1	0.010	0.127	11686
J1614+2604	0.131	FOS-H	1	—	—	1	—	—	4953
J1614+4859	3.799	STIS	0	—	—	0	—	—	9759
J1614+4704	1.859	STIS	1	0.826	1.611	0	—	—	9051
J1616+4154	0.440	COS	1	0.010	0.476	2	0.010	0.426	11598
J1617+0638	0.229	COS	1	0.010	0.329	2	0.010	0.216	11598
J1619+3342	0.470	COS	1	0.010	0.476	2	0.010	0.456	11598
J1619+3813	1.124	STIS	1	0.010	0.412	2	0.010	0.412	9874
J1620+1724	0.112	COS	1	0.010	0.193	1	0.010	0.100	12569
J1620+1736	0.555	FOS-H	1	0.344	0.654	1	0.344	0.539	2424,2578
		FOS-L	1	0.310	0.343	1	0.310	0.343	2424
J1624+2345	0.927	FOS-H	1	0.454	1.026	0	—	—	5304
J1625+5727	0.067	COS	1	0.010	0.166	2	0.010	0.056	12276
J1625+2646	2.526	FOS-H	1	0.830	1.695	0	—	—	6577
		FOS-L	1	0.540	0.829	0	—	—	6577
J1627+5522	0.133	COS	1	0.010	0.232	1	0.010	0.121	12029
		FOS-H	1	—	—	1	—	—	6781
J1630+3758	1.461	FOS-L	1	0.588	1.065	1	0.588	1.065	1144
J1631+4048	0.257	STIS	1	0.010	0.357	1	0.010	0.244	9506
J1631+1156	1.792	STIS	1	0.727	1.605	0	—	—	8569
J1632+3737	1.478	COS	1	0.010	0.480	1	0.010	0.480	11741
		FOS-H	1	0.481	1.577	1	0.481	1.453	3837,5698

Table A.5: — Continued

QSO	z_{em}^a	Instrument	Search Path			Statistical Path			Proposal ID
			F_{search}^b	Min z	Max z	F_{stat}^c	Min z	Max z	
J1633+3924	1.023	FOS-H	1	0.940	1.122	1	0.940	1.002	4953
J1634+7031	1.337	FOS-H	1	0.830	1.436	1	0.830	1.313	3221,3732
J1636+7205	0.187	STIS	1	0.019	0.286	1	0.019	0.175	9506
J1637+2509	1.110	STIS	1	0.549	1.209	0	—	—	9051
J1638+5720	0.745	FOS-H	1	0.367	0.844	1	0.367	0.727	4052
J1642+3924	2.383	COS	0	—	—	2	—	—	13398
J1642+3948	0.595	FOS-H	1	0.449	0.694	1	0.449	0.579	2578,6214
J1649+3047	1.350	STIS	0	—	—	1	—	—	8266
J1649+3046	1.122	STIS	1	0.567	1.222	1	0.567	1.101	8266
J1658+0515	0.879	FOS-H	1	0.883	0.978	1	—	—	2424,5441
		FOS-L	1	0.881	0.882	1	—	—	2424
J1659+3735	0.771	COS	1	0.162	0.459	0	—	—	12593
J1701+6411	2.722	FOS-H	1	0.354	1.695	1	0.354	1.695	2288,6433
		STIS	1	0.010	0.353	1	0.010	0.353	9982
J1701+2924	0.036	COS	1	0.010	0.136	1	0.010	0.025	12275
J1702+6058	0.164	STIS	1	0.011	0.263	2	0.011	0.152	8024
J1703+6141	0.077	COS	1	0.010	0.177	2	0.010	0.066	12276
J1703+5813	0.106	COS	0	—	—	2	—	—	12533
J1704+7057	2.015	STIS	1	1.115	1.606	0	—	—	8569
J1704+6044	0.371	FOS-H	1	0.010	0.470	1	0.010	0.357	2424,3418
J1706+3615	0.918	STIS	1	0.405	1.017	0	—	—	9051
J1710+5923	4.470	STIS	0	—	—	0	—	—	9759
J1711+6052	3.835	STIS	0	—	—	0	—	—	9759
J1712+5559	1.358	STIS	1	0.685	1.457	0	—	—	9382
J1714+5757	1.252	STIS	2	—	—	0	—	—	9382
J1715+6453	3.960	STIS	0	—	—	0	—	—	9759
J1715+4606	0.985	STIS	1	0.671	1.084	0	—	—	9051
J1715+5747	0.697	STIS	1	0.423	0.796	0	—	—	9382
J1716+5654	0.937	STIS	1	0.554	1.036	0	—	—	9382

Table A.5: — Continued

QSO	z_{em}^a	Instrument	Search Path			Statistical Path			Proposal ID
			F_{search}^b	Min z	Max z	F_{stat}^c	Min z	Max z	
J1716+5328	1.940	FOS-H	1	0.834	1.696	1	0.834	1.696	5664
		FOS-L	1	—	—	0	—	—	6577
J1717+6559	0.292	COS	1	0.010	0.206	2	0.010	0.206	12276
J1717+5500	0.211	STIS	0	—	—	1	—	—	9067
J1719+4858	0.025	FOS-H	1	—	—	1	—	—	5428
J1719+4804	1.084	FOS-H	1	0.343	1.183	1	0.343	1.063	4112,4817,6705
J1722+5442	1.215	STIS	1	0.650	1.314	0	—	—	9382
J1727+5302	1.444	STIS	1	0.666	1.543	0	—	—	9382
J1728+1415	0.184	STIS	1	0.010	0.283	1	0.010	0.172	8264
J1729+7032	0.533	STIS	0	—	—	1	—	—	9506
J1729+5758	1.342	STIS	1	0.549	1.441	0	—	—	9382
J1733+5533	1.072	STIS	1	0.518	1.171	0	—	—	9382
J1734+6702	0.026	COS	0	—	—	2	—	—	12276
J1736+5938	1.410	STIS	1	0.818	1.509	0	—	—	9382
J1742+1827	0.186	STIS	1	0.010	0.285	1	0.010	0.174	8684
J1800+7828	0.680	FOS-H	1	0.384	0.779	1	0.384	0.663	5441
J1821+6420	0.297	COS	1	0.010	0.209	1	0.010	0.209	12038
J1822+6420	0.297	FOS-H	1	0.010	0.396	1	0.010	0.284	1025,3221
J1824+1044	1.360	FOS-H	1	0.750	0.901	0	—	—	6577
J1825+1358	0.000	COS	1	0.010	0.099	1	—	—	12023
J1832+5340	0.039	COS	1	0.010	0.138	1	0.010	0.028	12275
J1842+7946	0.056	FOS-H	1	0.010	0.155	1	0.010	0.045	6097
J1858+5645	1.595	STIS	1	0.695	1.604	0	—	—	8569
J1902+3159	0.635	FOS-L	1	0.246	0.734	0	—	—	6577
J1921+5840	0.036	COS	1	0.010	0.136	1	0.010	0.026	12936
J1927+7358	0.302	FOS-H	1	0.010	0.401	1	0.010	0.289	4112,5441
J1939+7007	0.120	STIS	1	0.010	0.219	1	0.010	0.108	9506
J1940+6907	3.152	STIS	0	—	—	1	—	—	7272
J1944+7705	3.051	STIS	0	—	—	1	—	—	8582

Table A.5: — Continued

QSO	z_{em}^a	Instrument	Search Path			Statistical Path			Proposal ID
			F_{search}^b	Min z	Max z	F_{stat}^c	Min z	Max z	
J2006–0223	1.457	STIS	0	—	—	0	—	—	8569
J2009–4849	0.071	COS	1	0.010	0.171	1	0.010	0.060	11520
J2044–1043	0.035	COS	1	0.010	0.134	1	0.010	0.024	12916
		FOS-H	1	—	—	1	—	—	4045
J2051+1950	2.367	STIS	1	1.170	1.608	0	—	—	8569
J2114+0607	0.457	STIS	1	0.010	0.556	1	0.010	0.442	9277
J2115–4323	1.708	STIS	2	—	—	1	—	—	7359
J2115+0608	0.453	FOS-H	1	0.351	0.552	1	0.351	0.438	4112
J2120–4426	1.480	STIS	1	0.622	1.579	1	0.622	1.455	7359
J2131–1207	0.501	COS	1	0.053	0.480	2	0.053	0.480	13398
		FOS-H	1	0.481	0.600	1	0.481	0.486	4581
J2132+1008	0.061	COS	1	0.010	0.161	1	0.010	0.051	11524
J2136–6224	0.058	COS	1	0.010	0.158	1	0.010	0.048	12936
J2137–1433	0.200	FOS-H	1	0.010	0.299	1	0.010	0.188	1191
J2138–3828	0.183	COS	1	0.010	0.283	1	0.010	0.171	12936
J2139–2454	0.939	STIS	1	0.933	1.039	1	—	—	8225
J2143+1743	0.213	FOS-H	1	0.010	0.312	1	0.010	0.200	1192
J2144–0754	1.811	STIS	1	1.116	1.606	0	—	—	9051
J2148+0657	0.999	FOS-H	1	0.369	1.098	1	0.369	0.979	2424
J2151+2130	1.534	STIS	1	0.724	1.605	0	—	—	8569
J2153–1514	0.078	STIS	1	0.047	0.177	2	0.047	0.067	9858
J2154–4414	0.344	COS	1	0.010	0.443	1	0.010	0.330	11541
		STIS	1	—	—	1	—	—	9506
J2155–0922	0.192	COS	1	0.010	0.291	1	0.010	0.180	12038
		STIS	1	—	—	1	—	—	9181
J2156+2242	1.290	COS	1	0.162	0.460	0	—	—	12593
J2158–3013	0.116	COS	1	0.010	0.209	1	0.010	0.104	12038
		FOS-H	1	0.210	0.215	1	—	—	1029,5089
J2159–2417	0.862	STIS	0	—	—	1	—	—	8225

Table A.5: — Continued

QSO	z_{em}^a	Instrument	Search Path			Statistical Path			Proposal ID
			F_{search}^b	Min z	Max z	F_{stat}^c	Min z	Max z	
J2203+3145	0.297	FOS-H	1	0.010	0.396	1	0.010	0.284	2578
J2211-1705	1.210	STIS	2	—	—	1	—	—	7359
J2215-2944	2.706	FOS-H	1	0.983	1.696	1	0.983	1.696	6093
		STIS	1	0.731	0.982	0	—	—	8569
J2217+1414	0.066	COS	1	0.010	0.166	1	0.010	0.055	12604
J2218-6150	0.000	STIS	0	—	—	1	—	—	8287
J2218-0335	0.901	FOS-H	1	0.587	1.000	1	0.587	0.882	2578,4052,5002
J2221-1857	0.000	STIS	0	—	—	1	—	—	8287
J2225-0456	1.404	FOS-H	1	1.018	1.503	1	1.018	1.380	2578
J2232+1143	1.037	FOS-H	1	0.839	1.136	1	0.839	1.016	2578
J2233-6033	2.238	STIS	1	0.010	1.598	1	0.010	1.598	7633,8076
J2236+1343	0.325	STIS	1	—	—	1	—	—	9507
J2242+2943	0.024	COS	1	0.010	0.124	1	0.010	0.014	12212
J2245-4652	0.198	COS	1	0.010	0.297	1	0.010	0.186	12604
J2246-1206	0.630	FOS-H	1	0.345	0.729	1	0.345	0.613	3791
		FOS-L	1	—	—	1	—	—	3791
J2248-5109	0.100	COS	1	0.010	0.199	1	0.010	0.089	11686
J2252-5021	2.900	STIS	0	—	—	1	—	—	8287
J2253-3658	3.200	STIS	0	—	—	1	—	—	8287
J2253+1608	0.859	COS	1	0.010	0.480	2	0.010	0.480	13398
		FOS-H	1	0.481	0.958	1	0.481	0.840	2578,6214
		FOS-L	1	—	—	1	—	—	2424
J2254-1734	0.068	COS	1	0.010	0.167	1	0.010	0.057	12029
		FOS-H	1	—	—	1	—	—	6484
J2254+1136	0.323	FOS-H	1	0.010	0.422	1	0.010	0.309	2424,2578,3791
J2255-5435	0.000	STIS	0	—	—	1	—	—	8287
J2257+1340	0.593	COS	1	0.010	0.476	2	0.010	0.476	11598
J2258-2758	0.926	STIS	1	0.379	1.026	1	0.379	0.907	8225
J2303+0852	0.015	COS	1	0.010	0.115	1	—	—	12212

Table A.5: — Continued

QSO	z_{em}^a	Instrument	Search Path			Statistical Path			Proposal ID
			F_{search}^b	Min z	Max z	F_{stat}^c	Min z	Max z	
J2303–6807	0.512	FOS-H	1	0.391	0.611	1	0.391	0.496	2424
		FOS-L	1	—	—	1	—	—	2424
J2304+0311	1.052	STIS	1	0.010	0.415	0	—	—	7358
J2311+1008	0.432	FOS-H	1	0.010	0.531	1	0.010	0.417	4079,4953
J2316–2849	0.000	STIS	0	—	—	1	—	—	8287
J2316–3349	3.100	STIS	0	—	—	1	—	—	8287
J2321–7026	0.300	COS	1	0.010	0.399	1	0.010	0.287	12936
J2328+0022	1.308	STIS	1	0.412	1.408	0	—	—	9382
J2330–5506	0.494	STIS	1	0.287	0.593	1	0.287	0.479	9507
J2331+0038	1.486	STIS	1	0.638	1.585	0	—	—	9382
J2334+0052	1.040	STIS	1	0.428	1.139	0	—	—	9382
J2339–0029	1.340	STIS	1	0.809	1.439	0	—	—	9382
J2342–0322	0.896	FOS-H	1	0.354	0.995	1	0.354	0.877	2424,4000
		FOS-L	1	—	—	1	—	—	4000
J2345–0059	0.789	COS	1	0.010	0.476	2	0.010	0.476	11598
J2345–1555	0.621	COS	1	0.010	0.480	0	—	—	13008
J2346–0016	3.504	STIS	0	—	—	1	—	—	9067
J2346+0930	0.672	FOS-H	1	0.354	0.771	1	0.354	0.655	3791
		FOS-L	1	—	—	1	—	—	3791
J2350–4325	2.885	COS	1	0.010	0.187	0	—	—	11528
		FOS-H	1	0.340	1.695	1	0.340	1.695	6449
		STIS	1	0.188	0.339	1	0.010	0.339	8875
J2351–1427	2.933	STIS	0	—	—	1	—	—	8287
J2351–0108	0.174	COS	1	0.010	0.209	1	0.010	0.162	12569
		FOS-H	1	—	—	1	—	—	4953
J2352–0028	1.624	STIS	2	—	—	0	—	—	9382
J2353–0028	0.761	STIS	1	0.483	0.860	0	—	—	9382
J2355–3357	0.702	FOS-H	1	0.346	0.801	1	0.346	0.685	2424
		FOS-L	1	—	—	1	—	—	2424

Table A.5: — Continued

QSO	z_{em}^{a}	Instrument	Search Path			Statistical Path			Proposal ID
			$F_{\text{search}}^{\text{b}}$	Min z	Max z	$F_{\text{stat}}^{\text{c}}$	Min z	Max z	
J2358–5440	0.000	STIS	0	—	—	1	—	—	8287
J2359–3037	0.165	COS	1	0.010	0.210	2	0.010	0.153	12864

^aEmission redshift of quasar

^bSearch flag: (0) Low S/N or bad spectrum; (1) Included; (2) BAL quasar

^cStatistical flag: (0) Non-Statistical; (1) Statistical; (2) Galaxy Sample

Appendix B

Figures

This appendix contains the full figure sets for the figures described in the text.

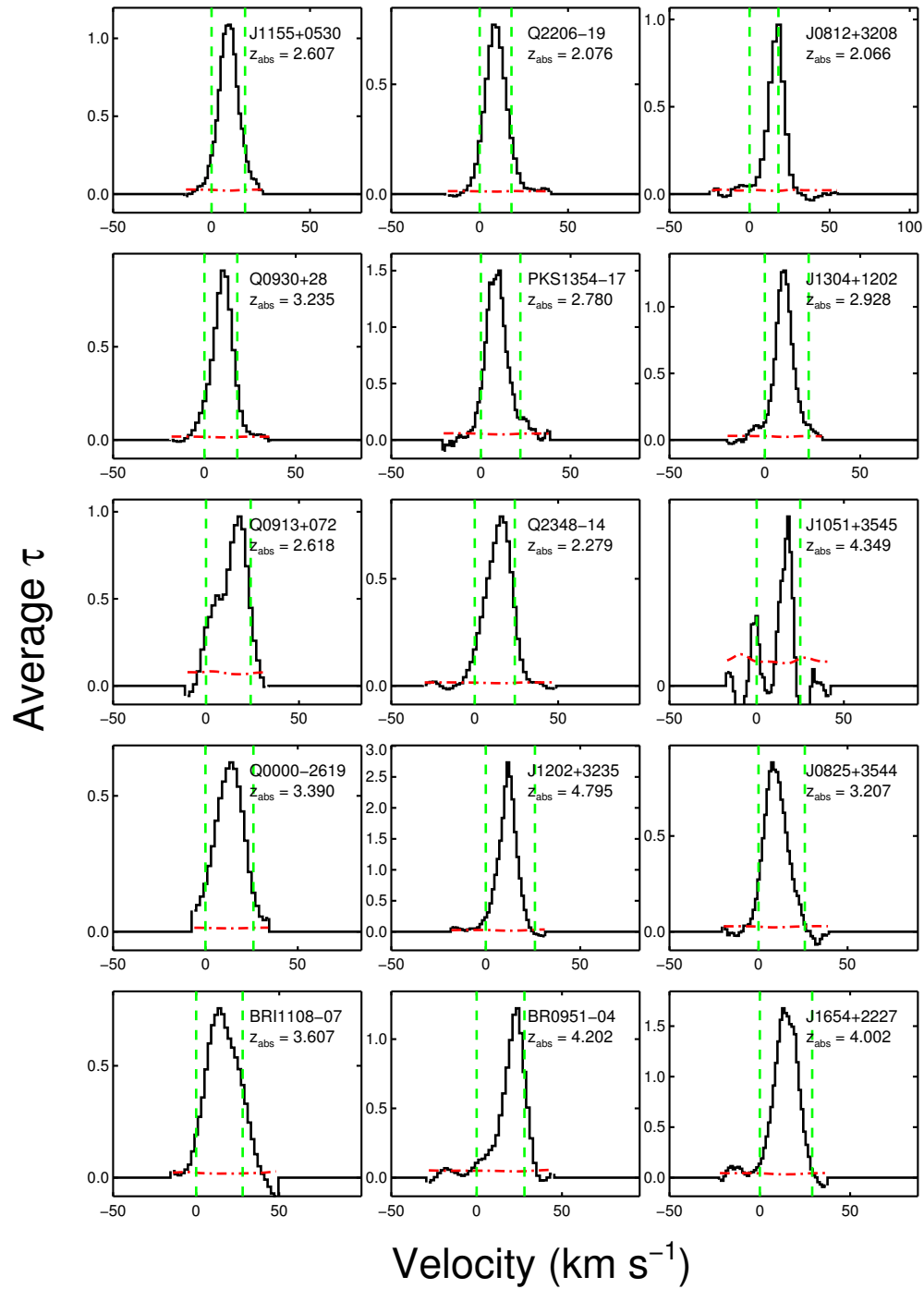


Figure B.1: See Figure 2.1 for details

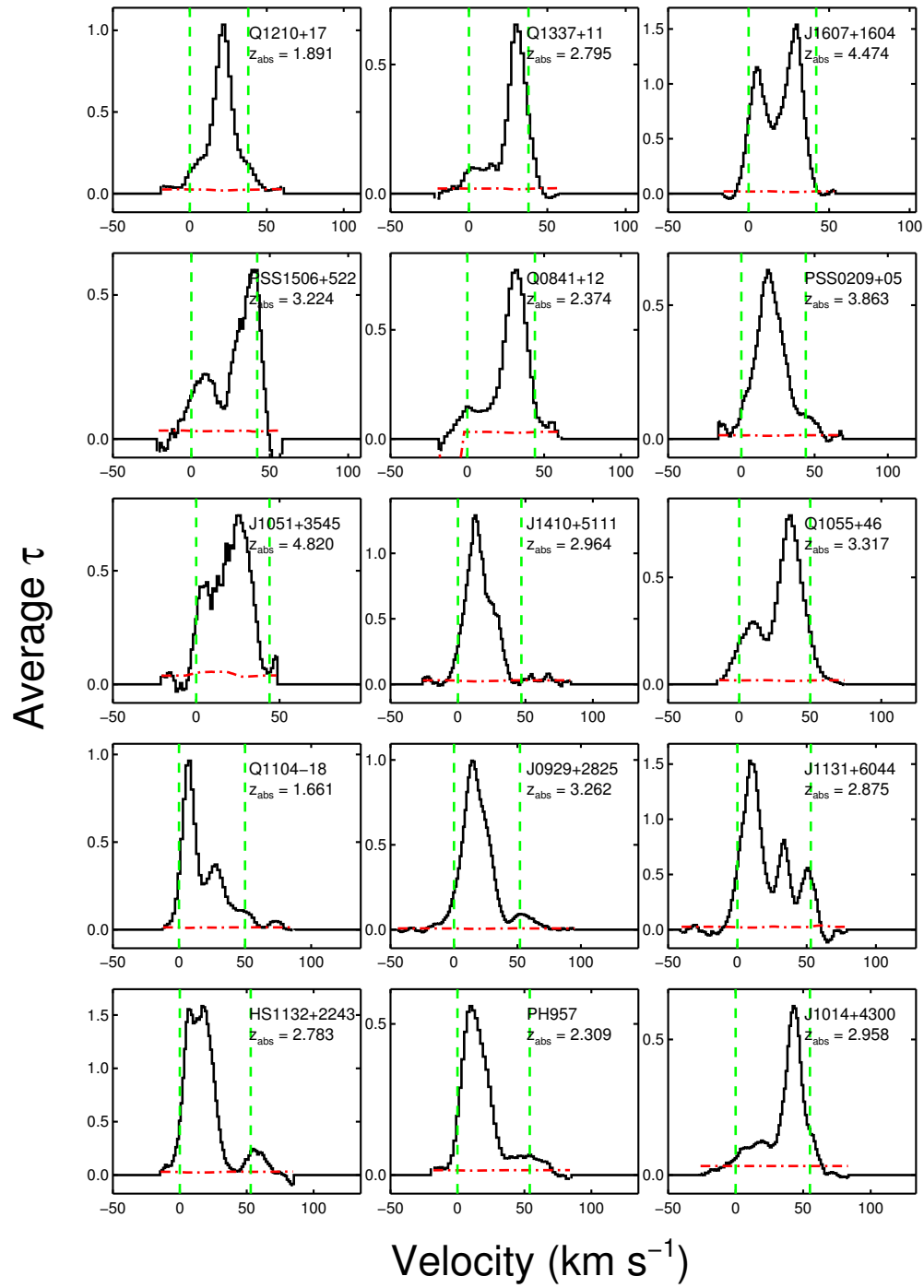


Figure B.1: — Continued

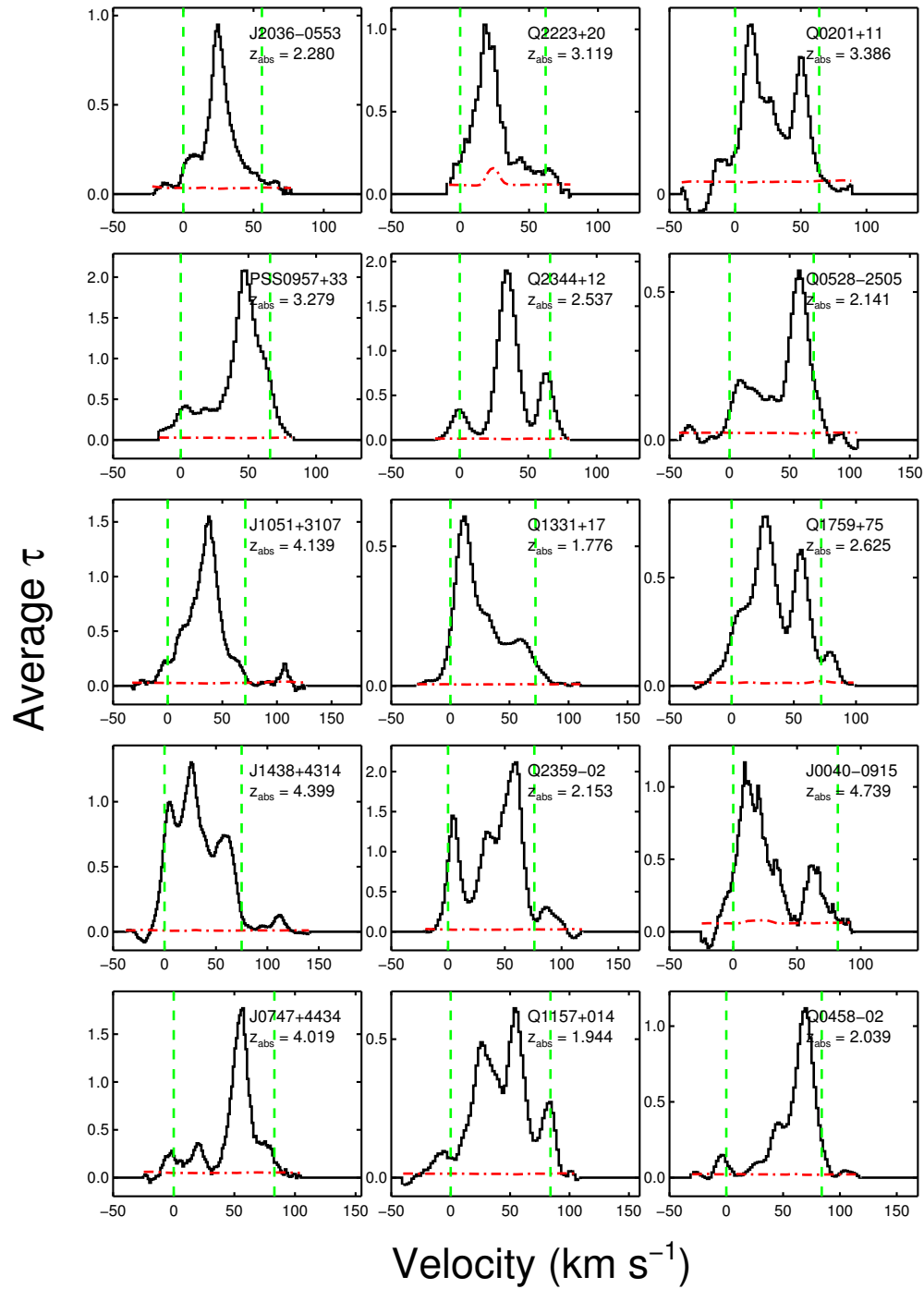


Figure B.1: — Continued

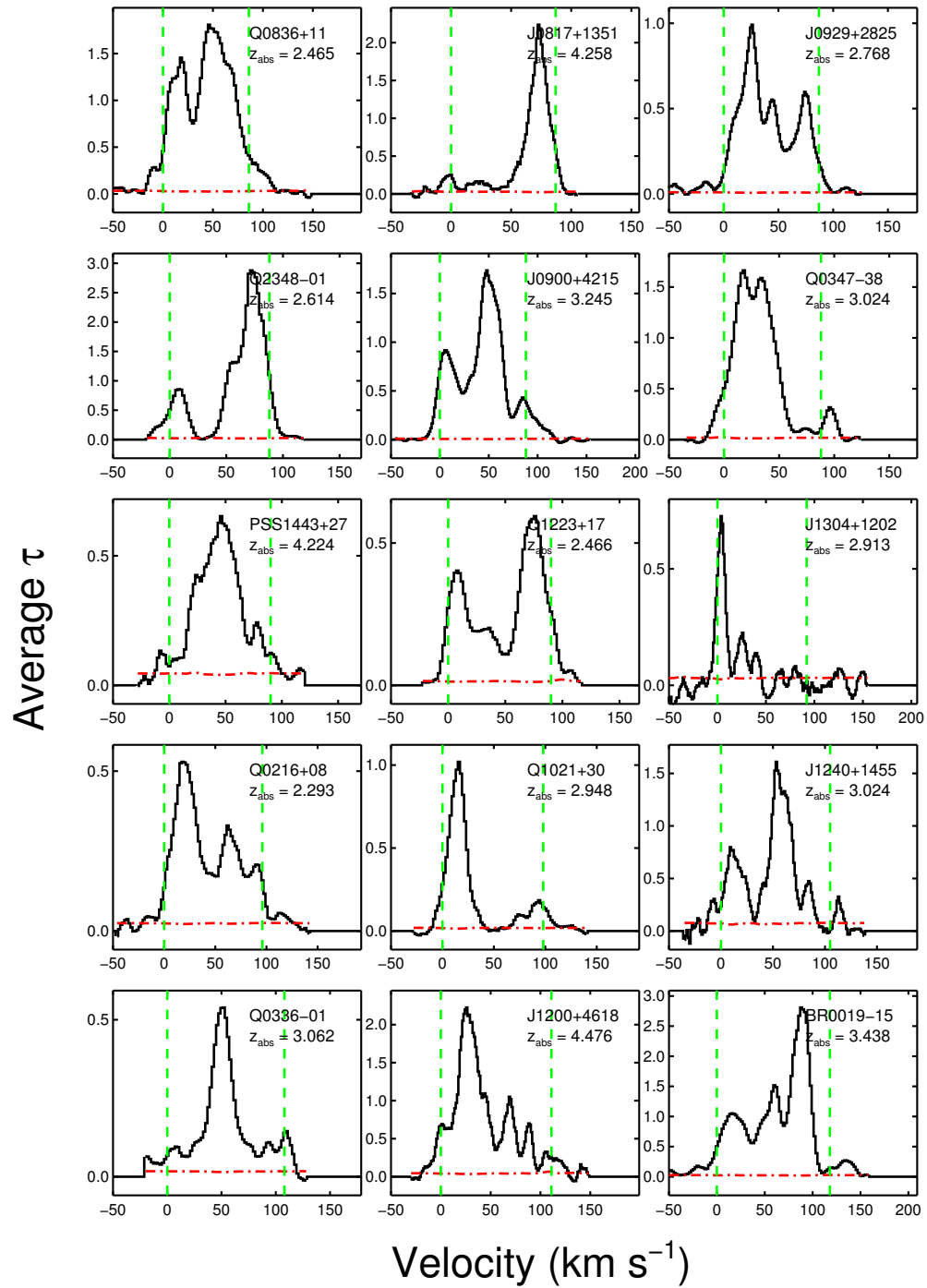


Figure B.1: — Continued

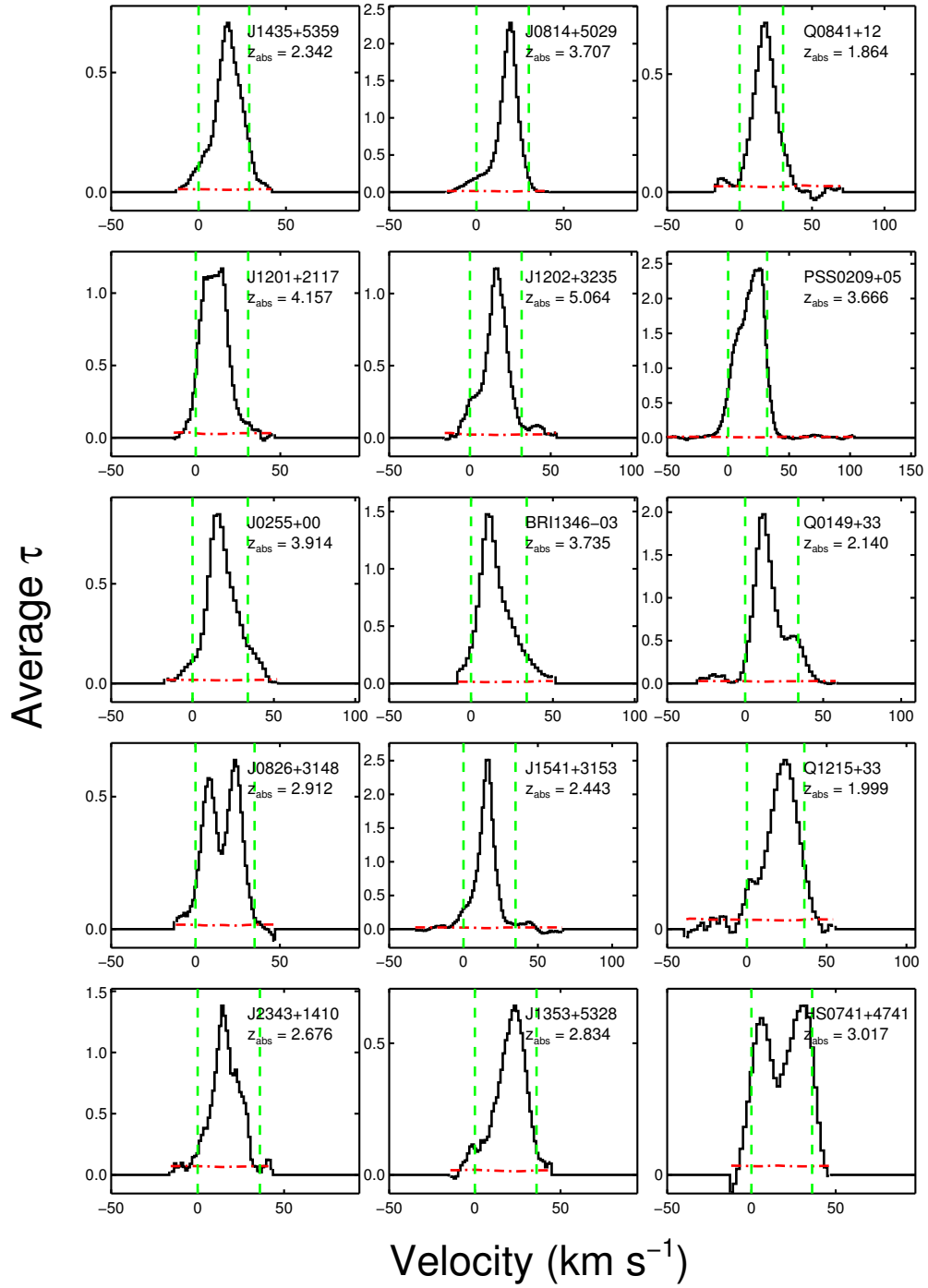
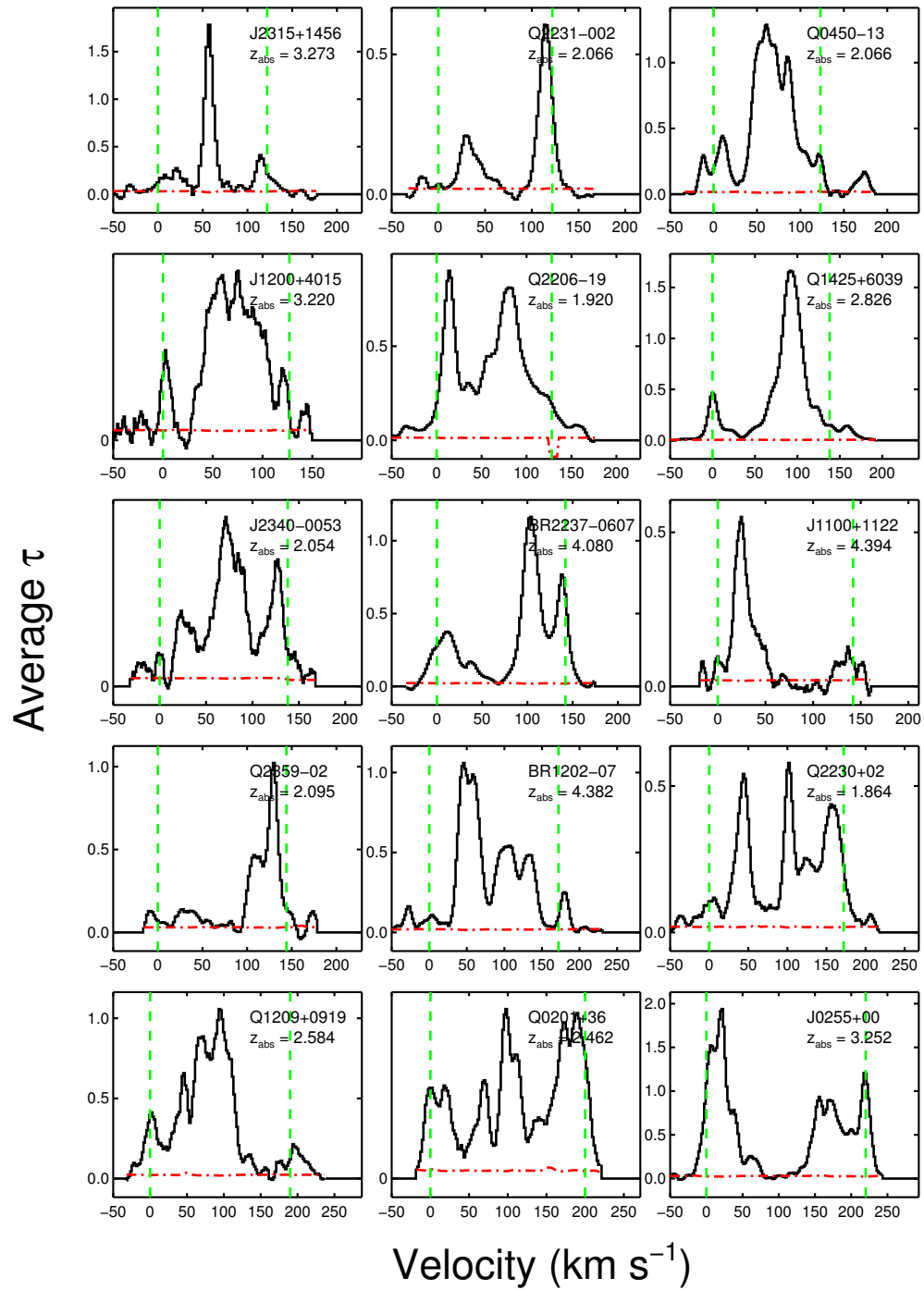


Figure B.1: — Continued



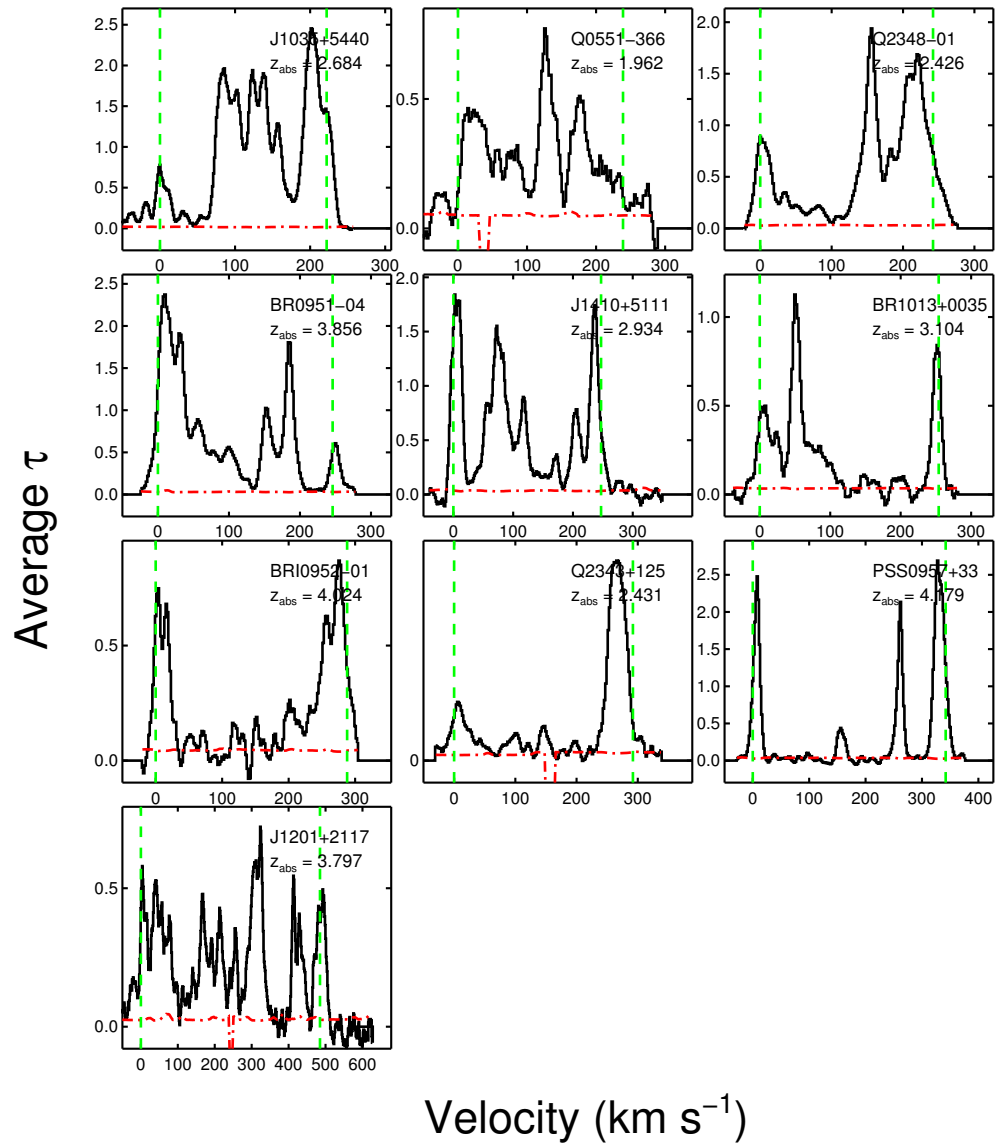


Figure B.1: — Continued

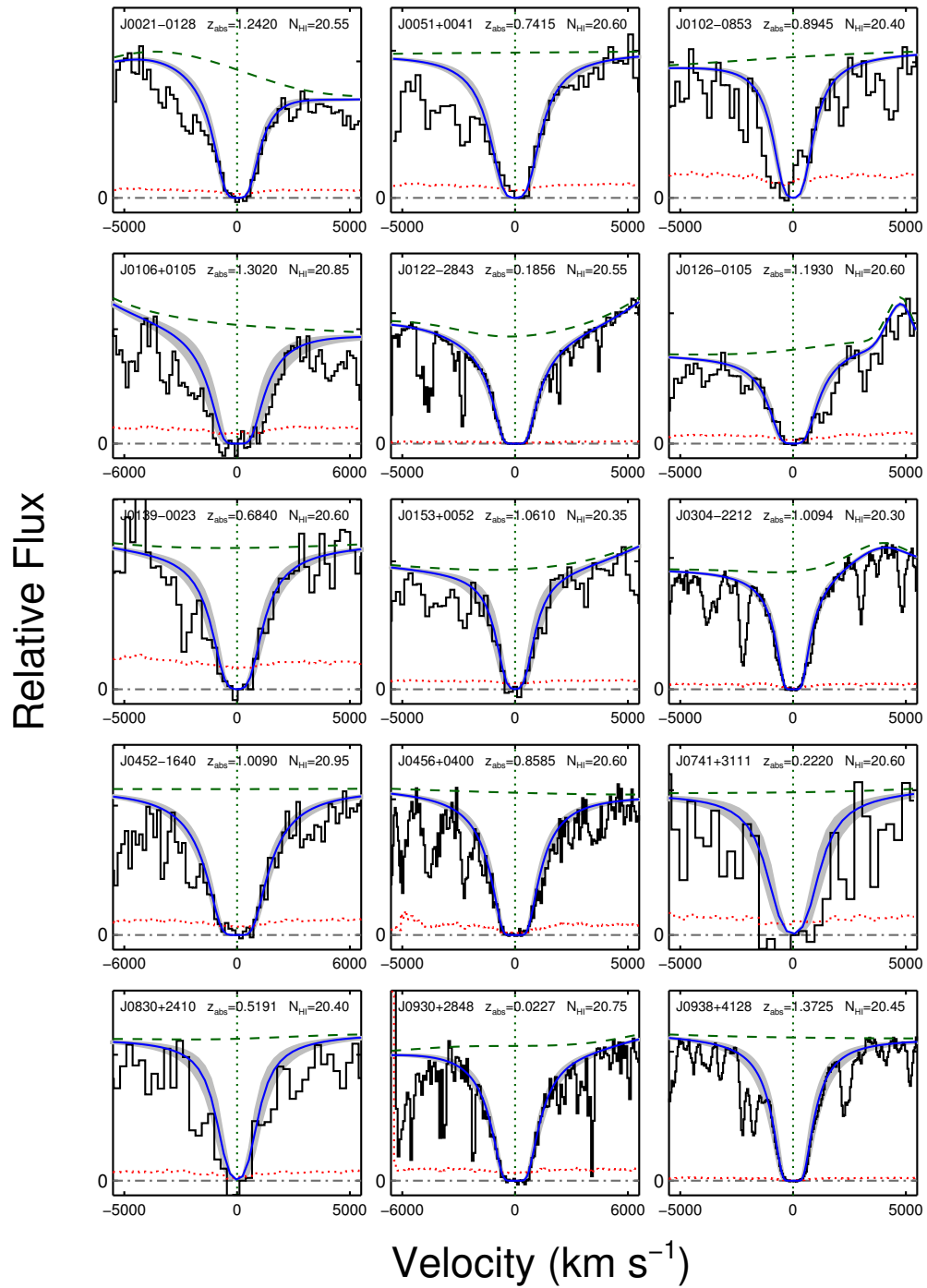


Figure B.2: See Figure 4.3 for details

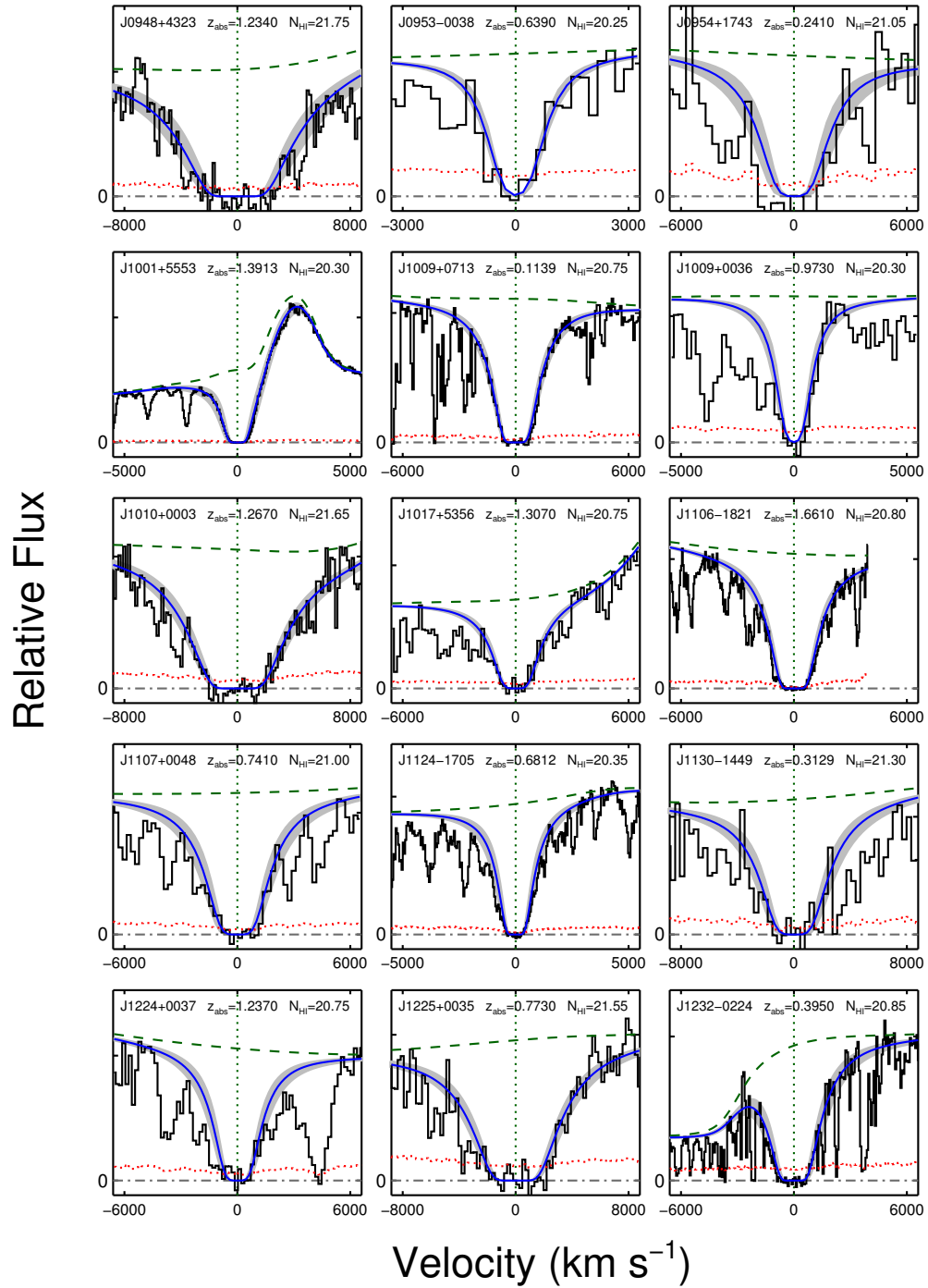


Figure B.2: — Continued

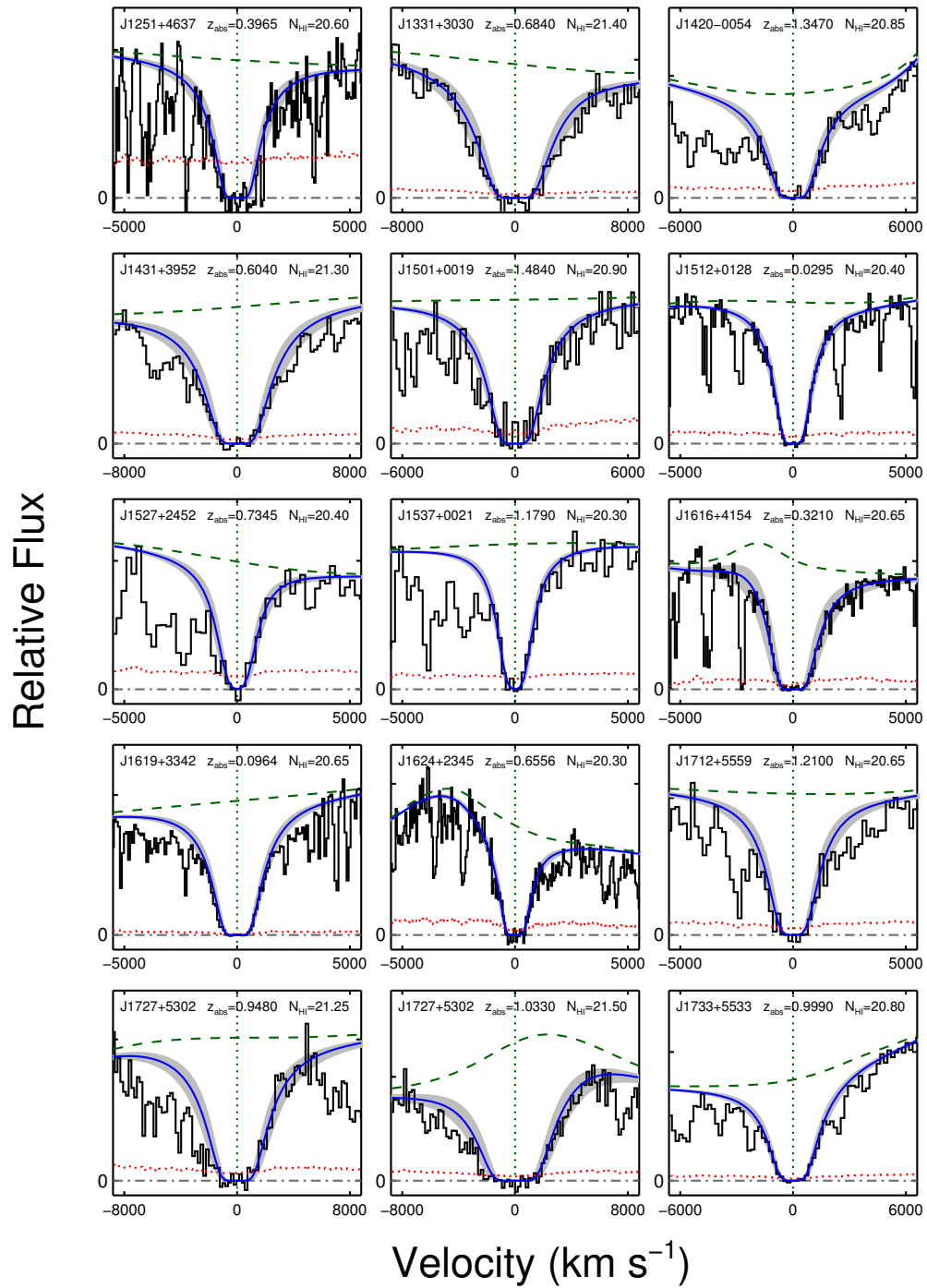


Figure B.2: — Continued

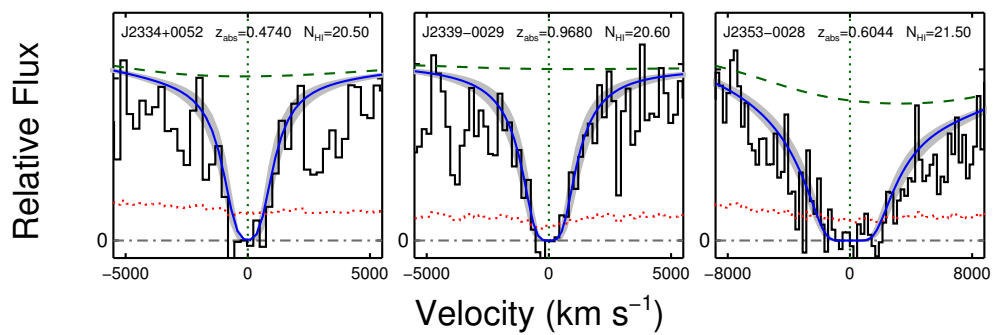


Figure B.2: — Continued